ORGANOANTIMONY AND ORGANOPHOSPHORUS COMPOUNDS FOR CHEMICAL SENSING: TOWARD DESIGNED FLUORIMETRIC AND COLORIMETRIC RESPONSES

A Dissertation

by

ANNA MARIE CHRISTIANSON

Submitted to the Office of Graduate and Professional Studies of
Texas A&M University
in partial fulfillment of the requirements for the degree of

DOCTOR OF PHILOSOPHY

Chair of Committee,	François P. Gabbaï
Committee Members,	Donald J. Darensbourg
	Oleg V. Ozerov
	Jodie L. Lutkenhaus
Head of Department,	Simon W. North

May 2017

Major Subject: Chemistry

ABSTRACT

The design of molecular chemical sensors has generally relied on the use of colored and/or luminescent organic dyes or transition metal complexes; however, recent advances have been made in the use of heavy main group elements such as phosphorus, selenium, antimony, and tellurium as functional elements in sensors. We have become interested in the use of heavy Group 15 elements for sensing, especially Lewis acidic organoantimony(V) derivatives, which may be used for the selective sensing of fluoride anions in water. Building upon our previous work, we have now developed a series of heavy Group 15-incorporating compounds featuring improved photophysical properties including visible-wavelength absorption and high quantum yield emission, sensitivity to a wider range of analytes for sensing, and a diverse manifold of sensing response mechanisms based on chemistry at the main group element. We have focused on uncovering these mechanisms through structural analysis and spectroscopic characterization supported by DFT computational methods, in order to gain understanding of the link between analyte recognition at the Group 15 element and the observed photophysical change.

To this end, we have synthesized and characterized antimony(III)- and antimony(V)-substituted derivatives of highly fluorescent BODIPY and fluorescein dyes, as well as intensely colored ruthenium polypyridyl complexes. The Lewis acidic Sb(V)-decorated BODIPY displays a “turn-on” fluorescent response to both fluoride and cyanide anions, while the Sb(III)-decorated fluorescein derivative functions as a “turn-

off" sensor for peroxide. The Sb(V)-substituted ruthenium polypyridyl complex also responds to fluoride and cyanide anions, with a response that is observable both colorimetrically and electrochemically. A phosphorus-decorated fluorescein derivative has also been developed as a "turn-on" fluorescent sensor for gold(III) ions in aqueous solution, which is functional at nanomolar concentrations of gold. Finally, a series of Sb(III)- and Sb(V)-incorporating heterocycles have been developed that feature direct interaction of antimony-based σ* orbitals with the organic π system. In these compounds, the incorporation of antimony within the π-conjugated structure provides direct control over the photophysical properties, which holds promise for the design of anion sensors as well as color-tunable materials.

DEDICATION

Ad Gloriam Dei

ACKNOWLEDGEMENTS

I would like to acknowledge everyone who has encouraged and supported me in reaching this point in my education, career, and identity. In a special way, I want to thank my awesome high school chemistry and physics teacher, Ruth Ann Pieri (also an Aggie chemist!) who first taught me about the exciting world of molecules. She was also the first to encourage me to pursue a degree in science, to which at the time I replied that I wasn't really so interested in that—well, now I really have to give her permission to smirk. Next, I want to thank my undergraduate chemistry professors: Dr. Bill Hendrickson, Dr. Scott Boegeman, Dr. Charles Eaker, Dr. Ellen Steinmiller, and Dr. Franklin Beckles. They are all champions and a great inspiration to me as I go forward in my teaching career. I also want to thank my undergraduate summer research advisors, Dr. Mikhail Barybin from University of Kansas and Dr. Frank Uhlig from Technische Universität Graz, for the great experiences I had working in their labs. It is because of the wonderful education I have received from these and many other teachers and professors that I want to join them in passing that knowledge on to others.

I want to thank my advisor, Dr. François Gabbaï, for being a fantastic boss and supporting me in both my research and my desire to teach. I have learned so much from him and been truly awed by his dedication and love for science. His patience and understanding during my inevitable struggles along the way have been invaluable in getting me this far, and his mentorship and questioning have challenged me to become a better scientist.

I want to thank my committee members: Dr. Don Darensbourg, who also gave me my first opportunity to do graduate research in his labs my first summer here; Dr. Oleg Ozerov, who taught me Organometallic Chemistry and has helped me take advantage of many opportunities in my grad school experience; and Dr. Jodie Lutkenhaus, who has been a very helpful and gracious committee member as well as an inspiring figure for me in her research. I also want to thank all the professors and staff at Texas A&M, and in a special way Dr. Tamara Powers and Dr. Christine Mullen, who have been amazingly supportive teaching and personal mentors to me during my time here. Finally, I have to give so much credit to my labmates I have worked with in the Gabbaï Group, past and present: Dr. Iou-Sheng Ke, Dr. Masato Hirai, Dr. James Stuart Jones, Dr. Kantapat Chansaenpak, Dr. Haifeng Yang, Dr. Baofei Pan, Dr. Kewei Huang, Dr. Boris Vabre, Dr. Daniel Tofan, Dr. Guillaume Bélanger-Chabot, Dr. Sumit Sahu, Dr. Rosmita Borthakur, Dr. Mitsukuni Tsunoda, Prof. Min Hyung Lee, Adriana Lunsford, Lauren Leamer, Srobona Sen, Ahmed Ali, Chang-Hong Chen, Mengxi Yang, Elham Tabei, Courtney Dickie, Ying-Hao Lo, Di You, Gregory Day, Christina Lollar, Kevin Jack, Lindy Chase Elrod, Minji Kim, Nilanjana Pati, Sebastien Lajeune, Mazarine Laurent, Austin Williamson, and especially my own undergraduate mentees, James Tyler Moore and Nicolas Capra. Every one of them deserves my gratitude for sharing with me their knowledge, support, comradeship, and stuff that I borrowed from their hoods.

On the personal side, I cannot express enough gratitude to my big, loving family. My parents and grandparents taught me the value of education, hard work, and virtue, always backing up their words by their example. My parents, Mitch and Liz DeLaRosa, sacrificed for me and supported me in going to a school I loved and studying the subject I was

interested in. My siblings Julia, Cecilia, Manuel, and Benny have been my friends and my inspiration to keep working hard to set them a good example. My new family Dana and Debbie Christianson, Joe, and Caitlin have been just as supportive of their daughter/sister-in-law since they have known me. I want to thank my many dear friends, too many to name, who have helped me stay sane and happy in this sometimes-crazy life. I also want to thank the community at St. Mary's Catholic Center in a special way for supporting me in prayer and in deed as only the Church can.

Penultimately (a good Latinate word), I want to thank my wonderful husband, Jon. His love, laughter, and encouragement have done more than he knows to keep me going on this path, and I can only hope to give him as much support in accomplishing his goals as he has for me.

Finally, I must thank my loving God—for His beautiful creation made with so much to discover, for his many blessings upon me and my loved ones in this life, and for the gift of His sustaining grace in my soul. All glory and thanks be to Him, now and ever and forever.

CONTRIBUTORS AND FUNDING SOURCES

This work was supervised by a dissertation committee consisting of Professor François Gabbaï (advisor), Professor Donald Darensbourg, and Professor Oleg Ozerov of the Department of Chemistry and Professor Jodie Lutkenhaus of the Department of Chemical Engineering.

All work for this dissertation was completed by the student, under the advisement of Professor François Gabbaï of the Department of Chemistry.

Graduate study was supported by a Graduate Diversity Fellowship from Texas A&M University and a Graduate Research Fellowship from the National Science Foundation (grant number DGE-1252521).

This work was made possible in part by support from the National Science Foundation under Grant Number CHE-1300371, the Welch Foundation under Grant Number A-1423, and Texas A&M University through the Arthur E. Martell Chair of Chemistry funds. Its contents are solely the responsibility of the authors and do not necessarily represent the official views of these foundations.

NOMENCLATURE

BODIPY	Boron dipyrromethane
Bpin	Pinacolatoboryl
COSY	Homonuclear correlation spectroscopy
CTABr	Cetyltrimethylammonium bromide
CTAC	Cetyltrimethylammonium chloride
DCM	Dichloromethane
DFT	Density functional theory
DMF	N,N-dimethylformamide
DMSO	Dimethylsulfoxide
HOMO	Highest occupied molecular orbital
HPLC	High performance liquid chromatography
LUMO	Lowest unoccupied molecular orbital
MeCN	Acetonitrile
MLCT	Metal-to-ligand charge transfer
MS	Mass spectrometry
NMR	Nuclear magnetic resonance
PeT	Photoinduced electron transfer
POPOP	1,4-bis(5-phenyloxazol-2-yl) benzene
ROS	Reactive oxygen species
TASF	Tris(dimethylamino)sulfonium difluorotrimethylsilicate

TBACN	Tetra-n-butylammonium cyanide
TBAF	Tetra-n-butylammonium fluoride
TCSPC	Time-correlated single-photon counting
TD-DFT	Time-dependent density functional theory
THF	Tetrahydrofuran
tht	Tetrahydrothiophene
TPABr	Tetrapropylammonium bromide

TABLE OF CONTENTS

Page

LIST OF FIGURES

Page

LIST OF TABLES

Page

1. INTRODUCTION TO ORGANOANTIMONY AND ORGANOPHOSPHORUS COMPOUNDS FOR APPLICATION IN CHEMICAL SENSING

1.1 Introduction

The chemistry of heavy main group elements offers new opportunities for the design of functional molecules and materials based on the unique properties of these elements.[1-7] As implied by their placement in the periodic table, the properties of the heavier elements of the p block bridge the gap between those of the second-row "organic" elements and those of the d-block transition metals.[8] Main group elements beyond the second row utilize s and p valence electrons in their bonding, like the organic elements; yet, they may readily adopt hypervalent configurations with as many as six ligands around the central element, similar to transition metal complexes.[8] The heaviest main group elements, such as tin, lead, and bismuth, display decidedly metallic properties both in their elemental and compounded forms, while, moving up and across the p block, elements such as arsenic and germanium display metalloidal properties, and, farther, phosphorus and sulfur act as true nonmetals. This rich diversity of the properties of the heavy main group elements is both the appeal and the challenge in exploring their chemistry, which may defy predictions based on analogies to the lighter elements, while opening up new potential to explore and create.

Perhaps nowhere is this diversity of properties in the main group elements so well exemplified as in the Group 15 pnictogens: nitrogen, phosphorus, arsenic, antimony, and bismuth. These elements carry five s/p valence electrons and are typically

found as compounds in the +III and +V oxidation states. Nitrogen and phosphorus, both nonmetals, form strong bonds to carbon and oxygen; in the +III state, they act as prototypical Lewis bases through the remaining lone pair of electrons. However, while nitrogen is more electronegative than carbon and readily forms strong π bonds, phosphorus is much less electronegative and its π bonds are highly polarized.[9] Going down the group, arsenic and antimony are usually classified as metalloids and bismuth as a metal. Covalent bonds to carbon become weaker and more polarized going down the group due to poor orbital overlap between carbon and the large, diffuse heavy elements.[7] As(III) and Sb(III) compounds are much weaker donors than amines or phosphines,[10-11] and Sb(III) and Bi(III) compounds can even display Lewis acidic properties despite the presence of a lone pair![12] In their higher oxidation state, Sb(V) compounds show even stronger Lewis acidity, and indeed are among the strongest Lewis acids known.[13-16] Due to the inert pair effect, bismuth is less readily oxidized to the +V state; Bi(III) compounds do not typically act as Lewis bases, and in fact, Bi^{3+} can exist as the free cation.[9] The heavy pnictogens including Sb and Bi also readily form hypervalent coordination complexes, which have been increasingly studied in recent years.[17-20] Nevertheless, this diverse chemistry of the heavier Group 15 elements leaves much still to be discovered. Recently, we have actively pursued the development of heavy Group 15 chemistry, especially of organoantimony(V) Lewis acids as anion sensors, as will be reviewed in this Introduction. The research discussed in this dissertation represents an extension of our previous work, expanding the possibilities that heavy Group 15 compounds hold for applications in chemical sensing.

1.2 Organoantimony(V) compounds as Lewis acids

We were first drawn to this field in the context of exploring organo-main group Lewis acids. Lewis acidic compounds are relevant to a wide variety of chemical applications, from chemical sensing[21-28] to small-molecule activation[29-34] to catalysis.[35-41] The prototypical organo-main group Lewis acids are organoboranes, such as the widely-used tris(pentafluorophenyl)borane,[42-43] which accept an electron pair at the vacant p orbital of the electron-deficient boron atom. However, organoantimony(V) species have recently received much attention as potentially stronger and more tunable Lewis acids than boranes. The antimony pentahalides SbF_5 and $SbCl_5$ are well-known to exhibit strong Lewis acidity, and have been shown both experimentally and theoretically to be more acidic than the corresponding boranes BF_3 and BCl_3.[13, 16] Indeed, SbF_5 is one of the major components of "magic acid" FSO_3H-SbF_5 and other superacids.[14-15] These compounds are highly corrosive and reactive toward water, which hampers their use in many practical applications. With replacement of the halides for organic substituents, however, the corrosivity and water-sensitivity of antimony(V) compounds can be suppressed while still allowing for strong Lewis acidity. For example, the simple organoantimony cation $[Ph_4Sb]^+$ is a strong enough Lewis acid to capture fluoride anions from water under biphasic conditions.[44-46]

The high Lewis acidity of antimony(V) derivatives may be rationalized on the basis of the large size of antimony, which readily accommodates coordination numbers up to six, as well as its electropositivity and polarizability that result in a buildup of

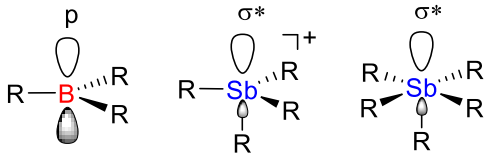

Figure 1. Representation of the operative electron-accepting orbitals in organoboron and organoantimony(V) Lewis acids.

positive charge at the antimony center. In terms of orbital interactions, the origin of Lewis acidity at antimony(V) centers is the presence of accessible σ* antibonding orbitals along bonds between antimony and a more electronegative element (Figure 1). Because of the electropositivity of antimony and the weakness of its covalent bonds, these σ* orbitals are mainly localized at the antimony center and are energetically low-lying. Thus, the binding of a Lewis base at antimony involves the donation of an electron lone pair to this orbital, as in the case of the vacant p orbital in organoboranes. This behavior is the same in both four-coordinate cationic stibonium compounds and five-coordinate neutral stiborane compounds, although in neutral stiboranes it is necessary for the structure to distort from the expected trigonal bipyramidal geometry toward a square pyramidal geometry that creates an open site at the antimony center for binding of the Lewis base.

In 2011, the Gabbaï group originally reported a study of bifunctional Lewis acids featuring a bidentate borane-onium ion motif, which hinted at the high affinity of antimony(V) for anions and led us to question whether cationic organostibonium compounds could rival or surpass organoboranes as functional organo-main group Lewis acids. It was found that the borane-stibonium compound [**1**]$^+$ exhibited higher fluoride

ion affinity than the analogous borane-phosphonium compound [**2**]$^+$ based on the competition experiment shown in Figure 2 below.[47]

The fluoride adduct **1**-F was independently prepared by reaction of [**1**]$^+$ with $[S(NMe_2)_3][Me_3SiF_2]$ (TASF) and characterized by X-ray crystallography. The crystal structure reveals that the fluoride anion is bound to both main group elements, forming a B-F-Sb bridging motif. The B-F bond distance (1.521(4)Å) is elongated relative to that in the borane-phosphonium analog **2**-F (1.482(3)Å) and in the monofunctional phosphonium-borane derivative *p*-$(MePh_2P)C_6H_4(BMes_2F)$ (1.476(4)Å), implying that the more Lewis acidic stibonium group pulls the fluoride anion closer to itself and farther away from the borane. The higher Lewis acidity of antimony compared to phosphorus is also evinced by the pnictogen-fluoride bond distances in these structures—despite the larger atomic radius of antimony, the Sb-F bond in **1**-F (2.450(2)Å) is actually shorter than the P-F bond in **2**-F (2.666(2)Å).[47]

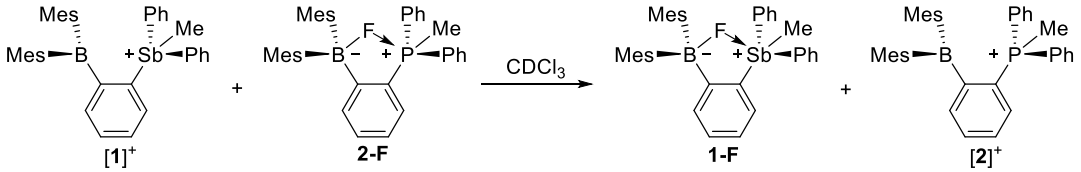

Figure 2. Competitive anion binding experiment between phosphonium-borane and stibonium-borane Lewis acids.

Cationic stibonium compounds are generally expected to be stronger Lewis acids than neutral stiboranes due both to Coulombic effects and reduced steric hindrance at the antimony center; however, further research in the Gabbaï group has shown that

stiboranes bearing electron-withdrawing ligands may also display significant Lewis acidity.[26, 48] Particularly, we have found that the Lewis acidity of neutral stiboranes is increased in spirocyclic derivatives such as **3** (Figure 3a).[26, 49] In these compounds, the chelating ligands enforce two angles smaller than 90° about the antimony center, which favors the distortion toward square pyramidal geometry and results in enhanced Lewis acidity at the open site thus formed. Fluoride titration studies on **3** in a 7:3 THF:H_2O mixture confirmed that this compound is able to capture fluoride under these conditions with a high equilibrium binding constant of 13,500 ± 1,400 M^{-1}. The distorted square pyramidal geometry at antimony in **3** is confirmed by a solid-state crystal structure, and DFT calculations of the frontier molecular orbitals show that the LUMO is located around the biphenyl ligand with a large contribution to the π system from the Sb-C_{Ph} σ* orbital, which projects out from the open face of the square pyramid, accounting for the Lewis acidity of **3**.[26, 49] The installation of two antimony(V) centers on a bidentate ligand framework has also been used as a strategy to obtain enhanced Lewis acidity in neutral organoantimony(V) compounds, as in the case of **4** (Figure 3b).[48] In this bifunctional Lewis acid, both antimony(V) centers cooperate to bind fluoride in a bridging motif, a

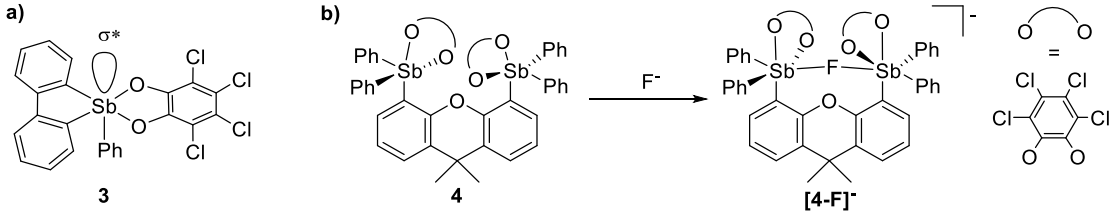

Figure 3. a) Lewis acidic spirocyclic neutral stiborane showing the location of the Sb-based σ* orbital.[26] b) Fluoride binding in the pocket of a bifunctional bis(stiborane).[48]

coordination that is favorable even in 95% H_2O mixtures, where fluoride anions are strongly solvated. These binding studies show that organoantimony(V) derivatives can behave as strong Lewis acids that are also water-compatible, and encouraged us to explore their use in practical applications. This dissertation will focus on the use of organoantimony compounds for the specific application of chemical sensing, especially in sensing of anions such as fluoride.

1.3 Principles of chemical sensing

At its most basic, a chemical sensor is any molecule or material that responds to the presence of an analyte by some observable change in properties. The ability to design chemical sensors with a specific response to a particular analyte is a powerful tool for chemical analysis in many contexts, from environmental monitoring to biological imaging to stimulus-responsive materials.[50-52] The most common and convenient type of chemical sensors are optical sensors, which display a change in photophysical properties in response to the analyte of interest. These photophysical responses may be colorimetric, involving light absorption, or fluorimetric, involving light emission, or both. They may consist of an increase or "turn-on" of absorption or emission at a given wavelength, or conversely a "turn-off" of absorption or emission, or a color change in which absorption or emission decreases at one wavelength and increases at another. These changes can then be monitored with quantitative accuracy by absorption and emission spectroscopy.

In an effective optical sensor, two processes must be coupled: the recognition event and the photophysical response.[52] First, the sensor must recognize the analyte of interest by a specific chemical interaction, such as the coordination of an ion or the catalysis of a chemical reaction. This interaction must be selective, i.e. it must interact only with the analyte of interest and avoid interferences from other species. Secondly, this chemical interaction must be transduced into a distinct, measurable photophysical change. Herein lies the challenge of chemical sensor design, since the analyte must not only interact chemically with the sensor, but must also be able to modulate its photophysical properties. In many molecular sensors, the recognition and response elements of the system are simply tethered together in a "receptor-spacer-reporter" arrangement (Figure 4).[50] This approach is effective when the photophysical properties of the reporter group, usually an organic dye or colored transition metal complex, are sensitive to remote electronic effects, such as inductive effects, charge transfer, or electron transfer in the excited state, which are modulated by analyte interaction with the receptor group.[50-52] Another strategy is to integrate the reporter and receptor groups, such that analyte interaction at the receptor directly modifies the structure and thus photophysical properties of the reporter group (Figure 4). For example, the analyte may

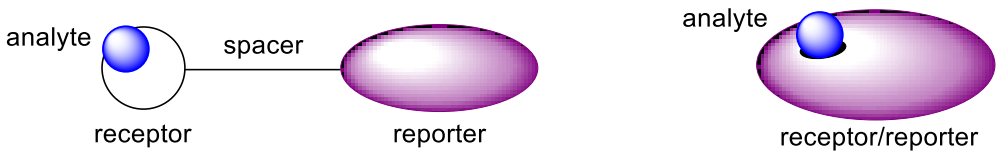

Figure 4. Schematic diagram of two approaches to the design of optical sensors, using a pendant or incorporated receptor group, respectively.

induce a chemical reaction that creates or liberates the reporter group, or may directly interfere with or enhance π conjugation across a chromophore or fluorophore.[53]

An ideal chemical sensor would display high selectivity to the analyte of interest and also high sensitivity of the response, in order to enable detection of low levels of analyte. In general, the more dramatic the overall photophysical response is, the more sensitive the sensor. In this regard, fluorimetric sensing has great advantages over colorimetric sensing, since the fluorescence phenomenon is rarer and thus less susceptible to interferences from other species. Fluorescence measurements can be made with excellent sensitivity and spatial precision, with relatively simple instrumentation. This is especially important for applications in biological imaging, where fluorescent probes may be used to tag molecules or identify species that can then be monitored *in vivo* in real time.[54] For this reason, the development of molecular fluorescent sensors for biological applications is a blossoming field. Numerous sensors have been developed for biologically relevant species such as thiols,[55] reactive oxygen species,[56-59] metal cations,[60-62] and anions.[63]

1.4 Organoantimony(V)-based anion sensors

The simple interaction of the coordination of an anion to a Lewis acid can form the basis of a strategy for designing anion-responsive sensors. The ability to recognize or extract a particular anion or set of anions has relevance to many fields including biochemistry, biomedicine, host-guest and supramolecular chemistry, toxicology, environmental remediation, organocatalysis, and chemical separation.[63] We therefore

saw an opportunity in this field for the application of organoantimony(V) Lewis acids that are able to bind anions in solution, including in aqueous media.

Among anions of interest for chemical sensing, fluoride stands out.[64-65] Fluoride is relevant to many applications touching upon human health and environmental analysis, making the ability to detect it in trace amounts (ppm or less) important, especially in water. [66-67] As is commonly known, fluoride in small amounts contributes to dental health, and is often added to public drinking water for this reason.[68-69] Fluoride has also been explored as a therapeutic agent in the treatment of osteoporosis to increase bone density.[66] However, fluoride consumed at excessive levels can cause health problems, including kidney damage and dental or skeletal fluorosis, a disease characterized by abnormal tooth or bone mineralization resulting in severe pain and risk of bone fractures.[70-73] Prevalence of fluorosis in certain geographic regions has been linked to high concentrations of fluoride in the water supply.[74-76] Because of these risks, water fluoridation in many countries is strictly regulated, and the World Health Organization's recommendation for fluoride levels in drinking water is only 0.5-1.0 ppm.[77-78] In the United States, the recommended fluoride level in drinking water was recently lowered from 1.2 ppm to 0.7 ppm, while the maximum contaminant level (MCL) for fluoride allowed by the Environmental Protection Agency is only 4 ppm, with a recommended secondary maximum contaminant level (SMCL) of 2 ppm.[79-80] In addition to its application in water quality analysis, fluoride detection may also be relevant to environmental and military applications.[21, 65] Fluoride is used in the enrichment of uranium as uranium hexafluoride (UF_6) for nuclear reactors and/or

weapons, and depleted UF_6 must be deconverted or carefully stored to prevent exposure to this hazardous gas.[81-82] Fluoride is also relevant to the detection of chemical weapons, being a byproduct of hydrolysis of the nerve agents soman and sarin, infamous most recently as the chemical warfare agent used in the 2013 Ghouta chemical attack in Syria.[83] Current methods of fluoride detection generally rely on the use of fluoride-ion selective electrodes and are well-established; however, the necessary instrumentation is fragile and non-portable and requires time-consuming sample manipulations.[65, 84-85] Development of colorimetric or fluorimetric sensing methods for fluoride that are portable and simple to use would therefore be advantageous.

Fluoride exhibits unique chemical properties as a hard Lewis base with a high charge density and small ionic radius, features that make fluoride detection challenging but also allow for selective sensor design. The major challenge to successful detection of fluoride in water is its high hydration energy of 510 kJ mol^{-1}.[86-87] To overcome this strong solvation effect, strong Lewis acids that are also water-compatible are required to bind fluoride in aqueous media. Organoboranes have been extensively studied for this purpose, with much success.[21, 23, 88] As described above, triarylboranes are intrinsically electron deficient due to the presence of an unoccupied p orbital at the trigonal planar boron center. Coordination of fluoride engages the empty p orbital and forms a tetrahedral fluoroborate species. A photophysical response may arise due to the quenching of transitions involving the borane p orbital and because of the geometrical rearrangement of the borane substituents upon fluoride binding.[21] Despite advances in organoborane-based sensors, however, many of these systems still suffer from poor

water solubility and hydrolytic stability. Lewis acidic anion sensors based on heavy group 15 elements, especially antimony(V), therefore offer an attractive alternative.

As discussed above, the simple organoantimony cation $[Ph_4Sb]^+$ has been known as a strong anion binding agent since 1956, when it was shown to be able to strip fluoride out of the aqueous layer of H_2O/CCl_4 biphasic mixtures.[44-46] However, interest in similar organoantimony compounds for fluoride sensing has only been renewed within the last decade. In 2012, following our initial reports of fluoride ion binding by borane-stibonium compound $[\mathbf{1}]^+$ [47] as well as by heterobimetallic Au-Sb and Hg-Sb complexes,[89-90] the Gabbaï group reported an initial example of a colorimetric fluoride sensor based on the heterobimetallic stibine-palladium complex $[\mathbf{5}]^+$.[24] In this complex, fluoride binding occurring at the antimony center is accompanied by a visible color change from yellow to deep orange (Figure 5). Crystallographic studies revealed the origin of the photophysical response in this case. In complex $[\mathbf{5}]^+$, the stibine moiety and two phosphine "arms" coordinate to Pd, which adopts a square planar geometry, while the third phosphine group of the ligand remains uncoordinated. However, fluoride binding at Sb triggers the coordination of this third phosphine arm to Pd to form the

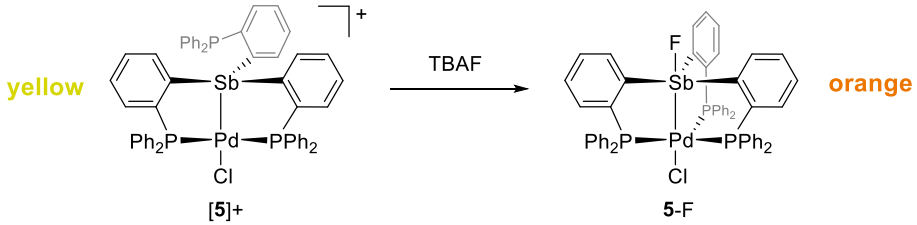

Figure 5. Colorimetric fluoride sensing with a heterobimetallic stibine-palladium complex.[24]

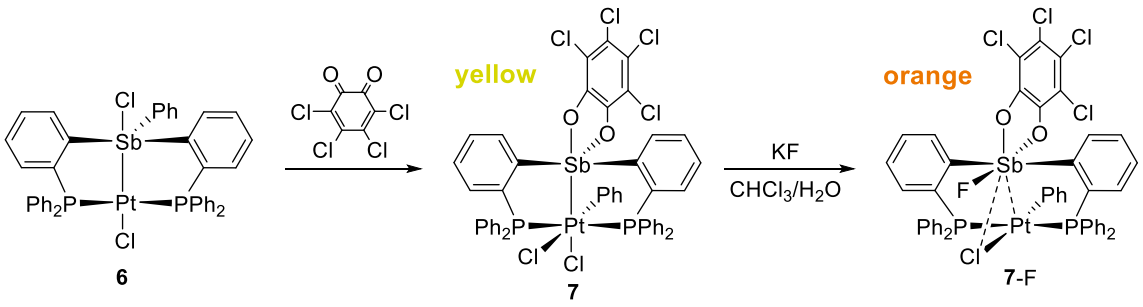

Figure 6. *ortho*-Chloranil oxidation and fluoride-binding behavior of bis(phosphinyl)-stibine platinum complexes.[91]

lantern complex **5**-F. The geometry change at Pd from square planar to trigonal bipyramidal results in new ligand-field transitions that account for the appearance of new absorption bands from 400-560 nm.[92] A visible color change was observable upon shaking of a biphasic mixture of $[\mathbf{5}]^+$ in CH_2Cl_2 and F^- in water at concentrations as low as 4 ppm. Moreover, the colorimetric response was found to be selective for F^- over Cl^-, Br^-, CH_3COO^-, NO_3^-, and $H_2PO_4^-$. Thus, complex $[\mathbf{5}]^+$ could be utilized as a "turn-on" colorimetric sensor for aqueous fluoride anions under biphasic conditions.

In another heterobimetallic example, the stiboranyl-platinum complex **7** also binds fluoride with a colorimetric change from yellow to orange, but by a different mechanism (Figure 6).[91] This complex is obtained by treatment of the Sb-Pt dichloride complex **6** with *ortho*-chloranil, which results in the coordination of the tetrachlorocatecholate group to Sb and a concurrent displacement of chloride to the Pt center. When complex **7** is exposed to KF in a biphasic system of CH_2Cl_2 and acidified water (0.1 M HCl), a reaction occurs with major structural rearrangement at the Sb-Pt

bond, as evidenced by crystallographic analysis of **7**-F (Figure 6). The structure reveals that one of the chloride ligands at Pt is substituted by fluoride, but the fluoride ligand migrates back to the Lewis acidic Sb center, forming a fluorostiborane unit. With this change, the Sb-Pt bond is broken, with the Sb-Pt interatomic distance lengthening from 2.59 to 3.09 Å. The Pt center adopts a square-planar geometry and sits over the face of the Lewis acidic fluorostiborane, which engages in weak Pt→Sb and Pt-Cl→Sb interactions. The structural and electronic changes result in the appearance of low-energy absorption bands in **7**-F and thus a colorimetric response. The original yellow color can be restored by the addition of $AlCl_3$ to the solution as a fluoride scavenger. Thus, in this compound, the presence of fluoride triggers the reversible switching of the Sb(V) ligand from an X-type to a Z-type ligand, manifested by a color change.

With the knowledge that Lewis acidic Sb(V) centers in heterobimetallic complexes could preferentially capture fluoride out of water, we began to explore new organoantimony compounds with organic chromophore and fluorophore groups as aqueous fluoride sensors. We were inspired by the work of Yamaguchi and Tamao, who had reported fluoride sensors based on triarylboranes such as the tri(9-anthryl)borane **8**

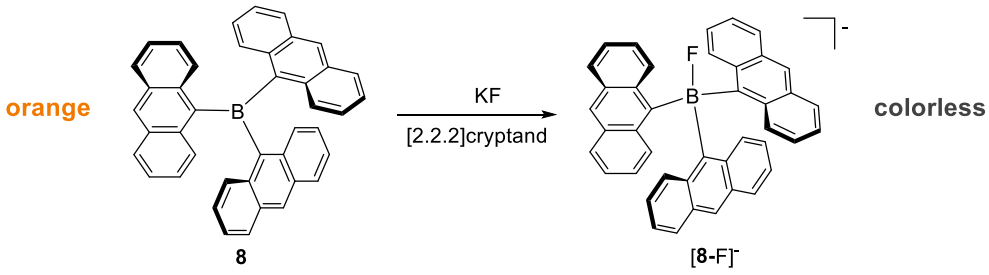

Figure 7. "Turn-off" response to fluoride binding in tri(9-anthryl)borane.[93-94]

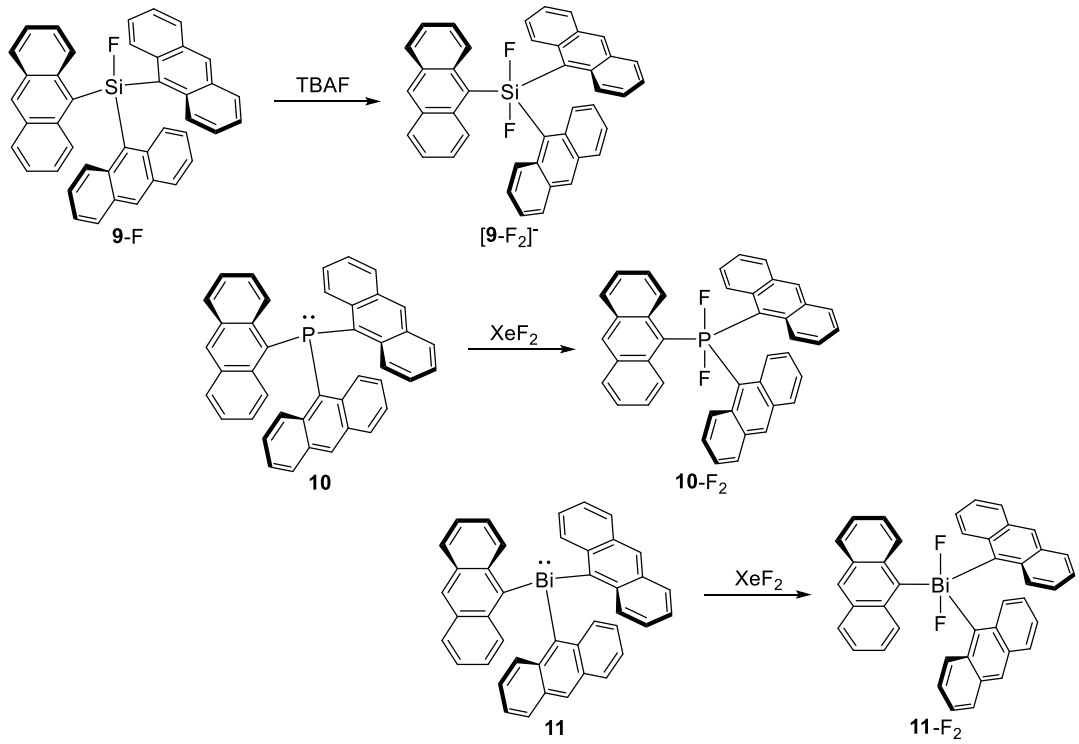

Figure 8. Tri(9-anthryl)-substituted main group species studied by Yamaguchi and Tamao.[95-98]

(Figure 7).[93-94, 99] In these compounds, the free borane is able to participate in π conjugation with its aryl ligands via the empty p orbital; this conjugation is broken with the binding of an anion to the borane center, resulting in a "turn-off" response of color and/or fluorescence. Yamaguchi and Tamao also investigated the photophysical properties of tri(9-anthryl)-substituted silicon, phosphorus, and bismuth species (Figure 8).[95-98] They observed distinct trends in the photophysical properties with changes in the coordination number of each main group element with addition of fluoride ligands: from fluorosilane **9**-F to the difluorosilicate, from phosphine **10** to the difluorophosphorane, and from bismuthine **11** to the difluorobismuthane. In each case, the 5-coordinate

difluoro derivatives showed blue-shifted UV-vis absorption bands, and in the case of [**9**-F_2]$^-$ and **10**-F_2, enhanced fluorescence from the anthryl groups, which the authors assigned to a change in through-space interactions among the anthryl substituents. Fluorescence spectra were not reported for or **11** or **11**-F_2, and these compounds were not explored further for fluoride sensing, but these studies offered initial evidence that the geometrical change upon fluoride binding to a Group 15 Lewis acid could have a modulating effect on the photophysical properties of fluorescent substituents such as 9-anthryl.

With this background, in 2012 the Gabbaï group reported a 9-anthryl-substituted antimony compound [**12**]OTf as a water-compatible "turn-on" fluorescent sensor for fluoride.[25] This 4-coordinate stibonium cation binds fluoride strongly to afford the 5-coordinate fluorostiborane **12**-F, as confirmed by X-ray crystallography and NMR spectroscopy of **12**-F, which shows a distinct ^{19}F signal at -75.8 ppm in $CDCl_3$ (Figure 9). The emission spectrum of [**12**]$^+$ in $CHCl_3$ shows very faint blue emission at λ_{max} = 427 nm with a quantum yield of Φ_F = 0.7%, but formation of the fluoride adduct **12**-F leads to a large increase of fluorescence, to a final quantum yield of Φ_F = 9.5%. This

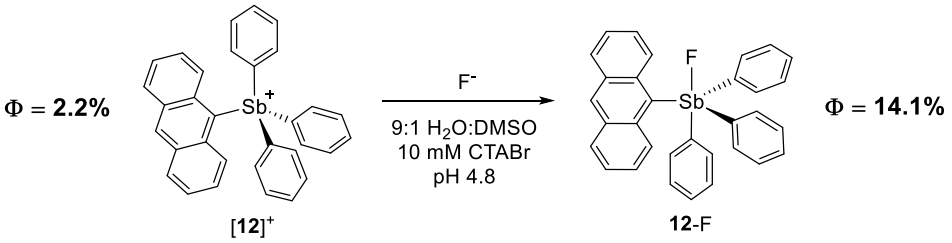

Figure 9. Fluoride binding to anthrylstibonium [**12**]$^+$ with "turn-on" of fluorescence.

"turn-on" response contrasts with the previously-reported triarylborane-based anion sensors, which exhibit "turn-off" responses. Remarkably, this binding and response also occurs in 90% water (9:1 H_2O:DMSO, buffered at pH 4.8 and containing 10 mM cetyltrimethylammonium bromide surfactant). A roughly 7-fold fluorescence increase is observed on formation of **12**-F under these conditions, from Φ_F = 2.2% to Φ_F = 14.1%. Fluoride titration data indicates that [**12**]$^+$ binds fluoride in this aqueous mixture with an equilibrium constant of 12,000 ± 1,100 M^{-1}, allowing for the sensing of ppm levels of fluoride by this method. No "turn-on" response or interference was observed from Cl^-, Br^-, I^-, NO_3^-, N_3^-, HCO_3^-, or HSO_4^-. Indeed, [**12**]$^+$ could be used to sense fluoride concentrations at and below 1 ppm in commercial bottled and tap water, with the fluorescence increase for samples of at least 1 ppm of fluoride being visible to the naked eye using a handheld UV lamp.

In a 2015 theoretical paper, Yokogawa and Irle performed DFT calculations on [**12**]$^+$ in order to elucidate the mechanism of the "turn-on" fluorescent response to fluoride.[100] They first optimized the geometry of both the ground state and first excited state of [**12**]$^+$. In the ground state, the energy minimum corresponded to an expected tetrahedral geometry of the ligands about Sb (Figure 10, **A**); however, in the excited state, two energy minima were found corresponding to two different geometries—one with the expected tetrahedral (**B**) and the other with a distorted seesaw geometry (**C**) about Sb. Using single-point energy calculations, the authors were able to map the potential energy surface of the excited state between the geometry of [**12**]$^+$ upon initial

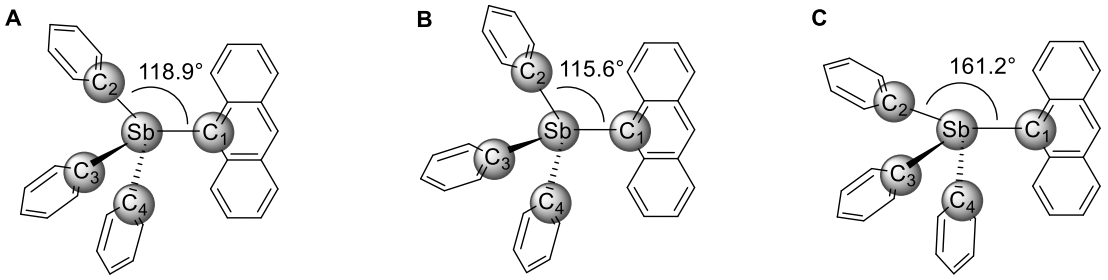

Figure 10. A: Ground-state structure of [**12**]$^{+}$**. B**: Tetrahedral excited-state structure of [**12**]$^{+}$. **C**: Seesaw excited-state structure of [**12**]$^{+}$.[100]

vertical excitation and these two minimum geometries. They found that barrierless relaxation may occur to either geometry, but that the seesaw geometry **C** is more stabilized by 8.8 kcal/mol. Importantly, analysis of the Kohn-Sham orbitals of the excited-state geometries **B** and **C** reveals that the geometry about Sb has a dramatic effect on the character of the frontier molecular orbitals. In the tetrahedral geometry **B**, the HOMO is localized in the π system of the anthryl substituent, and the LUMO in the π*, as expected for a system exhibiting π-π* emission. However, in the seesaw geometry **C**, the distortion of the ligands around Sb lowers the energy of an Sb-based σ* orbital below the π* orbital, replacing it as the LUMO. This effect produces a π-σ* excited state which is non-emissive, accounting for the low fluorescence observed in [**12**]$^{+}$. Coordination of a fluoride anion to [**12**]$^{+}$, however, engages the σ* orbital and renders access to the π-σ* "dark" state impossible. As a result, the HOMO and LUMO of [**12**]$^{+}$ again take on π-π* character, resurrecting the emission of the anthryl group. The ability of Sb to stabilize the σ* orbital and thus the "dark" state geometry was furthermore shown to be unique to Sb compared to its lighter congeners P and As.

We later extended our work on [**12**]$^+$ in a study of stibonium compounds bearing the extended aromatic substituents pyrene and perylene (Figure 11).[22] We hoped by this method to extend the wavelength of excitation of these fluoride sensors from the UV into the visible range and to increase the attainable fluorescence quantum yield. Gratifyingly, 1-pyrenyl-stibonium [**13**]$^+$ and 3-perylenyl-stibonium [**14**]$^+$ can bind fluoride in 90% water under the same conditions as 9-anthryl-stibonium [**12**]$^+$ to afford the corresponding fluorostiboranes, with a concomitant "turn-on" of fluorescence. In the case of [**13**]$^+$, the final emission is still quite weak, with fluorescence quantum yield increasing from Φ_F = 0.5% to Φ_F = 5.2%. In the case of [**14**]$^+$, however, the perylenyl substituent imparts stronger fluorescence, with an 8-fold emission increase from Φ_F = 7.3% to Φ_F = 59.2%, and excitation can be achieved in the visible range (λ_{exc} = 423 nm). [**14**]$^+$ thus represents an improved Sb(V) fluoride sensor, capable of selectively detecting fluoride at sub-ppm concentrations in water with a photophysical response visible to the naked eye.

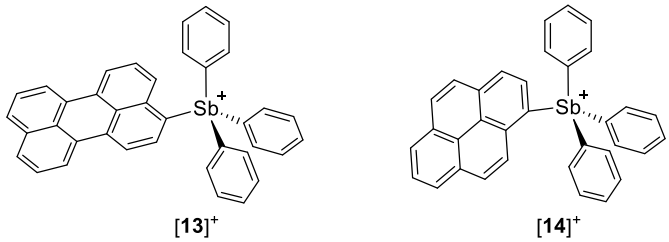

[**13**]$^+$ [**14**]$^+$

Figure 11. 1-Pyrenyl- and 3-perylenyl -substituted stibonium compounds studied as fluorescent fluoride sensors in aqueous media.[22]

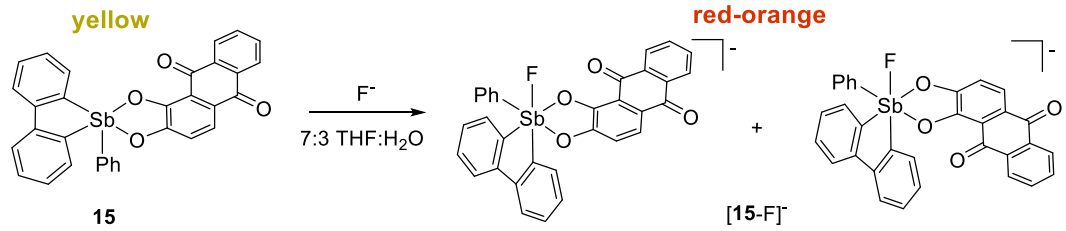

Figure 12. Fluoride binding to a neutral alizarin-substituted stiborane.

In addition to cationic stibonium compounds, the Gabbaï group also investigated neutral stiboranes as Sb(V)-based fluoride sensors, reporting the colorimetric and fluorimetric sensor **15** featuring the 1,2-dihydroxyanthraquinone (alizarin red) chromophore (Figure 12).[26] **15** was shown to bind fluoride in 7:3 THF:H_2O with a binding constant of 16,100 ± 1,100 M^{-1}, similarly to the tetrachlorocatecholate-substituted analog **3** described above. Fluoride binding induces a color change from yellow to red-orange due to the perturbation of the HOMO-LUMO separation of the alizarin moiety, and also enhances the alizarin emission at 616 nm, with a small but detectable fluorescence quantum yield increase from Φ_F = 0.3% to Φ_F = 3.0% for the fluoride adduct. A similar optical response was also observed for **15** in the presence of hydroxide; however, using a biphasic CH_2Cl_2:H_2O system in which the aqueous layer was buffered to pH 4.8, this interference could be avoided and **15** was able to respond selectively to F^-, with no interference observed from Cl^-, Br^-, NO_3^-, HCO_3^-, $H_2PO_4^-$, or HSO_4^-. Thus, **15** can be used for the "turn-on" detection of fluoride in commercial bottled and tap water at concentrations at and below 1 ppm.

As we have seen, there has been a considerable amount of progress made in the development of Sb(V)-based sensors for fluoride—however, thus far the extension of Sb(V)-based sensors for the detection of other species has been limited. The borane-stibonium compound [**1**]$^+$ described above as a fluoride binding agent was later shown to bind cyanide and azide anions as well (Figure 13).[101] In the cyanide adduct **1**-CN, interaction of CN with the Sb atom is limited to a weak side-on coordination, but in the azide adduct **1**-N_3, the azide anion binds through the terminal nitrogen in a B-N-Sb motif, with an Sb-N bond distance of 2.477(4)Å. These initial results demonstrated the potential that organoantimony(V) compounds have as binding materials for anions other than fluoride, including cyanide and azide. However, compound [**1**]$^+$ is not a stand-alone Sb(V)-based anion binder, nor does it exhibit any colorimetric or fluorescent response.

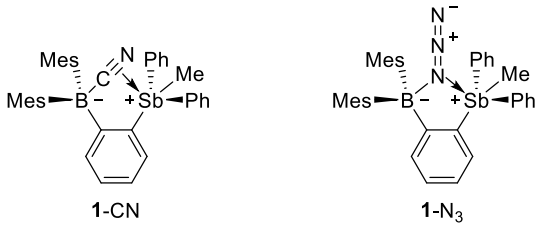

Figure 13. Cyanide and azide binding to a bidentate stibonium borane.

Only recently, the Gabbaï group reported a water-tolerant colorimetric Sb(V)-based sensor, not for anions, but for formaldehyde.[102] In this report, the fluorinated neutral Sb(V) compound **16** was found to possess strong Lewis acidity comparable to that of $B(C_6F_5)_3$ (Figure 14). **16** could be combined with P^tBu_3 in CH_2Cl_2 solution to

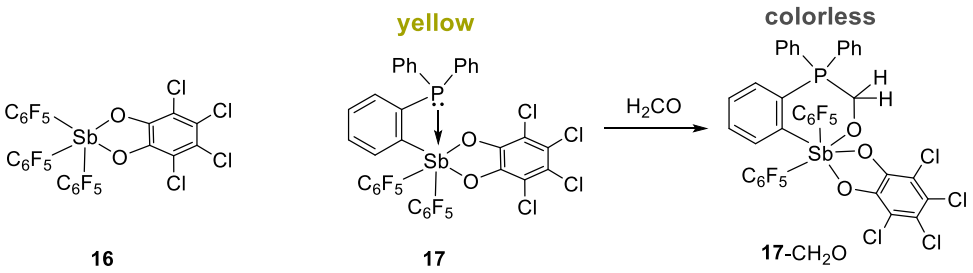

Figure 14. Fluorinated neutral Sb(V) compounds used for colorimetric sensing of formaldehyde.[102]

form a Frustrated Lewis Pair (FLP) system, which was shown to be able to activate and bind formaldehyde by NMR spectroscopy and X-ray crystallographic analysis. In a second iteration, the ambiphilic phosphino-stiborane **17** was synthesized, which combines the Sb(V) Lewis acid and phosphine Lewis base in a single molecule. **17** also reacts with formaldehyde to form the insertion adduct **17**-CH_2O (Figure 14). Exposure of **17** to 0.1% aqueous formaldehyde in a biphasic CH_2Cl_2:H_2O system containing the Triton X-100 surfactant results in binding of formaldehyde with a disappearance of the original yellow color of **17.** This colorimetric "turn-off" response was visible to the naked eye. Other than this isolated report, however, we are not aware of any further examples of Sb(V)-based sensors for analytes other than fluoride.

1.5 Phosphine-based PeT sensors for heavy late metals

Although we have focused our recent research on the development of antimony(V)-based anion sensors, we also recognized the potential of phosphorus-based compounds for chemical sensing—not of anions, but of metal cations. A multitude of

molecular fluorescent probes for metal cations, especially lighter metals such as Ca^{2+}, Zn^{2+}, Cu^{2+}, and Fe^{2+} have been developed, especially for *in vivo* detection. [54, 60-62] These sensors often feature N, O, and/or S-based donor groups that serve to coordinate to the metal cation of interest and induce a fluorescence "turn-on" response in an appended fluorescent dye via a photoinduced electron transfer (PeT) mechanism.[50-52] A PeT quenching effect is observed when either a filled donor orbital or an empty acceptor orbital falls between the π and π* energy levels responsible for the dye's emission, as shown schematically in Figure 15.[51-52] The interfering orbital allows the excited state of the molecule to relax to the ground state via a stepwise non-radiative pathway, thus quenching emission. When the donor or acceptor groups are removed, as in the case of donor group coordination to a metal cation, normal emission is restored, resulting in a "turn-on" response.

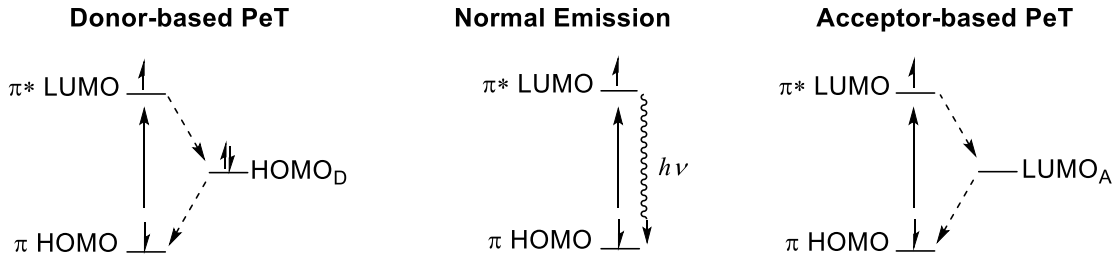

Figure 15. Schematic diagram of the frontier molecular orbital energy levels in fluorescent dyes affected by donor- or acceptor-based PeT.

Nevertheless, aside from a handful of sensors developed for the toxic mercury ion,[103-107] fluorescent probes that are selective for heavy late transition metals such as Pd, Pt, Ag, and Au are still few.[62, 108-114] However, given the heavy use of such metals in

catalysis and, increasingly, pharmaceuticals, concerns about their toxicity have prompted more researchers to seek improved detection methods for these ions in both environmental and biological samples.[115-117] Current analytical methods of heavy metal ion detection such as atomic absorption spectrometry (AAS), inductively coupled plasma atomic emission spectrometry and mass spectrometry (ICP-AES, ICP-MS), and electrochemical methods, while accurate, typically require complex sample preparation and highly trained users to operate the instrumentation, and are also not useful for *in vivo* sensing.[109] Fluorescence detection, on the other hand, also offers high sensitivity and accuracy along with the advantages of simple implementation and compatibility with *in vivo* imaging.

According to the principles of hard-soft acid-base theory, however, small, hard donor groups based on nitrogen or oxygen are not expected to coordinate strongly to large, diffuse heavy metal ions,[9] making selective detection of these metals using this type of PeT-based sensor difficult. By the same token, larger, softer donor groups based on sulfur or phosphorus should coordinate soft heavy late metals preferentially. However, despite the ubiquity of phosphine-based ligands in coordination and organometallic chemistry, phosphine groups do not appear to have been utilized in PeT-based fluorescent sensors for metal cations to date (*vide infra*). We therefore became interested in designing phosphine-based sensors to harness PeT effects from the phosphorus group for the "turn-on" fluorescent sensing of heavy late metal ions.

1.6 Research objectives

In our previous work described above, we have successfully developed antimony(V)-based colorimetric and fluorimetric sensors for fluoride; however, these sensors are still far from ideal in terms of strong photophysical responses. Our first generation of sensors suffered from low quantum yields of emission[26] and/or the necessity of excitation in the UV range,[25] which is less advantageous for practical applications. Although we have made some progress in improving these properties, for example, in perylenyl-stibonium compound [**14**]$^+$, there is still much room for improvement. Our first objective in extending this work, therefore, is to improve the photophysical properties of antimony(V)-based sensors, targeting strong colorimetric changes, increased quantum yields of emission, and visible-wavelength excitation and emission in antimony(V)-containing compounds. Secondly, we aim to extend the range of analytes detectable by heavy Group 15 element-based sensors. Specifically, we want to design antimony(V)-based sensors for toxic anions other than fluoride, and to investigate the use of phosphorus-based donors for PeT sensing of heavy late metals. Finally, in parallel with these objectives, we wish to develop a better understanding of the mechanisms governing the photophysical responses of the sensors we create. In this way, we hope to put the design of main group element-based sensors on a more rational plane going forward.

To accomplish these objectives, we pursue three specific strategies in the work discussed in this dissertation. Firstly, we synthesize and characterize antimony(III) and antimony(V) compounds bearing strong chromophores or fluorophores, which act as

intensely colored or emissive reporter groups in these sensors. Secondly, we explore another strong fluorophore decorated with a phosphine donor group as a PeT-based fluorescent sensor for heavy late metal ions. Thirdly, we investigate the properties of conjugated heterocycles incorporating antimony centers within the π system, which allow direct control over the photophysical properties of the molecule via antimony-based orbital interactions with the colored or luminescent framework.

2. ANTIMONY-SUBSTITUTED BODIPY FLUORESCENT DYES FOR FLUORIDE AND CYANIDE SENSING[*]

2.1 Introduction

Previous work from our group has demonstrated that Lewis acidic organoantimony(V) compounds can be applied as effective chemical sensors for fluoride anions, using a pendant chromophore or fluorophore group to act as an optical reporter for the binding event. Appropriate choice of a reporter group is essential for the success of this sensing strategy. The suitability of an optical reporter depends on its inherent photophysical properties and the potential for those properties to be controlled by the binding of anions at the antimony(V) center. The ideal reporter group would display fluorescence with a high quantum yield in the anion-bound form of the molecule so as to produce a dramatic and sensitive response, and would have excitation and emission wavelengths in the visible range. Although we have made progress toward realizing these goals,[22, 24-26] most of the antimony-based fluoride sensors we have developed suffer from low quantum yields and/or the necessity for excitation in the UV range. Therefore, in order to design better fluorescent Lewis acids for applications in anion sensing, we wished to study the effect of anion-binding antimony(V) groups on the photophysical properties of strong fluorophores with excitation and emission in the visible spectrum. By using fluorescent dyes with well-understood photophysical

[*] Reprinted in part with permission from "Anion sensing with a Lewis acidic BODIPY-antimony(V) derivative"; Christianson, A. M.; Gabbaï, F. P. *Chem. Commun.* **2017**, *53*, 2471-2474. Copyright 2017, The Royal Society of Chemistry.

properties, we also hoped to gain a clearer understanding of the mechanism by which fluoride binding at antimony causes a "turn-on" fluorescence response in the reporter group, as in the case of 9-anthryltriphenylstibonium (compound [**12**]$^+$ above).

BODIPY fluorescent dyes have been widely used in chemical sensing and biological imaging due to their strong emission and high photostability.[118-122] Excitation and emission ranges of BODIPY dyes typically lie in the green region near 500 nm, but can be tuned by varying the substituents on the BODIPY core to obtain dyes with colors spanning the visible range and even into the near IR.[123-126] BODIPY fluorophores have already been used in conjunction with Lewis acidic boranes for fluoride sensing by Thilagar and coworkers (compounds **18**-**21**, Figure 16).[125-129] These borane-BODIPY dyads and triads display divergent photophysical responses to fluoride binding at boron depending on the nature and extent of the electronic communication between the borane and BODIPY units. These studies show that substitution of BODIPY dyes

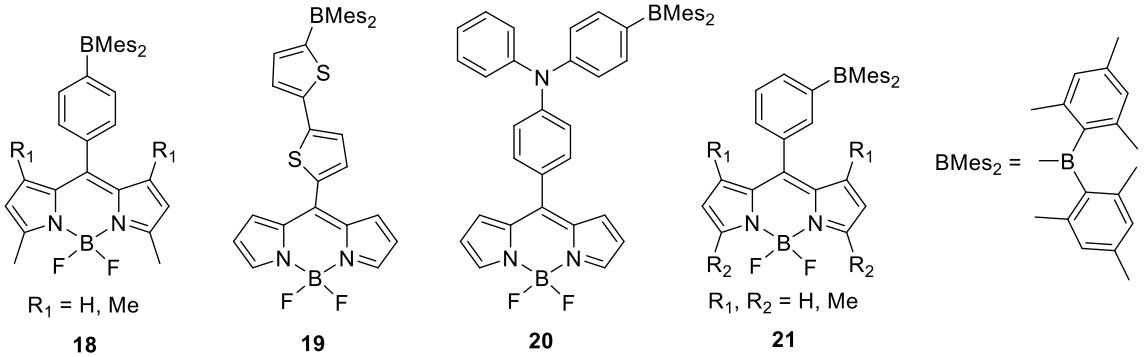

Figure 16. Borane-substituted BODIPY dyes developed by Thilagar and coworkers as fluorescent fluoride sensors.[125-129]

with a light main group element such as boron can influence the fluorescence properties of the compound dramatically.

On the other hand, few reports of BODIPY dyes substituted with heavy main group elements exist. However, a series of selenium-substituted BODIPYs reported in 2013 (compounds **22-23**, Figure 17) were shown to function as reversible sensors for the HClO-mediated redox cycle in living cells.[130-132] In these compounds, the emission of the BODIPY dye is theorized to be suppressed in the reduced form due to a remote photoinduced electron transfer (PeT) effect from the selenide group, which bears two lone pairs.[51-52] Upon oxidation to the selenoxide by HClO, the selenium substituent ceases to behave as an electron donor, and strong emission from the BODIPY group is revived. These studies demonstrate that the BODIPY dye's fluorescent properties may be modulated by a heavy main group substituent on the BODIPY framework that interacts with the fluorescent moiety in the excited state. Based on these examples, we reasoned that a BODIPY substituent should also be able to act as a good reporter group for antimony(V)-based anion sensors.

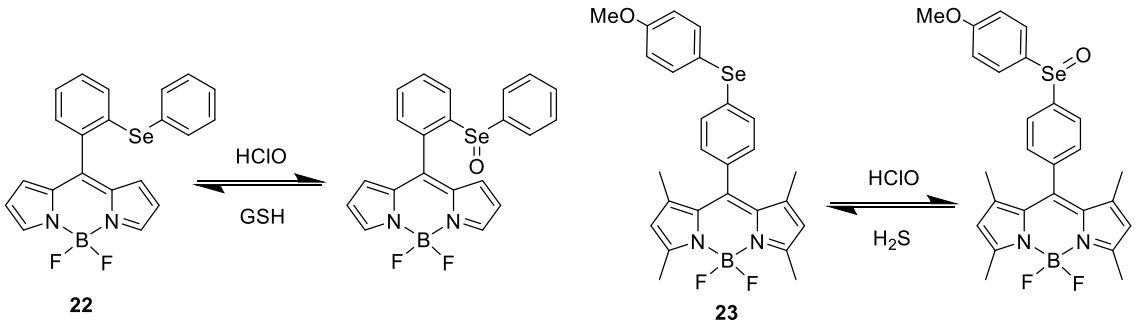

Figure 17. Se-substituted BODIPY dyes as reversible HClO redox sensors *in vivo*.[130, 132]

Synthetic methods for the installation of main group substituents on BODIPY dyes are often cumbersome, involving the synthesis of an intermediate main group element-substituted aldehyde, which must then survive the reaction conditions for forming the BODIPY framework from the desired pyrrole and BF_3.[127, 130, 132] However, an elegant synthesis of phosphine-substituted BODIPY dyes **24-27** was recently reported by Higham and coworkers (Figure 18), which offers the potential for more facile functionalization of BODIPYs with main group species utilizing lithium exchange reactions.[133] Because the B-F bonds of a conventional BODIPY dye would be vulnerable to attack by organolithium reagents, the key step to this synthesis involves the initial "masking" of the BF_2 unit by alkyl or aryl groups by treatment of the BODIPY dye with two equivalents of RLi. Higham and coworkers report selective replacement of F by Me or Ph despite the presence of an arylbromide substituent in the precursor BODIPY, in isolated yields of 40-44%.[134] A similar "masking" procedure was also reported by Sekar and Chattopadhyay using Et_2AlCl as the alkylating agent, producing BEt_2-BODIPYs in excellent yields.[135] They also demonstrate that this alkylation is reversible upon

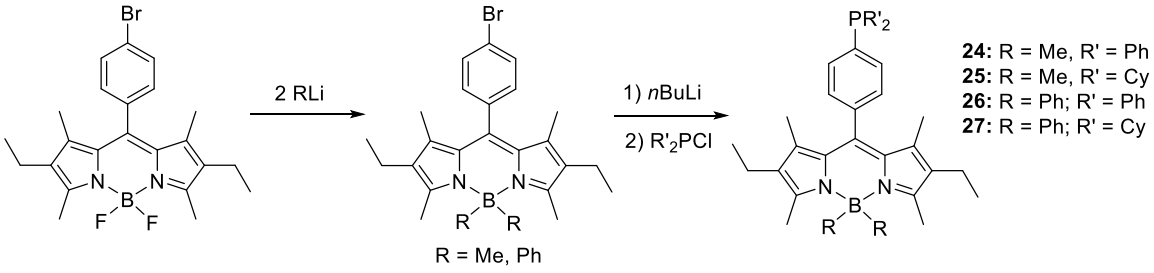

Figure 18. Synthesis of phosphine-substituted BODIPY dyes reported by Higham and coworkers.[133]

treatment with $BF_3{\cdot}Et_2O$ ("demasking") to regain the BF_2-BODIPY. Replacement of the boron-bound fluorides with Ph or Et results in detrimental quenching of the BODIPY fluorescence, presumably because of increased vibrations and rotations of these substituents that enable radiationless energy loss. However, Higham and coworkers report that substitution of F with Me groups results in less significant quenching, and BMe_2-BODIPY dyes retain high quantum yields of fluorescence.[133-134]

In this section, we describe the successful installation of Sb(III) and Sb(V) substituents on BODIPY fluorophores, using a modification of this synthetic method.[136] This work represents the first examples of BODIPY dyes containing antimony substituents, to our knowledge. We demonstrate that the Sb(V)-substituted BODIPY [**30**]$^+$ is Lewis acidic and binds anions in organic solvents with a "turn-on" fluorescence response. In addition to fluoride, this Sb(V) compound displays a binding affinity for other toxic anions including cyanide and, to a lesser extent, azide, offering the potential to extend the chemistry of Sb(V)-based sensors to more anions of interest.

2.2 Synthesis and characterization of Sb-substituted BODIPY dyes

The synthesis of diphenylstibine-substituted BODIPY **29** was achieved by a modification of the synthetic method described above by using $AlMe_3$ as the "masking" agent (Figure 19).[133-135] The p-bromophenyl-substituted BODIPY **28**-F_2 was first synthesized by literature methods,[137] then treated with $AlMe_3$ to produce the BMe_2-BODIPY **28**-Me_2 cleanly in excellent yield. Replacement of the B- F bonds with B-Me

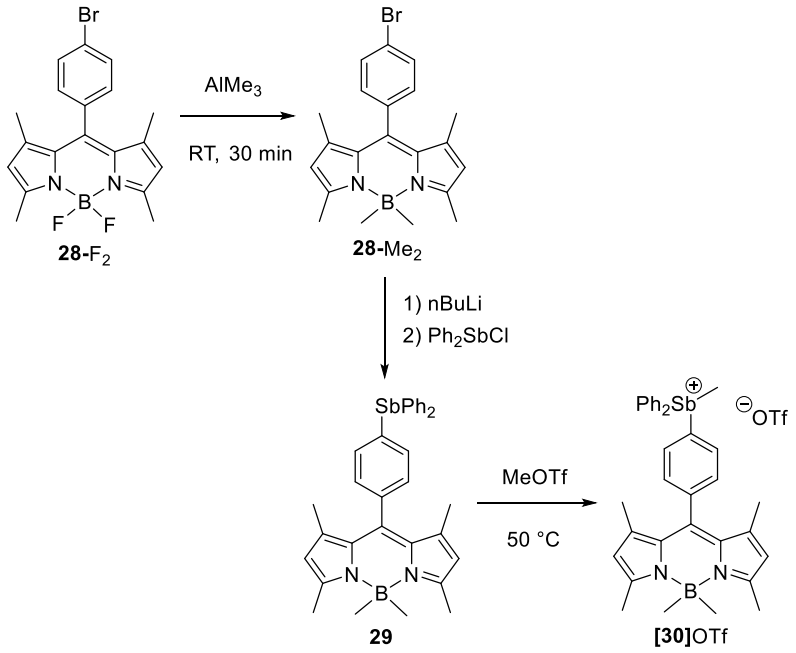

Figure 19. Synthesis of Sb(III)- and Sb(V)-substituted BODIPY dyes.

bonds allows the BODIPY dye to tolerate nucleophilic reaction conditions with minimal detriment to the fluorescence quantum yield.[134] Thus, **28**-Me_2 can undergo lithium-halogen exchange at the aryl group, and quenching with Ph_2SbCl yields the Sb(III)-substituted BMe_2-BODIPY **29**. This compound has been fully characterized spectroscopically, and the solid-state structure was confirmed by X-ray crystallography (Figure 20a). The crystal structure shows the expected substitution of the diphenylstibine moiety at the *para* position of the 5-aryl group, which is oriented orthogonally to the planar BODIPY framework.

The Sb(III) derivative **29** was treated with methyl triflate to afford the Sb(V) methylstibonium-substituted derivative **[30]**$^+$ as a triflate salt (Figure 19). This compound was air- and moisture-stable and could be purified by silica gel

chromatography. The crystal structure of **[30]**OTf reveals a close contact between the triflate anion and the Sb(V) center of 2.860(3) Å, which suggests Lewis acidity at this site (Figure 20b). The fact that the triflate anion is positioned *trans* from the BODIPY-substituted phenylene linker indicates an apicophilicity of this phenylene group which is induced by the electron-withdrawing nature of the BODIPY group.

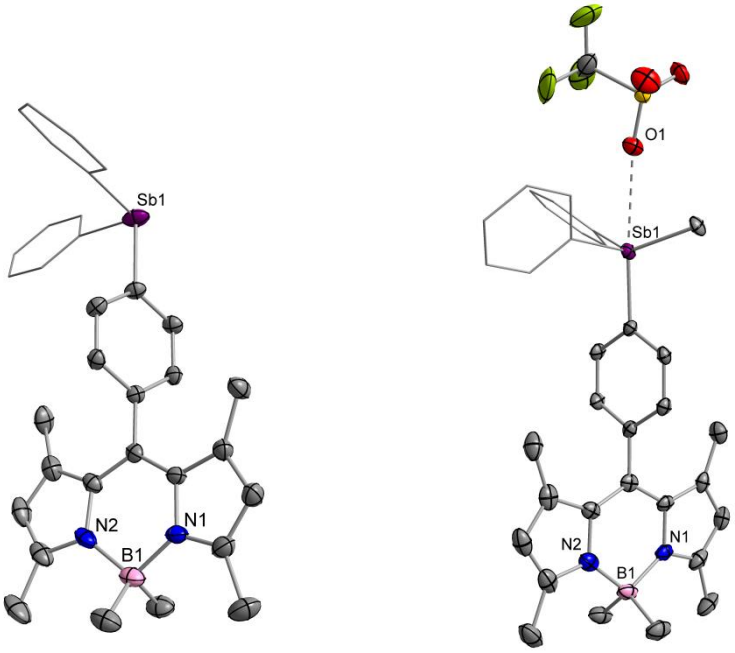

Figure 20. Crystal structures of a) **29** and b) **[30]**OTf. Hydrogen atoms omitted for clarity.

The photophysical properties of **29** and **[30]**OTf are very similar and display the characteristic profiles of BODIPY dyes, with maximum absorption and emission bands in the green region of the spectrum (Table 1). The fluorescence quantum yields are relatively low, at 13% for **29** and 15% for **[30]**OTf, respectively, although the emission

in solution is readily observable to the naked eye with irradiation by a handheld UV lamp. The substitution of the BF_2 group by two methyl groups may partially account for these low quantum yields; however, very similar phosphine-substituted BMe_2-BODIPY dyes reported by Higham and coworkers exhibited quantum yields more than twice as high.[133-134] Heavy atom quenching by the antimony atom could also be at play. In the case of **[30]**OTf, particularly, the influence of Sb-based σ*-orbitals in the excited state may also result in fluorescence quenching, as will be discussed below.

Table 1. Spectroscopic properties of **29** and **[30]**OTf.

Compound	Absorption maximum λ_{abs}	Emission maximum λ_{emiss}	Fluorescence quantum yield Φ_F [a]
29	494 nm	506 nm	0.13
[30]OTf	498 nm	515 nm	0.15

[a] Quantum yields determined in CH_2Cl_2 relative to fluorescein in 0.1 M aqueous NaOH ($\Phi_F = 0.91$)[138-139]

2.3 Anion binding by Sb(V) with a BODIPY reporter group

The structural characterization of compound [**30**]$^+$ indicates the potential for strong Lewis acidity at the Sb(V) center. Therefore, we tested the anion binding capability of [**30**]$^+$ toward fluoride, cyanide, and azide in organic solvents. Addition of fluoride (as TBAF or KF) to a solution of [**30**]OTf in $CDCl_3$ or CD_3OD results in marked upfield shifts of the ^{1}H NMR signals corresponding to the aryl and methyl groups of the methylstibonium moiety. Most indicatively, the signal corresponding to the

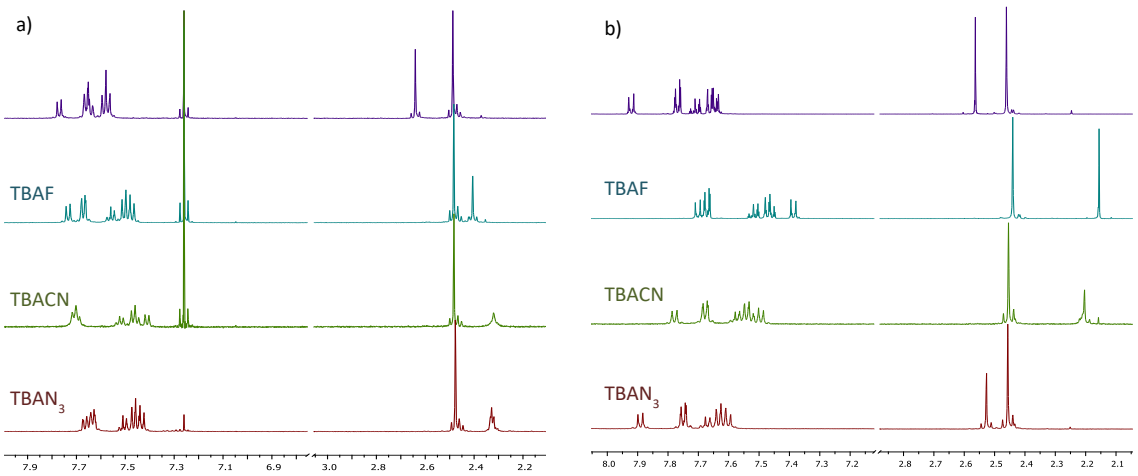

Figure 21. ^{1}H NMR spectral changes for **[30]**OTf upon addition of anions as tetrabutylammonium salts in a) $CDCl_3$ and b) CD_3OD.

methyl group protons shifts upfield from 2.64 to 2.41 ppm in $CDCl_3$ and from 2.56 ppm to 2.16 ppm in CD_3OD (Figure 21). These changes in the ^{1}H spectrum are indicative of adduct formation, since anion coordination to the methylstibonium would be expected to decrease the electron-withdrawing nature of the Sb(V) moiety and thus decrease deshielding of the methyl group protons. Although we were unable to identify a signal in the ^{19}F NMR spectrum corresponding to the Sb-bound fluoride, an X-ray structure of crystals isolated from the concentrated NMR solution of [**30**]OTf with KF unambiguously confirms the formation of the adduct **30**-F (Figure 22). The Sb atom adopts a trigonal bipyramidal geometry, with a τ value of 0.92.[140] The fluoride anion binds to the Sb center in an apical position *trans* to the BODIPY-substituted group, as in the case of the triflate anion in compound [**30**]OTf. The Sb-F bond distance of 2.095(4) Å is comparable to those observed in previously reported tetraarylfluorostiboranes, thus indicating the tight binding of the fluoride anion.[22, 25] Additionally, a methanol solvent

molecule co-crystallizes with the fluoride adduct, forming a hydrogen bond with fluoride with an O-F separation of 2.71Å.

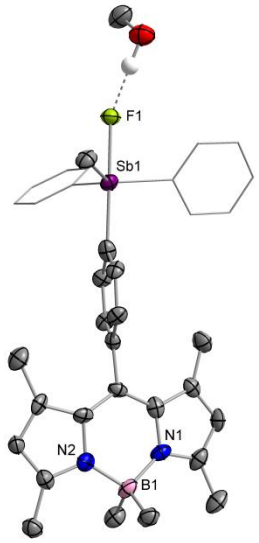

Figure 22. Crystal structure of **30**-F. Hydrogen atoms not involved in hydrogen bonding omitted for clarity. Selected bond length (Å): Sb1-F1, 2.095(4).

Interestingly, addition of the toxic anions cyanide and azide as tetrabutylammonium salts to solutions of **[30]**OTf in $CDCl_3$ results in similar upfield shifts of the ^{1}H NMR signals as for fluoride, indicating that they can also form Lewis adducts with **[30]**$^+$ at Sb (Figure 21, Table 2). This observation is significant because, although we have reported a borane-stibonium compound that is able to bind cyanide and azide as well as fluoride,[101] we had not yet discovered an Sb-based sensor for anions other than fluoride. For example, the behavior of [**30**]OTf is in contrast to the behavior of the analogous methylstibonium compound [Ph_3SbMe]OTf, which lacks the BODIPY

Table 2. Summary of ^{1}H NMR chemical shifts corresponding to the Sb-bound methyl group of [**30**]OTf and [Ph_3SbMe]OTf upon anion addition.

Compound	δ in $CDCl_3$		δ in CD_3OD	
[**30**]OTf	Original	2.64 ppm	Original	2.56 ppm
	TBAF	2.41 ppm	KF	2.16 ppm
	TBACN	2.32 ppm	TBACN	2.20 ppm
	$TBAN_3$	2.33 ppm	$TBAN_3$	2.53 ppm
[Ph_3SbMe]OTf	Original	2.57 ppm		
	TBAF	1.99 ppm		
	TBACN	2.50 ppm		
	$TBAN_3$	2.40 ppm		

substituent. Addition of fluoride to [Ph_3SbMe]OTf in $CDCl_3$ results in substantial upfield shifts of the ^{1}H signals, but addition of cyanide or azide produces only small changes to these signals, suggesting that these anions are not coordinated strongly to the Sb(V) center (Table 2). **[30]**OTf therefore demonstrates stronger Lewis acidity compared to [Ph_3SbMe]OTf in coordinating cyanide and azide, due to the influence of the more electron-withdrawing BODIPY substituent. Anion binding by **[30]**$^{+}$ was observed to be dependent on solvent conditions, however. In more polar, coordinating solvents such as CD_3CN and CD_3OD, upfield shifts indicative of anion binding are only observed with addition of F^- and CN^-, while addition of N_3^- has almost effect (Figure 21, Table 2). Thus, methylstibonium **[30]**$^{+}$ shows a selectivity for F^- and CN^- in these solvents and could potentially serve as a dual sensor for these two anions.

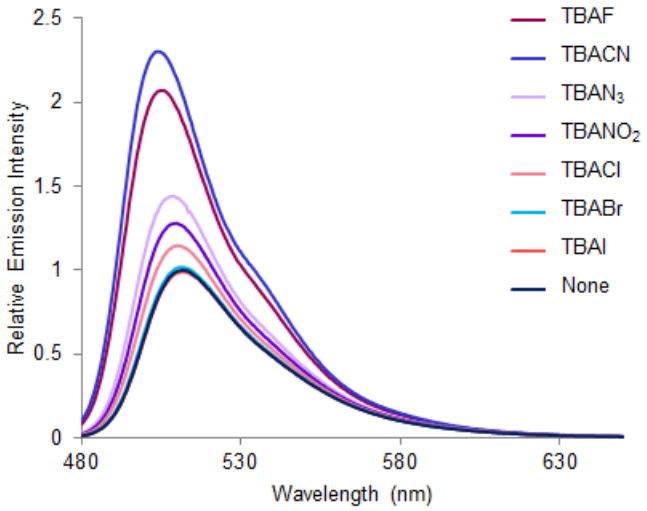

Figure 23. Relative emission spectra of [**30**]$^+$ treated with 5 equivalents of various anions as tetrabutylammonium (TBA) salts in MeCN.

Gratifyingly, addition of F^- and CN^- to solutions of **[30]**$^+$ in acetonitrile also results in a distinct enhancement of the BODIPY-based emission. The emission spectra of **[30]**$^+$ in the presence of different anions in acetonitrile are shown in Figure 23. Treatment of **[30]**$^+$ with excess F^- or CN^- results in a 2.1- or 2.3-fold increase in fluorescence, respectively. As expected from the NMR data discussed above, treatment with excess N_3^- results in a smaller 1.4-fold increase in emission, consistent with poorer binding of azide to **[30]**$^+$ in a polar, coordinating solvent such as MeCN. Other anions, including Cl^-, Br^-, I^-, and NO_2^-, produced little or no enhancement of the BODIPY fluorescence. Thus, compound **[30]**$^+$ behaves as a modestly selective sensor for fluoride and cyanide anions in MeCN. Titration data for [**30**]$^+$ treated with F^- and CN^- are consistent with 1:1 adduct formation, as expected for anion coordination to the Sb(V) center (See Experimental details). Binding constants were calculated from fitting the

titration curves and revealed that [**30**]$^+$ binds fluoride with a $K(F^-) > 10^7$ M^{-1} and cyanide with a $K(CN^-) = 1.6\times10^6$ ($\pm1\times10^5$)M^{-1}. The limits of detection of the two anions were determined to be 0.25 μM for fluoride (~5 ppb) and 0.31 μM for cyanide (~8 ppb). Significantly, this is our first observation of a "turn-on" fluorescence response of an Sb(V) compound to any anion other than fluoride. This suggests that triarylmethylstibonium species may be able to be developed as sensors for a wider range of toxic anions than fluoride alone. The solvent medium is a key factor in determining selectivity for any particular anion or anions, since the anion's affinity for the Sb(V) receptor will always be balanced against solvation. In this case, **[30]**$^+$ binds F^- and CN^- strongly in MeCN, but N_3^- only weakly. The anion binding behavior of **[30]**$^+$ is tolerant of ambient moisture in the solvent; however, we found that intentional addition of water interferes with the binding and "turn-on" response to F^- and CN^- in MeCN, precluding the use of **[30]**$^+$ as a sensor for aqueous samples of these anions.

2.4 Computational studies

In order to understand the mechanism behind the observed "turn-on" response to anion binding, DFT optimized ground state structures for free **[30]**$^+$ and the anion-bound forms **30**-F and **30**-CN were computed (Figure 24). In the fluoride- and cyanide-bound forms of the molecule, the HOMO and LUMO are localized in the π-π* system of the BODIPY group, as would be expected for an unsubstituted BODIPY dye. In the free stibonium **[30]**$^+$, on the other hand, the LUMO is localized on the $SbPh_2Me$ fragment. Significant contribution from an Sb-Ph σ* orbital is evident, as we expect for a Lewis

acidic Sb(V) center. If this orbital is populated in the excited state, it may result in a less emissive state than the expected pure π* orbital, which would explain the observed quenching of fluorescence in the free stibonium form of **[30]**$^+$. This effect is neutralized by anion binding, which engages the low-lying σ* orbital.

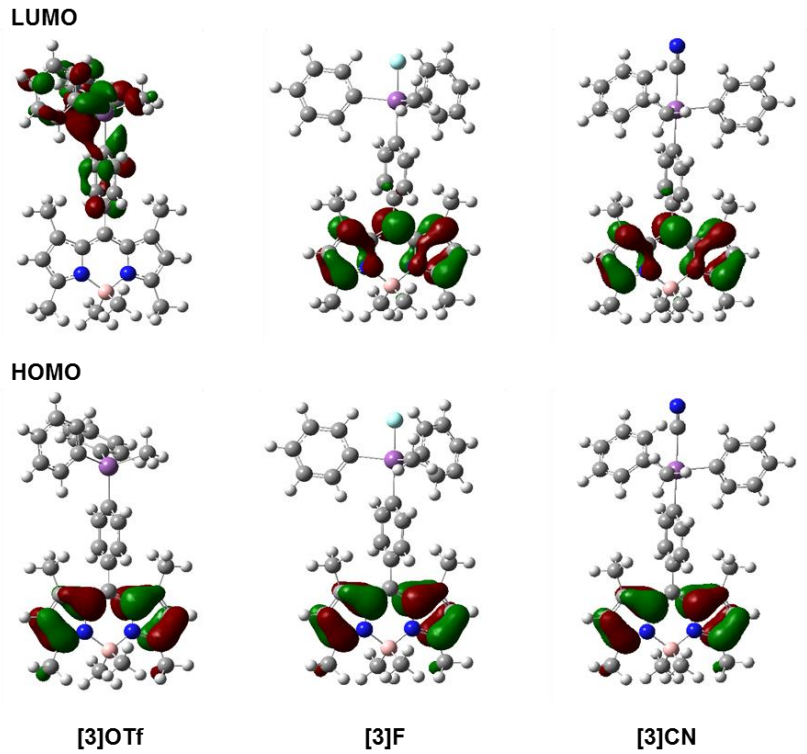

Figure 24. Contour plots of computed frontier molecular orbitals of the S_0-optimized geometries of [**30**]$^+$, **30**-F and **30**-CN.

As described above, Yokogawa and Irle have shown in a recent theoretical study of the 9-anthrylstibonium fluoride sensor [**12**]$^+$ that the origin of the fluorescence "turn-on" response in that system is relaxation of the free stibonium molecule in the excited state to a geometry that favors electron localization in a σ*-dominated orbital at the

Sb(V) center rather than the π* orbital of the fluorophore, thus quenching emission in the absence of a bound anion.[100] To determine if a similar mechanism might underlie the "turn-on" fluorescence response observed in [**30**]$^+$, we performed TD-DFT optimization calculations of the first excited state of [**30**]$^+$. We were able to identify two geometries at energy minima—a "bright" state (Structure **A**) and a "dark" state (Structure **B**) (Figure 25). The energies of both S_1-optimized geometries **A** and **B** are very similar to each

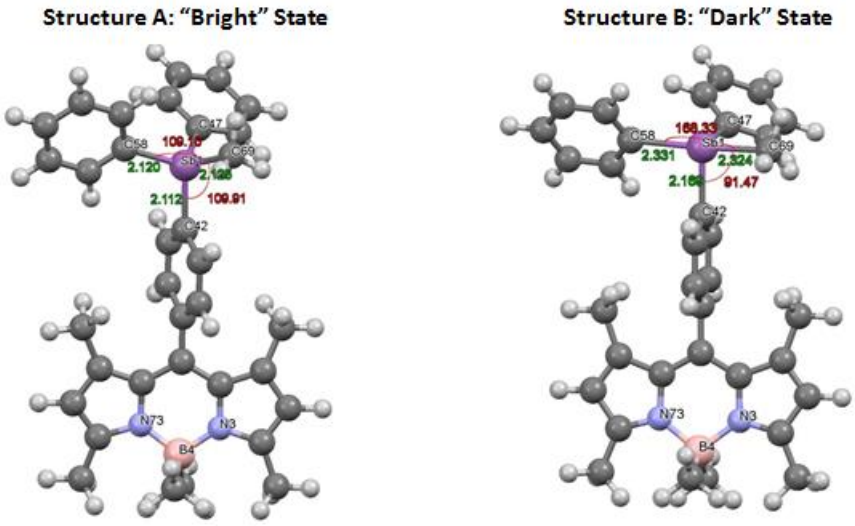

Figure 25. Structures of S_1-optimized geometries **A** and **B**. Bond distances displayed in angstroms (Å) and bond angles in degrees (°).

Table 3. Energies calculated for the optimized ground and excited states of **[30]**$^+$.

	S_0 Optimized	S_1 Vertical Excitation	S_1 Optimized **A**	S_1 Optimized **B**
Energy (HF)	-1692.495	-1692.386	-1692.3998	-1692.3996
Relative Energy (eV)	0.00	2.96	2.58	2.59
HOMO-LUMO gap (eV)	3.11	N/A	2.63	1.03

other, 2.58-2.59 eV above the energy of the S_0 ground state and 0.37-0.38 eV below the energy of S_1 upon vertical excitation, which suggests that both geometries may be accessible in the excited state (Table 3). In geometry **A**, the substituents surround the antimony atom in a distorted tetrahedral arrangement with no prominent open site. Therefore, Sb-based σ* orbitals do not contribute to the frontier molecular orbitals in this geometry, which are localized in the π-π* system of the BODIPY fragment (Figure 26). This "bright" state should be highly emissive. In geometry **B**, the substituents around antimony distort towards a see-saw structure with a large open site at antimony. The ground-state HOMO in this geometry remains localized in the BODIPY π system, but

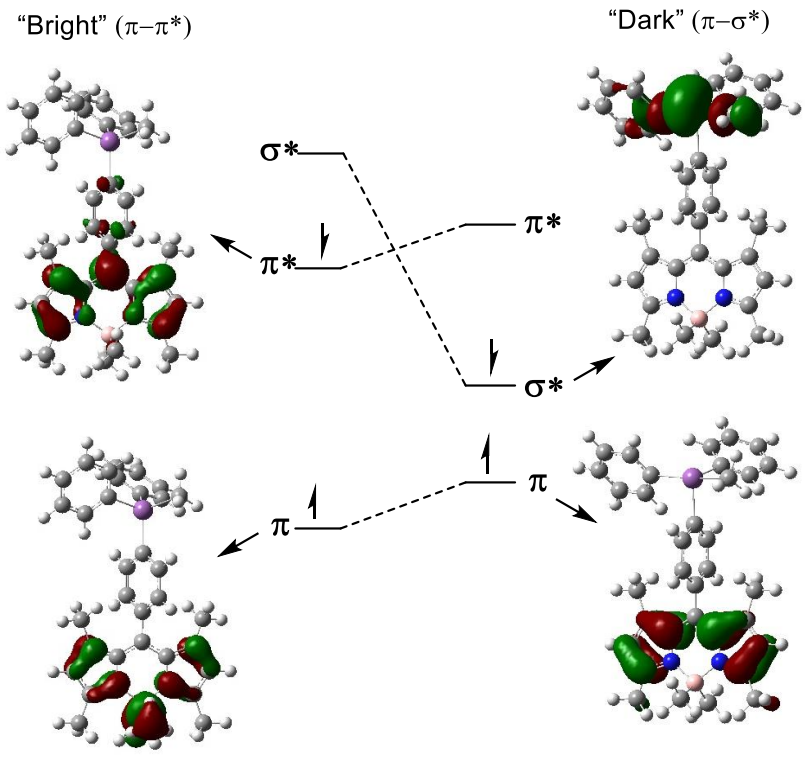

Figure 26. Energy diagram with contour plots of computed frontier molecular orbitals of **[30]**$^+$ in the two optimized geometries of the first excited state.

the ground-state LUMO is localized exclusively in the Sb-based σ* orbitals made prominent by the distortion of the substituents around the Sb center (Figure 26). This state is likely to have low emission due to the removal of electrons from the BODIPY π-π* system. The HOMO-LUMO gap of structure **B** also shrinks dramatically, increasing the likelihood of radiationless deactivation of the excited state in this geometry by internal conversion (Table 3).[141-142] The accessibility of this "dark" state after excitation would therefore partially quench the BODIPY emission in [**30**]$^+$, but anion binding at Sb would occupy the low-lying σ* orbitals and remove the influence of the "dark" state. Thus, full emission from the BODIPY π-π* system would be restored, resulting in the observed "turn-on" response. Between these results and those reported by Yokogawa and Irle, this excited-state mechanism may thus be presented as a general phenomenon for stibonium-based anion sensors bearing a pendant fluorophore.

2.5 Conclusions

In conclusion, we have reported the first examples of Sb(III)- and Sb(V)-substituted BODIPY dyes and shown that the methylstibonium-substituted **[30]**$^+$ is capable of binding anions in organic solvents. **[30]**$^+$ shows evidence for binding of fluoride, cyanide, and azide in chloroform, while showing modest selectivity for fluoride and cyanide in polar, coordinating solvents. The binding of fluoride and cyanide in acetonitrile is accompanied by a fluorescence "turn-on" response, which allows this compound to be used as a dual sensor for these two anions. Computational studies indicate that this "turn-on" response originates from the interference of Sb-based σ*

orbitals with the BODIPY emission in the free stibonium form, confirming the mechanism proposed by Yokogawa and Irle. This finding sheds light on the strategy of designing anion sensors based on the coupling of a Lewis acidic Sb(V) group with a pendant fluorophore. Compound **[30]**$^{+}$ unfortunately could not be used in aqueous media; however, this work indicates that the development of Sb(V)-based fluorescent sensors for anions other than fluoride should be possible. Future work may be directed toward creating water-compatible sensors for toxic anions such as cyanide and azide in aqueous samples.

2.6 Experimental details

General Methods. All preparations were carried out under an N_2 atmosphere using standard Schlenk techniques unless otherwise stated. Solvents were dried by refluxing under N_2 over Na/K (Et_2O, THF); all other solvents were ACS reagent grade and used as received. Starting materials and reagents were purchased and used as received, except for Ph_2SbCl, which was synthesized according to literature procedures.[143] NMR spectra were recorded using a Varian Unity Inova 500 FT NMR (499.58 MHz for ^{1}H, 125.63 MHz for ^{13}C, 470.00 MHz for ^{19}F) spectrometer. Chemical shifts (δ) are given in ppm and are referenced against residual solvent signals (^{1}H, ^{13}C) or external $BF_3{\cdot}Et_2O$ (-153.00 ppm) for ^{19}F. Elemental analyses were performed at Atlantic Microlab (Norcross, GA). Absorbance measurements were taken on a Shimadzu UV-2502PC UV-Vis spectrophotometer against a solvent reference. Fluorescence measurements were taken on samples in capped quartz cuvettes under air on a PTI

QuantaMaster spectrofluorometer with entrance and exit slit widths of 2 nm. Quantum yield measurements were referenced against a value of 0.91 for fluorescein in 0.1 M NaOH.[138-139]

Synthesis of 28-F_2. **28**-F_2 was synthesized by a modification of literature procedures.[144] A solution of 2,4-dimethylpyrrole (1.49 g, 15.7 mmol) and *p*-bromobenzaldehyde (1.50 g, 8.1 mmol) in 100 mL CH_2Cl_2 was treated with 5 drops of trifluoroacetic acid. The solution was allowed to stir overnight under N_2 at room temperature resulting in a yellow solution. To this was added solid *p*-chloranil (1.94 g, 7.9 mmol), resulting in the formation of a precipitate and a color change to deep red. After stirring overnight under N_2, this solution was treated with neat NEt_3 (8 mL) and, after 10 minutes, with neat $BF_3{\cdot}Et_2O$ (8 mL) which was added via syringe. These additions resulted in a dark brown-black solution. This mixture was stirred for 6 h at room temperature, then quenched with 100 mL H_2O. The organic layer was extracted 3x with H_2O and once with brine, then dried over $MgSO_4$ and filtered through a pad of silica, washing with additional CH_2Cl_2. The dark red filtrate was reduced and purified by flash chromatography on silica gel (gradient of 0-100% CH_2Cl_2 in hexanes). The first major fraction was evaporated and washed with pentane to yield **28**-F_2 as a bright red-orange powder. Yield: 550 mg (17%). ^{1}H NMR (499.58 MHz, $CDCl_3$: 7.26 ppm): δ 7.64 (d, 2, J = 8.4 Hz), 7.18 (d, 2, J = 8.4 Hz), 5.99 (s, 2), 2.55 (s, 6), 1.41 (s, 6). Spectral data are in accord with previous reports.[144]

Synthesis of 28-Me_2. A solution of **28**-F_2 (550 mg, 1.36 mmol) in 15 mL of dry toluene was treated with trimethylaluminum (250 mg, 3.47 mmol) in 5 mL of dry

toluene and stirred at room temperature for 30 minutes. The reaction was quenched with H_2O and the organic fraction separated, dried over $MgSO_4$, and filtered. The filtrate was evaporated and washed with pentane to yield the crude product as an orange powder. The product could be further purified by flash chromatography on silica gel (gradient of 0-100% CH_2Cl_2 in hexanes). The first major fraction yielded **28**-Me_2 as a bright orange crystalline solid. Yield: 505 mg (94%). ^{1}H NMR (499.58 MHz, $CDCl_3$: 7.26 ppm): δ 7.62 (d, 2, *J* = 8.4 Hz), 7.21 (d, 2, *J* = 8.4 Hz), 5.99 (s, 2), 2.48 (s, 6), 1.39 (s, 6), 0.26 (s,6). ^{13}C NMR (125.63 MHz, $CDCl_3$: 77.00 ppm), δ: 152.51 (s), 140.35 (s), 138.65 (s), 135.37 (s), 132.08 (s), 130.28 (s), 129.52 (s), 122.67 (s), 121.79 (s), 16.43 (s), 14.88 (m), 9.52 (br). Elemental Analysis Calculated for $C_{21}H_{24}BN_2Br$: C, 63.83; N, 7.09; H, 6.12. Found: C, 63.63; N, 6.94; H, 6.27.

Synthesis of 29. A solution of **28**-Me_2 (400 mg, 1.01 mmol) in 20 mL Et_2O was treated dropwise with *n*-butyllithium (0.45 mL, 2.65 M in hexanes, 1.19 mmol) at -78° C. Upon stirring, the solution was allowed warm to room temperature over a period of 45 minutes. It was then cooled back to -78° C at which point Ph_2SbCl (357 mg, 1.15 mmol) in 5 mL THF was added via cannula. The mixture was allowed to stir and warm to room temperature overnight. The reaction was quenched with 20 mL of H_2O and extracted with 3 20-mL portions of ethyl acetate. The organic fraction was washed with brine, dried over $MgSO_4$, and filtered. The filtrate was reduced and purified by flash chromatography on silica gel, eluting as the second major fraction with 10% ethyl acetate in hexanes. The product was dried to yield **29** as an orange powder. Orange crystals suitable for X-ray diffraction were obtained by slow evaporation of a

CH_2Cl_2:Et_2O solution. Yield: 158 mg (26%). ^{1}H NMR (499.58 MHz, $CDCl_3$: 7.26 ppm): δ 7.52 (d, 2, *J* = 7.9 Hz), 7.43 (m, 4), 7.35 (m, 6), 7.27 (d, 2, *J* = 7.9 Hz), 5.98 (s, 2), 2.48 (s, 6), 1.40 (s, 6), 0.26 (s,6). ^{13}C NMR (125.63 MHz, $CDCl_3$: 77.00 ppm), δ: 152.18 (s), 141.57 (s), 139.00 (s), 138.75 (s), 138.08 (s), 136.78 (s), 136.48 (s), 136.21 (s), 129.70 (s), 129.44 (s), 128.94 (s), 128.79 (s), 121.60 (s), 16.44 (s), 14.65 (s), 9.56 (br). Elemental Analysis Calculated for $C_{33}H_{34}BN_2Sb$: C, 67.04; N, 4.74; H, 5.80. Found: C, 67.16; N, 4.73; H, 5.95.

Synthesis of [30]OTf. 29 (110 mg, 0.19 mmol) and methyl triflate (135 mg, 0.82 mmol) were combined in 15 mL of dry CH_2Cl_2 under N_2 and the solution was refluxed at 50° C for 5 h. The resulting dark orange solution was reduced and purified by flash chromatography on silica gel, eluting as the second major fraction with 3% MeOH in CH_2Cl_2. The product was dried and reprecipitated with Et_2O to yield [**30**]OTf as an orange powder. Orange crystals suitable for X-ray diffraction were obtained by slow evaporation of a CH_2Cl_2:Et_2O solution. Yield: 56 mg (40%).^{1}H NMR (499.58 MHz, $CDCl_3$: 7.26 ppm): δ 7.77 (d, 2, *J* = 8.1 Hz), 7.65 (m, 6), 7.58 (m, 6), 6.00 (s, 2), 2.64 (s, 3), 2.49 (s, 6), 1.38 (s, 6), 0.26 (s, 6). ^{13}C NMR (125.63 MHz, $CDCl_3$: 77.00 ppm), δ: 152.98 (s), 141.38 (s), 139.11 (s), 138.42 (s), 135.13 (s), 135.05 (s), 132.91 (s), 130.73 (s), 130.52 (s), 129.22 (s), 126.21 (s), 125.29 (s), 122.10 (s), 118.94 (s), 16.47 (s), 14.81 (s), 9.40 (br), 5.21 (s). ^{19}F NMR (470.00 MHz $CDCl_3$, $BF_3{\cdot}Et_2O$: -153.00 ppm), δ: -78.38 ppm. Elemental Analysis Calculated for $C_{35}H_{37}BF_3N_2O_3SSb$: C, 55.66; N, 3.71; H, 4.94. Found: C, 55.60; N, 3.77; H, 4.86.

Computational Methods. All computations were performed using the Gaussian 09 suite of programs.[145] Ground state optimization calculations for [**30**]$^+$, **30**-F, and **30**-CN were performed using the B3LYP functional, with the mixed basis set: Sb, aug-cc-pVTZ-PP; B/F, 6-31g(d′); C/H/N, 6-31g(d). Excited state optimization calculations for [**30**]$^+$ were also performed using the B3LYP functional, with the same mixed basis set. An acetonitrile solvent function using the polarizable continuum model (PCM) was also applied for excited state calculations.

For the excited state optimizations of [**30**]$^+$, the following approach was taken. First, the ground state (S_0) geometry of [**30**]$^+$ was optimized, including the PCM solvent function for acetonitrile. The resulting S_0-optimized geometry was then used in a single-point TD-DFT calculation to determine the vertical excitation energy of electronic transitions to the first few singlet excited states. The first singlet excited state S_1 was confirmed to have primarily $\pi \rightarrow \pi^*$ character and to have significant oscillation strength, so this state was chosen for optimization. A TD-DFT geometry optimization of the excited state S_1 was then performed, starting from the S_0-optimized geometry. The resulting S_1-optimized geometry is shown in Figure 25 above as structure **A**. A second TD-DFT geometry optimization of the excited state S_1 was performed in which the initial geometry of the molecule was modified, distorting the geometry around Sb toward an open, see-saw structure; this calculation yielded a different optimized geometry of comparable energy, which is shown in Figure 25 above as structure **B**.

Crystallography. Crystal data, details of data collection, and structure refinement parameters for compounds **29, [30]**OTf, and **30**-F are compiled in Table 4. The crystallographic measurements were performed at 110(2) K using a Bruker APEX-II CCD area detector diffractometer, with a graphite-monochromated Mo-Kα radiation (λ = 0.71069 Å). In each case, a specimen of suitable size and quality was selected and mounted onto a nylon loop. The semi-empirical method SADABS[146] was applied for absorption correction. The structure was solved by direct methods and refined by the full-matrix least-square technique against F2 with the anisotropic temperature parameters for all non-hydrogen atoms. All H atoms were geometrically placed and refined in riding model approximation. Data reduction and further calculations were performed using the Bruker SHELXTL[147] and ShelXle[148] program packages.

Table 4. Crystallographic details for **29, [30]**OTf, and **30**-F.

	29	[**30**]OTf	**30**-F
Chemical formula	$C_{33}H_{34}BN_2Sb$	$C_{34}H_{37}BN_2Sb \cdot (CF_3O_3S)$	$C_{34}H_{37}BFN_2Sb \cdot (CH_4O)$
M_r	591.18	755.29	657.26
Crystal system, space group	Monoclinic, *C*2/*c*	Monoclinic, $P2_1/c$	Monoclinic, $P2_1/c$
a, *b*, *c* (Å)	50.4025 (18), 11.0109 (4), 10.1952 (4)	13.6694 (6), 24.9626 (12), 10.0894 (5)	12.917 (3), 23.857 (4), 10.1194 (18)
α, β, γ (°)	90, 97.294 (1), 90	90, 94.504 (2), 90	90, 92.282 (13), 90
V (Å^3)	5612.3 (4)	3432.1 (3)	3115.9 (10)
Z	8	4	4
μ (mm^{-1})	1.01	0.92	0.92

Table 4, cont'd.

	29	[**30**]OTf	**30**-F
Crystal size (mm)	0.20 × 0.11 × 0.04	0.37 × 0.18 × 0.03	0.52 × 0.02 × 0.02
No. of measured, independent and observed reflections [$I > 2\sigma(I)$]	60468, 6964, 4990	99924, 7050, 5899	27085, 4881, 2792
R_{int}	0.068	0.092	0.196
$R[F^2 > 2\sigma(F^2)]$, $wR(F^2)$, S	0.052, 0.124, 1.08	0.044, 0.096, 1.12	0.059, 0.149, 0.99
No. of parameters	383	422	380
No. of restraints	4		
$\Delta\rho_{max}$, $\Delta\rho_{min}$ (e Å^{-3})	2.51, −2.40	2.68, −0.67	0.60, −1.06

Absorption and Emission Spectroscopy. Normalized absorption and emission spectra of compounds **29** and [**30**]OTf in dichloromethane are shown below. Emission spectra were obtained with λ_{exc} = 490 nm. Fluorescence quantum yields were calculated based on gradients of integrated emission (IE) versus absorbance at λ_{exc} (Abs) for a series of measurements on the sample and fluorescence standard (fluorescein in 0.1 M NaOH),[138-139]according to the following equation:[149]

$$\Phi_{sample} = \Phi_{std} \times \frac{IE_{sample}}{IE_{std}} \times \frac{Abs_{std}}{Abs_{sample}} \times \left(\frac{\eta_{sample}}{\eta_{std}}\right)^2$$

$$= \Phi_{std} \times \frac{Grad_{sample}}{Grad_{std}} \times \left(\frac{\eta_{sample}}{\eta_{std}}\right)^2$$

where η was taken as 1.33 for 0.1 M NaOH and as 1.424 for dichloromethane. The resulting gradient plots obtained are shown below for compounds **29** and [**30**]OTf.

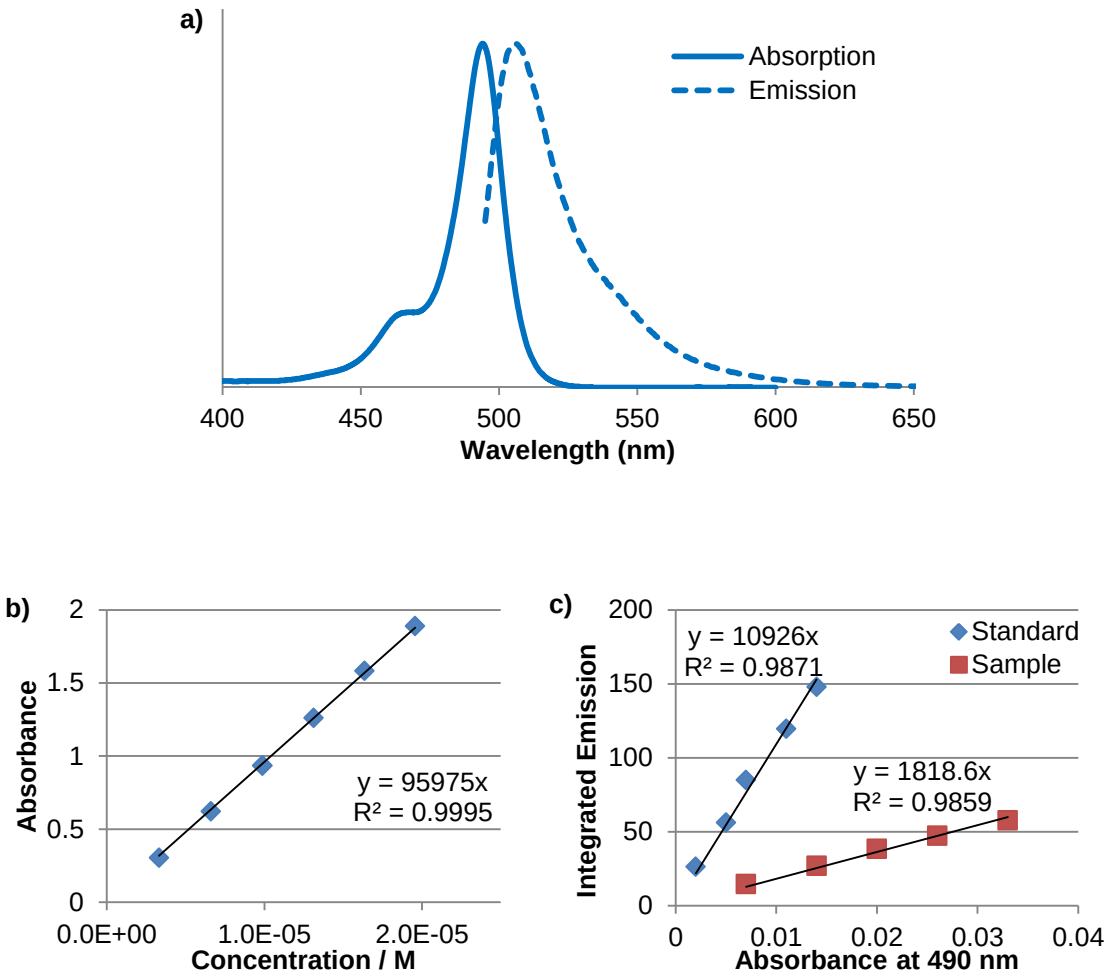

Figure 27. a) Normalized absorption and emission spectra of **29**. b) Beer-Lambert absorbance plot of **29**. c) Quantum yield gradient plot of **29**.

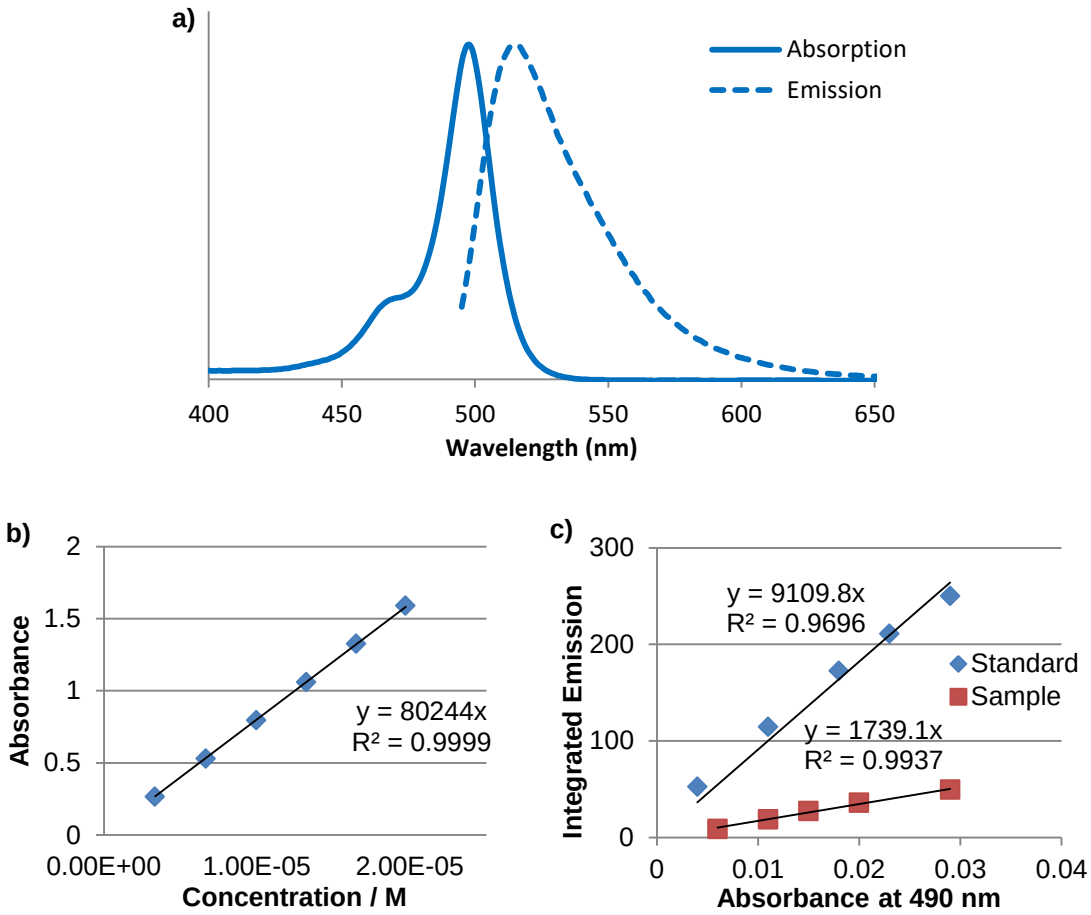

Figure 28. a) Normalized absorption and emission spectra of [**30**]OTf. b) Beer-Lambert absorbance plot of [**30**]OTf. c) Quantum yield gradient plot of [**30**]OTf.

Titration Data. Titrations of [**30**]OTf were carried out by addition of 10-μL aliquots of TBAF or TBACN stock solution into 3.00-mL samples of [**30**]OTf in acetonitrile. Emission spectra were obtained 3 minutes after mixing with λ_{exc} = 475 nm. The resulting spectra and titration curves for the binding of fluoride and cyanide to [**30**]OTf are shown as Figures 29-30 below. Binding constants ($K(F^-/CN^-)$) were calculated by fitting the data according to a known method.[25]

Limits of detection were calculated based on the titration data according to a literature method.[104, 150-151] Fluorescence intensities were normalized between the minimum and maximum fluorescence intensity at 504 nm for [**30**]OTf treated with TBAF or TBACN and plotted against the log of concentration of added anion. These plots are shown as Figure 31 below. The point at which a linear regression fitted to this data crosses the ordinate axis was taken as the limit of detection for fluoride or cyanide by [**30**]OTf under these experimental conditions.

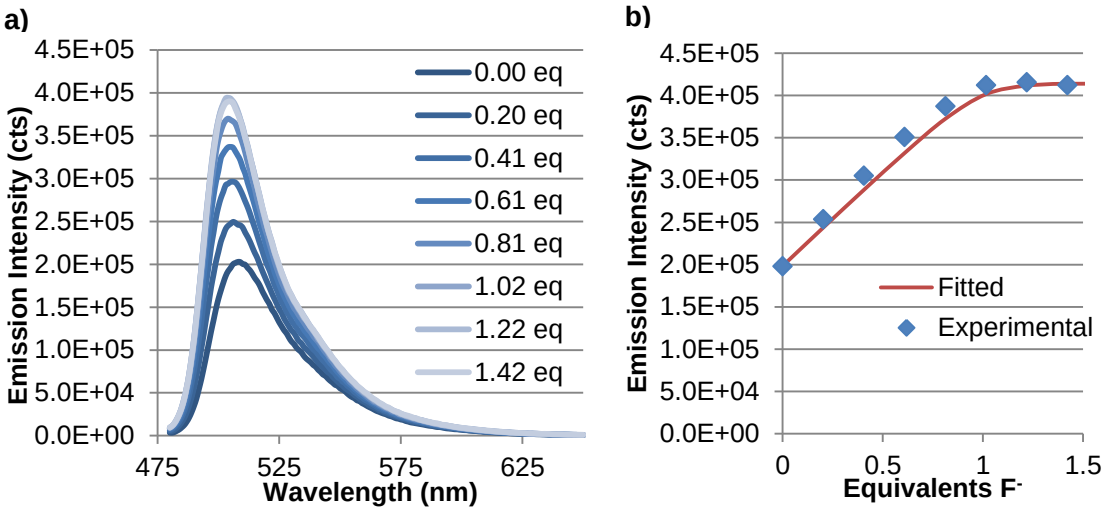

Figure 29. a) Emission spectra obtained upon titration of [**30**]OTf with TBAF. Concentration of [**30**]OTf = 2.00×10^{-6} M. Stock solution of TBAF = 1.22×10^{-4} M. b) Titration curve of emission at 504 nm with addition of TBAF.

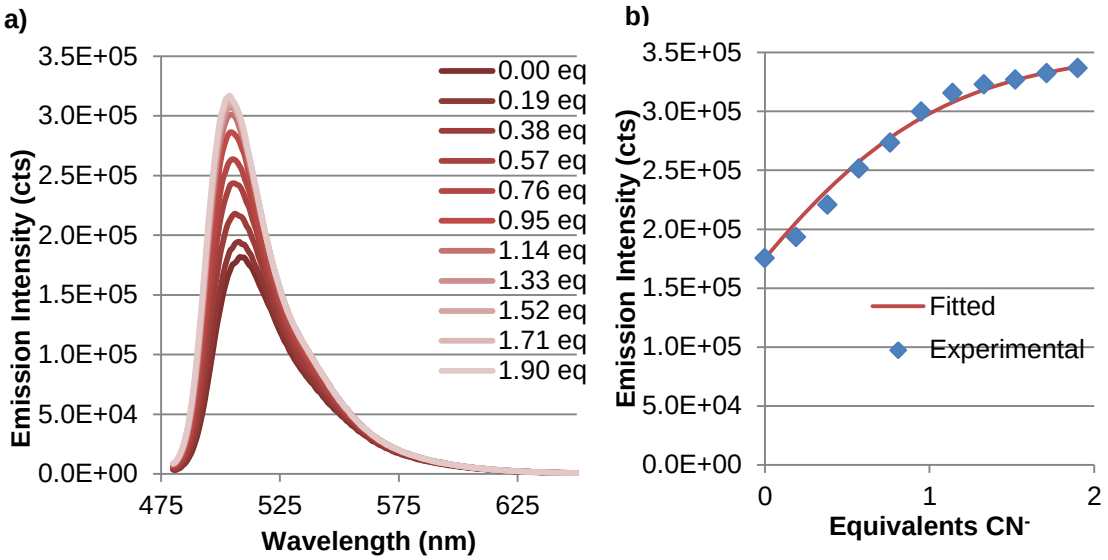

Figure 30. a) Emission spectra obtained upon titration of [**30**]OTf with TBACN. Concentration of [**30**]OTf = 1.93×10^{-6} M. Stock solution of TBACN = 1.10×10^{-4} M. b) Titration curve of emission at 504 nm with addition of TBACN.

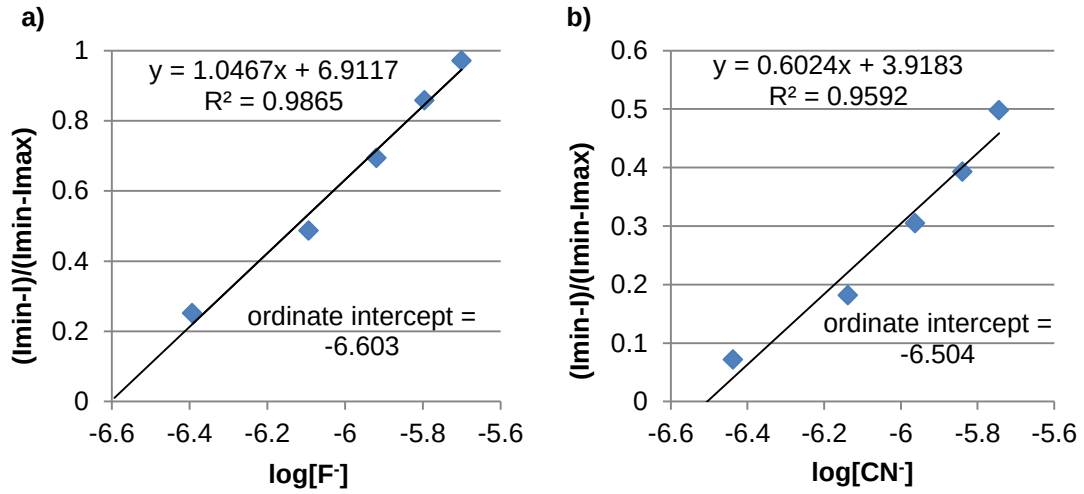

Figure 31. Linear regressions of normalized fluorescence intensities of [**30**]OTf titrated with a) TBAF, b) TBACN.

3. AN ANTIMONY-DECORATED FLUORESCEIN DERIVATIVE WITH UNIQUE REACTIVITY AND FLUORESCENCE "TURN-OFF" RESPONSE TOWARD HYDROGEN PEROXIDE

3.1 Introduction

In exploring antimony-based sensors bearing strongly fluorescent groups, we sought to develop sensors with improved photophysical responses and to understand more thoroughly how those photophysical responses are stimulated by the analyte recognition event. In turn, this knowledge would enable us to design sensors with predictable photophysical responses and potentially explore new analytes beyond fluoride. To further those objectives, we turned our attention to fluorescein as a candidate for a fluorescent reporter group.

The fluorescein-type dyes are well-known and widely used in biological imaging and sensing due to their high quantum yields and molar extinction coefficients, long-wavelength emission, and tunability. The emission wavelength and quantum yield of the fluorescein moiety can be influenced by donor or acceptor substituents as well as external stimuli such as pH.[152-153] Numerous chemical sensors based on fluorescein (and closely-related dyes such as rhodamine) have been developed for a variety of analytes including pH,[154-157] metal cations,[54, 60, 113, 158-163] reactive oxygen species,[57-59, 164-166] and other biologically important species,[167-175] often *in vivo*.

The fluorescein dye structure consists of a 6-hydroxyxanthen-3-one (sometimes called 6-hydroxyfluorone) π-conjugated framework, which is responsible for the color

and fluorescence properties of the dye, substituted at the bridgehead carbon of the tricyclic system (C9) with an aryl group (Figure 32).[176] This 9-aryl group may be variously substituted at the *ortho*, *meta*, and/or *para* positions. In the eponymous fluorescein, first synthesized by Baeyer in 1871,[177] the 9-aryl group is substituted with an *ortho*-carboxylate moiety, which allows fluorescein to be used as a fluorescent pH indicator (Figure 33). In aqueous solutions above pH 6.4, fluorescein exists as a dianion, with both the carboxylate and the hydroxyxanthene groups deprotonated.[152-153] This form of the molecule is highly fluorescent with a bright yellow-green emission with a quantum yield of 0.91.[138-139, 153] In pH conditions between 4.3-6.4, fluorescein exists mainly in a monoanionic form which is moderately fluorescent (quantum yield 0.37); however, below pH 4.3, fluorescein loses fluorescence completely. This is because the doubly protonated neutral form of the molecule rapidly tautomerizes to a spirocyclic derivative, in which the *ortho*-carboxylate substituent "backbites" onto the xanthene

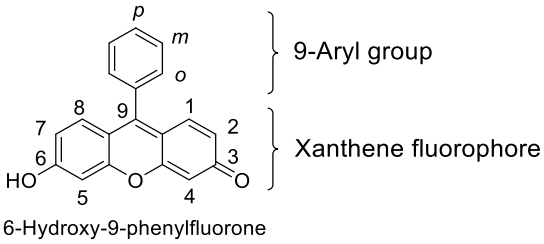

Figure 32. Structure and numbering system for fluorescein derivatives. *N.B.* Although the name "fluorescein" properly applies to 6-hydroxy-9-(2-carboxyphenyl)-fluorone and its derivatives bearing an *ortho*-carboxylate group, the term is often expanded to include related derivatives of 6-hydroxy-9-phenylfluorone that do not bear a carboxylate group. Since the term "fluorone" is less commonly and consistently used, we have chosen to describe all such compounds as fluorescein derivatives or "decorated fluoresceins" in this dissertation.[176]

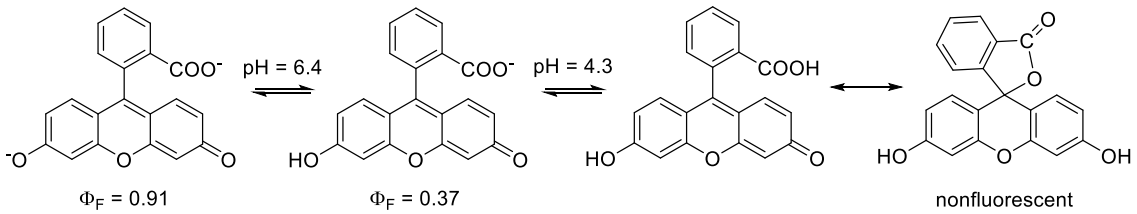

Figure 33. Dianionic, monoanionic, and neutral "lactone" forms of fluorescein at different pH.[152-153]

structure at the electrophilic carbon C9, forming a five-membered lactone ring (Figure 33). In this process, π conjugation across the tricyclic system is lost, destroying the fluorescent properties. This "on-off" fluorimetric response to pH has been used to create fluorescent sensors for intracellular pH based on fluoresceins with different substitution patterns to adjust the pKa of the dye to the pH range of interest.[154] Sensors for other analytes have also been developed on similar principles, inducing the closing or opening of a spirocyclic ring on the dye backbone to quench or revive fluorescence, respectively.[57, 113, 157, 164, 166-167]

In addition to carboxylate groups, fluorescein derivatives may be substituted by donor or acceptor groups that control photophysical properties by a photoinduced electron transfer (PeT) process (Figure 34). Functionalizing the 9-aryl group with a single amine group, which acts as a PeT donor, drastically reduces the fluorescence quantum yield, from 0.91 to 0.014. Functionalizing instead with an electron-accepting nitro group also quenches fluorescence, to a quantum yield of 0.29.[153] These examples illustrate that the fluorescence properties of fluorescein can be controlled by a remote

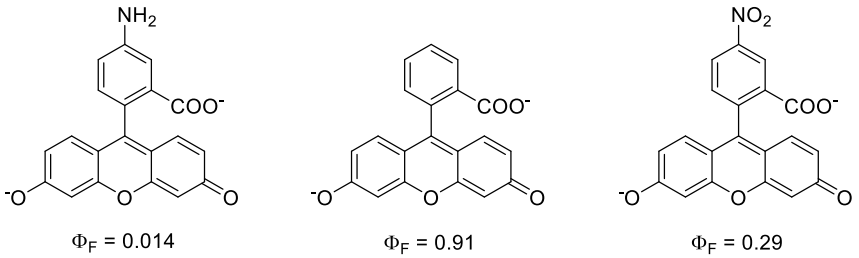

Figure 34. Amino- and nitro-substituted fluorescein dyes exhibiting PeT quenching effects.[52, 153]

substituent on the 9-aryl group via a PeT strategy. Neutralization of the PeT-quenching group will revive strong fluorescein emission, behavior which can clearly be used as a switching strategy for chemical sensing. For example, in 2000, Nagano and coworkers reported the fluorescein derivative **31** functionalized with an *N*,*N*-bis(2-pyridylmethyl)-ethylenediamine (TPEN) group as a Zn^{2+}-selective metal sensor (Figure 35).[163] In the uncomplexed form, **31** displays low fluorescence (Φ_F = 0.023) due to the donor PeT effects of the amine and pyridyl substituents. Upon addition of Zn^{2+}, the nitrogen donor groups coordinate to the metal cation, neutralizing the PeT effect, and the fluorescence intensity of the dye increases more than 50-fold. With this background in mind, we were

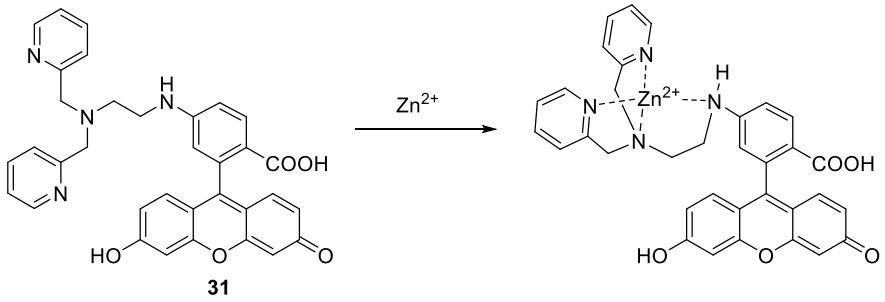

Figure 35. Zn^{2+}-selective fluorescent sensor reported by Nagano based on PeT control of fluorescein emission.[163]

interested to know whether heavier group 15 elements such as antimony could induce PeT effects as a substituent on fluorescein dyes, thereby paving the way for their use as PeT sensors.

Despite their extensive use, however, very few fluorescein-type dyes have been reported that incorporate main group elements beyond the first row as substituents. Prior to our work (*vide infra*)[178], only two examples of phosphine-substituted fluoresceins[179] and one example of a phosphine-substituted rhodamine[113] had been reported, to our knowledge. The phosphine-decorated fluoresceins **32** and **33**, patented by Nagano and Urano as reactive oxygen species (ROS) sensors, incorporate a phosphorus center at the *para* position of the 9-phenyl group of a fluorescein or 2,7-dichlorofluorescein derivative (Figure 36).[179] The authors showed that oxidation of the phosphine to a phosphine oxide with H_2O_2 in pH 7.4 aqueous solution results in a dramatic increase in fluorescence, presumably due to alleviation of PeT quenching by the phosphine donor. Indeed, a number of other phosphino-fluorophores have been reported as peroxide sensors based on a similar PeT strategy.[180-186] To our knowledge, however, no examples

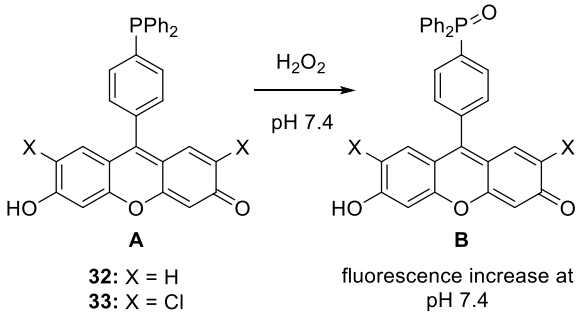

Figure 36. *Para*-phosphine-decorated fluoresceins reported as peroxide sensors at biological pH.[179]

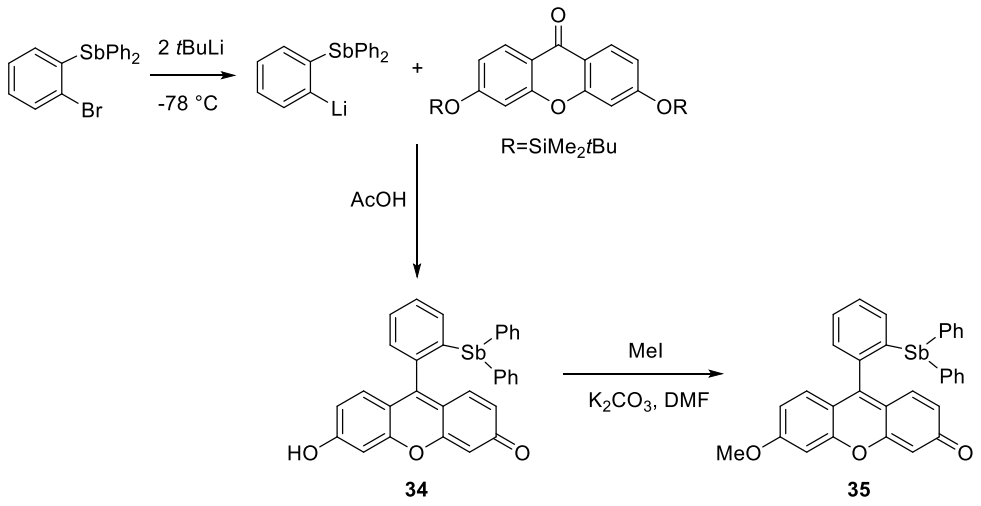

Figure 37. Synthesis of Sb-decorated fluorescein derivatives.

of antimony-substituted fluorescein derivatives had been previously reported. We were thus interested to see whether substitution of fluorescein with an antimony center would also allow control over the photophysical properties. In this section we will describe the results of our synthesis of an antimony-decorated fluorescein and the corresponding phosphorus-decorated fluorescein with the main group substituent at the *ortho* position of the 9-aryl group. We will show how these two fluorescein dyes display divergent reactivity toward hydrogen peroxide, with dramatically different effects on the photophysical properties of the fluorophore, which highlights the unique chemistry of antimony as compared to its lighter Group 15 congener.

3.2 Synthesis and characterization of an Sb(III)-decorated fluorescein

Our initial target compound **34**, shown in Figure 37, was synthesized by procedures adapted from the synthesis of the phosphine-decorated fluorescein reported

by Nagano and Urano.[179] The lithium salt of (*o*-bromophenyl)diphenylstibine was reacted with a *t*-butyl-dimethylsilyl-protected xanthone precursor of fluorescein, followed by cleavage of the protecting groups with acetic acid to yield the conjugated system **34**. The red-orange product obtained at this step was insoluble in most organic solvents and difficult to purify; however, treatment of **34** with methyl iodide converted the alcoholic proton of the fluorescein group to a methyl group and improved the solubility and ease of purification and characterization. The structure of the final product **35** was confirmed by NMR, ESI-MS, and X-ray crystallography (Figure 38). In the crystal structure, the 9-aryl group is oriented orthogonally to the planar tricyclic system, as expected for a fluorescein derivative with a bulky substituent at the *ortho* position.[171] The Sb substituent is placed relatively close to the π system, at a distance of

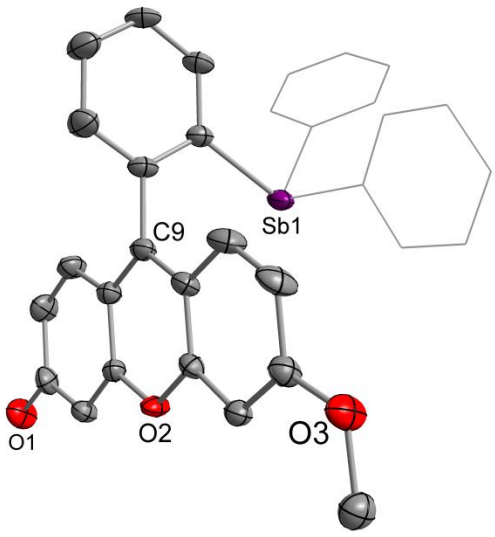

Figure 38. Crystal structure of **35**. Hydrogen atoms omitted for clarity. A second enantiomer present in the crystal with the $SbPh_2$ substituent placed on the opposite side of the tricyclic system is not shown.

approximately 3.26 Å (averaged between two enantiomers present in the crystal) from the electrophilic bridgehead carbon C9, which is within the sum of the van der Waals radii of Sb and C (3.9 Å),[187] but well outside the sum of their covalent radii (2.12 Å).[188]

The bright orange compound exhibits yellow fluorescence in solution with a λ_{max} of 565 nm (λ_{exc} = 459 nm) and a quantum yield of 0.015 in acetonitrile (Figure 39). The methylation of the xanthene hydroxyl group would be expected to decrease the quantum yield of emission by locking the molecule in a neutral form similar to the monoanionic form of fluorescein described above (Figure 33), which is also supported by the characteristic fine structure observed in the absorption and emission profiles of **35** (Figure 39).[152] However, even accounting for this effect, the quantum yield of compound **35** is very low for a fluorescein derivative. The low emission of **35** may indicate some

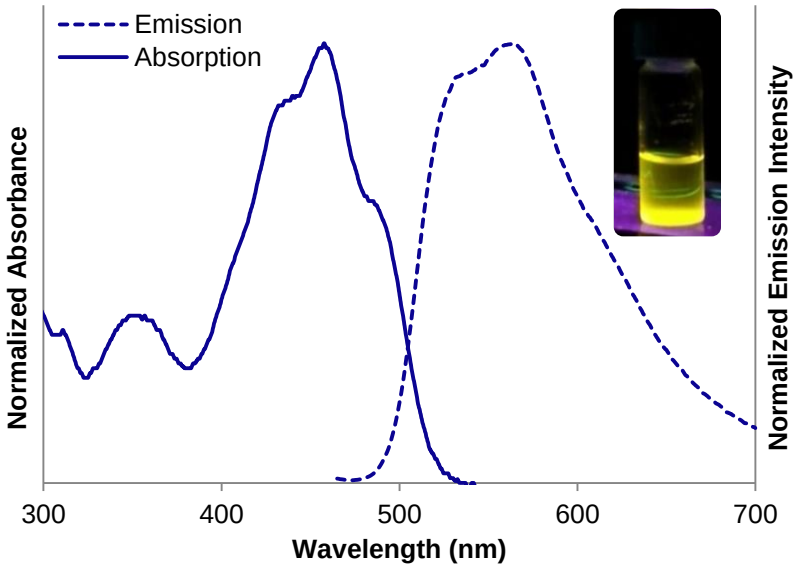

Figure 39. Normalized absorption and emission spectra of **35** in acetonitrile. Emission spectrum determined with λ_{exc} = 459 nm. Inset: Visible fluorescence of **35** in acetonitrile over a handheld UV lamp.

quenching due to a PeT effect from the stibine; however, it may also be a result of some heavy atom quenching by Sb, or a combination of these effects. The emission of **35** may be compared to that of the Sb(III)-decorated BODIPY **29**, which exhibited a quantum yield of 0.13. This quantum yield was also low for a BODIPY derivative, but not as far reduced as that of **35**. This difference could reflect the closer proximity of the Sb atom to the fluorescent dye structure in **35**, which may intensify PeT and/or heavy atom quenching effects. Despite the low quantum yield, however, the fluorescence is clearly visible to the naked eye under a handheld UV lamp (Figure 39).

With this compound in hand, we explored routes toward the oxidation of the Sb center to Sb(V) (Figure 40). Oxidation of **35** with two equivalents of $CuBr_2$ afforded the dibromostiborane **36**, as evidenced by ^1H NMR and mass spectrometric analysis (ESI-MS(+) 734.95 *m/z*), and treatment with *ortho*-chloranil also produced the dark red-brown

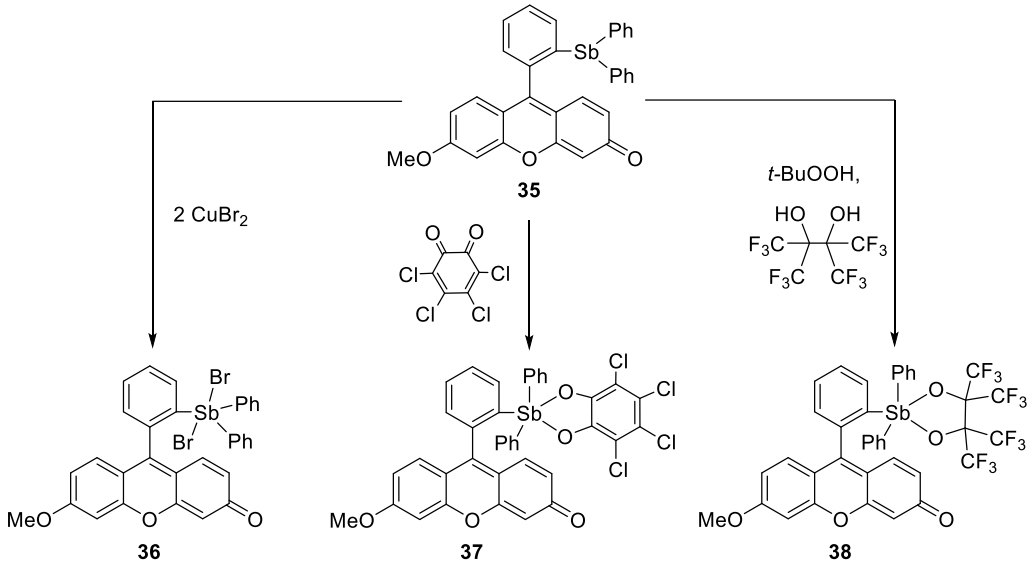

Figure 40. Synthesis of Sb(V)-decorated fluoresceins **36-38**.

oxidized product **37** (ESI-MS(+) 820.96 *m/z*), but these compounds did not exhibit fluorescence. Oxidation with perfluoropinacol using *tert*-butylhydroperoxide[189-192] was also successful to yield **38** (ESI-MS(+) 909.07 *m/z*), yielding a yellow product which still exhibited fluorescence in solution. We attempted to coordinate fluoride to the Sb(V) center of this compound, in the hopes that the stiborane would be able to act as a Lewis acidic sensor for fluoride. However, addition of TBAF to **38** did not result in fluoride binding, but rather decomposition with liberation of the perfluoropinacolate ligand. Moreover, the purities of compounds **36-38** were not sufficiently good to pursue photophysical characterization, and we were not able to obtain crystals for structural characterization.

3.3 "Turn-off" photophysical response to peroxide

Interestingly, treatment of **35** with peroxide alone—either *t*-BuOOH or H_2O_2—results in oxidation with concomitant loss of color and fluorescence over time. UV-vis absorption and emission spectra for the reaction of **35** with H_2O_2 are shown in Figure 41. Complete loss of visible absorbance and fluorescence occurs over time, although the reaction is not immediate. Distinct shifts in the ^{1}H NMR spectrum of **35** appear (see Experimental details), and ESI-MS analysis of the final solution shows two molecular ion peaks at 593.07 *m/z* (corresponding to [**35** +O+H]$^+$) and 611.11 *m/z* (corresponding to [**35** +H_2O_2+H]$^+$) (Figure 42). These features suggest a monomeric oxidized product of **35**, possibly the stibine oxide, which may exist in hydrated and dehydrated forms.

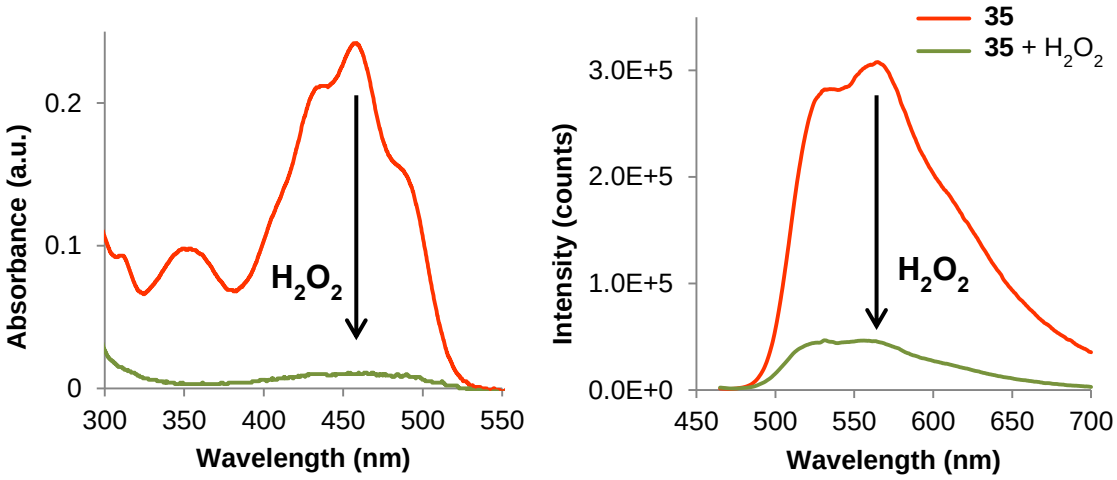

Figure 41. Absorption and emission spectra of **35** in MeCN (λ_{exc} = 459 nm) before and after reaction with H_2O_2. Initial concentrations: 4.1×10^{-5} M **35**, 4.1×10^{-3} M H_2O_2. Final spectra taken after 1 hr of reaction time.

This product is not readily obtained from exposure of **35** to ambient air as is the case for similar phosphine compounds (*vide infra*); both color and fluorescence persist for weeks in solution under ambient conditions. Kinetic experiments under pseudo-first-order

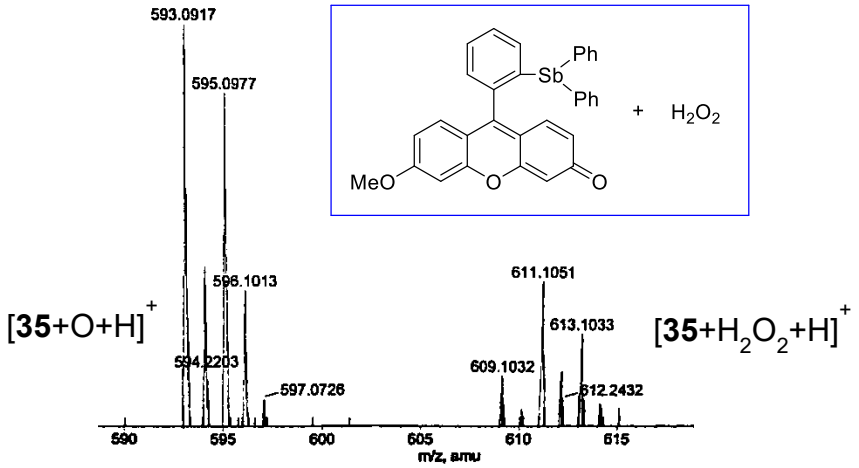

Figure 42. ESI-MS(+) molecular ion peaks observed for the mixture of **35** with H_2O_2.

conditions indicated that the reaction is first order in both **35** and H_2O_2 and proceeds with a rate constant of 0.166 $M^{-1}s^{-1}$ (k_{obs} = 2.5-7.0×10^{-4} s^{-1} for [H_2O_2] = 1.6-4.1×10^{-3} M). This rate is modest but comparable to the rates of reaction of boronate-based "turn-on" fluorescent probes that can be used for *in vivo* detection of hydrogen peroxide (k_{obs} = 3.7-8.1×10^{-3} s^{-1} for [H_2O_2] = 1.0×10^{-2} M),[57] albeit with a less sensitive "turn-off" response in the case of **35**.

The "turn-off" response of stibine **35** to peroxide stands in direct contrast to the "turn-on" response to peroxide observed for the phosphine derivatives **32-33** described above; additionally, we synthesized the *ortho*-phosphine-decorated analog of **35**, **39**, to see whether the positioning of the phosphine group changes the reactivity (Figure 43).[178] Compound **39** could be oxidized to the corresponding phosphine oxide **40** by treatment with H_2O_2, and both compounds were obtained in >97% purity and spectroscopically

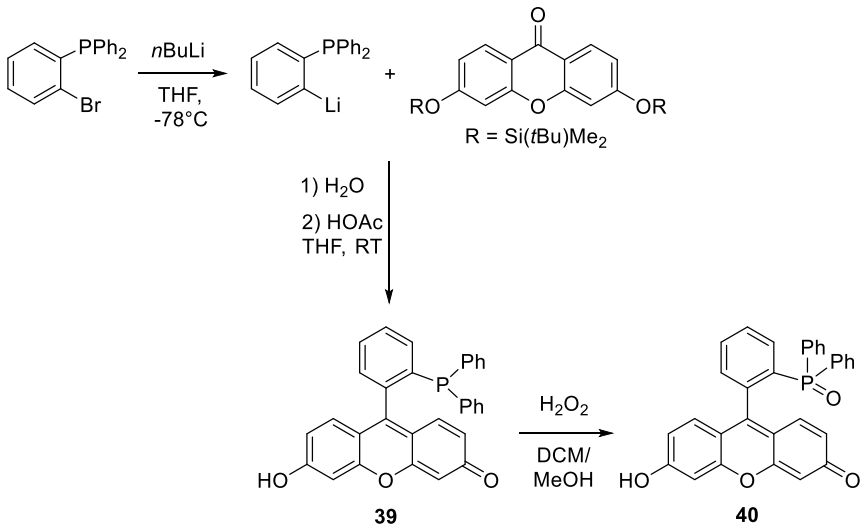

Figure 43. Synthesis of *ortho*-phosphine-decorated fluorescein **39** and its phosphine oxide derivative **40**.

characterized. Both **39** and **40** exhibited fluorescence with emission maxima at 540 nm and 544 nm, respectively; however, in this case, the quantum yield of the phosphine oxide **40** (Φ_F = 0.54) is much higher than that of the phosphine **39** (Φ_F = 0.12). This behavior accords with that reported for the *para*-phosphine-decorated fluoresceins reported previously, as well as other phosphine-decorated fluorophores used as peroxide probes.[179-186] Evidently, the *ortho*-phosphine-decorated fluorescein **39** responds to peroxide by a similar PeT mechanism as these others; however, a different mechanism is at play in the *ortho*-stibine-decorated derivative **35**.

In the case of the phosphine, oxidation by peroxide results in the formation of a monomeric phosphine oxide with a formal P=O double bond, which was confirmed by

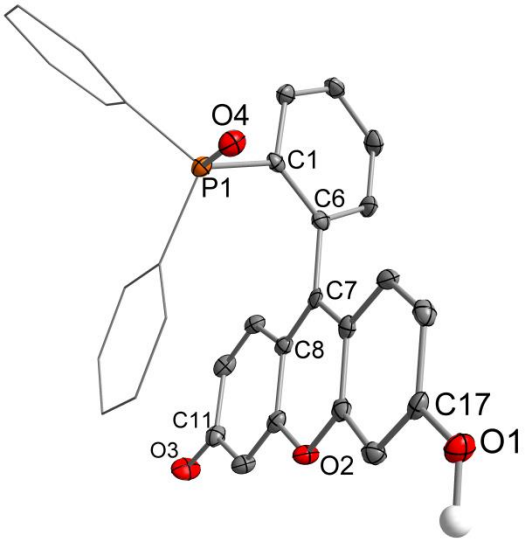

Figure 44. Crystal structure of **40.** Ellipsoids shown at 50% probability. Hydrogen atoms (except the phenolic proton) and solvent molecules omitted for clarity. Selected bond lengths (Å) and angles (°):) P1-O4 1.496(2), C17-O1 1.349(3), C11-O3 1.241(3), ∠O4-P1-C1-C6 87.15(18), ∠C1-C6-C7-C8 104.7(3).

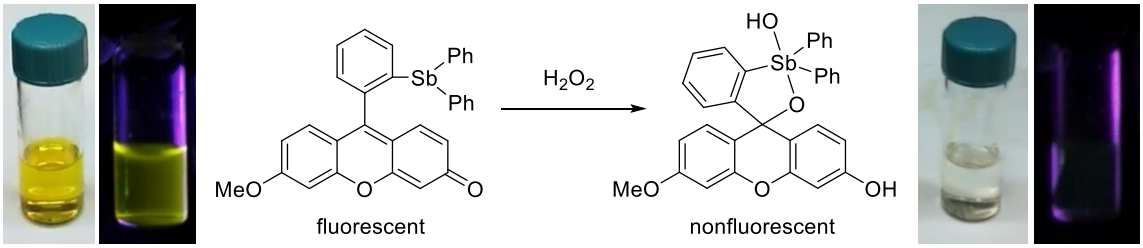

Figure 45. Reaction of **35** with H_2O_2. Inset photos show color and fluorescence loss after 1 hour reaction.

crystallographic characterization of **40** (Figure 44). The crystal structure reveals that the phosphine oxide moiety is twisted approximately 90° out of plane with the 9-phenylene ring on which it is a substituent, rendering no possibility of interaction between the π system of the emissive moiety and either the phosphorus or oxygen atom. The engagement of the phosphine lone pair of **39** in the phosphorus-oxygen bond upon oxidation thus serves to increase the quantum yield of **40** by alleviation of PeT quenching effects.[179] It is known, however, that oxidations of stibines rarely yield monomeric stibine oxide moieties. Due to its size and diffuse orbitals, Sb is reluctant to participate in multiple bonds to O and instead tends to aggregate into Sb_2O_2-bridged dimers or polymers.[193-197] In the case of **35**, we do not see any evidence for dimerization of the oxidized product, but the mass spectroscopic analysis does suggest the possibility of a hydrated form of the stibine oxide (*vide supra*), which we envisioned could take the form depicted in Figure 45. The stibine oxide donates to the electrophilic bridgehead carbon of the fluorescent structure to form a five-membered ring, and addition of H_2O across the Sb center and the phenolic oxygen of the fluorescein moiety results in a unique hydroxyl-Sb(V)-oxide bridging structure. The quaternization of the bridgehead

carbon breaks the conjugation of the fluorescent framework, thus causing the loss of color and fluorescence that is observed.

3.4 Synthesis of xanthylium analog of cyclized stibine oxide hydrate

Although we were not able to obtain crystalline samples of the oxidized product of **35** for X-ray analysis, we were able to synthesize an analogous compound, [**41a**]$^+$, based on a xanthylium chromophore similar to the fluorescein fluorophore (Figure 46). This bright red compound readily oxidizes on exposure to air with a concomitant loss of color, forming compound **41b**, which we were able to characterize by single-crystal X-ray diffraction (Figure 47). The crystal structure confirms the existence of the unique bridging Sb(V)-oxide structure, with the Sb(V) center additionally coordinating either a hydroxide or a fluoride anion stripped from the BF_4^- counteranion of [**41a**]$^+$. The spirocyclization to form this structure breaks the conjugation of the xanthylium

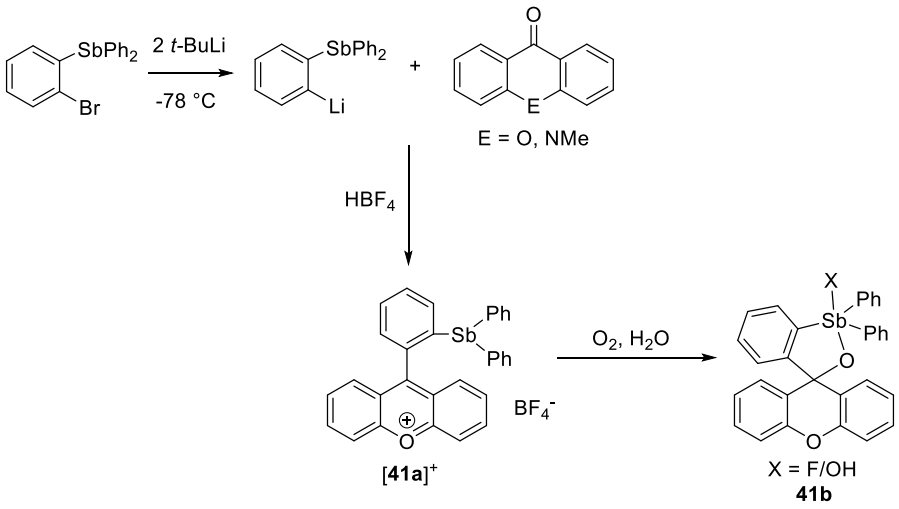

Figure 46. Synthesis of *ortho*-stibine-decorated xanthylium [**41a**]$^+$.

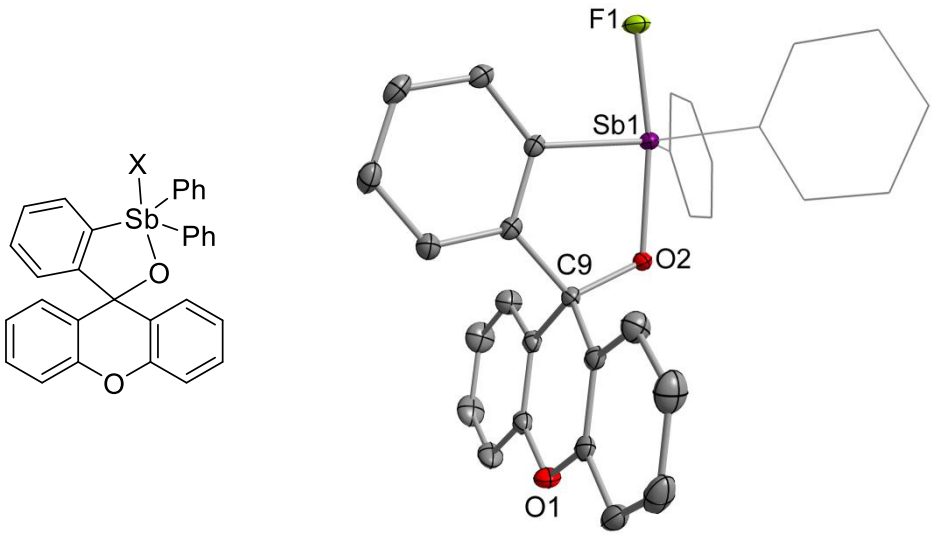

Figure 47. Structure and crystal structure of oxidized **41b**, showing the bridging Sb-O-C moiety. Hydrogen atoms are omitted for clarity. Selected bond lengths (Å): Sb1-F1 1.984(1), Sb1-O2 2.030(1), O2-C9 1.426(2). Atom F1 is assigned as a fluoride, presumably stripped from the BF_4^- counteranion of **41a**; however, it could also be the oxygen atom of a hydroxide group deriving from adventitious water. It is not possible to distinguish definitively between these two crystallographically, but we have chosen to label it as a fluoride since no evidence for hydrogen bonding was observed in the crystal structure, as might be expected for a hydroxyl group.

chromophore, thus accounting for the loss of the original red color. It is likely that **35** takes a similar form upon reaction with H_2O_2 and forms this Sb(V)-oxide bridging motif which gives rise to the "turn-off" response in color and fluorescence.

3.5 Conclusions

We have reported the first example of an antimony-substituted fluorescein derivative, with a diphenylstibine group installed at the *ortho* position of the fluorescein 9-aryl group. This derivative displays yellow fluorescence in organic solutions, but treatment with hydrogen peroxide quenches both color and emission over time, with a

reaction rate constant of 0.166 $M^{-1}s^{-1}$. The complete "turn-off" response of compound **35** to peroxide suggests a mechanism in which Sb(III) is oxidized to an Sb(V) oxide, which then spirocyclizes with the electrophilic bridgehead carbon of the tricyclic dye structure, forming a unique hydroxyl-Sb(V)-oxide bridging moiety. Deconjugation of the π structure due to this spirocyclization destroys the color and fluorescence properties of the dye, resulting in the observed "turn-off" response. This process is analogous to the known spirocyclization of fluorescein to a neutral, nonfluorescent lactone form at low pH, and was further supported by the isolation and structural characterization of the Sb(V)-substituted xanthylium **41b** showing a similar Sb(V)-oxide spirocycle. This response mechanism to peroxide is completely different from the PeT-based mechanism governing the "turn-on" response of phosphine-decorated fluoresceins to oxidation. The divergent reactivity is contingent upon the unique chemistry of antimony as compared to phosphorus, because of the larger element's tendency to form cyclic or chain structures rather than discrete double bonds with oxygen.

3.6 Experimental details

General Methods. All preparations were carried out under an N_2 atmosphere using standard Schlenk techniques unless otherwise stated. Solvents were dried by refluxing under N_2 over Na/K (Et_2O, THF); all other solvents were ACS reagent grade and used as received. Starting materials and reagents were purchased and used as received. Ph_2SbCl[143] and 3,6-dihydroxyxanthone,[198] were synthesized according to literature procedures. The known compound *o*-$(Ph_2Sb)C_6H_4Br$ was synthesized

according to a modified method as described below.[199] The synthesis of phosphine-decorated fluoresceins **39** and **40** are described in the next section (see page 110). NMR spectra were recorded using a Varian Unity Inova 500 FT NMR (499.41 MHz for ^{1}H, 125.59 MHz for ^{13}C) or an Inova 300 FT NMR (299.96 MHz for ^{1}H, 282.21 MHz for ^{19}F) spectrometer. Chemical shifts (δ) are given in ppm and are referenced against residual solvent signals (^{1}H, ^{13}C) or external $BF_3 \cdot Et_2O$ (-153.00 ppm) for ^{19}F. Mass spectrometry was carried out by the Texas A&M Chemistry Mass Spectrometry Facility. Elemental analyses were performed at Atlantic Microlab (Norcross, GA). Absorbance measurements were taken on a Shimadzu UV-2502PC UV-Vis spectrophotometer against a solvent reference. Fluorescence measurements were taken on samples in capped quartz cuvettes under air on a PTI QuantaMaster spectrofluorometer with entrance and exit slit widths of 2 nm. Quantum yield measurements were referenced against a value of 0.91 for fluorescein in 0.1 M NaOH.[138-139]

Synthesis of (*o*-bromophenyl)diphenylstibine.[199] 1,2-dibromobenzene (1.05 g, 4.45 mmol) was dissolved in 15 mL each freshly distilled diethyl ether and THF and cooled to -110 °C. *n*-Butyllithium (1.8 mL, 2.3 M in hexanes, 4.14 mmol) was added slowly dropwise, and the tan suspension stirred 30 minutes at -110 °C. Ph_2SbCl (1.31 g, 4.21 mmol) in 5 mL each diethyl ether and THF was then added dropwise to the reaction flask. The pale yellow solution was allowed to warm to room temperature overnight, changing to a colorless cloudy mixture. The reaction was quenched with 2 mL of water, then the mixture filtered through Celite and evaporated to an oily residue. This was taken up in CH_2Cl_2 and passed through a plug of silica gel, then evaporated again to a whitish

oil, which was reprecipitated with ether and methanol to yield a white solid. Yield: 895 mg (49%). ^{1}H NMR (499.41 MHz, $CDCl_3$: 7.26 ppm): δ 7.47 (d, 1), 7.33 (d, 4), 7.26 (m, 6), 7.08 (m, 2), 6.93 (d, 1).

Synthesis of 3,6-di(*tert*-butyldimethylsiloxy)xanthone.[164] 3,6-dihydroxy-xanthone (3.46 g, 15 mmol) and imidazole (6.0 g, 88 mmol) were dissolved in 10 mL DMF under N_2. *tert*-Butyldimethylsilyl chloride (6.8 g, 45 mmol) was added portionwise to the reaction flask, and the mixture was stirred at room temperature for 5 hours, producing an orange pasty suspension. The mixture was quenched with 50 mL H_2O and extracted three times with ethyl acetate. The organic fraction was washed with H_2O and brine, dried over $MgSO_4$, and evaporated to an orange residue, which was washed with methanol and hexane to yield a peach-orange crystalline powder. Yield: 5.88 g (85%). ^{1}H NMR (299.96 MHz, $CDCl_3$: 7.26 ppm), δ: 8.20 (d, 2), 6.85 (d, 2), 6.84 (s, 2), 1.01 (s, 18), 0.29 (s, 12). Spectral data are in accordance with previous literature.[164]

Synthesis of 34.[179] *o*-$(Ph_2Sb)C_6H_4Br$ (597 mg, 1.38 mmol) was dissolved in 10 mL diethyl ether and treated dropwise with *t*-butyllithium (1.65 mL, 1.7 M in pentane, 2.81 mmol) at -78 °C and let stir for 1 hour at this temperature. 3,6-di(*t*-butyldimethylsiloxy)xanthone (634 mg, 1.39 mmol) in 1:1 Et_2O/THF was then added dropwise, forming an orange-yellow solution. The reaction mixture was kept cold (below -50 °C) for at least 4 hours, then allowed to warm to room temperature overnight. The mixture was quenched with 20 mL H_2O and extracted three times with ethyl acetate. The organic fraction was washed with brine, dried over $MgSO_4$, and evaporated to an orange residue. This was dissolved in a few mL of THF in an open flask, and 0.5 mL

acetic acid was added. After stirring 30 minutes, the solvents were removed, yielding a red solid residue. This was washed with ether and pentane to obtain a solid powder, which was further washed with at least 100 mL of methanol to remove side products. The remaining red-orange solid was washed again with pentane and dried under vacuum. Yield: 288 mg (37% yield). ^{1}H NMR (499.42 MHz, $(CD_3)_2SO$: 2.50 ppm): δ 7.60 (m, 1), 7.53 (t, 1), 7.42 (m, 4), 7.37 (m, 1), 7.28 (m, 7), 6.76 (d, 2), 6.46 (s, br, 2), 6.35 (d, br, 2). ^{13}C NMR (125.62 MHz, $(CD_3)_2SO$: 39.52 ppm), δ: 156.91 (s), 150.89 (s), 149.87 (s), 139.90 (s), 139.29 (s), 137.49 (s), 136.16 (s), 135.72 (s), 135.20 (br), 130.43 (s), 130.12 (s), 129.59 (s), 129.30 (s), 129.18 (s), 128.89 (s), 128.75 (s), 110.82 (s), 101.63 (s). ESI-MS(-): 560.94 *m/z*.

Synthesis of 35.[173] 34 (288 mg, 0.51 mmol) and K_2CO_3 (128 mg, 0.93 mmol) were dissolved in 5 mL DMF and treated with iodomethane (189 mg, 1.33 mmol). The red mixture was allowed to stir at room temperature overnight, then quenched with 20 mL H_2O and extracted three times with CH_2Cl_2. The extract was washed three times with H_2O and once with brine, dried over $MgSO_4$, and filtered through Celite. The filtrate was evaporated to an orange solid residue, which was washed with ether and pentane to yield an orange powder. Yield: 204 mg (69%). m.p. 210-211 °C. ^{1}H NMR (499.41 MHz, $CDCl_3$: 7.26 ppm): δ 7.55 (d, 1), 7.51 (t, 1), 7.45 (t, 1), 7.26 (m, 11), 6.92 (d, 1), 6.90 (d, 1), 6.75 (d, 1), 6.60 (dd, 1), 6.40 (d, 1), 6.29 (dd, 1), 3.92 (s, 3). ^{13}C NMR (125.59 MHz, $CDCl_3$: 77.16 ppm): δ 185.82, 164.38, 158.74, 154.58, 140.39, 140.12, 137.94, 137.63, 136.84, 136.35, 136.28, 130.64, 130.02, 129.94, 129.68, 129.31, 129.15, 129.12, 129.06, 128.98, 128.85, 119.06, 115.00, 113.25, 106.10, 100.51, 56.12. ESI-

MS(+): 577.07 *m/z*. Elemental Analysis Calculated for $C_{32}H_{23}O_3Sb$: C, 66.58; H, 4.02. Found: C, 66.29; H, 4.57.

Synthesis of 36. 35 (62 mg, 0.107 mmol) was treated with $CuBr_2$ (67 mg, 0.300 mmol) in 1:1 CH_2Cl_2:MeOH at -78 °C, then allowed to come to room temperature. The CuBr precipitate was filtered off and the solution evaporated and washed with pentane to yield a red-brown solid. Product analyzed by NMR and MS without further purification. ^{1}H NMR (299.96 MHz, $CDCl_3$: 7.26 ppm): δ 8.76 (d, 1), 8.10 (d, 4), 7.59 (t, 1), 7.47 (t, 1), 7.37 (m, 6), 7.07 (d, 1), 6.73 (d, 1), 6.60 (d, 1), 6.39 (m, 3), 6.27 (m, 1), 3.80 (s, 1). ESI-MS(+): 734.95 *m/z*.

Synthesis of 37. 35 (25 mg, 0.043 mmol) was combined with 1 equivalent of *ortho*-chloranil in hexane and stirred 1 hr. The solution was evaporated to yield a red-brown solid. Product analyzed by NMR and MS without further purification. ^{1}H NMR (499.41 MHz, $CDCl_3$: 7.26 ppm): δ 7.74 (m, 2), 7.67 (m, 2), 7.54 (m, 2), 7.43 (m, 3), 7.40 (m, 3), 7.33 (m, 2), 6.88 (d, 1), 6.64 (d, 1), 6.45 (dd, 1), 6.31 (d, 1), 6.16 (s, 1), 5.79 (dd, 1), 3.85 (s, 3). ESI-MS(+): 820.96 *m/z*.

Synthesis of 38. A solution of **35** (100 mg, 0.173 mmol) in toluene was treated with a slight excess of *t*-butylhydroperoxide (70% aqueous solution) and let stir and warm to room temperature. The solution was extracted and evaporated to yield a yellow solid. Product analyzed by NMR and MS without further purification. ^{1}H NMR (499.42 MHz, CD_3CN: 1.94 ppm): δ 7.93 (d, 1), 7.86 (d, 1), 7.77 (d, 1), 7.62 (m, 1), 7.50 (m, 2), 7.46 (m, 1), 7.37 (m, 2), 7.28 (m, 2), 7.20 (m, 2), 7.13 (m, 2), 6.95 (m, 2), 6.73 (dd, 1),

6.65 (d, 1), 6.34 (dd, 1), 5.97 (d, 1), 3.88 (s, 3). ^{19}F NMR (282.21 MHz CD_3CN, $BF_3{\cdot}Et_2O$: -153.00 ppm), δ: -68.43 (br, 6), -68.93 (br, 6). ESI-MS(+): 909.07 *m/z*.

Synthesis of [41a]BF_4. *o*-$(Ph_2Sb)C_6H_4Br$ (400 mg, 0.93 mmol) was dissolved in 10 mL diethyl ether and treated dropwise with t-butyllithium (1.23 mL, 1.7 M in pentane, 2.09 mmol) at -78 °C and let stir for 1 hour at this temperature. Xanthone (182 mg, 0.93 mmol) in 1:1 Et_2O/THF was then added dropwise, forming an orange suspension. The reaction mixture was kept cold (below -50 °C) for at least 4 hours, then allowed to warm to room temperature overnight. The mixture was quenched with 20 mL 5% NH_4Cl and extracted two times with diethyl ether. The organic fraction was washed with brine, dried over $MgSO_4$, and filtered, then degassed and put under N_2 again. This solution was treated with 1 mL of 48% HBF_4 solution at room temperature, resulting in the precipitation of a red-orange solid. After 30 minutes, the solid precipitate was filtered off, and dried *in vacuo*. The dull red-orange solid [**41a**]BF_4 was stored in an N_2 glovebox to prevent air oxidation. Colorless crystals of the oxidized product **41b** suitable for X-ray diffraction were obtained from evaporation of a MeCN/Et_2O solution under ambient air. Yield: 280 mg (49% yield). ^{1}H NMR (499.42 MHz, CD_3CN: 1.94 ppm): δ 8.53 (t, 2), 8.28 (d, 2), 8.02 (d, 2), 7.83 (t, 2), 7.74 (m, 3), 7.45 (m, 2), 7.23 (m, 2), 7.14 (m, 7). ESI-MS(+): 531.11 *m/z*.

NMR Spectroscopy. ^{1}H NMR spectra monitoring the reaction of **35** with H_2O_2 in d6-acetone are shown below in Figure 48. ^{1}H NMR characterization of compounds **36-38** and [**41a**]BF_4 are shown below in Figures 49-52.

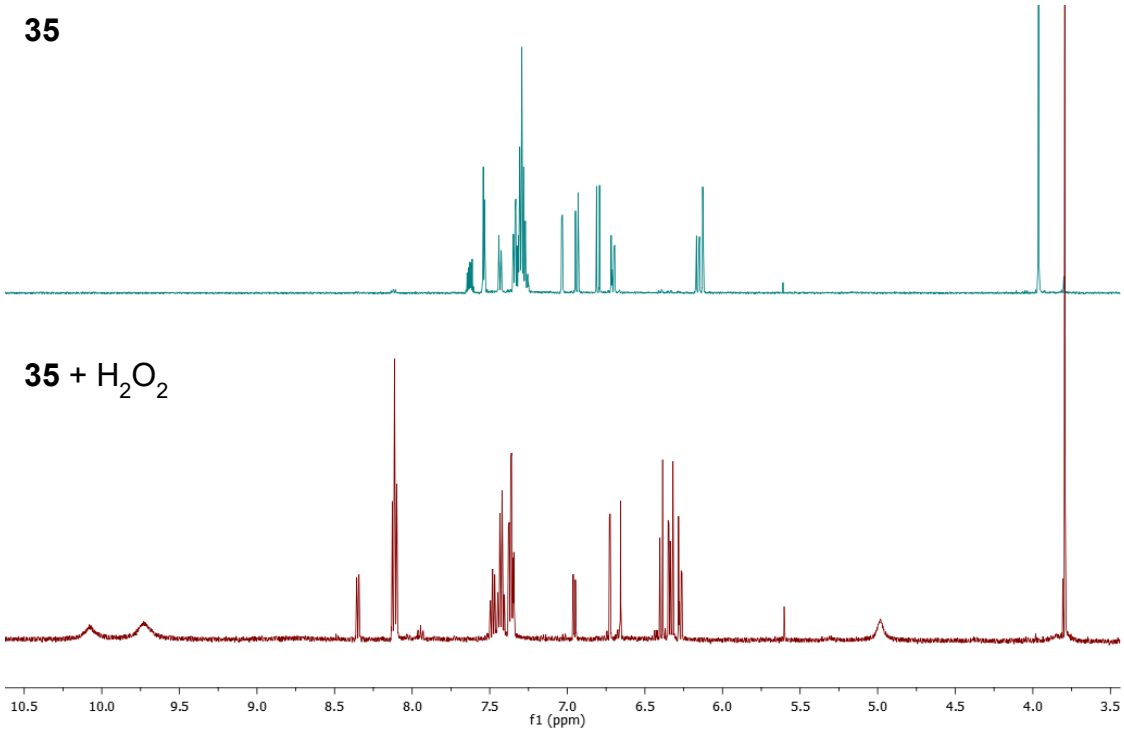

Figure 48. ^{1}H NMR spectra of **35** in d6-acetone before and after addition of H_2O_2.

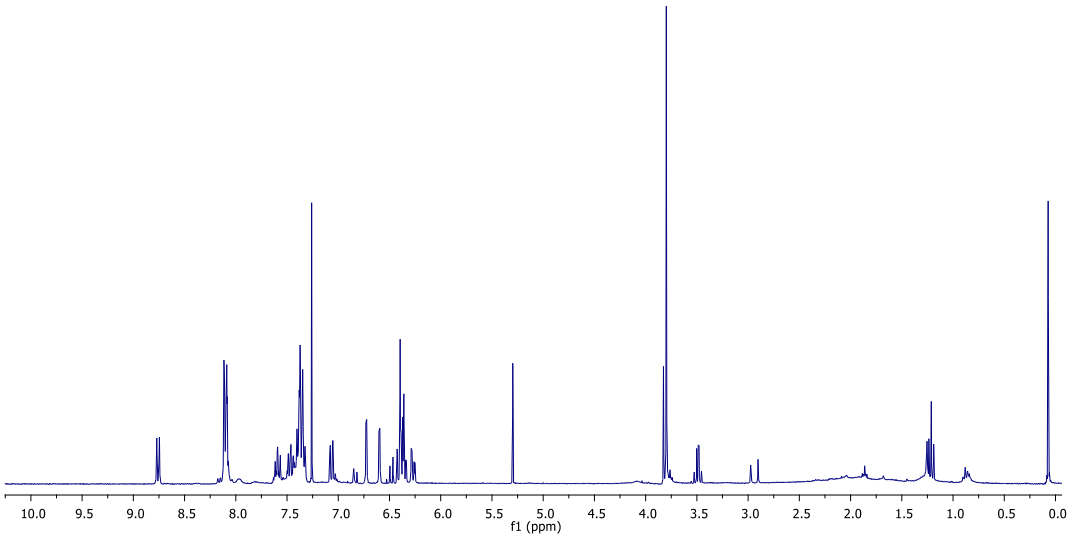

Figure 49. ^{1}H NMR spectrum of **36** in $CDCl_3$.

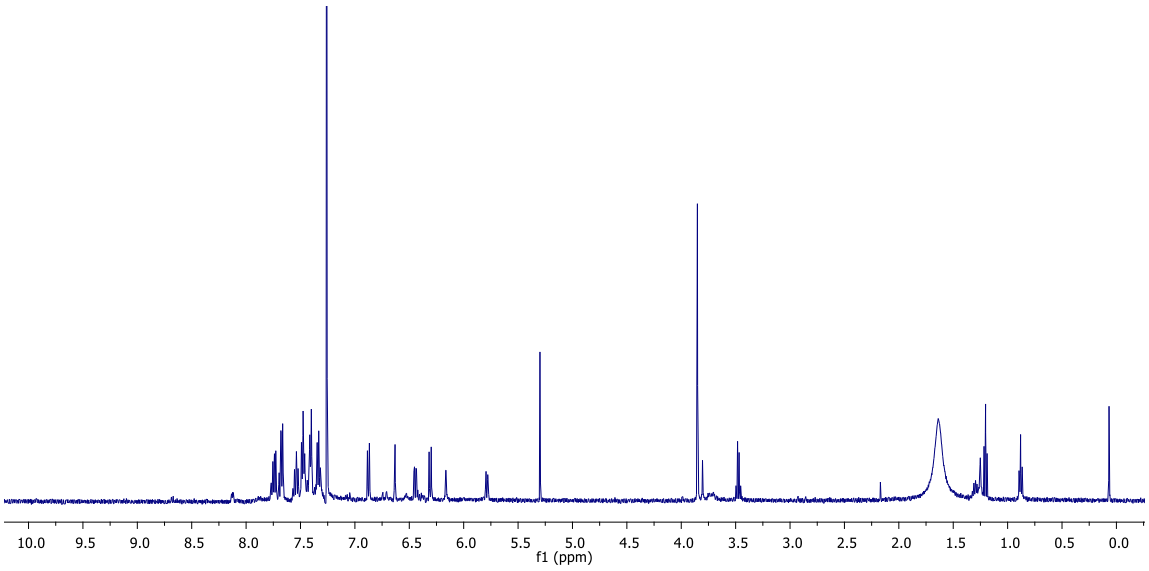

Figure 50. ^{1}H NMR spectrum of **37** in $CDCl_3$.

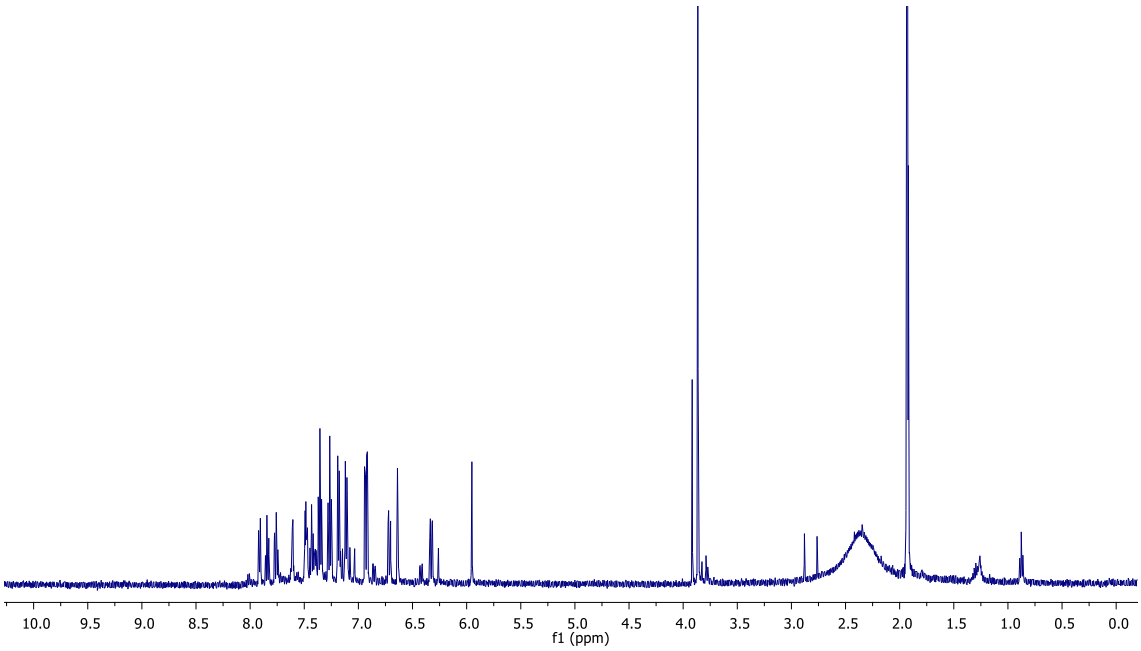

Figure 51. ^{1}H NMR spectrum of **38** in CD_3CN.

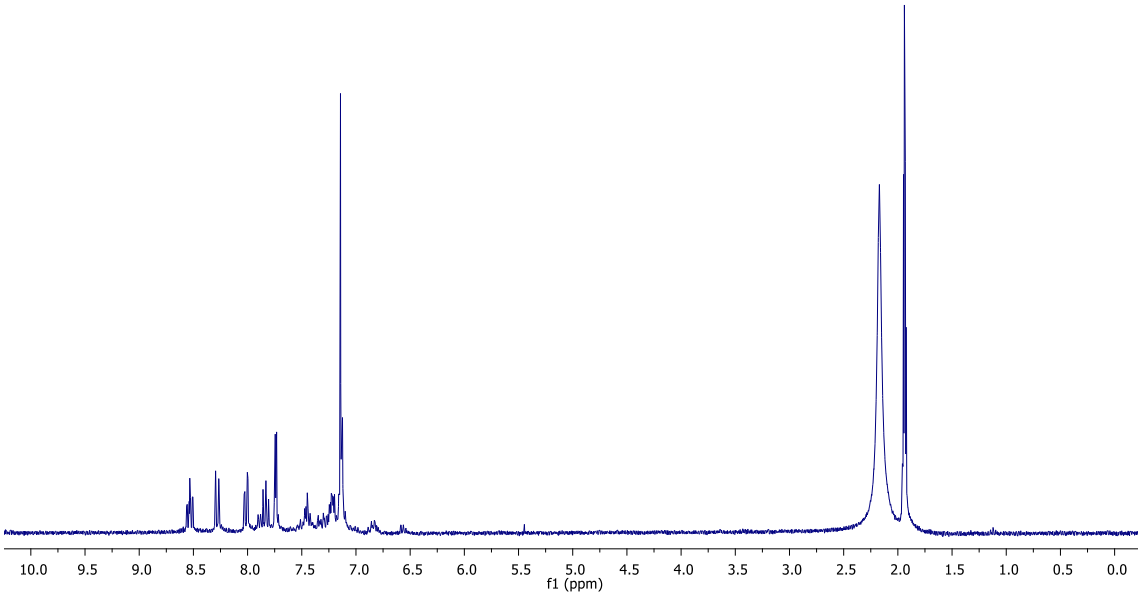

Figure 52. ^{1}H NMR spectrum of **[41a]**BF_4 in CD_3CN.

Crystallography. Crystal data, details of data collection, and structure refinement parameters for compounds **35, 40,** and **41b** are compiled in Table 5. The crystallographic measurements were performed at 110(2) K using a Bruker APEX-II CCD area detector diffractometer, with a graphite-monochromated Mo-Kα radiation (λ = 0.71069 Å). In each case, a specimen of suitable size and quality was selected and mounted onto a nylon loop. The semi-empirical method SADABS[146] was applied for absorption correction. The structure was solved by direct methods and refined by the full-matrix least-square technique against F2 with the anisotropic temperature parameters for all non-hydrogen atoms. All H atoms were geometrically placed and refined in riding model approximation. Data reduction and further calculations were performed using the Bruker SHELXTL[147] and ShelXle[148] program packages.

Table 5. Crystallographic details for compounds **35, 40**, and **41b.**

	35	**40**	**41b**
Chemical formula	$C_{32}H_{23}O_3Sb$	$C_{31}H_{21}O_4P$	$C_{31}H_{22}FO_2Sb$
M_r	577.25	488.45	567.24
Crystal system, space group	Triclinic, *P*	Orthorhombic, $P2_12_12_1$	Monoclinic, $P2_1/n$
a, *b*, *c* (Å)	11.279 (2), 11.800 (3), 19.575 (4)	11.0829 (3), 13.6669 (4), 15.3382 (5)	8.2504 (5), 20.1720 (12), 14.7811 (8)
α, β, γ (°)	95.426 (2), 96.031 (2), 99.749 (2)	90, 90, 90	90, 95.583 (1), 90
V (Å^3)	2536.7 (9)	2323.26 (12)	2448.3 (2)
Z	4	4	4
μ (mm^{-1})	1.12	0.16	1.16
Crystal size (mm)	0.27 × 0.07 × 0.06	0.21 × 0.04 × 0.04	0.30 × 0.22 × 0.18
No. of measured, independent and observed reflections [$I > 2\sigma(I)$]	31539, 12471, 9982	63956, 4749, 3879	30061, 6032, 5725
R_{int}	0.038	0.133	0.021
$R[F^2 > 2\sigma(F^2)]$, $wR(F^2)$, *S*	0.031, 0.075, 1.02	0.043, 0.087, 1.08	0.018, 0.044, 1.06
No. of reflections	12471	4749	6032
No. of parameters	651	329	316
$\Delta\rho_{max}$, $\Delta\rho_{min}$ (e Å^{-3})	0.64, −0.51	0.24, −0.32	0.46, −0.29

Absorption and Emission Spectroscopy. Normalized absorption and emission spectra of compound **35** in acetonitrile are shown in Figure 39 above, with λ_{exc} = 459 nm for emission spectra. The molar absorption coefficient of **35** at 459 nm was determined to be ε = 7847 $M^{-1}cm^{-1}$ (shown below in Figure 53). Fluorescence quantum

yields were calculated based on gradients of integrated emission (IE) versus absorbance at λ_{exc} (Abs) for a series of measurements on the sample and fluorescence standard (fluorescein in 0.1 M NaOH),[138-139] according to the following equation:[149]

$$\Phi_{sample} = \Phi_{std} \times \frac{IE_{sample}}{IE_{std}} \times \frac{Abs_{std}}{Abs_{sample}} \times \left(\frac{\eta_{sample}}{\eta_{std}}\right)^2$$

$$= \Phi_{std} \times \frac{Grad_{sample}}{Grad_{std}} \times \left(\frac{\eta_{sample}}{\eta_{std}}\right)^2$$

where η was taken as 1.33 for 0.1 M NaOH and as 1.344 for acetonitrile. The resulting gradient plot obtained is shown below for compound **35**. Absorption and emission spectroscopy data for compounds **39** and **40** is given in the next section (see page 118).

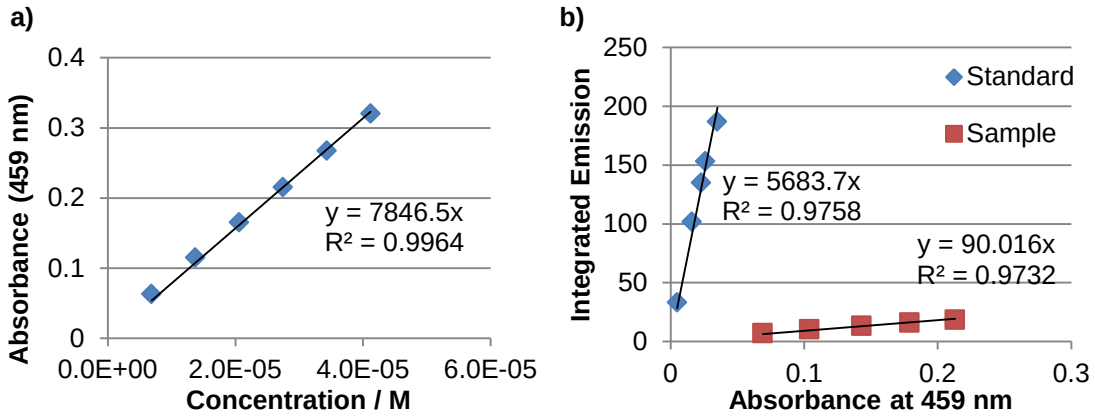

Figure 53. a) Beer-Lambert absorbance plot for **35**. b) Quantum yield gradient plot for **35**.

Kinetic Studies. The reaction of stibine **35** with peroxides is expected to proceed via the mechanism outlined below:[189]

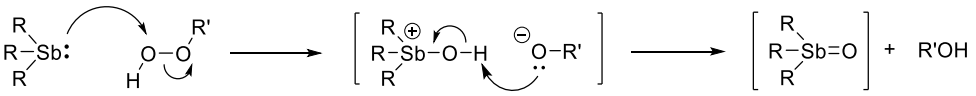

The key step in this mechanism involves the cleavage of the peroxide O-O bond by an S_N2-like displacement by the stibine. Because this is a bimolecular step, the rate of this reaction would be expected to proceed according to the following rate law:

$$r = k\,[\mathbf{35}]\,[H_2O_2]$$

which is first order in both stibine **35** and H_2O_2. In order to confirm this behavior, pseudo-first order kinetic experiments were undertaken. A 3.00-mL solution of **35** in MeCN at a concentration of $[\mathbf{35}]_o = 6.65\times10^{-6}$ M was treated with a large excess of H_2O_2 ($[H_2O_2]_o = 4.02\times10^{-3}$ M), and the absorbance of **35** over time was recorded, assuming absorbance to be directly proportional to [**35**] at this concentration, according to the Beer-Lambert law. The resulting decay of the absorbance is shown in Figure 54 below. The natural logarithm of absorbance at 459 nm was found to be linearly related to time in minutes according to the expected first order rate law:

$$\ln[A] = \ln[A]_o - kt$$

with an observed rate constant of $k = 0.0682$ min^{-1}. This data confirms that the reaction proceeds first order with respect to **35**.

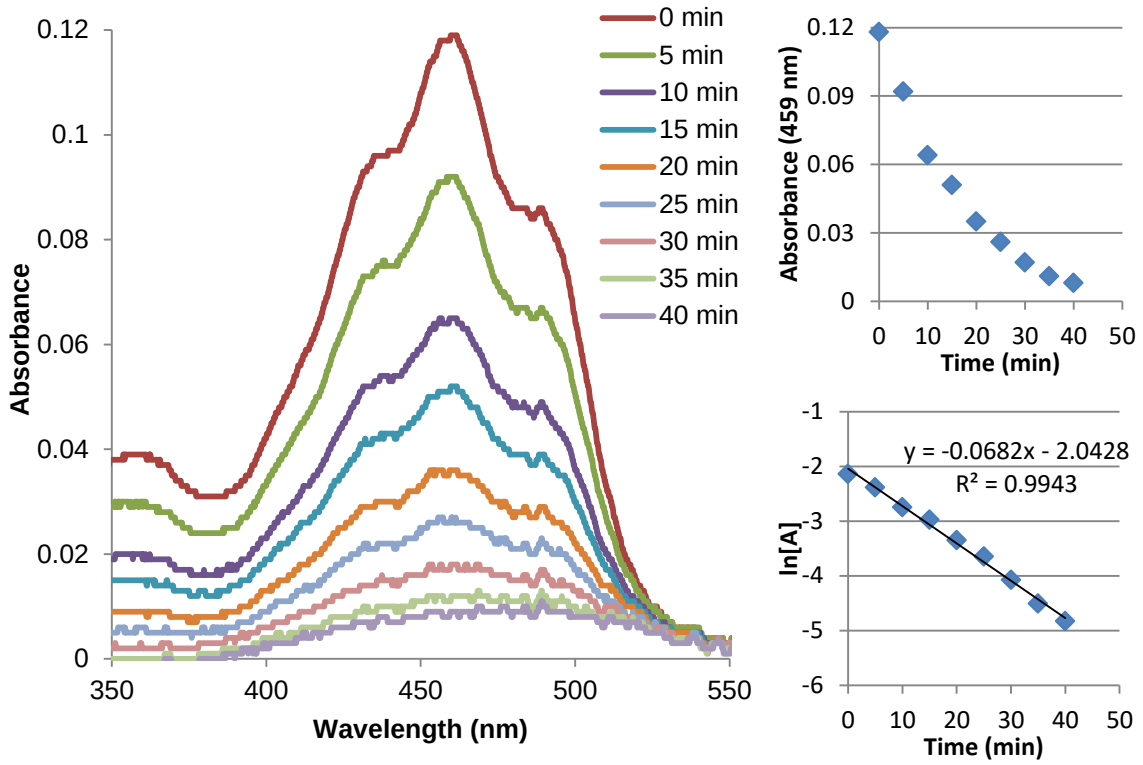

Figure 54. Decay of absorbance of **35** over time upon addition of a large excess of H_2O_2 ($[\mathbf{35}]_o = 6.65\times10^{-6}$ M; $[H_2O_2]_o = 4.02\times10^{-3}$ M). Inset: Graph of the decay of absorbance at 459 nm, first order plot for ln[A] vs time.

Next, pseudo-first order initial rates were obtained for the reaction of **35** with varying concentrations of H_2O_2. A 3.00-mL solution of **35** in MeCN at a concentration of $[\mathbf{35}]_o = 6.87\times10^{-5}$ M was treated with 40-, 60-, 80-, and 100-uL aliquots of a stock solution of H_2O_2 of concentration $[H_2O_2] = 0.1246$ M. The resulting plots of absorbance at 459 nm for the first five minutes of reaction are shown in Figure 55 below. Because the slopes of the initial linear decays scale linearly with the amount of H_2O_2 added, this data confirms that the reaction proceeds first order with respect to H_2O_2, in accord with the expected rate law.

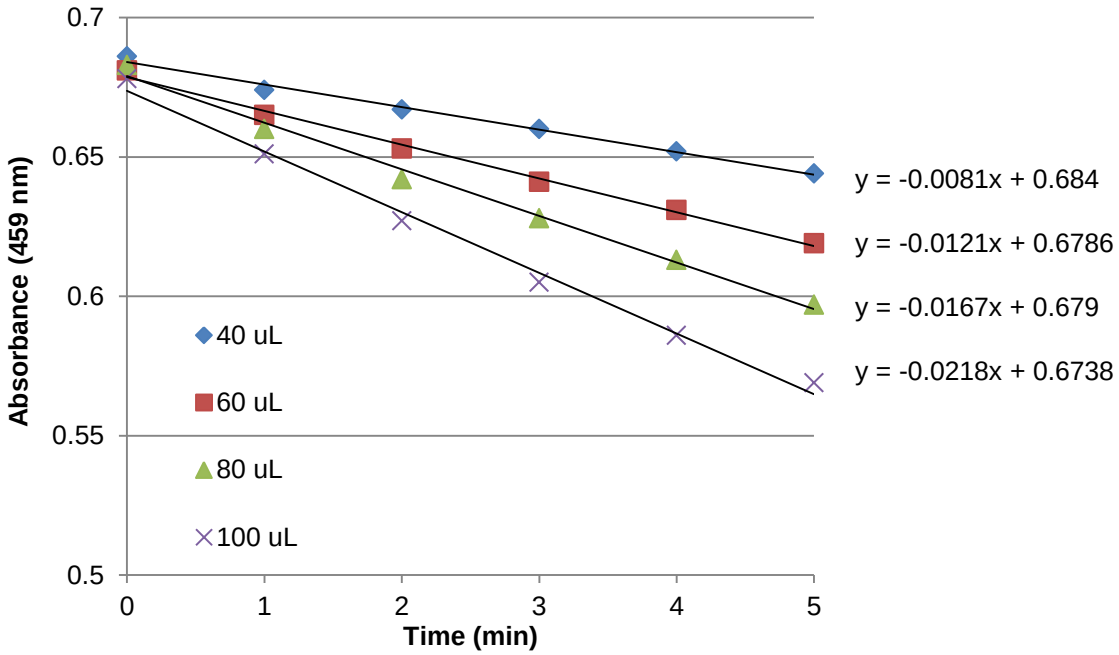

Figure 55. Pseudo-first order initial decays of absorbance of **35** with addition of varying amounts of H_2O_2 ($[\mathbf{35}]_o = 6.87\times10^{-5}$ M).

The slopes of the pseudo-first order initial decays were then used to determine the reaction rate constant *k*. Under pseudo-first order conditions with an excess of H_2O_2, the rate law reduces to

$$r_o = k_{obs}\,[\mathbf{35}]_o \qquad \text{where} \qquad k_{obs} = k\,[H_2O_2]_o$$

The initial rate r_o for each measurement is given by the slope of the linear decay of absorbance divided by the molar absorptivity ε obtained from the Beer-Lambert curve (Figure 53 above). Using this data, we can construct a plot of k_{obs} vs. $[H_2O_2]_o$ where the slope of the line is equal to the rate constant *k* (Figure 56 below). From this curve, we obtain a rate constant of $k = 9.97\ M^{-1}min^{-1} = 0.166\ M^{-1}s^{-1}$.

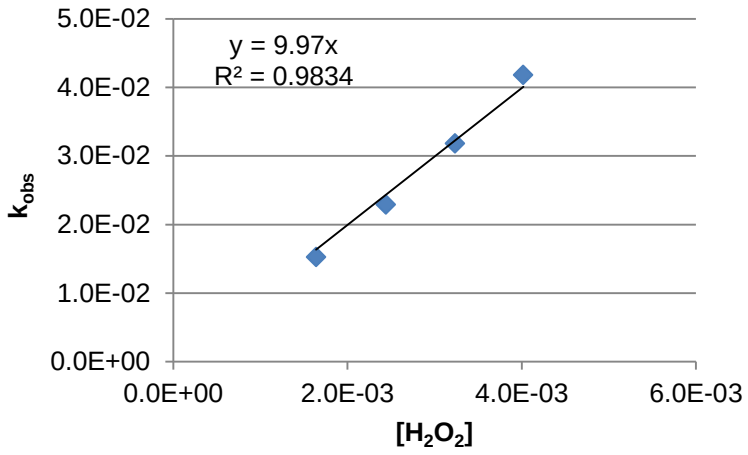

Figure 56. Pseudo-first order plot of k_{obs} vs. $[H_2O_2]_o$ where $[\mathbf{35}]_o = 6.87\times10^{-5}$ M.

4. A PHOSPHINE-DECORATED FLUORESCEIN DERIVATIVE FOR "DOUBLE TURN-ON" FLUORESCENCE SENSING OF GOLD(III) IONS IN AQUEOUS SOLUTION[†]

4.1 Introduction

As discussed in the preceding section, a number of fluorescent phosphine derivatives have been reported in recent years as sensors for reactive oxygen species (ROS) such as hydrogen peroxide, which are important biological analytes.[179-186] Several examples are shown in Figure 57, including the *para*-phosphine-decorated fluoresceins patented by Nagano and Urano discussed previously.[179] All of these derivatives display fluorescence "turn-on" responses to ROS based on a photoinduced electron transfer (PeT) strategy. In the absence of oxidant, the phosphine acts as a PeT donor in the excited state due to its lone pair, quenching fluorescence; however, oxidation of the

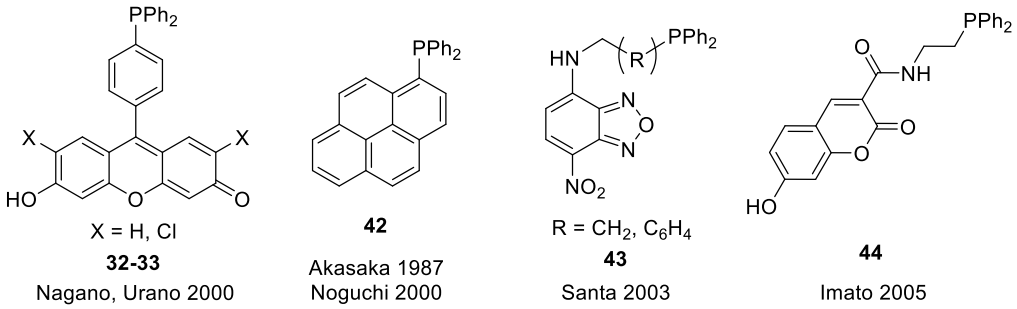

Figure 57. Selected examples of fluorescent phosphines used as ROS probes.[179-183]

[†] Reprinted in part with permission from "Synthesis and Coordination Chemistry of a Phosphine-Decorated Fluorescein: "Double Turn-On" Sensing of Gold(III) Ions in Water"; Christianson, A. M.; Gabbaï, F. P. *Inorg. Chem.* **2016,** *55*, 5828-35, Copyright 2016 by the American Chemical Society.

phosphine by ROS deactivates the phosphorus-to-fluorophore PeT process, resulting in a resurrection of the fluorophore's emission.[51-52] It occurred to us that a similar "turn-on" response could also result from metal coordination to a phosphine rather than oxidation, since both processes would serve to engage the phosphorus lone pair in bonding and thus reduce or remove its role in PeT quenching (Figure 58).

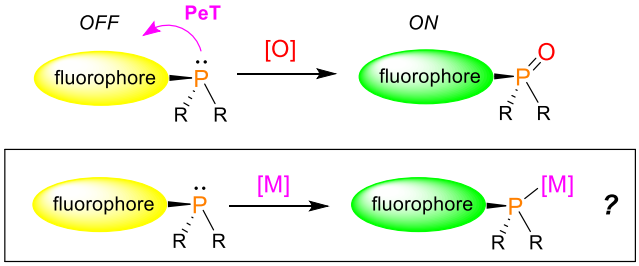

Figure 58. PeT strategy for sensing based on phosphine oxidation or metal coordination.

Although such fluorescence "turn-on" responses are ubiquitous for metal sensors containing N, O, and S donors as metal binding sites,[51-52, 62, 108-109] a review of the literature indicates that this approach had never been implemented in sensors possessing phosphine donors. However, several reports of luminescent phosphine-metal complexes suggest that these complexes can retain high emission and that the luminescence properties may be sensitive to the nature of the metal coordination environment.[113, 121-122, 133-134, 200-204] In some cases, no evidence for fluorescence "turn-on" based on the removal of PeT quenching in the free phosphine is observed, as in the case of Higham and coworkers' phosphine-substituted BODIPY fluorophores (Figure 18 above), which form complexes with Cu(I), Ag(I), Au(I), and Re(I) fragments without major

perturbation of the emission.[133-134] In another report, coordination of Au(I) by a phosphine-phenanthrene ligand resulted in quenched fluorescence but enhanced phosphorescence of the phenanthrene moiety.[201] Coordination of Au(I) units to phosphole luminophores also typically quenches emission to some extent due to the heavy atom effect.[205-221] However, Plenio and coworkers recently reported that phosphine-substituted BODIPY dyes **45** and **46**, in which the phosphorus substituent is situated more closely to the BODIPY fluorophore than in Higham's case, do indeed show low emission that is revived upon coordination to coinage metals (Figure 59).[122] A series of Au(I) complexes with different ligands at gold were studied, and the fluorescence quantum yield was found to depend qualitatively on the electron density at gold, with amino- or thiolato-gold complexes exhibiting low fluorescence, whereas cationic gold complexes with a non-coordinating anion such as nonaflate exhibited enhanced fluorescence. These changes are presumed to be related to the extent of electron donation of the phosphine to the metal, where the phosphine would coordinate

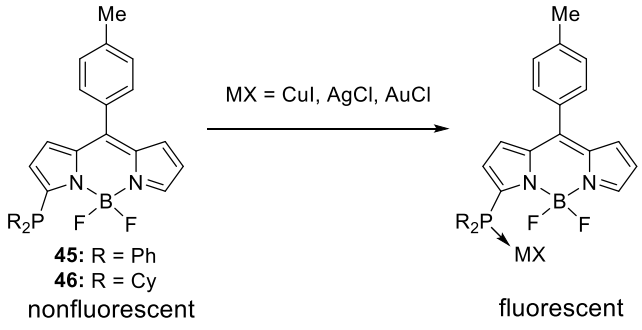

Figure 59. Phosphine-substituted BODIPY dyes reported by Plenio and coworkers and their corresponding coinage metal complexes, which increase fluorescence due to the removal of PeT quenching effects.[135]

more strongly to a more electron-deficient Au(I) center, thus more effectively suppressing the PeT quenching. In this case, the sensitivity of the phosphine-substituted fluorophore to the coordination environment of Au(I) was used for *in situ* monitoring of the reaction steps in gold-catalyzed reactions involving alkynes. However, a similar strategy has not been used for the development of sensors for metals themselves.

To our knowledge, only one fluorescent metal sensor incorporating a phosphorus group has been reported, the phosphine-substituted rhodamine **47** shown in Figure 60, which was used as a palladium sensor.[113] In this case, the phosphine does coordinate to the Pd(II) analyte; however, the origin of the "turn-on" fluorescent response is rather due to the coordination of the nearby amine group, which opens up the spirolactam rhodamine dye to its highly-fluorescent xanthene form. This example therefore does not illustrate the PeT strategy we proposed; however, it does show that the incorporation of phosphine groups in metal sensors may confer selectivity for heavy late transition metals such as palladium, based on the preference of soft phosphine donor groups for these metals. Heavy late metals are not only considered precious, but are also typically quite toxic and therefore pose environmental concerns. Other than for Hg,[103-107] however,

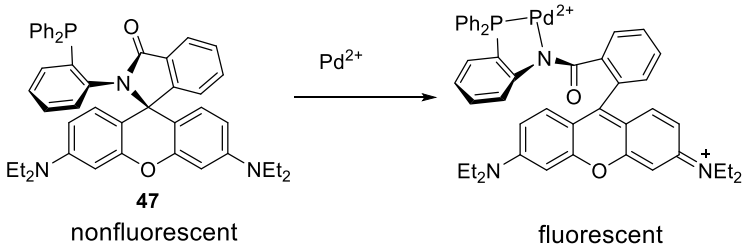

Figure 60. Phosphine-substituted rhodamine dye reported as a fluorescence "turn-on" sensor for palladium.[113]

few fluorescent probes have been developed to detect heavy late metals such as Pd, Pt, Ag, and Au compared to lighter metals.[62, 109-114] Thus, with the increasing use of these metals in catalysis and as potential drug targets, interest has grown in fluorescent detection methods for them in both environmental and biological contexts.[109]

We were especially interested to design a fluorescent sensor for gold ions in aqueous media. Interest in fluorescence detection methods for gold ions in biological and environmental samples[108-109, 222-223] has grown along with the recent explosion of research into organometallic gold compounds for pharmaceuticals[224-227] and homogeneous catalysis.[228-232] Methods for imaging gold species *in vivo* have been sought to aid in understanding the mechanism of action of gold-based therapeutic agents and the distribution of gold species in living systems.[109-112, 227] Additionally, the toxicity of many gold compounds,[115-117] like those of other heavy metals, make their trace detection in drug formulations and environmental samples important, especially with their expanding use in industrial catalysis. To that end, a number of reaction-based fluorescent probes for gold have been developed,[105, 110-112, 120, 233-235] but very few coordination-based sensors are known for this metal.[151, 160, 236-239] We therefore chose to target a gold sensor in which the fluorescent response would be based on the coordination of a phosphine bearing a pendant fluorescent group.

In this section, we report studies of the *ortho*-phosphine-decorated fluorescein **39** as a fluorimetric sensor for gold. In this compound, the primary recognition site for gold ions is a triarylphosphine positioned in the immediate vicinity of a fluorophore, which we reasoned would be conducive to a large fluorescent response via a PeT strategy. We

have isolated and structurally characterized the products of the coordination of gold(I) fragments to both one and two phosphinofluorescein units, and we have shown that compound **39** behaves as a "turn-on" fluorescent sensor for gold cations in neutral water that is sensitive to the ppm level.

4.2 Synthesis and structural characterization of phosphinofluorescein-Au(I) complexes

The synthesis of *ortho*-phosphinofluorescein **39** was shown in the preceding chapter in Figure 43, and was accomplished by the same adapted method as for the *ortho*-stibinofluorescein **34**.[179] The phosphine-decorated fluorescein **39** was isolated as a bright red-orange powder in greater than 97% bulk purity, as confirmed by NMR spectroscopy and HPLC analysis. The ^{31}P NMR spectrum of **39** displays a singlet peak at -15.4 ppm, characteristic of a triarylphosphine. The product was further confirmed by high-resolution mass spectrometry, where a molecular ion peak at *m/z* 473.13 ($M+H^+$) appears in the positive spectrum. Compound **39** is stable to air and moisture in the solid state. It is moderately soluble in DMSO but only sparingly so in DCM and MeOH. Stock solutions of **39** in degassed DMSO can be kept fresh for at least 24 hours; however, over time or when no special precaution is taken to avoid exposure to oxygen, compound **39** is converted into the corresponding phosphine oxide derivative **40** characterized by a ^{31}P NMR resonance at 26.3 ppm. As noted in the preceding section, compound **40** could also be independently synthesized by treatment of **39** with H_2O_2, allowing confirmation of the ^{31}P NMR assignment. The structure of **40** was again confirmed by high-resolution

mass spectrometry, which shows a molecular ion peak at *m/z* 489.12, and unambiguously by single-crystal X-ray diffraction analysis (Figure 44 above).

The coordination of the phosphinofluorescein ligand **39** to Au(I) centers was next explored. Reaction of equimolar amounts of **39** and (tht)AuCl readily yielded the red-orange phosphine gold chloride compound **39**-AuCl in high purity (Figure 61). Coordination of the phosphine group resulted in a large downfield shift in the ^{31}P NMR signal to 24.5 ppm, and the positive high-resolution mass spectrum shows a molecular ion peak at *m/z* 705.07, corresponding to the 1:1 AuCl complex. The solid-state structure of this complex was confirmed by single-crystal X-ray diffraction analysis (Figure 62). Although the structure of **39**-AuCl is affected by some positional disorder, the structure is sufficiently clear to establish the coordination of the phosphorus atom to the gold chloride fragment. The chloride and phosphine ligands are coordinated to the gold center in a linear fashion as expected, with P-Au-Cl angles of 176.9(2)° and 173.7(2)° for each of the disordered components. The *ortho*-phenylene linker connecting the phosphine to

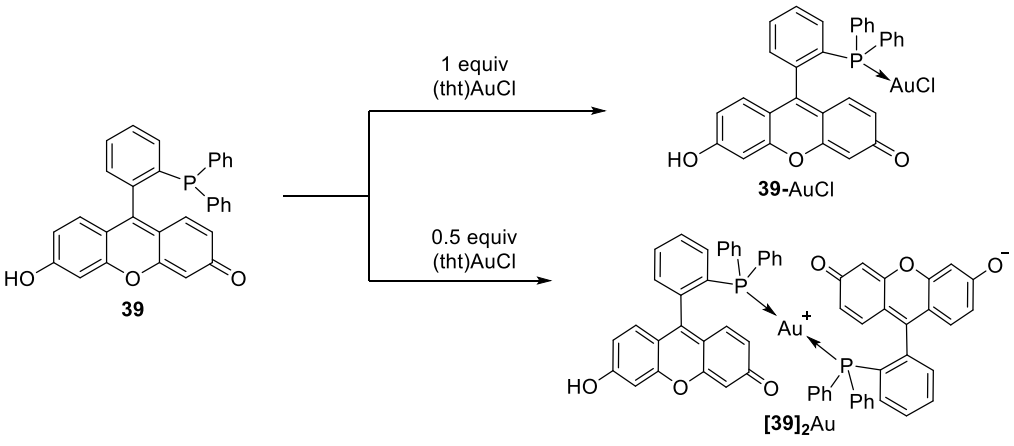

Figure 61. Synthesis of phosphinofluorescein-Au(I) complexes **39**-AuCl and [**39**]$_2$Au.

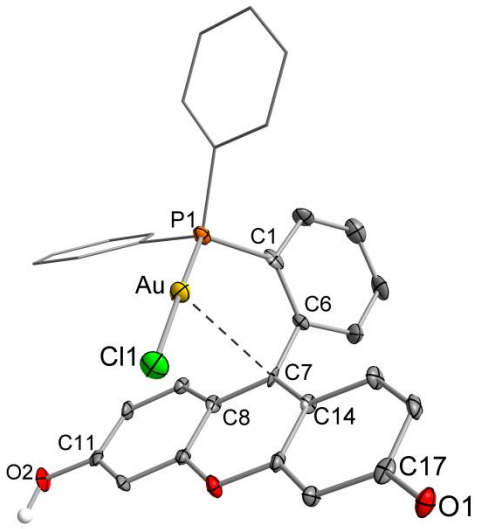

Figure 62. Crystal structure of **39**-AuCl showing one of the disordered components (ellipsoids shown at 50% probability). Hydrogen atoms (except the phenolic proton) and solvent molecules omitted for clarity. Selected bond lengths (Å) and angles (°): Au-C7 3.174(7), P1-Au 2.258(8), Au-Cl1 2.238(3), C17-O1 1.246(10), C11-O2 1.332(9), ∠P1-Au-Cl1 176.9(2), ∠Au-P1-C1-C6 29.2(11), ∠C1-C6-C7-C8 71.8(11).

the fluorescein is oriented orthogonally to the fluorescein plane, as was the case for the phosphine oxide **40**. In this case, however, the gold chloride fragment is not turned away from the fluorescein structure, but is positioned directly above the tricyclic plane, with short C(7)-Au distances of 3.174(7) Å and 3.170(7) Å for each of the disordered components. These distances are well within the sum of the van der Waals radii of C and Au, 3.80 Å,[187] suggesting the possibility of an interaction between the two atoms, or between Au and the π system of the fluorophore.

Addition of two equivalents of ligand **39** to (tht)AuCl resulted in the isolation of the unusual bis(phosphino)gold complex [**39**]$_2$Au (Figure 61). The ^{31}P NMR of this compound in d^6-DMSO shows a low, broad peak around 25 ppm, which could arise

from hydrogen bonding or different speciation in solution. The mass spectrum of this compound shows a molecular ion peak in the positive scan at 1141.17 *m/z*, corresponding to the bis(phosphino)gold cation; the negative scan shows a peak at 1175.11 *m/z*, corresponding to the bis(phosphino)gold chloride complex. The solution-state structure of [**39**]$_2$Au was therefore difficult to establish with certainty; however, the solid-state structure of the complex was definitively established by single-crystal X-ray diffraction analysis. Red crystals were obtained by slow evaporation of a DMSO:MeOH solution of [**39**]$_2$Au, which revealed the structure shown in Figure 63. Rather than the bis(phosphino)gold chloride complex we originally expected, the crystal structure reveals a unique zwitterionic bis(phosphino)gold complex. Chloride has been extruded from the cationic Au center by the bulky phosphine ligands, and is in fact not to be

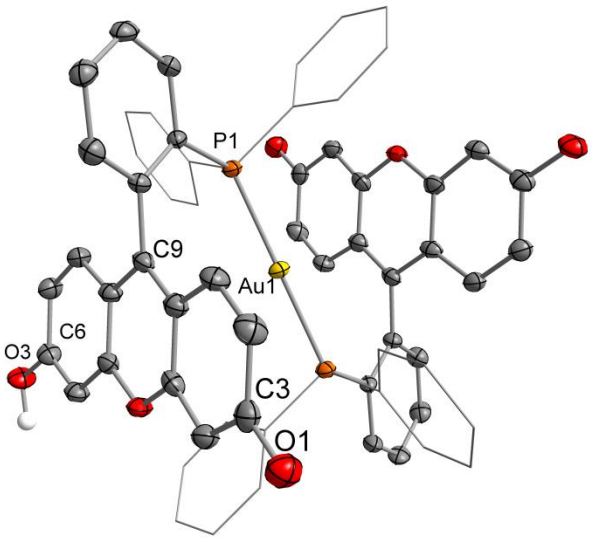

Figure 63. Crystal structure of [**39**]$_2$Au. Hydrogen atoms (except those involved in hydrogen bonding) omitted for clarity. Selected bond lengths: Au1-C9: 3.419 Å, C3-O1: 1.259(5) Å, C6-O2: 1.334(4) Å.

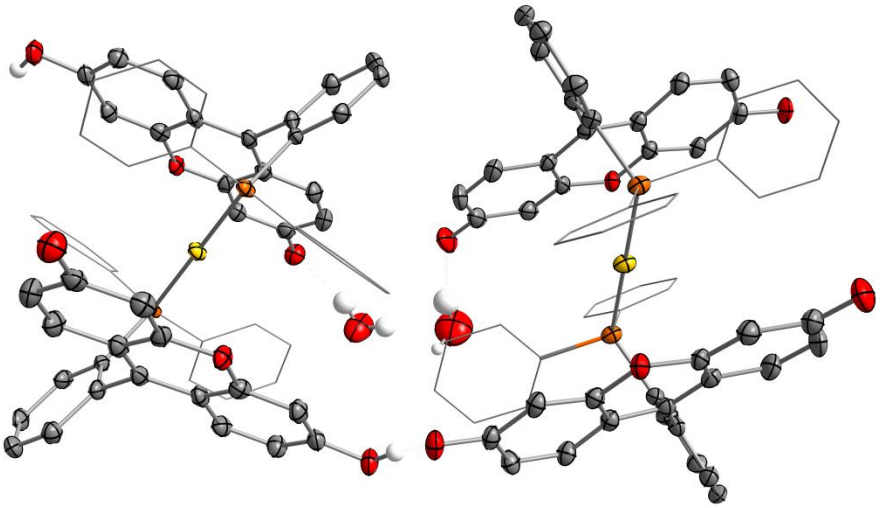

Figure 64. Hydrogen bond structure of [**39**]$_2$Au in the solid state for one pair of bis-(phosphino)gold units, including two co-crystallized water molecules.

found within the crystal structure as a counteranion. Rather, the charge is balanced by the deprotonation of the phenolic alcohol group of one of the two phosphinofluorescein ligands on Au, resulting in a zwitterionic complex overall. In the crystal structure, the protonated and deprotonated ligands are held together by hydrogen bonds which bridge adjacent complexes through the fluorescein ligands and co-crystallized H_2O (Figure 64). Because of the hydrogen bond network, both phosphinofluorescein ligands about each Au atom in [**39**]$_2$Au are equivalent in the crystal and the structure is symmetric; however, there is only one proton present per bis(phosphino)gold unit overall. In solution, exchange of protons between the protonated and deprotonated ligands and solvent may account for the broad peak around 25 ppm seen in the ^{31}P NMR. In compound [**39**]$_2$Au, the Au center is held closely between the two conjugated structures of the ligands, but the distance between the cationic Au and the electrophilic carbons C9

and C9' is lengthened to 3.42 Å, which may be influenced by steric effects and the loss of any Au→C interaction in the structure containing Au(I) as a cation.

4.3 Photophysical properties of **39**-[**39**]$_2$Au

We were interested to explore the compatibility of compounds **39**-[**39**]$_2$Au with aqueous media for the purposes of sensing. Although insoluble in pure water, **39**-[**39**]$_2$Au could be dissolved in aqueous buffer solutions in high enough concentrations for spectroscopic measurements by adding cetyltrimethylammonium chloride (CTAC) as a surfactant. The photophysical properties of **39**-[**39**]$_2$Au were therefore studied in aqueous solutions of 10 mM sodium phosphate buffered at pH 7.4 with 10 mM CTAC. The absorption and emission spectra of all four compounds are characteristic of

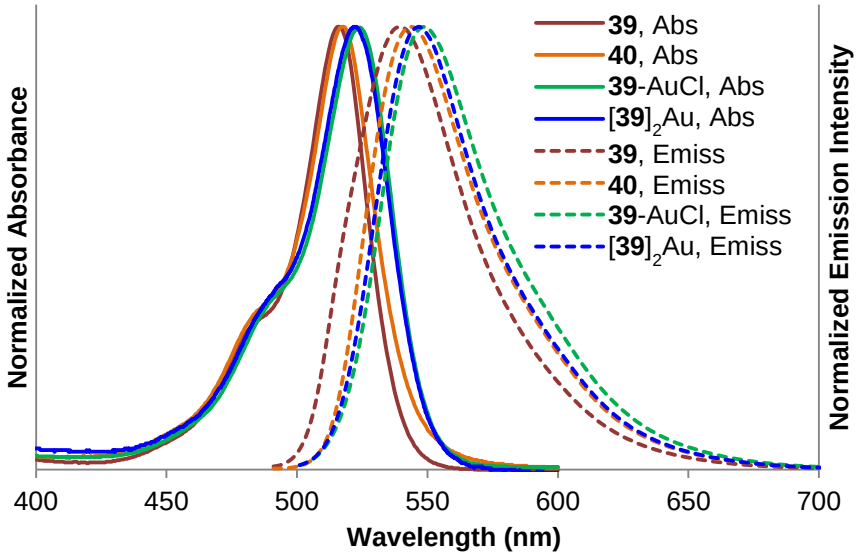

Figure 65. Normalized absorption and emission spectra of **39**-[**39**]$_2$Au. Spectra were taken on 10 μM solutions in aqueous 10 mM sodium phosphate buffered at pH 7.4, with 10 mM CTAC. λ_{exc} = 485 nm for emission spectra.

fluorescein derivatives (Figure 65). Compound **39** displays a fairly sharp absorbance band with a maximum at 516 nm and a high molar extinction coefficient of 90,900 M^{-1} cm^{-1} (Figure 65).[152-153] The fluorescence spectrum shows a broad emission band with λ_{max} = 540 nm and a fluorescence quantum yield of 0.12. The absorption and emission maxima of **39** are significantly redshifted compared to the parent dye, fluorescein (λ_{max} = 501 and 523 nm for absorption and emission, respectively, measured in the same medium). The fluorescence quantum yield of 0.12 exhibited by **39** is relatively low for a fluorescein derivative, since fluorescein itself is known for its high quantum yield of 0.91.[138-139, 153, 240] Protonation of the xanthene fluorophore in **39** is not responsible for the low emission, since the shapes of the absorption and emission profiles of **39** are indicative of the deprotonated anionic state (Figure 66). The spectra remain unchanged in buffer solutions from pH 6.0-9.0, and only at lower pH does the absorption profile change to a shape characteristic of the protonated form of fluorescein derivatives, with a concurrent drop in molar extinction coefficient and fluorescence intensity.[152]

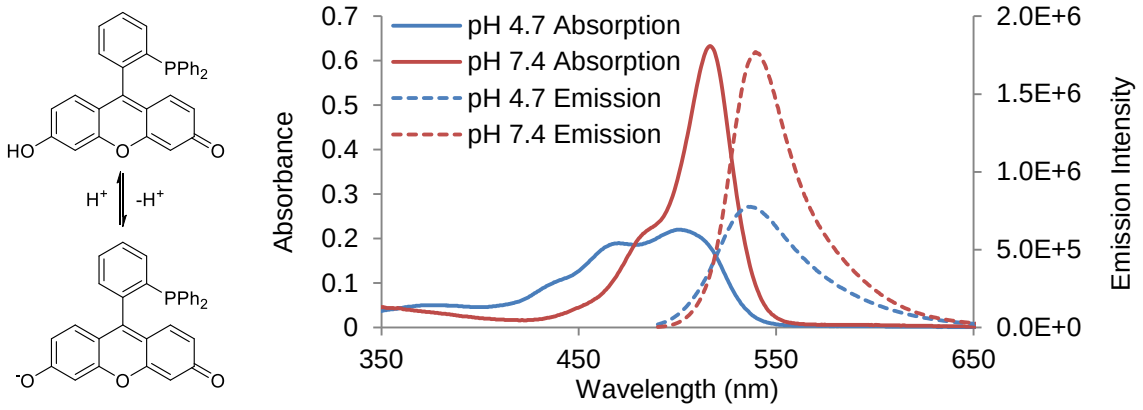

Figure 66. UV-vis absorption and emission spectra of **39** recorded at pH 4.7 and 7.4 buffer solution (λ_{exc}=485 nm with 2 nm slit widths for emission spectra).

The modest quantum yield exhibited by **39** therefore likely indicates quenching of the emission by PeT from the phosphine to the fluorophore, as invoked for similar phosphine-based ROS probes (Figure 57 above). [179-183] The absorption and emission spectra of **40**-[**39**]$_2$Au are very similar to those of **39**, indicating that the character of the electronic transitions remains the same for each compound, although the coordination of gold in compounds **39**-AuCl and [**39**]$_2$Au induces a small but noticeable redshift in the absorption and emission maxima (Table 6). More importantly, **40**-[**39**]$_2$Au all display significantly higher quantum yields of fluorescence than **39**. The quantum yield of **40** is increased more than four times, to 0.54, while those of **39**-AuCl and [**39**]$_2$Au increase somewhat less, to very similar values of 0.29 and 0.32. This shows that the formation of the P=O unit in **40** and the phosphine-gold coordination in **39**-AuCl and [**39**]$_2$Au engages the phosphorus lone pair and alleviates the PeT fluorescence quenching effect at play in the free ligand **39**.

Table 6. Photophysical properties of compounds **39**-[**39**]$_2$Au.

Compound	$\lambda_{max,abs}$, nm	$\lambda_{max,emiss}$, nm	Φ_F [a]	τ [b], ns
39	516	540	0.12	0.62, 4.70
40	517	544	0.54	5.16
39-AuCl	524	549	0.29	1.83, 3.53
[**39**]$_2$Au	522	547	0.32	n. m.

[a] Quantum yields relative to fluorescein in 0.1 M NaOH (0.91)[138-139]. [b] Lifetimes determined by exponential fitting of TCSPC fluorescence decay. The lifetime of compound [**39**]$_2$Au was not measured. All measurements were taken in 10 mM pH 7.4 sodium phosphate buffer with 10 mM CTAC.

Additionally, fluorescence lifetimes were obtained for compounds **39, 40**, and **39**-AuCl and the results support the existence of PeT effects in this system (Table 6, Figure 67). In the case of **39**, a biexponential fluorescence decay is observed, consisting of a dominant fast component with τ_1 = 0.62 ns, A_1 = 0.941, indicative of quenching, and a minor second component closer to the expected lifetime of fluorescein with τ_2 = 4.70 ns, A_2 = 0.059 (A_1 and A_2 are the amplitude contributions of the two respective processes to the overall decay). We assign the dominant fast component to a conformation of the molecule affected by PeT quenching from the phosphine. The second, slower component could be assigned to a conformation of **39** in which PeT is prevented. This idea has been argued for other chromophores quenched by PeT.[241-244] However, given the high dilution at which these measurements are carried out, we cannot definitively exclude that a small portion of phosphine **39** may be oxidized into **40** *in situ*, explaining the presence of this slower, minor component. In the decay spectra of

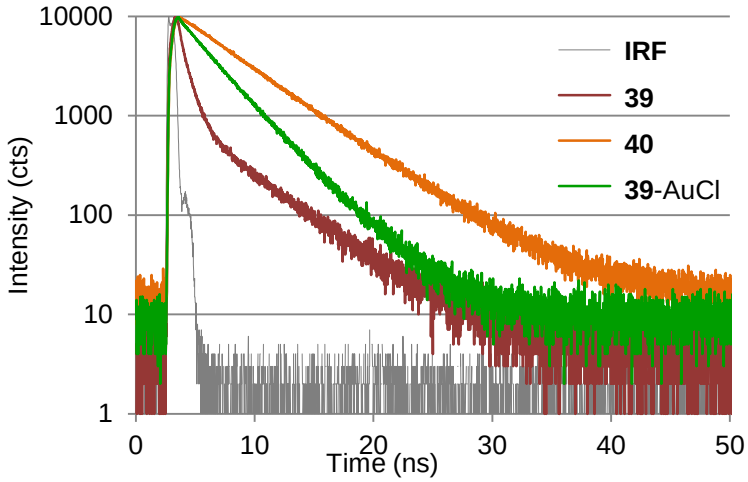

Figure 67. TCSPC fluorescence decay spectra for compounds **39, 40**, and **39**-AuCl in 10 mM pH 7.4 sodium phosphate buffer with 10 mM CTAC**.**

40, where PeT quenching is removed, no fast component is apparent and monoexponential decay is observed with $\tau = 5.16$ ns (Figure 67). In the case of **39**-AuCl, a biexponential decay is again observed, with $\tau_1 = 1.83$ ns, $A_1 = 0.288$, and $\tau_2 = 3.53$ ns, $A_2 = 0.712$. Here, we see that both lifetime components are shortened compared to that of **40**, but the shorter-lifetime component is the minor component of the decay, in contrast to the case of **39**. The biexponential decay may again derive from the existence of two conformations of **39**-AuCl that are differently affected by quenching effects. In this case, we assign this quenching to spin orbit coupling from the heavy gold atom. Such heavy atom effects would account for the shortening of both lifetime components compared to the expected lifetime for a fluorescein of 4-5 ns, as well as the lowered quantum yield of **39**-AuCl compared to **40**.[236, 245] Notably, we did not observe any evidence for phosphorescence in complex **39**-AuCl, either under ambient or air-free conditions, in contrast to other systems containing heavy atoms.[201] In any event, it is clear that the dominant PeT process that quenches the emission of **39** is removed by oxidation or coordination of the phosphine group in **40** and **39**-AuCl, respectively. These results indicated that a potential "turn-on" sensing response could be obtained with **39** in the presence of metal species.

4.4 "Turn-on" fluorescent sensing of aqueous metal species

We explored the use of phosphinofluorescein **39** in a simple sensing system for metal ions in aqueous solution. 1.0 μM solutions of **39** were prepared in 10 mM aqueous sodium phosphate at pH 7.4 with 10 mM CTAC, and aqueous samples of a range of

transition metals as nitrate or chloride salts were injected into the cuvette. Figure 68 shows the resulting changes in emission for various metals added to **39** in excess (5 equivalents). No change in emission is observed in the presence of first-row transition metals or middle transition metals such as Ru(II), Rh(II), Rh(III), or Ir(III). However, a significant increase in emission is evident for the heavy coinage metals Ag(I), Au(I), and

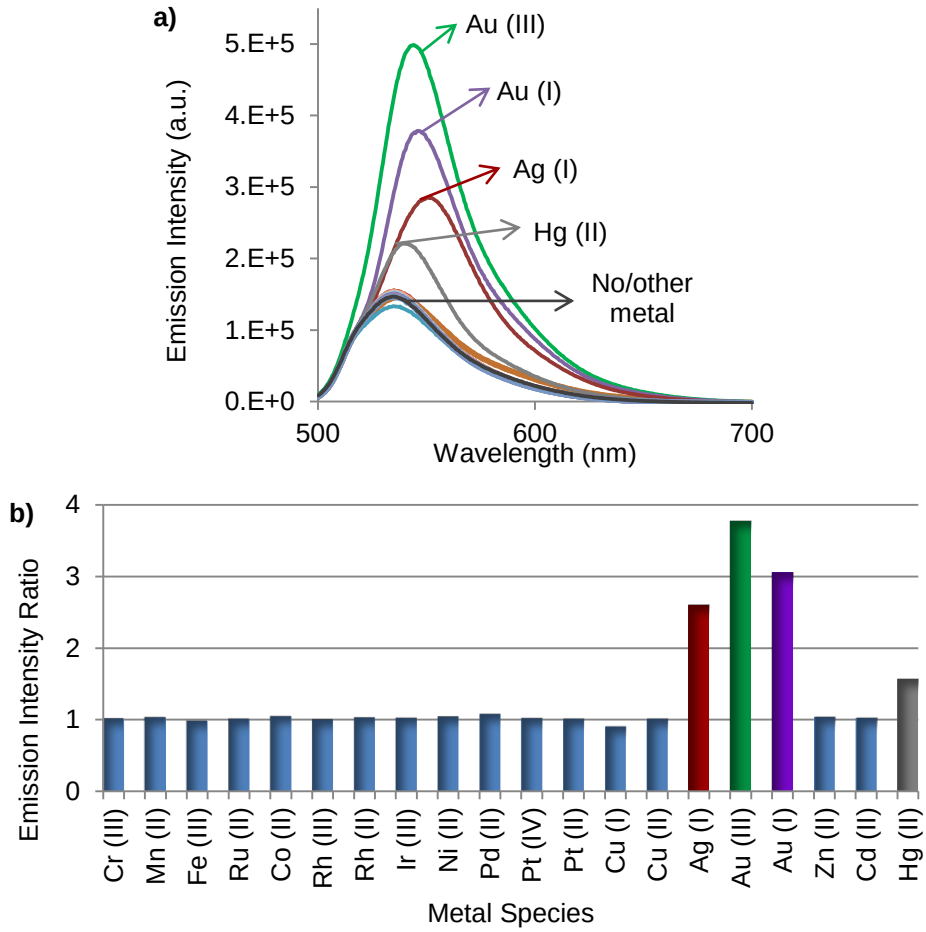

Figure 68. Selectivity of "turn-on" fluorescence response of **39** to 5 equivalents of various metal species in a 1.0 μM aqueous solution of 10 mM sodium phosphate buffer at pH 7.4 with 10 mM CTAC. a) Fluorescence spectra of **39** before and after mixing with metal solution. b) Relative response of **39** to each metal species. Emission intensity ratio taken at λ_{max} for the mixture 1 minute after adding metal solution.

Au(III) and for Hg(II). The increase in emission at λ_{max} is rather small for Hg(II), 1.6 times at saturation, and no response is seen for its lighter congener, Cd(II). More pronounced emission increases of 2.6- and 3.1-fold are observed for Ag(I) and Au(I) species, respectively, but the largest response is seen for Au(III) species, with a 3.8-fold increase in emission. As expected, the "turn-on" fluorescence response of **39** is selective toward heavy late metal ions, which can be rationalized by their preferential coordination of soft donor ligands such as phosphines.[246] Surprisingly, no immediate response to Cu(I), Cu(II), Pd(II), Pt(II), or Pt(IV) was seen in this system, even though these metals might also be expected to coordinate phosphine ligands. In the case of Pd(II) and, to a smaller extent, Pt(IV), an increase in fluorescence could be observed over 40 minutes, indicating the possible slow formation of a complex (See Experimental details). We do not fully understand the sluggishness of the Pd(II) and Pt(IV) response, but we hypothesize that slow kinetics of ligand displacement may hinder immediate complex formation and thus delay the fluorescence response for these metals, especially given the high concentration of competing chloride ligands in the aqueous buffer containing CTAC. For the purposes of sensing, however, neither is a significant interferent when the fluorescence measurement is made immediately upon mixing. Thus, under the conditions of the experiment, we observe a satisfying selectivity in the fluorescence "turn-on" response of **39** for gold and silver, especially Au(III), with only minor interference from mercury. Competition studies were also carried out for mixtures of metals, adding 1.0 equivalent of Au(III) along with 1.0 equivalent of Cr(III), Mn(II),

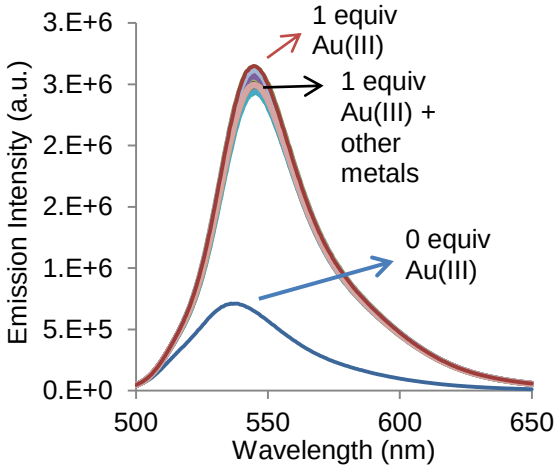

Figure 69. Fluorescence response of **39** to Au(III) in the presence of other metals. Emission spectra were taken on 5.0 μM samples of **39** in 10 mM sodium phosphate buffer at pH 7.4 with 10 mM CTAC.

Fe(III), Co(II), Ni(II), Pd(II), Cu(II), Ag(I), Zn(II), Cd(II), or Hg(II), respectively (Figure 69). In each case, the full response to Au(III) is seen without apparent interference from the added metal ions. The response of **39** to Au(III) is even unaffected by the presence of Ag(I) and Hg(II), to which it responds independently.

The interactions of **39** with Au, Ag, and Hg ions were studied in further detail by titrations, ^{31}P NMR spectroscopy, and mass spectrometry (Figure 70). With incremental addition of Au(I) to **39**, a steady increase in emission is observed, along with a 10-nm (333 cm^{-1}) redshift in the maximum wavelength of emission. The emission then plateaus sharply at 1 equivalent of Au(I), consistent with a quantitative 1:1 adduct formation. Absorbance also decreases and shifts to the red by 8 nm (296 cm^{-1}) (See Experimental details). These changes are consistent with the photophysical properties already

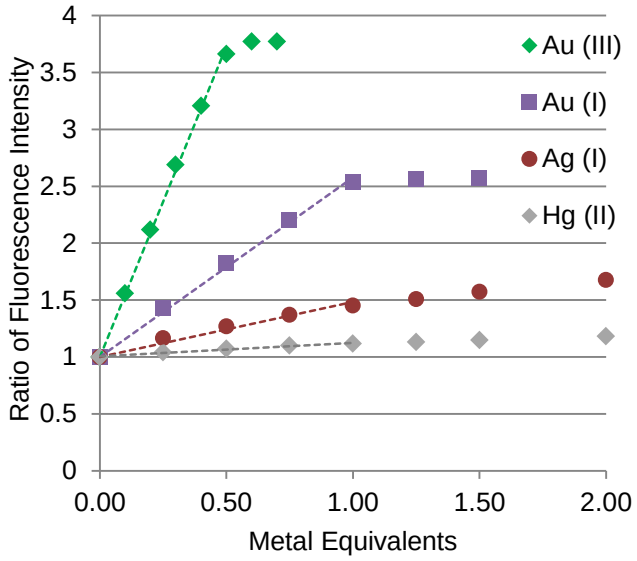

Figure 70. Changes in fluorescence intensity for titrations of **39** with Hg(II), Ag(I), Au(I), and Au(III). Emission intensity ratio taken at λ_{max} for the mixture after adding metal.

established for the isolated phosphine gold chloride complex **39**-AuCl, and the overall increase in integrated emission (2.5-fold at saturation) accords with the independently determined quantum yields of 0.29 for compound **39**-AuCl and 0.12 for **39** (*vide supra*). This was confirmed by following the reaction *in situ* by ^{31}P NMR spectroscopy: on addition of 1 equivalent of Au(I) as (tht)AuCl to a DMSO sample of **39**, the peak for the free ligand at -15.4 ppm disappears and a new peak at 24.6 ppm appears, the same as that observed for isolated compound **39**-AuCl. Although it is possible that bis(phosphino)gold species like [**39**]$_2$Au are also formed with the addition of Au(I) to **39** at lower concentrations of gold, the smooth linear increase of emission with Au(I) titration rather suggests the exclusive formation of the 1:1 phosphine:gold complex; however, these species may be in rapid equilibration with each other. In the cases of

Hg(II) and Ag(I), a similar incremental increase in emission is seen upon titration with the metal, with a redshift of 6-13-nm of the emission maximum (202-432 cm^{-1}). However, the fluorescence intensity does not fully plateau even after addition of 2 equivalents of metal, probably indicating a weaker association of **39** with these ions. Complex formation can nevertheless be observed by ^{31}P NMR, albeit in DMSO and at higher concentrations. Indeed, after addition of $AgNO_3$ to **39**, the free ligand ^{31}P NMR peak again disappears and a broad doublet centered at 3.3 ppm is observed, with an average $^{107,109}Ag$-^{31}P coupling constant of 690 Hz. This coupling constant is consistent with a 1:1 phosphine:silver complex.[247] The positive ESI mass spectrum shows a molecular ion peak at *m/z* 579.10 with the expected isotopic pattern corresponding to [**39**+Ag]$^+$, indicating the presence of a stable 1:1 complex. Similarly, after addition of $HgCl_2$ to **39**, the free ligand peak in the ^{31}P NMR disappears and a broad downfield peak at 33.9 ppm appears. In the positive ESI mass spectrum, the molecular ion peak appears at *m/z* 709.09 with the expected isotopic pattern corresponding to [**39**+HgCl]$^+$, which is consistent with 1:1 coordination of **39** to $HgCl_2$ with loss of chloride during ionization. We were unable to isolate or structurally characterize complexes of **39** with Hg or Ag. However, the photophysical and spectroscopic data support the idea that the fluorescence increase observed for these metal species results from the formation of 1:1 coordination complexes between the phosphine ligand and the metals, which most likely exist as metal chlorides under the conditions of the experiment.

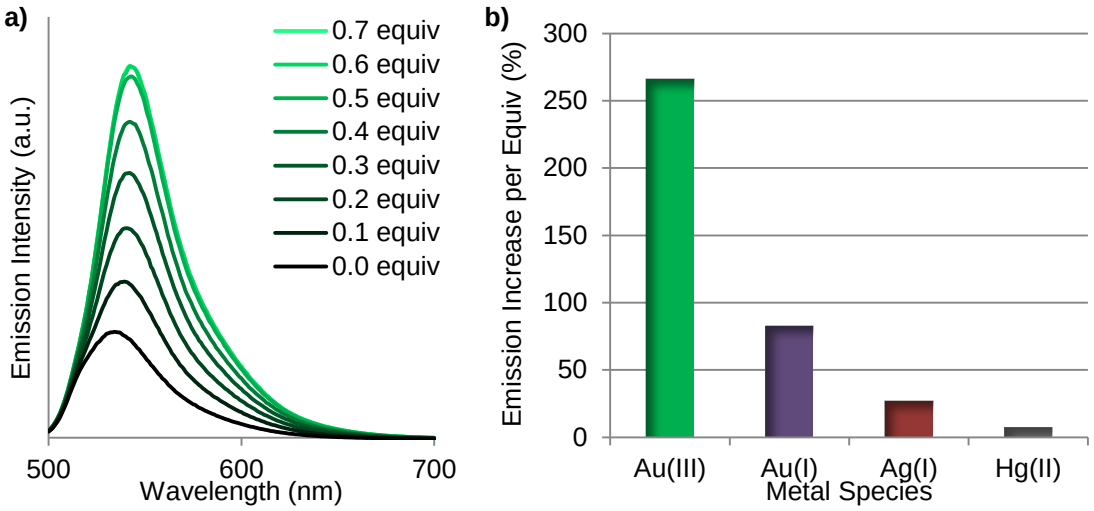

Figure 71. a) Emission spectra of titration of **39** with Au(III), showing the "turn-on" fluorescence response. b) Relative increases in the emission of **39** per metal equivalent added for Au(III), Au(I), Ag(I), and Hg(II).

In the case of Au(III), however, different behavior is observed (Figures 70-71). The fluorescence intensity increases more sharply with incremental addition of Au(III) and reaches a plateau at only 0.5 equivalents. Thus, the effective selectivity of **39** for Au(III) within the range of 0-0.5 equivalents of metal is more than twice as high as for Au(I) or any other metal. Per metal equivalent, the sensing response to Au(III) is approximately 3.2 times more sensitive than to Au(I), 10 times more sensitive than to Ag(I), and 38 times more sensitive than to Hg(II) (Figure 71b). A calibration curve for the addition of Au(III) to **1** in the sensing range shows a linear increase in fluorescence at λ_{max} = 542 nm from 0-500 nM Au(III) (Figure 72). The limit of detection based on this titration data was determined to be 7.6×10^{-8} M (76 nM) Au(III), or ~15 ppb (See Experimental details). This limit of detection is comparable to other reported fluorescent sensors for gold, confirming the high sensitivity of **39** as a sensor.[109]

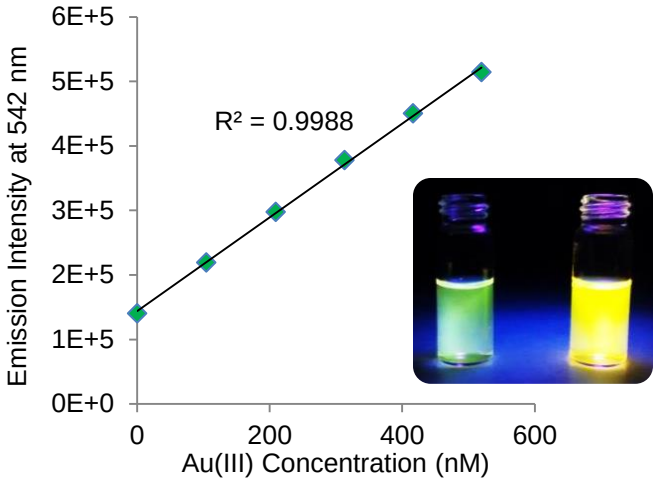

Figure 72. Calibration curve for the response observed upon addition of Au(III) to **39** (1.0 μM) in the sensing range (<0.5 equivalents Au(III)). The emission intensity is measured at λ_{max} = 542 nm with λ_{exc} = 485 nm. Inset: Photos of the fluorescence of a solution of **39** (20 μM) under a handheld UV lamp (λ_{exc} = 254 nm) before and after addition of Au(III), showing the visible increase in fluorescence.

We hypothesized that this behavior toward Au(III) was the result of a combination of a reaction- and coordination-based interaction of **39** with Au(III) as shown below in Figure 73. Per gold equivalent, one equivalent of **39** is oxidized to phosphine oxide **40** with reduction of Au(III) to Au(I);[248-249] a second equivalent of **39** coordinates to the resulting Au(I) to form one equivalent of phosphine gold chloride complex **39**-AuCl, accounting for the 2:1 stoichiometry observed in the fluorescent response of **39** to Au(III). Both products **40** and **39**-AuCl display stronger emission than **39**, but **40** more so than **39**-AuCl. Thus, the overall fluorescence enhancement of **39** in the presence of Au(III) is larger than that in the presence of Au(I) alone—rather, the final emission intensity corresponds to the average quantum yield of the products **40** and

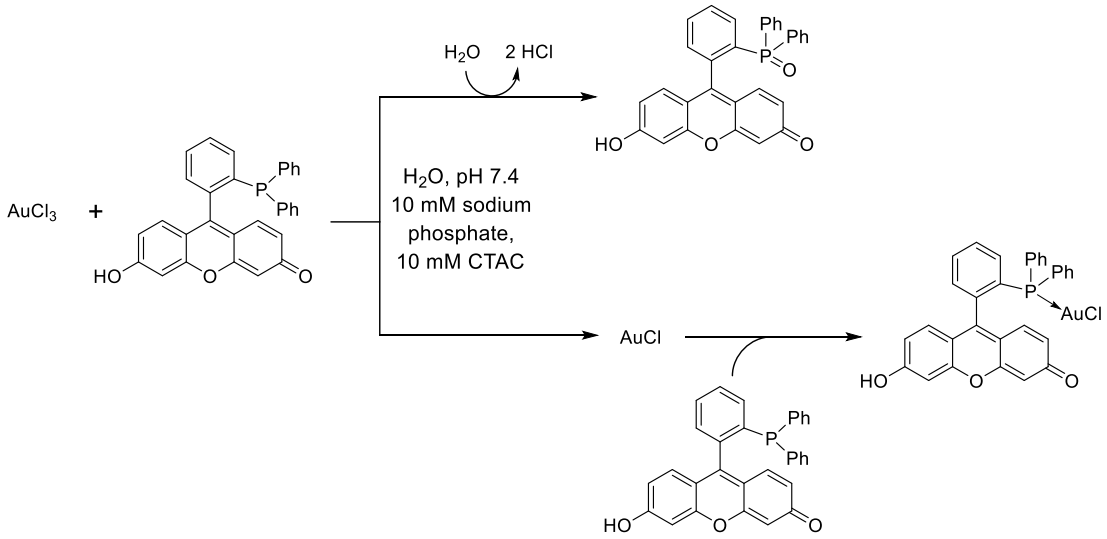

Figure 73. Reaction of **39** with Au(III) chloride species in aqueous solution.

39-AuCl (42%). We monitored this reaction *in situ* by ^{31}P NMR in DMSO and observed that, indeed, addition of 0.5 equivalents of $CsAuCl_4$ to **39** results in the formation of two new ^{31}P NMR signals at 26.6 and 24.4 ppm. These signals correspond closely to those observed for the independently synthesized compounds **40** and **39**-AuCl. Mass spectrometry of the product of the same reaction further confirms the presence of compounds **40** and **39**-AuCl by their characteristic molecular ion peaks at *m/z* 489.15 and 705.10 in the ESI positive scan. Thus, this new gold ion sensor shows a dual response mechanism resulting in a "double turn-on" of fluorescence. **39** not only acts as a coordination-based sensor by forming a complex with the metal ion, but also acts as a reaction-based sensor since it undergoes a redox reaction to form the phosphine oxide. This duality allows us to harness two processes that both afford higher quantum yield fluorophores based on removal of PeT quenching in the phosphinofluorescein.

4.5 Conclusions

In conclusion, we have synthesized an *ortho*-phosphine-decorated fluorescein derivative and characterized its coordination to gold(I) centers. Depending on the stoichiometry, one or two phosphinofluorescein ligands may coordinate to the gold(I) center, placing the metal fragment in close proximity to the fluorescent dye structure, as shown by X-ray crystallography. Despite the presence of the heavy gold atom, coordination of the phosphine group significantly increases the fluorescence through the repression of PeT quenching effects. This fluorescent response to metal coordination could be used in a simple sensing system for metal species in aqueous solution. The phosphinofluorescein **39** selectively responds to heavy late metals, including silver, gold, and mercury, with a high sensitivity toward gold(III). This response was shown to originate from a "double turn-on" phenomenon involving concurrent oxidation and coordination of the phosphine group of **39** to produce the strongly fluorescent phosphine oxide and phosphine gold chloride derivatives. This allows the phosphinofluorescein **39** to function as a sensitive and selective sensor for gold(III) species in water.

The nature of the fluorescent response is interesting and unusual among fluorescent sensors in that it is both coordination- and reaction-based. Coordination-based chemical sensors for gold are rare in themselves, and typical examples of this kind of metal sensor require a multi-donor coordinating group to achieve selectivity, obtained via somewhat cumbersome synthetic protocols.[62, 109, 151, 160, 236-238] Compound **39**, however, achieves a considerable sensitivity and selectivity to gold(III) utilizing only one donor phosphine group and is readily accessed from commercially available

precursors in a few steps. Reaction-based sensors for gold have typically involved gold-promoted bond cleavage or cyclization utilizing the alkynophilicity of gold.[105, 109-111, 234-235] These approaches may be very effective but often encounter issues with reaction side products and low solubility in aqueous solution without large proportions of organic solvents. In the case of compound **39**, however, the reaction-based component of the "turn-on" response is based on a simple redox reaction producing the phosphine oxide **40**, and the sensor can be used in a fully aqueous system using the widely-available CTAC surfactant, with a negligible amount of organic solvent needed. The phosphinofluorescein **39** may thus find utility as a gold(III) sensor, especially for environmental analysis. The susceptibility of the phosphine group toward oxidation may limit its potential for use in biological systems where reactive oxygen species are present, however. More broadly, this work shows that phosphine donor groups can be useful tools in the design of fluorescent probes selective for gold, or other heavy late metals, based on the PeT strategy that has been used to great effect for lighter-metal sensors. Such simple and sensitive probes will be beneficial as the use of gold species for catalysis and medicine continues to expand.

4.6 Experimental details

General Methods. All preparations were carried out under an N_2 atmosphere using standard Schlenk techniques unless otherwise stated. Starting materials and reagents including metal salts were purchased and used as received, except for *o*-$(Ph_2P)C_6H_4Br$,[250] 3,6-dihydroxyxanthone,[198] and (tht)AuCl,[251-252] which were prepared

according to previously reported procedures. Solvents were dried by refluxing under N_2 over Na/K (Et_2O, THF); all other solvents were ACS reagent grade and used as received. NMR spectra were recorded using a Varian Unity Inova 500 FT NMR (499.41 MHz for ^1H, 125.59 MHz for ^{13}C) or a Varian Unity Inova 400 FT NMR (399.59 MHz for ^1H, 100.45 MHz for ^{13}C, 161.74 MHz for ^{31}P) spectrometer. Chemical shifts (δ) are given in ppm and are referenced against residual solvent signals (^1H, ^{13}C) or external H_3PO_4 (^{31}P). Mass spectrometry was carried out by the Texas A&M Chemistry Mass Spectrometry Facility. Elemental analyses were performed at Atlantic Microlab (Norcross, GA). HPLC measurements were performed on a Beckman SystemGold instrument with a 128 Solvent Module and 168 Detector, with UV detection at 254 nm and 280 nm channels. Absorbance measurements were taken on a Shimadzu UV-2502PC UV-Vis spectrophotometer against a solvent reference. Steady-state fluorescence measurements were taken on samples in capped quartz cuvettes under air on a PTI QuantaMaster spectrofluorometer with entrance and exit slit widths of 2 nm. Quantum yield measurements were referenced against a value of 0.91 for fluorescein in 0.1 M NaOH.[138-139] Time-correlated single-photon counting (TCSPC) was employed to obtain fluorescence lifetime decay spectra. Measurements were taken on a Fluorotime 100 fluorometer with a 405 nm solid-state picosecond diode laser source (PicoQuant). Instrument response functions (IRF) were determined from the scattering signal with a solution of Ludox HS-40 colloidal silica (0.01% w/w particles in water). TCSPC analysis was performed on Fluofit (PicoQuant) software. The decay spectra measured at

the magic angle (54.7°) were modeled by mono- or biexponential tailfitting as indicated for each compound to obtain lifetime values; χ^2 values < 1.2 were obtained in all cases.

General Procedure for Metal Sensing Tests. A 1.0×10^{-3} M stock solution of **39** was prepared in DMSO. A 1.0-μM solution of **39** was prepared in pH 7.4 10 mM aqueous sodium phosphate with 10 mM CTAC by dilution of this stock solution, and 3-mL aliquots were taken for fluorescence measurements. 5-μL aliquots of 3.0×10^{-3} M metal solutions (5 equivalents) were injected into the cuvette. Fluorescence spectra were recorded immediately (~1 minute) after mixing. The metal salts used were: $Cr(NO_3)_3\cdot9H_2O$, $Mn(NO_3)_2$, $Fe(NO_3)_3\cdot9H_2O$, $Ru(NO)(NO_3)_3$, $Co(NO_3)_2\cdot6H_2O$, $Rh(NO_3)_3\cdot2H_2O$, $RhCl_3$, $IrCl_3$, $Ni(NO_3)_2\cdot6H_2O$, $PdCl_2$ and Na_2PdCl_4 (average value shown in Figure 62), $(DMSO)PtCl_2$, K_2PtCl_6, $Cu(NO_3)_2\cdot2.5H_2O$ and $CuCl_2\cdot2H_2O$, $Cu(MeCN)_4BF_4$, $AgNO_3$, $CsAuCl_4$, $Zn(NO_3)_2\cdot6H_2O$, $Cd(NO_3)_2\cdot4H_2O$, $HgCl_2$, $Al(NO_3)_3\cdot9H_2O$, $Pb(NO_3)_2$. These were formulated as aqueous solutions except for $(DMSO)PtCl_2$ (DMSO), (tht)AuCl (DMSO), $CsAuCl_4$ (DMSO), and $Cu(MeCN)_4BF_4$ (MeCN) for solubility reasons.

Synthesis of 3,6-di(*tert*-butyldimethylsiloxy)xanthone.[164] 3,6-dihydroxy-xanthone (3.46 g, 15 mmol) and imidazole (6.0 g, 88 mmol) were dissolved in 10 mL DMF under N_2. *tert*-Butyldimethylsilyl chloride (6.8 g, 45 mmol) was added portionwise to the reaction flask, and the mixture was stirred at room temperature for 5 hours, producing an orange pasty suspension. The mixture was quenched with 50 mL H_2O and extracted three times with ethyl acetate. The organic fraction was washed with H_2O and brine, dried over $MgSO_4$, and evaporated to an orange residue, which was washed with

methanol and hexane to yield a peach-orange crystalline powder. Yield: 5.88 g (85%). ^{1}H NMR (299.96 MHz, $CDCl_3$: 7.26 ppm), δ: 8.20 (d, 2), 6.85 (d, 2), 6.84 (s, 2), 1.01 (s, 18), 0.29 (s, 12). Spectral data are in accordance with previous literature.[164]

Synthesis of 39. *o*-$(Ph_2P)C_6H_4Br$ (550 mg, 1.6 mmol) was dissolved in 15 mL THF and treated dropwise with *n*-butyllithium (0.75 mL, 2.2 M in hexane, 1.7 mmol) at -78 °C and let stir for 1 hour at that temperature. 3,6-di(*tert*-butyldimethylsiloxy)-xanthone (736 mg, 1.6 mmol) in 5 mL THF was then added via cannula, and the orange solution left to stir and warm to room temperature overnight. The mixture was quenched with 20 mL H_2O and extracted three times with ethyl acetate. The organic fraction was washed with brine, dried over $MgSO_4$, and evaporated to an orange residue. This was dissolved in a few mL of THF and 0.5 mL acetic acid was added. After stirring 30 minutes, the solvents were removed, yielding a red solid residue. This was washed with ether, methanol, and pentane to obtain a crimson powder. Yield: 297 mg (39%). ^{1}H NMR (499.42 MHz, $(CD_3)_2SO$: 2.50 ppm), δ: 11.10 (br, 1), 7.63 (m, 2), 7.42 (m, 1), 7.34 (m, 7), 7.09 (m, 4), 6.65 (d, 2), 6.47 (br, 2), 6.33 (br, 2). ^{13}C NMR (125.77 MHz, $(CD_3)_2SO$: 39.52 ppm), δ: 156.03 (br), 149.20 (s), 138.99 (d), 136.76 (d), 135.54 (d), 134.11 (s), 133.14 (d), 132.07 (s), 131.50 (d), 130.28 (s), 129.75 (s), 129.69 (s), 129.62 (s), 128.98 (s), 128.71 (d), 114.87 (br), 103.24 (br). ^{31}P NMR (161.73 MHz, $(CD_3)_2SO$, 85% H_3PO_4: 0.00 ppm), δ: -15.4 ppm. ESI-MS(+): 473.13 *m/z*. ESI-MS(-): 471.05 *m/z*. HRMS (ESI+): *m/z* calculated for $C_{31}H_{21}O_3P$: 473.1307 $[M+H]^+$; found: 473.1303. NMR and Elemental Analysis indicated variable amounts of water present; purity confirmed to >97% by HPLC.

Synthesis of 40. To a suspension of **39** (62 mg, 0.13 mmol) in 20 mL 1:1 DCM:MeOH was added a slight excess of H_2O_2 (30% aqueous). The mixture was stirred until it became a clear solution and conversion was complete by ^{31}P NMR. The solution was filtered through a silica plug and evaporated to yield a bright orange powder, which could be further purified by column chromatography on silica gel using a 0-15% MeOH in DCM eluent. Yield: 47 mg (73%). Orange crystals suitable for X-ray diffraction were grown from a concentrated DMF solution. ^{1}H NMR (499.42 MHz, $(CD_3)_2SO$: 2.50 ppm), δ: 11.01 (br, 1), 7.81 (t, 1), 7.71 (t, 1), 7.51 (m, 3), 7.44 (m, 5), 7.38 (m, 4), 6.63 (d, 2), 6.32 (br, 4). ^{13}C NMR (100.47 MHz, $(CD_3)_2SO$: 39.52 ppm), δ: 156.14 (br), 148.72 (s), 136.95 (d), 133.71 (d), 132.66 (s), 132.53 (s), 132.20 (s), 131.95 (s), 131.59 (d), 131.32 (d), 131.03 (d), 130.61 (s), 129.24 (d), 128.80 (d), 128.40 (d), 115.47 (br), 102.95 (br). ^{31}P NMR (161.73 MHz, $(CD_3)_2SO$, 85% H_3PO_4: 0.00 ppm), δ: 26.31 ppm. ESI-MS(+): 489.09 *m/z*. ESI-MS(-): 487.08 *m/z*. HRMS (ESI+): *m/z* calculated for $C_{31}H_{21}O_4P$: 489.1256 $[M+H]^+$; found: 489.1247. NMR and Elemental Analysis indicated variable amounts of water present; purity confirmed to >99% by HPLC.

Synthesis of 39-AuCl. A suspension of **39** (100 mg, 0.21 mmol) in 50 mL 1:1 THF:MeOH was added to a suspension of (tht)AuCl (68 mg, 0.21 mmol) in 50 mL THF in an open flask at room temperature. The flask was stoppered and the mixture stirred in the dark overnight. The resulting orange suspension was fully dissolved in CH_2Cl_2 and MeOH and passed through a silica plug, then the solvent evaporated and the residue washed with ether to afford a red-orange solid. Yield: 104 mg (70%). Red crystals suitable for X-ray diffraction were grown from a concentrated DMF solution. ^{1}H NMR

(499.42MHz, $(CD_3)_2SO$: 2.50 ppm), δ: 11.22 (br, 1), 7.85 (t, 1), 7.78 (t, 1), 7.62-7.40 (m, 12), 6.46 (d, 2), 6.41 (br, 2), 6.17 (br, 2). ^{13}C NMR (100.47 MHz, $(CD_3)_2SO$: 39.52 ppm), δ: 156.11 (br), 147.63 (br), 138.38 (d), 134.84 (d), 133.93 (d), 132.64 (s), 132.36 (s), 131.58 (d), 130.34 (d), 129.70 (s), 129.69 (d), 128.45 (s), 128.13 (s), 127.84 (s), 127.54 (s), 114.78 (br), 103.84 (s). ^{31}P NMR (161.73 MHz $(CD_3)_2SO$, 85% H_3PO_4: 0.00 ppm), δ: 24.54 ppm. ESI-MS(+): 705.09 *m/z*. ESI-MS(-): 703.24 *m/z*. HRMS (ESI+): *m/z* calculated for $C_{31}H_{21}AuClO_3P$: 705.0661 $[M+H]^+$; found: 705.0685. Elemental Analysis Calculated for $C_{31}H_{21}AuClO_3P$: C, 52.82; H, 3.00. Found: C, 53.31; H, 3.40.

Synthesis of $[39]_2Au$. A suspension of **39** (100 mg) in THF:MeOH was added to a suspension of (tht)AuCl (34 mg) in THF in an open flask at room temperature. The flask was stoppered and the mixture stirred in the dark overnight. The resulting pink-orange suspension was fully dissolved in CH_2Cl_2 and MeOH and passed through a silica plug, then the solvent evaporated and the residue washed with ether to afford a bright red solid. Yield: 71 mg (59%). Red crystals suitable for X-ray diffraction were grown from slow evaporation of a DMSO:MeOH solution. ^1H NMR (499.42 MHz, $(CD_3)_2SO$: 2.50 ppm): δ 7.76 (m, 1), 7.71 (m, 1), 7.49 (m, 8), 7.31 (m, 4), 6.46 (d, 2), 6.31 (br, 2), 6.15 (d, 2). ^{31}P NMR (161.73 MHz, $(CD_3)_2SO$, 85% H_3PO_4: 0.00 ppm): δ 24.7 (br). ^{13}C NMR was not measured for this compound due to low solubility. ESI-MS (+): 1141.17 *m/z*. ESI-MS(-): 1175.11 *m/z*.

HPLC Chromatography. HPLC was performed to assess purity of compounds **39** and **40** using a stepped gradient method with MeCN (0.1% TFA) and H_2O (0.1% TFA) at a flow rate of 1.0 mL/min. 20-µL samples in DMF were injected at 20% MeCN, and this composition was held for 4 minutes before a gradient increase to 50% MeCN over another 4 minutes. The remainder of the method was isocratic at 50% MeCN.

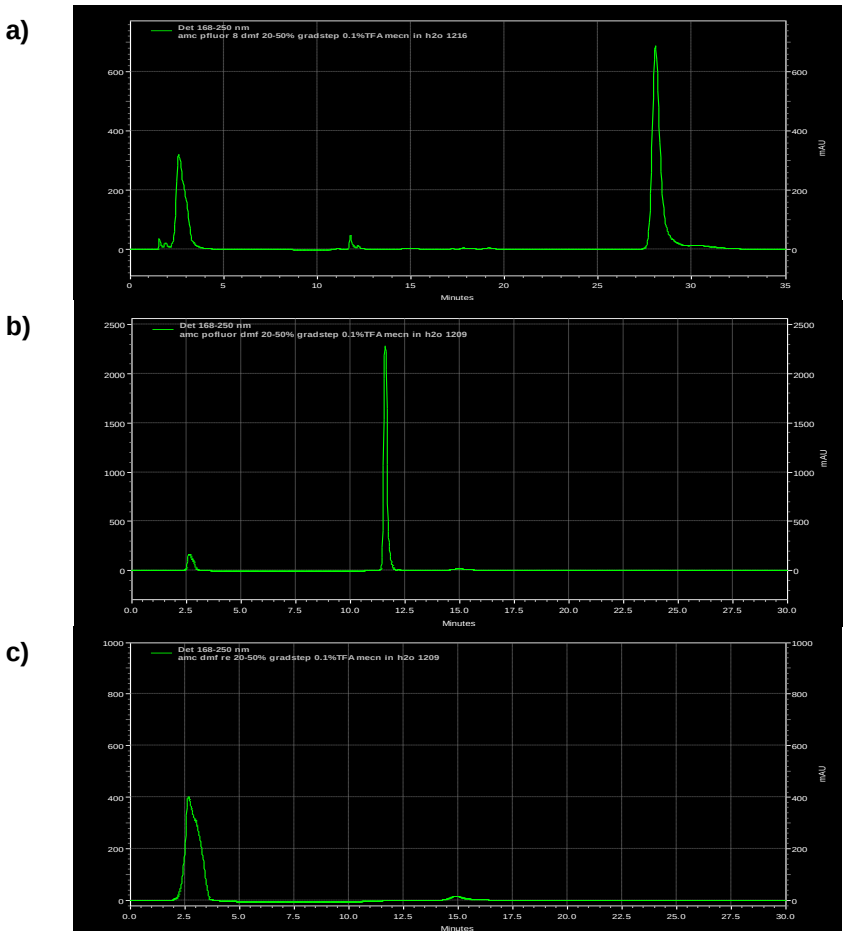

Figure 74. a) HPLC chromatogram of **39**. The peak at RT=28.1 min corresponds to **39** (97.3%) and the peak at RT=11.8 min corresponds to **40** (2.7%). The peaks before RT=4 min result from the DMF injection solvent and the small peak at RT=15 min results from a method artifact. b) HPLC chromatogram of **40**. The peak at RT=11.6 min corresponds to **40** (>99%). c) Blank chromatogram of DMF injection solvent, showing the method artifact peaks at RT=2.6 min and RT=15.0 min.

Crystallography. Crystal data, details of data collection, and structure refinement parameters for compounds **39**-AuCl and [**39**]$_2$Au are compiled in Table 7. The crystallographic measurements were performed at 110(2) K using a Bruker APEX-II CCD area detector diffractometer, with a graphite-monochromated Mo-Kα radiation (λ = 0.71069 Å). In each case, a specimen of suitable size and quality was selected and mounted onto a nylon loop. The semi-empirical method SADABS[146] was applied for absorption correction. The structure was solved by direct methods and refined by the full-matrix least-square technique against F2 with the anisotropic temperature parameters for all non-hydrogen atoms. All H atoms were geometrically placed and refined in riding model approximation. Data reduction and further calculations were performed using the Bruker SHELXTL[147] and ShelXle[148] program packages.

Table 7. Crystallographic details for compounds **39**-AuCl and [**39**]$_2$Au.

	39-AuCl	[**39**]$_2$Au
Chemical formula	$C_{31}H_{21}AuClO_3P$ ·0.52(C_3H_7NO)	$C_{62}H_{41}AuO_6P_2$ ·2(H_2O)
M_r	743.26	1176.89
Crystal system, space group	Monoclinic, $P2_1/n$	Triclinic, P
a, b, c (Å)	16.2869 (16), 11.0402 (11), 16.8176 (17)	12.778 (2), 13.638 (2), 16.266 (3)
α, β, γ (°)	90, 113.422 (1), 90	84.252 (2), 69.041 (2), 70.246 (2)
V (Å^3)	2774.8 (5)	2490.7 (8)
Z	4	2
μ (mm^{-1})	5.49	3.08

Table 7, cont'd.

	39-AuCl	[**39**]$_2$Au
Crystal size (mm)	0.19 × 0.10 × 0.02	0.32 × 0.18 × 0.17
No. of measured, independent and observed [$I > 2\sigma(I)$] reflections	33732, 6866, 5599	30647, 12265, 9564
R_{int}	0.052	0.030
$R[F^2 > 2\sigma(F^2)]$, $wR(F^2)$, S	0.029, 0.064, 1.03	0.029, 0.084, 1.07
No. of reflections	6866	12265
No. of parameters	637	680
No. of restraints	594	12
$\Delta\rho_{max}$, $\Delta\rho_{min}$ (e Å^{-3})	1.51, −1.23	1.45, −0.56

Absorption and Emission Spectroscopy. Normalized absorption and emission spectra of compounds **39**-[**39**]$_2$Au are shown in Figure 65 above, with λ_{exc} = 485 nm for emission spectra. The molar absorption coefficients of **39**-[**39**]$_2$Au at λ_{max} were determined according to Beer-Lambert calibration curves (shown below in Figures 75-78). Fluorescence quantum yields were calculated based on gradients of integrated emission (IE) versus absorbance at λ_{exc} (Abs) for a series of measurements on the sample and fluorescence standard (fluorescein in 0.1 M NaOH),[138-139] according to the following equation:[149]

$$\Phi_{sample} = \Phi_{std} \times \frac{IE_{sample}}{IE_{std}} \times \frac{Abs_{std}}{Abs_{sample}} \times \left(\frac{\eta_{sample}}{\eta_{std}}\right)^2$$

$$= \Phi_{std} \times \frac{Grad_{sample}}{Grad_{std}} \times \left(\frac{\eta_{sample}}{\eta_{std}}\right)^2$$

where η was taken as 1.33 for 0.1 M NaOH and as 1.338 for the 10 mM sodium phosphate buffer solution.[253] The resulting gradient plots obtained are shown below.

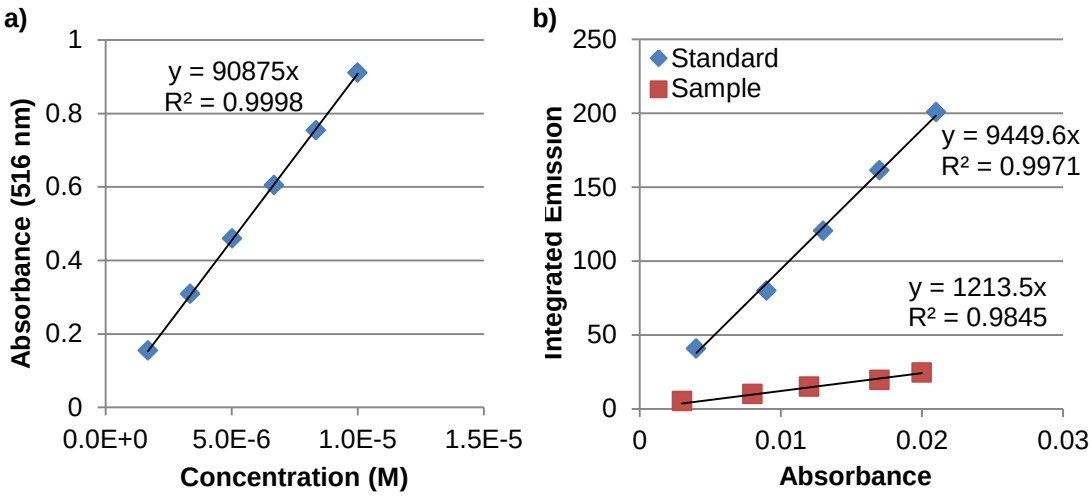

Figure 75. a) Beer-Lambert absorbance plot for **39**. b) Quantum yield gradient plot for **39**.

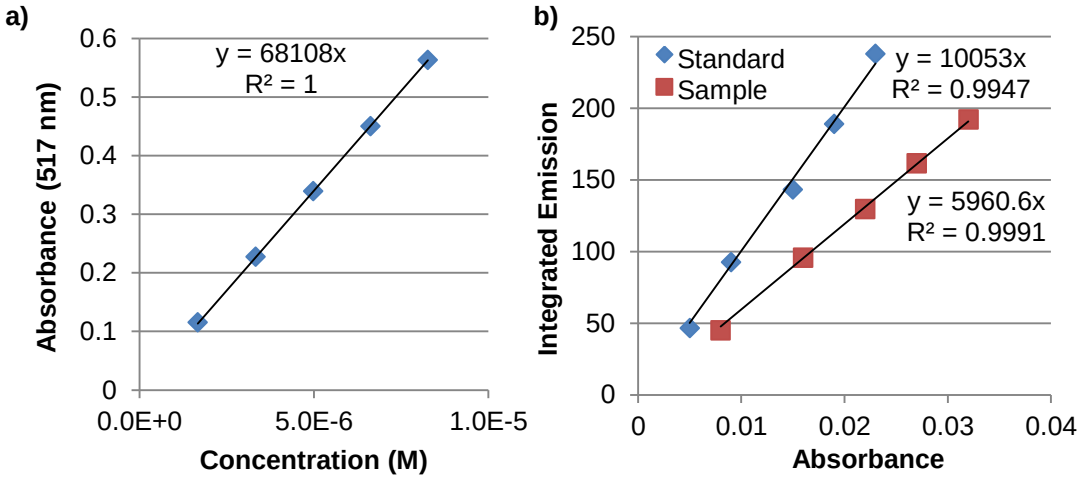

Figure 76. a) Beer-Lambert absorbance plot for **40**. b) Quantum yield gradient plot for **40**.

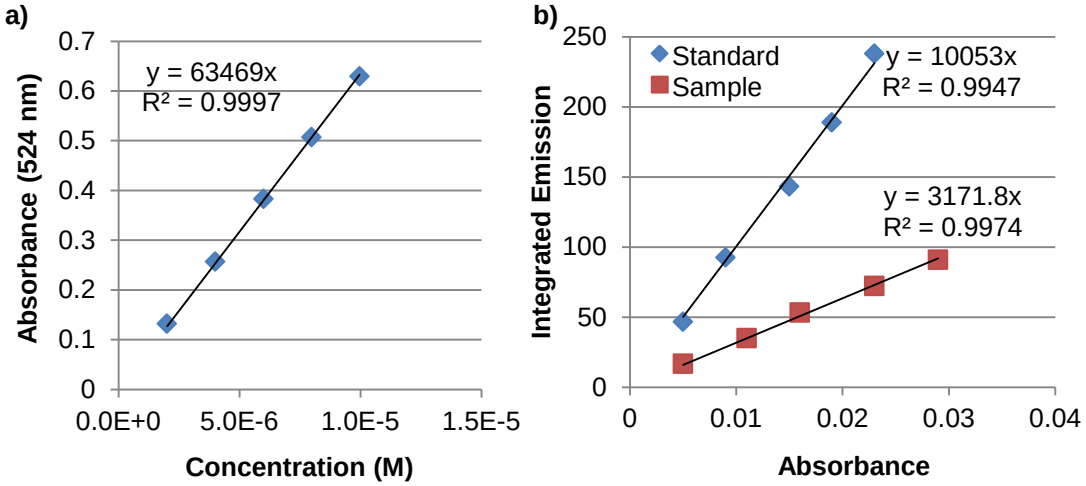

Figure 77. a) Beer-Lambert absorbance plot for **39**-AuCl. b) Quantum yield gradient plot for **39**-AuCl.

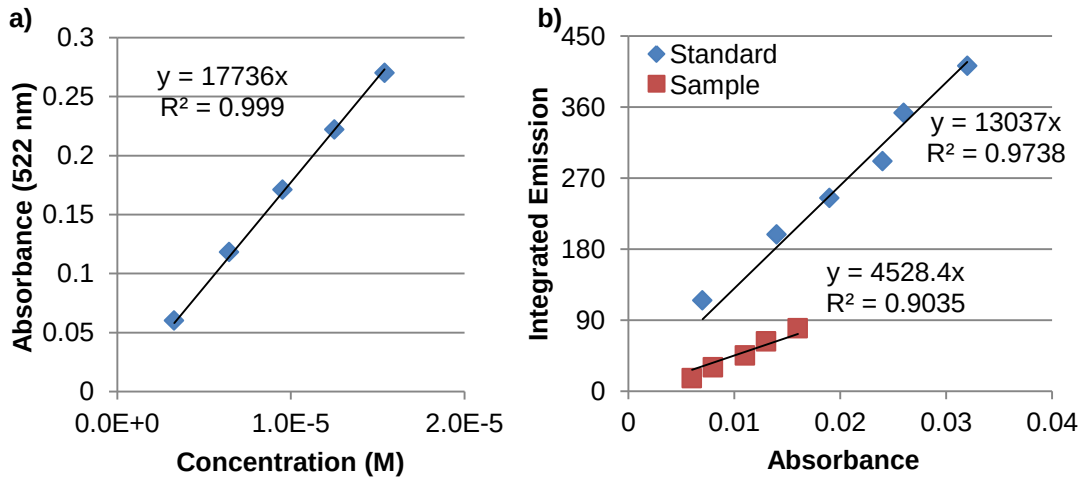

Figure 78. a) Beer-Lambert absorbance plot for [**39**]$_2$Au. b) Quantum yield gradient plot for [**39**]$_2$Au.

Fluorescence Lifetime Measurements. Time-correlated single-photon counting (TCSPC) was employed to obtain fluorescence decay spectra for compounds **39, 40,** and **39-**AuCl. Excitation was done using a pulsed diode laser at 405 nm, and emission was detected utilizing a long-wavelength pass filter (>480 nm) to remove signal from scattered light. The resulting spectra, recorded at the magic angle (54.7°), are shown in Figures 79-81 with fitting functions and residuals determined by multiexponential analysis in the FluoFit software program (PicoQuant). In all cases χ^2 values < 1.2 were obtained, and the residuals closely match the calculated decay models.

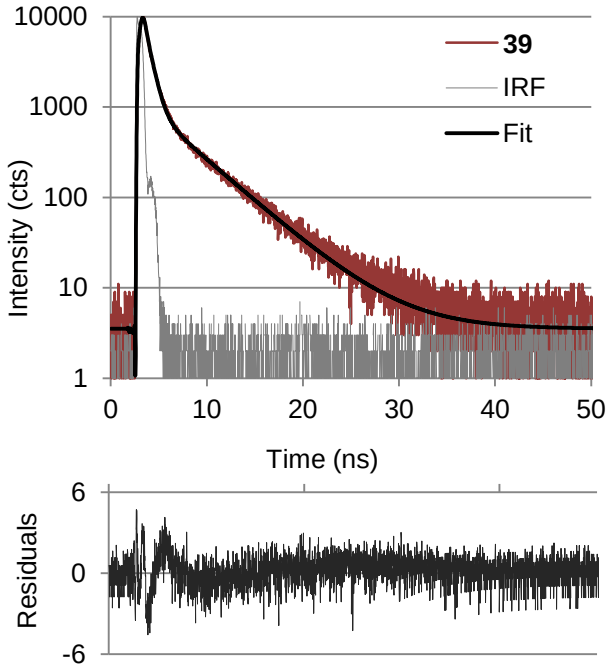

Figure 79. Decay spectra with modeled fit functions and residuals for **39**.

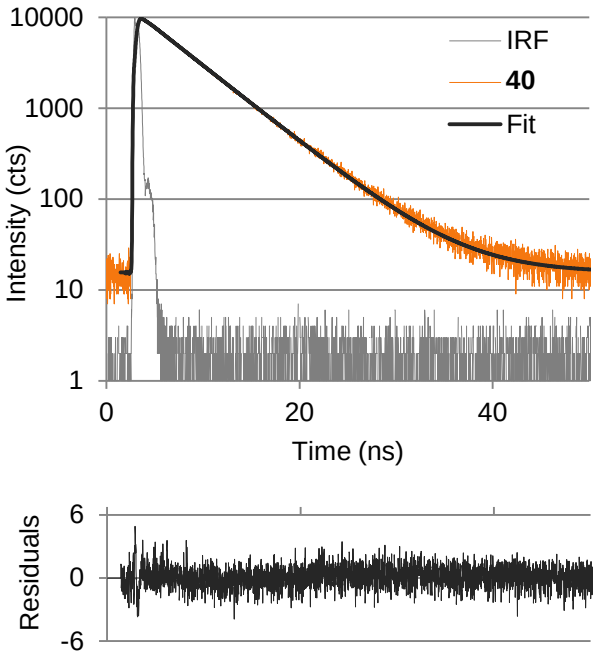

Figure 80. Decay spectra with modeled fit functions and residuals for **40**.

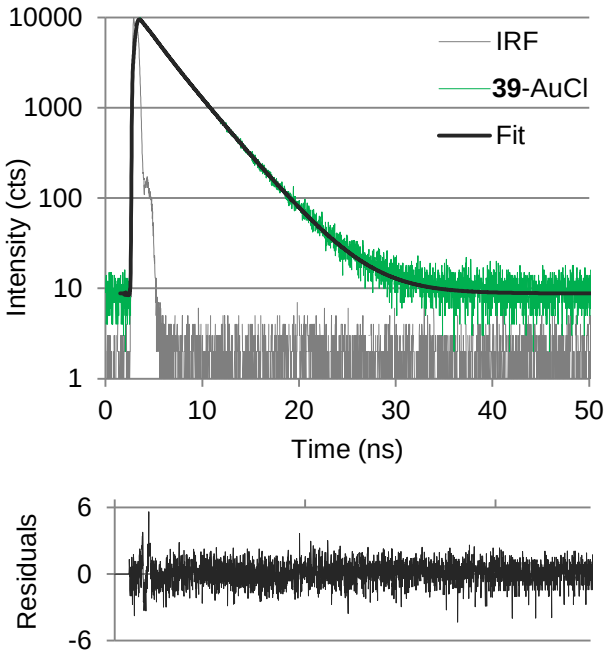

Figure 81. Decay spectra with modeled fit functions and residuals for **39**-AuCl.

Delayed Response of 1 to Pd(II) and Pt(IV). Compound **39** shows a delayed fluorescence response to Pd(II) and Pt(IV) in aqueous solution. A 2.5-mL sample of a 1.0 μM solution of **39** was prepared in pH 7.4 10 mM aqueous sodium phosphate with 10 mM CTAC. A 5-μL aliquot of 2.6×10^{-3} M $PdCl_2$ in DMSO (5 equivalents) was injected into the cuvette. Fluorescence spectra were recorded immediately (1 minute) after mixing and subsequently at 10-minute intervals. The results are shown in Figure 82a. An emission increase grows in over time on allowing the sample to equilibrate, saturating after about 40 minutes. The same experiment was carried out for K_2PtCl_6, adding a 50-μL aliquot of 3.0×10^{-3} M K_2PtCl_6 in water (5 equivalents) into 3.0 mL of a 10 μM solution of **39**. A similar slow response is observed (Figure 82b), saturating after about 40 min, though with a much lower overall increase in fluorescence than for Pd(II). No response is seen for Pt(II) under the same conditions.

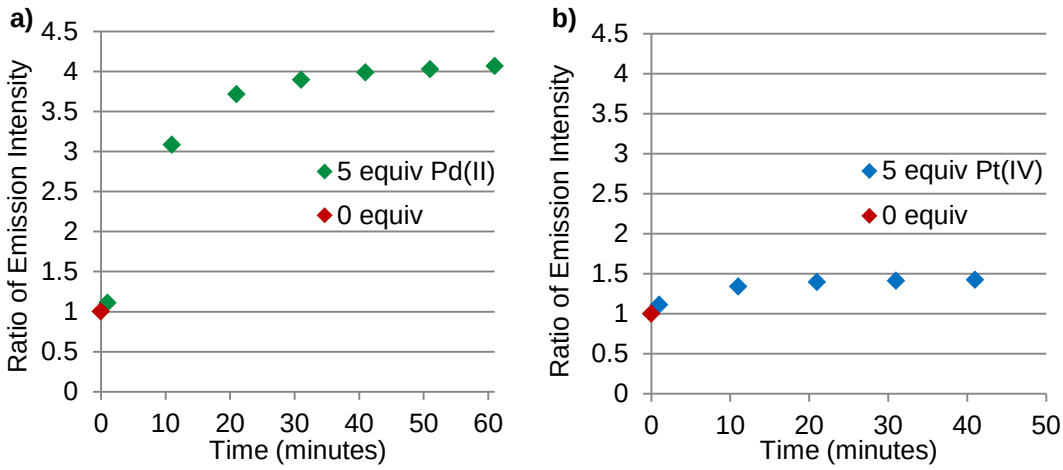

Figure 82. Change in emission intensity of **39** over time in response to 5 equivalents of a) Pd(II) and b) Pt(IV). Emission ratios reported at λ_{max} at each point.

Metal Titrations of 39 with Au(III), Au(I), Ag(I), and Hg(II). Fluorescence measurements were taken on a 1.0 μM solution of **39** prepared by injecting 30 μL of 1.0×10^{-4} M DMSO stock solution into 3.00 mL of aqueous sodium phosphate buffer (10 mM, pH 7.4) with 10 mM CTAC. 5-μL aliquots of a 5.3×10^{-5} M solution of Au(III) or 1.5×10^{-4} M solutions of Au(I), Ag(I), and Hg(II) were injected into the cuvette and the fluorescence spectra recorded immediately (1 minute) after mixing. Corresponding absorption spectra were taken on 10.0 μM samples by the same procedure.

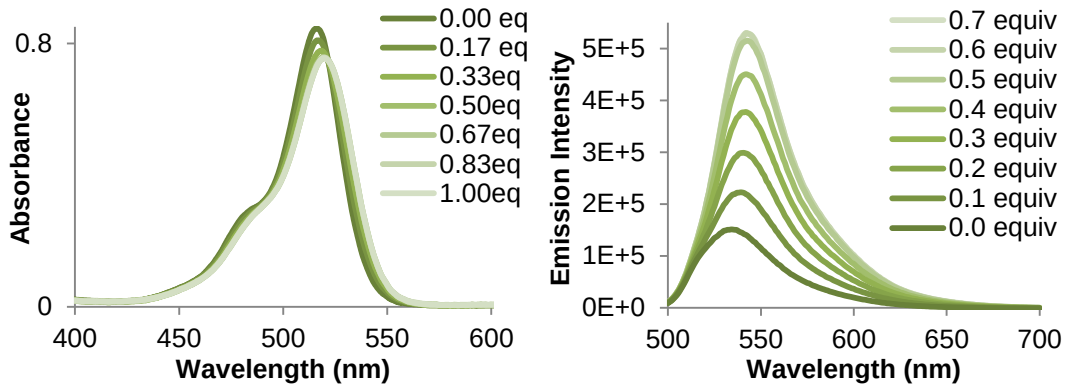

Figure 83. Absorption and emission spectra of **39** titrated with Au(III).

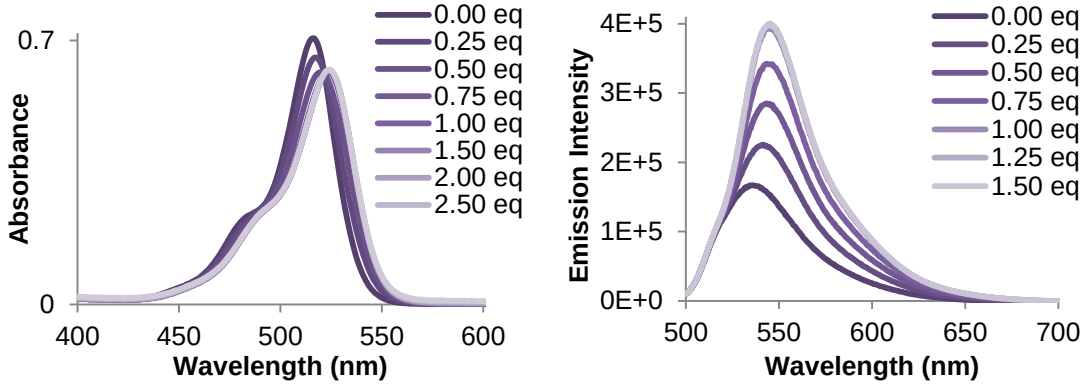

Figure 84. Absorption and emission spectra of **39** titrated with Au(I).

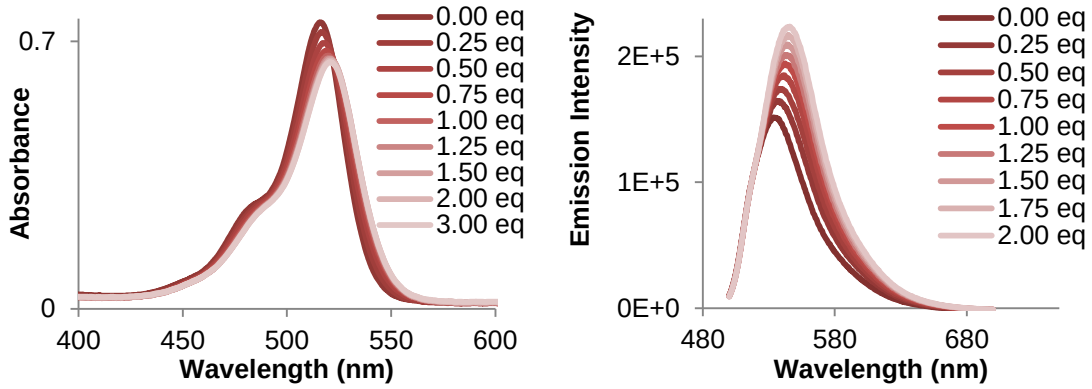

Figure 85. Absorption and emission spectra of **39** titrated with Ag(I).

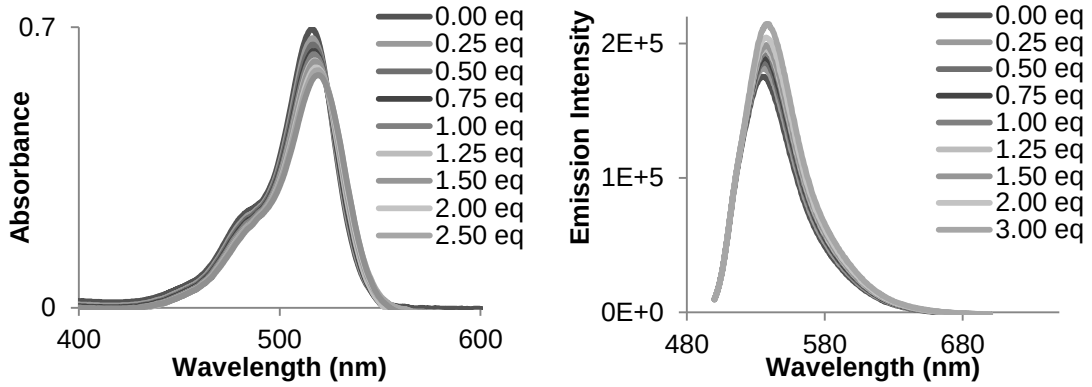

Figure 86. Absorption and emission spectra of **39** titrated with Hg(II).

Determination of Limit of Detection for Au(III) Response. The detection limit for Au(III) was calculated using the titration data as measured above using a literature method.[104, 150-151] Fluorescence intensities were normalized between the minimum and maximum fluorescence intensity at 542 nm (measured at 0 and 5.2×10^{-7} M Au(III) ion, respectively) and plotted against the concentration of Au(III) added. The resulting plot is shown below in Figure 87. A linear regression fitted through this data crossed the ordinate axis at -7.1165, or [Au] = 7.6×10^{-8} M, and this was taken as the limit of detection for Au(III) by **39** under these experimental conditions.

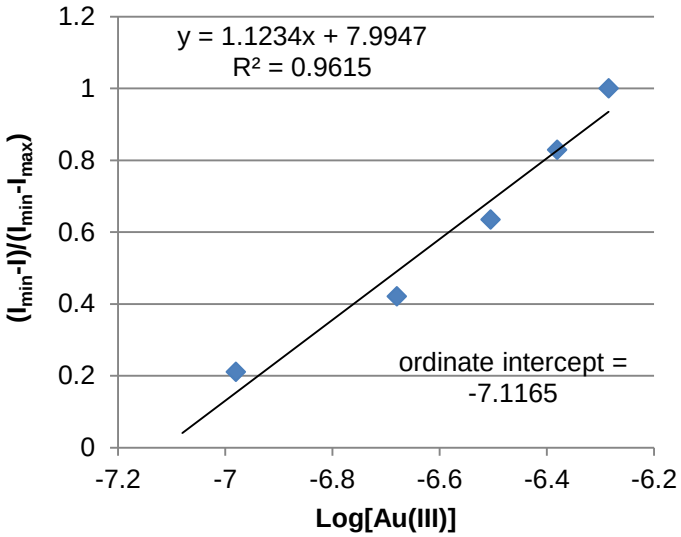

Figure 87. Linear regression of normalized fluorescence intensities of **39** titrated with Au(III).

5. ANTIMONY-SUBSTITUTED PHENYLPYRIDINE LIGANDS FOR RUTHENIUM POLYPYRIDYL CHROMOPHORES: PHOTOPHYSICAL AND ELECTROCHEMICAL EFFECTS OF ANION BINDING AT THE PERIPHERY OF A METAL COMPLEX[‡]

5.1 Introduction

In addition to antimony(V)-based fluoride sensors utilizing an organic fluorophore or chromophore such as anthracene[25] or alizarin[26], our group has researched heterobimetallic complexes containing antimony and transition metals such as palladium and platinum in the context of anion sensing.[24, 91] In continuation of our strategy of coupling antimony(V) centers to strong fluorophores or chromophores to improve their properties as sensors, we also looked to explore metal complexes as photophysical reporter groups for antimony(V)-based anion sensors. Transition metal complexes often display bright colors due to d-d, MLCT, or LMCT transitions in the visible spectrum, and many also display luminescence.[9] Moreover, the photophysical properties of these complexes are highly responsive to changes in geometry and/or electronics at the transition metal center. Incorporating an antimony(V) group on a metal complex such that anion binding can influence the environment of the secondary metal center should therefore enable us to design a sensor with a predictable photophysical response to

[‡] Reprinted with permission from "Fluoride and cyanide anion sensing by an Sb(V)-substituted cyclometalated Ru polypyridyl complex", Christianson, A. M.; Gabbaï, F. P. *J. Organomet. Chem.* **2017**, In Press. Copyright 2017, Elsevier.

anions. We first looked to a representative class of metal complex chromophores—cyclometalated ruthenium polypyridyl complexes.

The distinctive photophysical properties of ruthenium polypyridyl complexes have found application in many fields, including chemical sensing as well as solar energy conversion, photocatalysis, and photodynamic therapy.[254-261] These complexes absorb strongly in the visible region primarily because of MLCT transitions from ruthenium to the polypyridyl ligands such as bipyridyl (bpy), phenanthryl (phen), and terpyridyl (terpy). The light-induced charge separation achieved by these processes allows ruthenium polypyridyl complexes to be used as light harvesters in applications such as dye-sensitized solar cells.[262-266] The redox chemistry of these complexes also features a Ru(II/III) oxidation couple that is readily accessible electrochemically; this feature has been used in the design of electrocatalysts.[255, 267] The properties of ruthenium polypyridyl complexes are tunable by modification of the ligands, allowing access to a wide range of absorption and emission colors and electrochemical reactivity.

The incorporation of a cyclometalated (N^C) ligand such as phenylpyridyl (ppy) adds a further level of control over the photophysical and redox properties of these complexes.[268] Compared to complexes of type $[Ru(N^N)_3]^{2+}$, cyclometalated complexes of type $[Ru(N^N)_2(N^C)]^{+}$ have higher electron density at ruthenium due to the stronger donation of the formally carbanionic N^C ligand and the lower overall charge of the complex. This increased electron density raises the energy of the ruthenium-based d electrons, leading to red-shifted MLCT absorbance bands and a more readily accessible Ru(II/III) oxidation potential in cyclometalated complexes.[266, 269-273] Furthermore,

because of σ donation of the N^C ligand is much stronger than that of the N^N ligands, substituents on the cyclometalating ligand have a strong influence on the electron density at ruthenium, resulting in pronounced effects on the absorption profile of the complex. Electron-withdrawing groups draw away electron density from Ru, lowering the metal-based d orbitals and blueshifting absorption, whereas electron-donating groups raise the d orbitals and redshift absorption.[266, 272] A corresponding effect is observed in the Ru(II/III) redox couple: electron-withdrawing groups raise the oxidation potential, while electron-donating groups lower it.[269, 274] For example, the substitution of the phenylpyridyl ligand of the cyclometalated ruthenium polypyridyl complex $[(bpy)_2Ru(ppy)]^+$ with a single nitro group induces a shift in the maximum absorbance band from 543 to 495 nm, and a 120-mV shift in the Ru(II/III) redox couple to higher potential (Figure 88).[272]

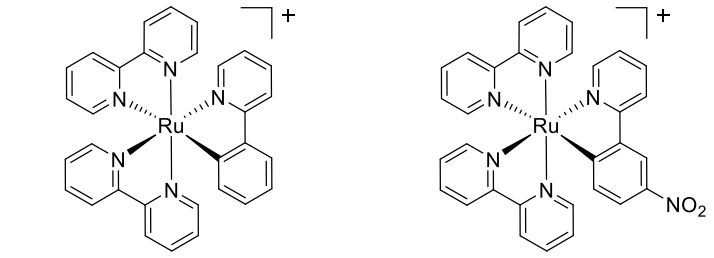

Figure 88. Structures of $[(bpy)_2Ru(ppy)]^+$ and $[(bpy)_2Ru(NO_2\text{-}ppy)]^+$ with a comparison of their photophysical and electrochemical properties.

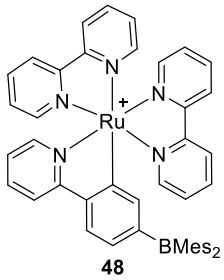

48

Figure 89. Previously-reported fluoride and cyanide sensor based on a dimesitylborane-substituted Ru polypyridyl complex.

This simple electronic modulation of the photophysical and electrochemical properties of ruthenium polypyridyl complexes can form the basis for rational design of chemical sensors. In our group, we have already utilized this strategy in the reported dimesitylborane-substituted ruthenium polypyridyl complex **48** shown in Figure 89.[275] The Lewis acidic borane is able to coordinate fluoride or cyanide anions in organic solvent, with a corresponding change in absorbance and oxidation potential of the ruthenium complex. As expected, the electron-withdrawing effect of the borane group is passivated upon anion binding, and the addition of fluoride or cyanide anions to **48** is accompanied by a red shift in the absorbance bands and a lowered Ru(II/III) oxidation potential. In the case of **48**, fluoride binding at boron was weaker than cyanide binding by two orders of magnitude in acetonitrile.[275] Since we have been interested in developing sensors for cyanide as well as fluoride based on Lewis acidic antimony(V) compounds, we chose to target an antimony(V)-substituted analog of **48** to see if the same photophysical response to anions would obtain using the ruthenium complex as the

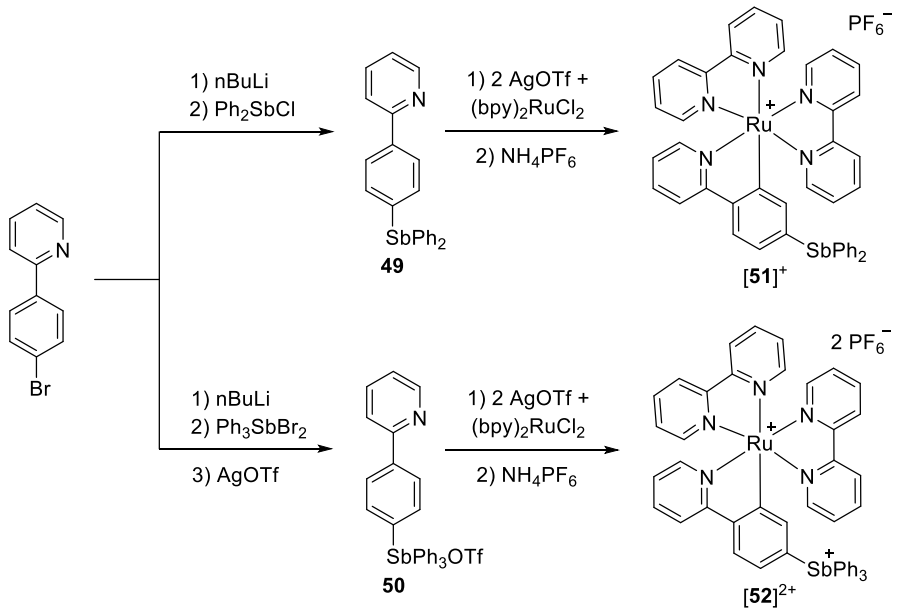

Figure 90. Synthesis of Sb-substituted cyclometalated Ru complexes.

reporter group. In this section, we report our successful installation of a cationic methylstibonium group on a cyclometalating phenylpyridine ligand of a Ru polypyridyl complex, and show that fluoride and cyanide binding at the antimony(V) center modulate the photophysical and electrochemical properties of the complex.[276]

5.2 Synthesis of Ru polypyridyl complexes with Sb-substituted cyclometalating ligands

The Sb(III)-substituted phenylpyridine ligand **49** was synthesized by lithiation of 2-(4-bromophenyl)pyridine and quenching with diphenylantimony chloride, and the corresponding Sb(V)-substituted phenylpyridine ligand **50** by the same route, quenching with triphenylantimony dibromide (Figure 90). In the case of **50**, the second bromide

substituent on Sb was abstracted using silver triflate to yield the tetraarylstibonium ligand with a weakly coordinating triflate anion. Both phenylpyridine ligands were characterized by ^{1}H NMR and then used without further purification to form the cyclometalated complexes. Cyclometalation reactions sometimes employ rather high temperatures under aqueous conditions[277-278]; however, we found that our Sb-substituted phenylpyridine ligands did not withstand temperatures above about 100 °C but were prone to decomposition with loss of the Sb substituent, possibly due to hydrolysis. Cyclometalation was therefore carried out by an adaptation of Constable's method,[270, 274] refluxing ligands **49** and **50** in degassed EtOH with $(bpy)_2Ru(OTf)_2$, which was generated *in situ* by treatment of $(bpy)_2RuCl_2 \cdot 2H_2O$ with AgOTf. Treatment of the products with NH_4PF_6 as an anion exchange reagent afforded Sb-substituted Ru polypyridyl complexes [**51**]PF_6 and [**52**]$(PF_6)_2$ as deep purple solids, which were stable to purification by silica gel chromatography (Figure 90). [**51**]PF_6 and [**52**]$(PF_6)_2$ are soluble in polar organic solvents including DMSO, MeCN, and CH_2Cl_2, but insoluble in H_2O and less polar solvents such as Et_2O.

The structures of complexes [**51**]PF_6 and [**52**]$(PF_6)_2$ were confirmed by NMR spectroscopy in d_6-DMSO (Figure 91). Both complexes display a complicated ^{1}H NMR spectrum because the cyclometalating ligand breaks the symmetry of the pseudo-octahedral Ru complex, making each aromatic hydrogen magnetically distinct. However, in both cases, one diagnostic signal appears as an upfield-shifted singlet; this corresponds to the hydrogen at the 3 position of the phenylpyridyl ligand, adjacent to the

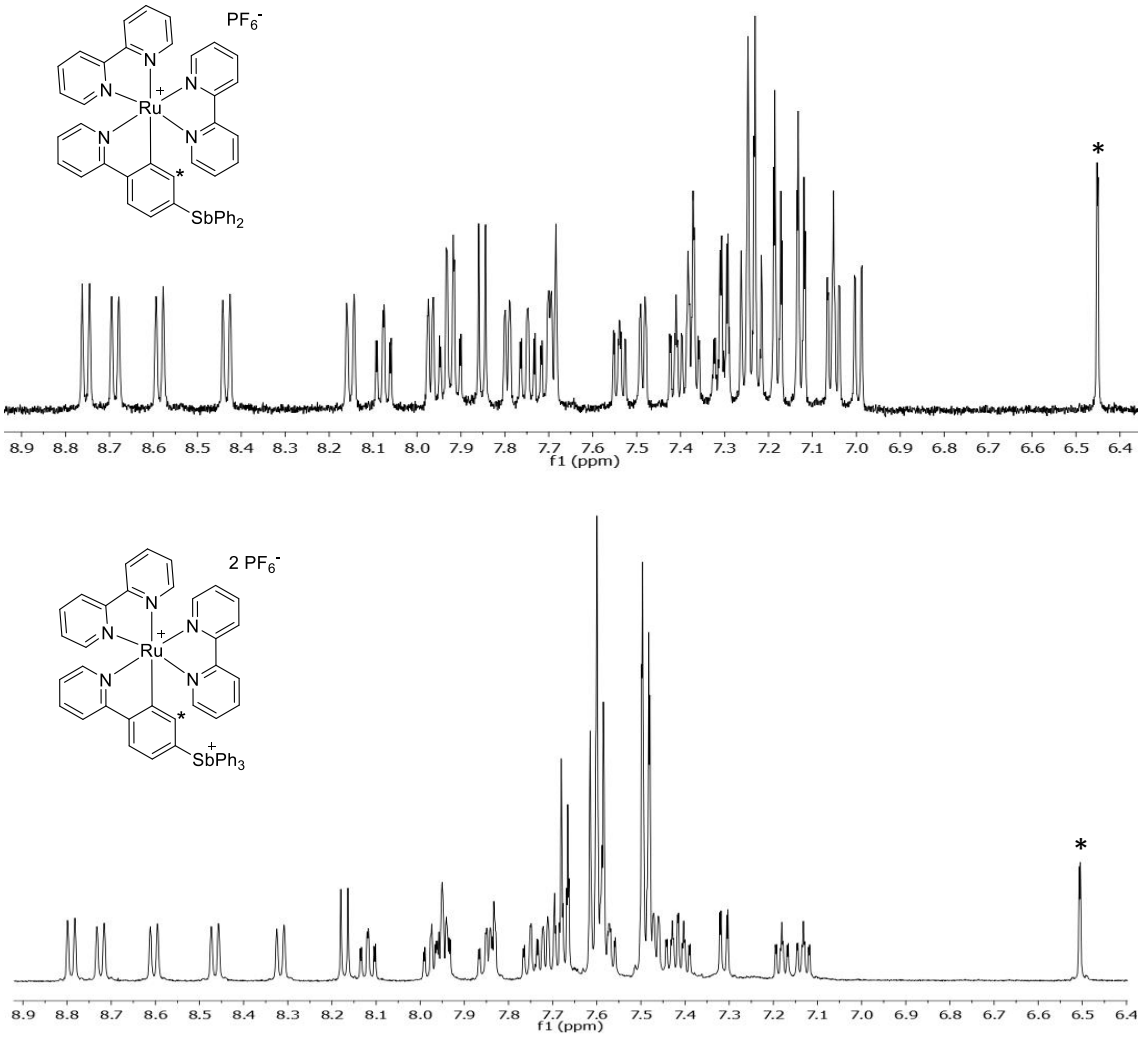

Figure 91. ^{1}H NMR spectra of complexes [**51**]PF_6 and [**52**]$(PF_6)_2$ in d_6-DMSO. Assignment of the signal for the proton *ortho* to the cyclometalating carbon is indicated by an asterisk (*) for each spectrum.

C-donor group. This signal is expected to be upfield-shifted in cyclometalated Ru complexes of this type because of its proximity to the cyclometalating carbon, and the lack of splitting confirms the substitution at the 4 position of the phenylpyridyl by the antimony moiety.[270, 272, 279] Two-dimensional COSY NMR analysis was carried out on

complex [**51**]PF_6 to better assign the remaining signals (See Experimental details). Coupling between adjacent protons on any of the pyridyl rings could be identified by this method, allowing many of these signals to be corroborated with each other. The signals corresponding to the Sb(III)-bound phenyl groups in complex [**51**]PF_6 overlap with several other peaks, but can be roughly assigned between 7.4-7.2 ppm, in the expected range for triarylantimony compounds. In complex [**52**]$(PF_6)_2$, the signals corresponding to the Sb(V)-bound phenyl groups increase in intensity and appear further downfield-shifted to between 7.7-7.5 ppm, as expected due to the oxidation of the Sb center. Additionally, by comparing the ^{1}H and ^{19}F NMR spectra using 2', 3', 4', 5', 6'-pentafluoroacetophenone as an internal standard, a 1:1 ratio of Ru complex to PF_6^- anion can be established in compound [**51**]PF_6 and a 1:2 ratio of Ru complex to PF_6^- anion in compound [**52**]$(PF_6)_2$, confirming the monocationic and dicationic natures of the complexes, respectively (See Experimental details). Furthermore, mass spectrometric analysis of [**51**]PF_6 reveals a monocationic molecular ion peak at 842.08 *m/z* corresponding to [**51**]$^+$, and analysis of [**52**]$(PF_6)_2$ reveals a dicationic molecular ion peak at 459.57 *m/z*, half the molecular weight of [**52**]$^{2+}$.

5.3 Photophysical and electrochemical properties of complexes [**51**]$^+$ and [**52**]$^{2+}$

The photophysical and electrochemical properties of [**51**]PF_6 and [**52**]$(PF_6)_2$ were compared to those of the known parent complex $[(bpy)_2Ru(ppy)]PF_6$ in acetonitrile solution (Table 8).[270] In the case of [**51**]$^+$, the absorbance profile matches very closely to

Table 8. Photophysical and electrochemical properties of cyclometalated Ru complexes in MeCN.

Compound	Absorbance Maxima, nm	ε, $M^{-1}cm^{-1}$ (λ_{max})	Ru(II/III) Oxidation Potential vs Fc/Fc^{+}
$[(bpy)_2Ru(ppy)]PF_6$	368, 404, 491, 547	10,300 (547 nm)	+0.06 V
[**51**]PF_6	364, 404*, 492, 543	9,900 (543 nm)	+0.06 V
[**52**]$(PF_6)_2$	357, 392*, 490, 523	10,400 (523 nm)	+0.21 V

* Shoulder peak.

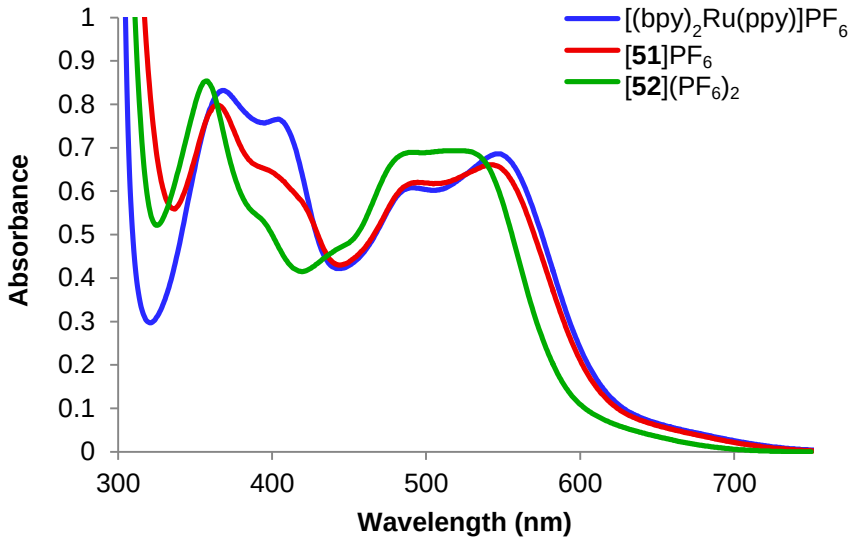

Figure 92. UV-vis absorption spectra of cyclometalated Ru complexes in MeCN.

that of the complex without the $SbPh_2$ substituent, with broad bands in the near UV with maxima at 364 and 404 nm, as well as a broad band across the visible region with maxima at 492 and 543 nm (Figure 92). The $–SbPh_2$ group, therefore, appears to be neither significantly electron donating nor withdrawing, comparable to a hydrogen substituent. On the other hand, while the pattern of the absorption spectrum of [**52**]$^{2+}$

remains similar to that of [**51**]$^{+}$, the major absorption bands of [**52**]$^{2+}$ in the near UV and visible range are blueshifted by 10-20 nm. This effect is consistent with a significantly increased electron-withdrawing capacity for the stibonium substituent, and shows that the Sb(V) group has a pronounced effect on the photophysical properties of the complex in [**52**]$^{2+}$.

The electrochemistry of [**51**]PF_6**,** [**52**]$(PF_6)_2$, and [$(bpy)_2$Ru(ppy)]PF_6 was also investigated with cyclic voltammetry (Figure 93). Again, the electrochemical profile of [**51**]$^{+}$ appears very similar to the unsubstituted complex, with a reversible couple at +0.06 V corresponding to the Ru(II/III) oxidation and two reversible reduction events at -2.03 V and -2.33 V corresponding to bipyridine ligand reductions. Complex [**51**]$^{+}$ also

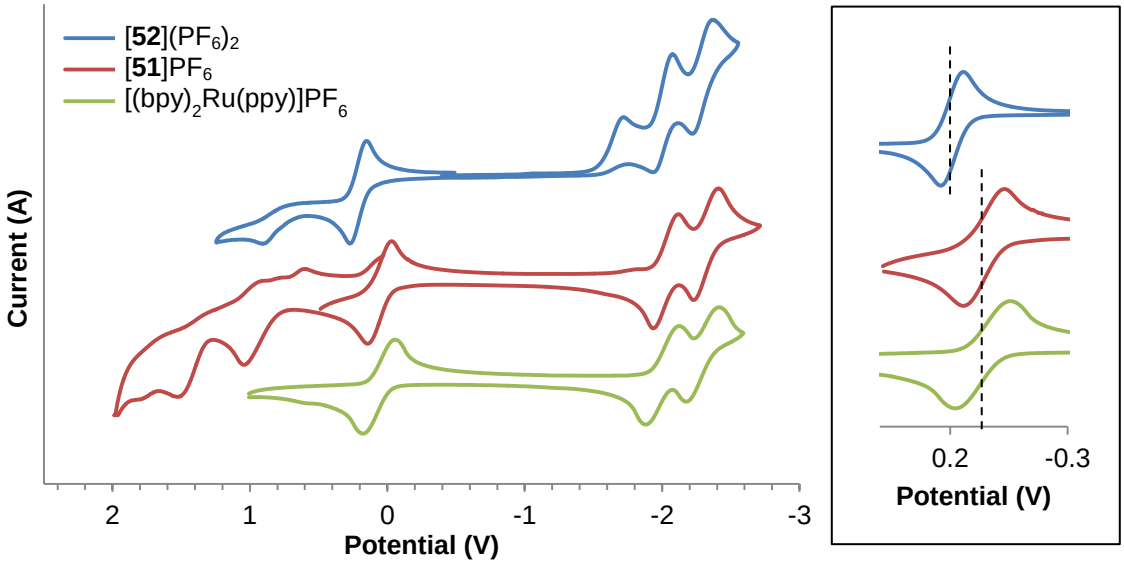

Figure 93. Cyclic voltammograms of [**51**]PF_6**,** [**52**]$(PF_6)_2$, and [$(bpy)_2$Ru(ppy)]PF_6 (2×10^{-3} M samples in MeCN with 0.1 M $TBAPF_6$ as electrolyte, scan rate 0.1 V/s, potentials referenced to Fc/Fc^{+} in the same solvent). Inset: Ru(II/III) oxidation couples for the three compounds, highlighting the change in oxidation potential induced by the Sb(V) ligand substituent.

shows several irreversible oxidation features above +0.5 V which do not appear in the voltammogram of $[(bpy)_2Ru(ppy)]PF_6$, and therefore likely correspond to Sb-based oxidations. For complex $[\mathbf{52}]^{2+}$, a reversible couple is again observed for the Ru(II/III) oxidation; however, it is shifted to +0.21 V, approximately 150 mV to higher potential. In addition to the two reversible ligand-based reductions, complex $[\mathbf{52}]^{2+}$ also displays an irreversible reduction at E_p = -1.72 V, possibly corresponding to a reduction of the Sb(V) group. The distinct change in the Ru(II/III) oxidation potential indicates that the Ru center in complex $[\mathbf{52}]^{2+}$ is less electron-rich and therefore less readily oxidized. Thus, both the spectroscopic and electrochemical properties of $[\mathbf{51}]^{+}$ and $[\mathbf{52}]^{2+}$ indicate that in terms of electron-donating or electron-withdrawing capability on the phenylpyridine ligand, the $–SbPh_2$ group is comparable to a hydrogen substituent, whereas the $–SbPh_3^{+}$ group is more comparable to a strongly electron-withdrawing nitro group.[271-272, 274]

5.4 Fluoride and cyanide sensing by complex $[\mathbf{52}]^{2+}$

Having established that the tetraarylstibonium ligand substituent in complex $[\mathbf{52}]^{2+}$ exerts a strong enough electron-withdrawing effect on the Ru center to influence the photophysical and electrochemical properties, we next investigated its anion coordination behavior in organic solvents. Addition of the soluble fluoride salt TASF to a solution of $[\mathbf{52}](PF_6)_2$ in d_6-DMSO resulted in distinct changes to the ^1H NMR spectrum, with the peaks assigned to the Sb-bound Ph groups becoming broadened and shifted slightly upfield to between 7.6-7.3 ppm. This is consistent with fluoride

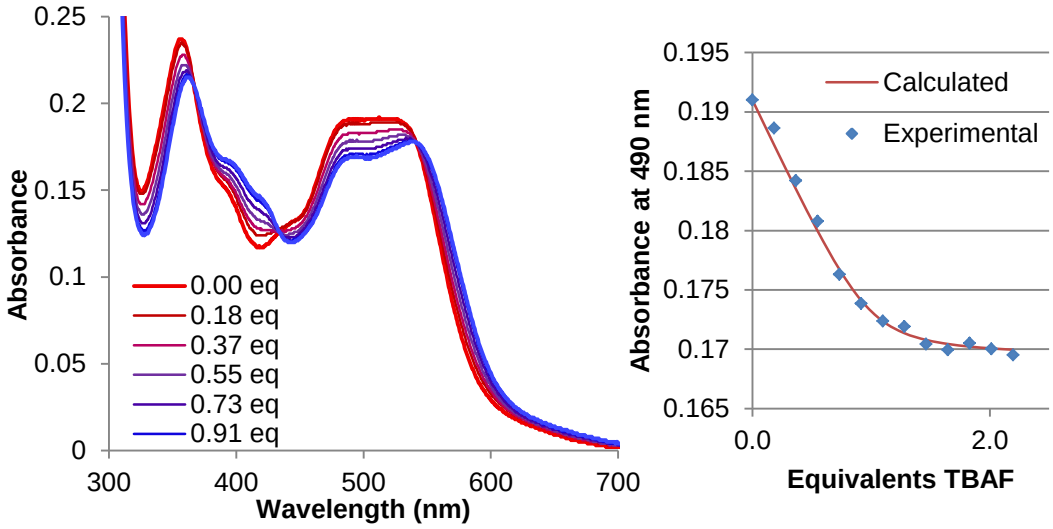

Figure 94. Changes in UV-vis absorption spectrum of $[\mathbf{52}]^{2+}$ (1.84×10^{-5} M in MeCN) upon titration with TBAF. Inset: Experimental and calculated 1:1 binding isotherm for the addition of F^- to $[\mathbf{52}]^{2+}$, based on the absorbance measured at 490 nm.

coordination to the Sb(V) center, which would be expected to passivate its electron-withdrawing influence on the Sb-bound Ph groups. Additionally, a signal appears at -77.2 ppm in the ^{19}F NMR spectrum, consistent with an Sb-bound fluoride. Finally, the formation of a fluoride adduct $[\mathbf{52}\text{-F}]^+$ was further confirmed by mass spectrometry, which showed a monocationic molecular ion peak at 938.17 *m/z*.

As expected, addition of fluoride to $[\mathbf{52}]^{2+}$ also induces a significant change in the absorption spectrum of the Ru polypyridyl complex (Figure 94). With incremental addition of TBAF to $[\mathbf{52}]^{2+}$, the broad MLCT absorbance band between 480-530 nm decreases somewhat in intensity and shifts approximately 10-15 nm to the red, with a shift of the longest-wavelength maximum absorbance peak from 523 to 537 nm. This absorption change can also be seen visually as a subtle color change from red-purple to purple-black. Fluoride binding at the Sb(V) center would decrease the charge and

electron-withdrawing effect of the substituent, causing a release of electron density back to Ru and resulting in a bathochromic shift of MLCT absorptions. Indeed, the final absorbance spectrum of [**52**-F]$^{+}$ is more reminiscent of the spectrum of [**51**]$^{+}$ or the unsubstituted [(bpy)$_2$Ru(ppy)]$^{+}$ than of [**52**]$^{2+}$, indicating that the coordination of fluoride dramatically affects the electron-withdrawing effect of the Sb(V) group. The observed behavior is in good accord with that of our previously-reported borane-substituted Ru complex **48**, which also shows a distinct redshift in absorbance with anion binding at boron.[275] The absorption changes upon titration of [**52**]$^{2+}$ with fluoride were fitted to a 1:1 binding isotherm to determine an anion binding constant of $K(F^-) = 1.4\times10^6(\pm2\times10^5)$ M^{-1} in acetonitrile, showing that fluoride binding by the tetraarystibonium moiety is quite strong. However, it is still reversible—treatment of [**52**-F]$^{+}$ with a small amount of Al(NO$_3$)$_3$ as a fluoride scavenger results in complete reversion to the absorbance spectrum of [**52**]$^{2+}$ (Figure 95).

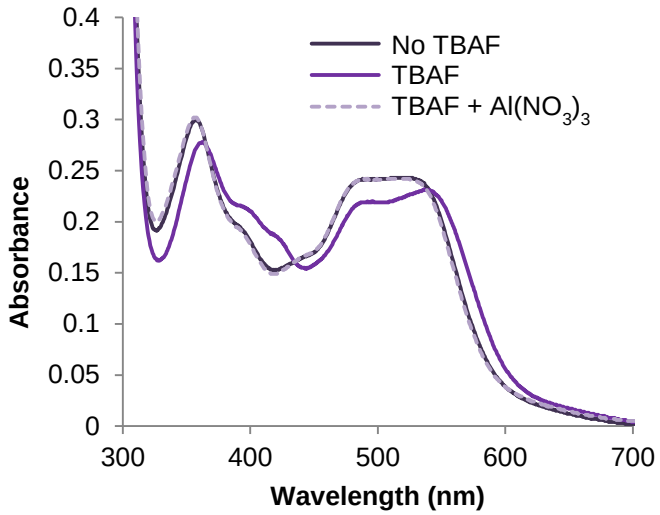

Figure 95. Reversibility of fluoride binding to [**52**]$^{2+}$ with addition of Al(NO$_3$)$_3$.

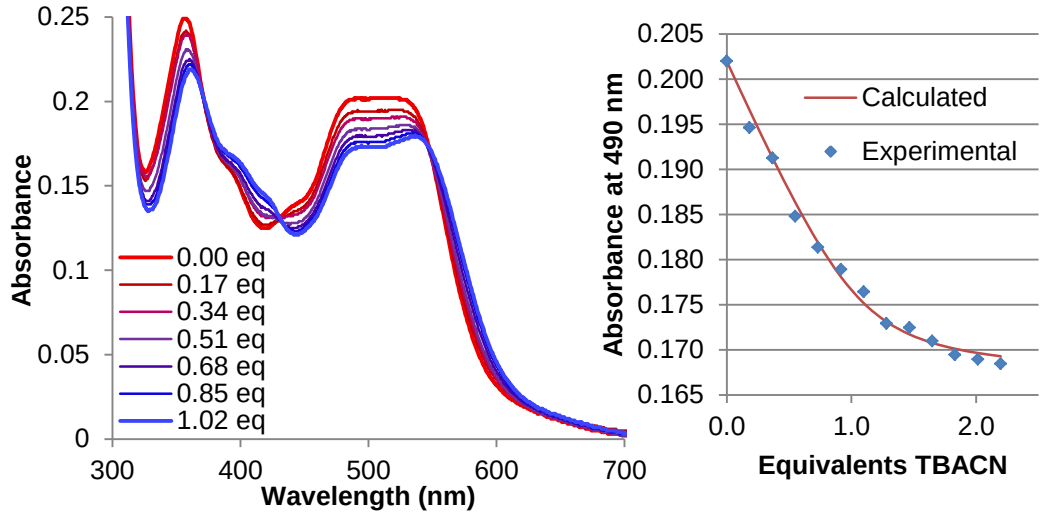

Figure 96. Changes in UV-vis absorption spectrum of $[\mathbf{52}]^{2+}$ (1.94×10^{-5} M, MeCN) upon titration with TBACN. Inset: Experimental and calculated 1:1 binding isotherm for the addition of CN^- to $[\mathbf{52}]^{2+}$, based on the absorbance measured at 490 nm.

To complete the comparison of complex $[\mathbf{52}]^{2+}$ with the borane-substituted complex **48**, the response of $[\mathbf{52}]^{2+}$ to the toxic cyanide anion was investigated. Incremental addition of TBACN to $[\mathbf{52}]^{2+}$ in acetonitrile results in very much the same changes to the absorption spectrum as in the case of F^-, which suggests that complex $[\mathbf{52}]^{2+}$ is also able to coordinate CN^- anions at the Sb(V) center (Figure 96). A binding constant of $K(CN^-) = 6.8\times10^5(\pm6\times10^4)$ M^{-1} in acetonitrile was determined for the addition of CN^- to $[\mathbf{52}]^{2+}$, indicating that the binding of cyanide to $[\mathbf{52}]^{2+}$ is weaker than that of fluoride. This is in contrast to the behavior of our previously-reported borane-substituted system **48**, which instead displayed a higher binding constant for cyanide than fluoride.[275] This difference may reflect an inherently higher affinity for cyanide in boron-based rather than antimony-based Lewis acids, or it may be due to the difference in steric congestion around the Lewis acidic site, which is much greater in the case of

[**52**]$^{2+}$ due to the fourth aryl substituent at Sb. The binding of cyanide to [**52**]$^{2+}$ is also reversible, with addition of $Al(NO_3)_3$ to a solution of [**52**-CN]$^{+}$ resulting in complete reversion to the absorption spectrum of [**52**]$^{2+}$ (Figure 97).

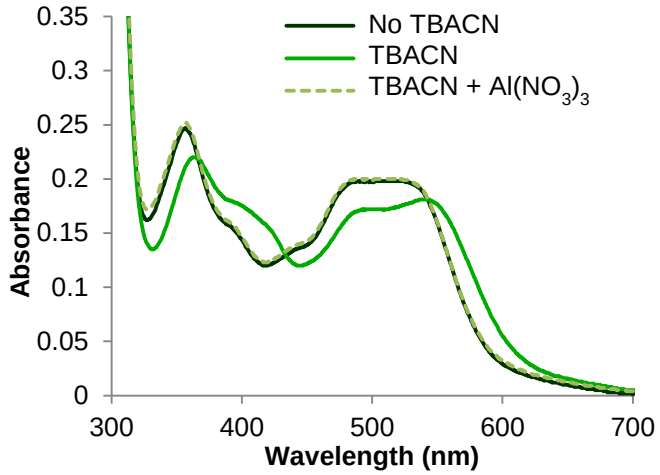

Figure 97. Reversibility of cyanide binding to [**52**]$^{2+}$ with addition of $Al(NO_3)_3$.

The binding of F^- and CN^- to complex [**52**]$^{2+}$ was also monitored electrochemically. Addition of 1 equivalent of TBAF to an acetonitrile solution of [**52**]$(PF_6)_2$ results in a shift of the Ru(II/III) oxidation potential of approximately 100 mV to lower voltage, from +0.21 V to +0.10 V (Figure 98a). The irreversible reduction at -1.72 V in the voltammogram of [**52**]$^{2+}$ also disappears completely upon addition of fluoride. These changes are again consistent with our hypothesis, in which fluoride binding at Sb releases electron density from the Sb(V) substituent toward the Ru center, making oxidation of the Ru center more favorable. However, upon addition of TBACN

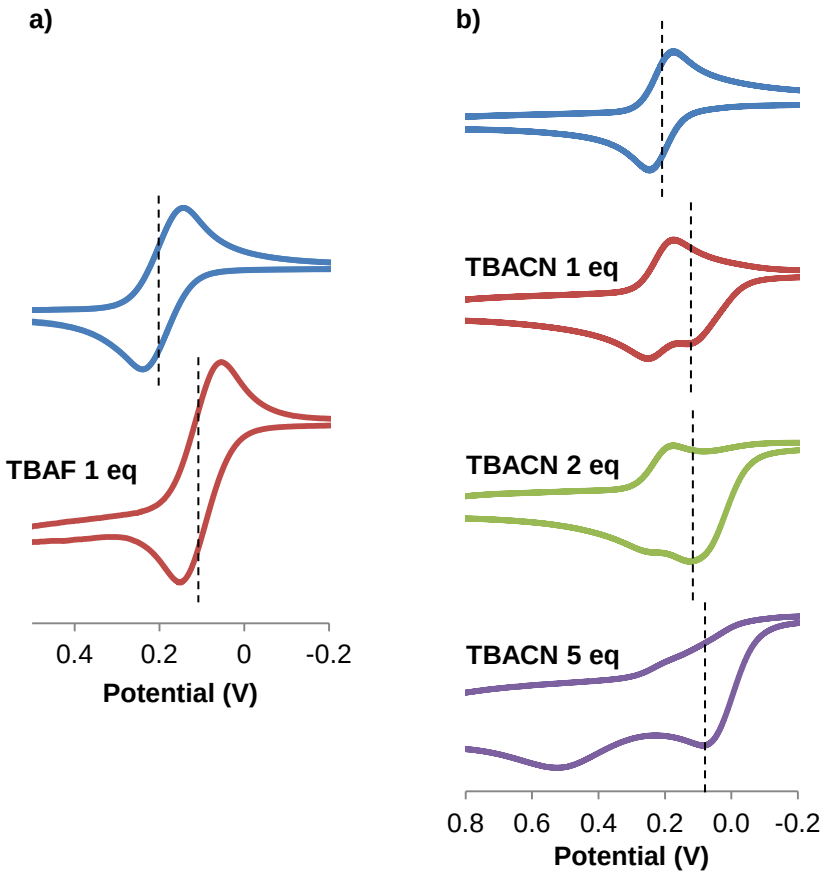

Figure 98. Cyclic voltammograms of the Ru(II/III) oxidation couple for a) TBAF and b) TBACN added to $[\mathbf{52}]^{2+}$ (2×10^{-3} M samples in MeCN with 0.1 M $TBAPF_6$ as electrolyte, scan rate 0.1 V/s, potentials referenced to Fc/Fc^{+} in the same solvent).

to an acetonitrile solution of $[\mathbf{52}]^{2+}$, more complicated behavior is observed in the cyclic voltammogram. After addition of 1 equivalent of TBACN, the original Ru(II/III) oxidation couple at +0.21 V is still observable, but another irreversible oxidation feature of comparable intensity appears at lower potential (E_p = +0.13 V). With addition of further equivalents of CN^-, this irreversible wave shifts further to lower potential (E_p = +0.08 V) and becomes more prominent until the original reversible oxidation couple disappears (Figure 98b). After addition of 5 equivalents of TBACN, a second

irreversible oxidation feature also appears at approximately +0.53 V. The persistence of the original Ru(II/III) oxidation couple of [**52**]$^{2+}$ with addition of multiple equivalents of TBACN may reflect the lower binding constant of CN^- to the Sb(V) center of [**52**]$^{2+}$ as verified by the absorbance titrations. However, the irreversible character of the oxidation feature that replaces it suggests that the product of CN^- addition to [**52**]$^{2+}$ may not be stable under oxidizing conditions. It is possible that cyanide-induced decomplexation of the Ru bipyridyl complex is occurring, since ligand displacements of polypyridyl ligands such as bipyridine and phenanthroline by cyanide under conditions of excess CN^- are known.[280-281] In the titration experiments shown in Figures 94-97, the changes in absorbance and reversibility of the system are clean and do not seem to indicate any decomposition. However, under the conditions of those measurements, the concentration of [**52**]$^{2+}$ is more dilute by two orders of magnitude and CN^- is not added in large excess, nor is an oxidizing potential applied. The possible decomposition observed in the cyclic voltammogram may therefore be influenced by the conditions of the electrochemical measurements.

5.5 Conclusions

As we anticipated, the incorporation of an antimony(V)-containing substituent on a cyclometalating ligand of a ruthenium polypyridyl complex significantly influences the photophysical and electrochemical properties due to its strong electron-withdrawing nature. Fluoride or cyanide binding at the antimony center modulates this electron-withdrawing effect and thus induces a colorimetric and electrochemical change in the

ruthenium-centered system, allowing it to be used for sensing of those anions. The practical advantages of the antimony(V)-substituted complex [**52**]$^{2+}$ as an anion sensor are limited, since this sensor did not function in aqueous solution, and did not bind cyanide as strongly as the analogous borane-substituted complex. However, it is significant that this sensor functions on the basis of a rational design, and that very simple modulations of the electron-withdrawing influence of the antimony(V) substituent at the periphery of the ruthenium polypyridyl complex can produce substantial changes in electronics at the second metal center. The incorporation of antimony-containing ligands into metal polypyridyl complexes could therefore be explored further for purposes other than anion sensing, such as controlling catalytic reactivity by "switching" the electronic influence of the ligand via oxidation or anion binding.

5.6 Experimental details

General Methods. All preparations were carried out under an N_2 atmosphere using standard Schlenk techniques unless otherwise stated. Et_2O and THF were dried by refluxing under N_2 over Na/K; all other solvents were ACS reagent grade and used as received. 2-(4-bromophenyl)pyridine,[282] Ph_3SbBr_2,[283] $(bpy)_2RuCl_2 \cdot 2H_2O$,[284] and $[(bpy)_2Ru(ppy)]PF_6$[270] were prepared according to previously reported procedures. Other starting materials and reagents including TBAF and TBACN were purchased and used as received. NMR spectra were recorded using a Varian Unity Inova 500 FT NMR (499.58 MHz for ^1H, 125.63 MHz for ^{13}C, 469.99 MHz for ^{19}F) spectrometer. Chemical

shifts (δ) are given in ppm and are referenced against residual solvent signals (^{1}H, ^{13}C) or external $BF_3 \cdot Et_2O$ (-153.00 ppm) for ^{19}F. Mass spectrometry was carried out by the Texas A&M Chemistry Mass Spectrometry Facility. Elemental analyses were performed at Atlantic Microlab (Norcross, GA). Absorbance measurements were taken on a Shimadzu UV-2502PC UV-Vis spectrophotometer against a solvent reference. Cyclic voltammetry measurements were taken on deaerated solutions in acetonitrile with 0.1 M $TBAPF_6$ as electrolyte, at a scan rate of 0.1 V/s. All potentials were referenced against Fc/Fc^+ in the same solvent. The spectroscopic and electrochemical properties of $[(bpy)_2Ru(ppy)]PF_6$ have been reported previously, but were reproduced under the conditions stated in these experiments for comparison to [**51**]PF_6 and [**52**]$(PF_6)_2$. [270]

Synthesis of 49. 2-(4-bromophenyl)pyridine (465 mg, 1.99 mmol) in 10 mL THF was treated with *n*-butyllithium (0.80 mL, 2.65 M in hexanes, 2.12 mmol) dropwise at -78° C. The dark brown solution was stirred for 1 hr at that temperature, then a THF solution of Ph_2SbCl (650 mg, 2.09 mmol) was added via cannula. The mixture was left to stir at ambient temperature overnight. The solvent was evaporated and the residue taken into CH_2Cl_2 and filtered through Celite. The filtrate was reduced and purified by flash chromatography on silica gel, eluting with 30% CH_2Cl_2 in hexanes. The second major fraction was evaporated to an oily residue, which was recrystallized from ether/pentane to yield a flaky white solid. Yield: 190 mg (22%). ^{1}H NMR (499.58 MHz, $CDCl_3$: 7.26 ppm): δ 8.69 (d, 1), 7.94 (d, 2), 7.76-7.70 (m, 2), 7.57 (d, 2), 7.47 (m, 4), 7.34 (m, 6), 7.23 (m, 1). ^{13}C NMR (125.63 MHz, $CDCl_3$: 77.16 ppm), δ: 157.41 (s),

149.89 (m), 139.82 (s), 139.72 (s), 138.43 (s), 136.90 (s), 136.84 (s), 136.39 (s), 129.06 (s), 128.81 (s), 127.38 (s), 127.34 (s), 127.26 (s), 122.39 (s), 120.74 (s).

Synthesis of 50. 2-(4-bromophenyl)pyridine (503 mg, 2.15 mmol) in 12 mL 5:1 Et_2O:THF was treated with *n*-butyllithium (0.9 mL, 2.65 M in hexanes, 2.39 mmol) dropwise at -78° C. The pale solution was stirred for 1 hr at that temperature, then the solvent was removed by cannula filtration and the product resuspended in 20 mL Et_2O. This solution was then added via cannula into a THF solution of Ph_3SbBr_2 (1.08 g, 2.11 mmol) at -78° C. The mixture was left to stir at ambient temperature overnight. The solvent was evaporated and the residue taken into CH_2Cl_2 and filtered through Celite. The filtrate was reduced and taken into ethyl acetate, precipitating a white solid which was removed by another filtration through Celite. The filtrate was reduced and purified by flash chromatography on silica gel, eluting with 15% MeOH in CH_2Cl_2. The second major fraction was evaporated to an oily residue, which was washed with ether and pentane to yield a foamy solid which was used without further purification (512 mg). This product was dissolved in 10 mL 1:1 CH_2Cl_2:MeOH in air and treated with AgOTf (313 mg, 1.22 mmol), stirring for 1 hr in the dark. The mixture was evaporated, taken into CH_2Cl_2, and filtered through Celite. The filtrate was reduced and purified by flash chromatography on silica gel, eluting with 15% MeOH in CH_2Cl_2. The first major fraction was evaporated to an oily residue, which was washed with ether and pentane to yield a foamy solid, which was used without further purification. Yield: 265 mg (19%). ^{1}H NMR (499.58 MHz, $CDCl_3$: 7.26 ppm): δ 8.74 (m, 1), 8.24 (d, 2), 7.85 (m, 4), 7.76 (m, 6), 7.70-7.62 (m, 9), 7.36 (m, 1).

Synthesis of [51]PF_6. AgOTf (150 mg, 0.58 mmol) was added to a solution of $(bpy)_2RuCl_2 \cdot 2H_2O$ (100 mg, 0.19 mmol) in 20 mL degassed acetone. The mixture was refluxed in the dark 2 h, then filtered through Celite under N_2, reduced, and redissolved in 5 mL degassed EtOH. The solution was transferred into a solution of **49** (256 mg, 0.60 mmol) and 0.5 mL NEt^iPr_2 in EtOH under N_2. The mixture was refluxed at 100° C for 18 h, then cooled to room temperature. The mixture was treated with NH_4PF_6 (~250 mg), then the solvent was evaporated and the residue extracted with CH_2Cl_2 and filtered through Celite. The filtrate was reduced and purified by flash chromatography on silica gel, eluting with 10% MeCN in CH_2Cl_2. The second major fraction was evaporated and reprecipitated with Et_2O to yield a dark red-purple solid. Yield: 144 mg (76%). ^{1}H NMR (499.58 MHz, $(CD_3)_2SO$: 2.50 ppm): δ 8.76 (d,1), 8.69 (d,1), 8.59 (d,1), 8.44 (d, 1), 8.15 (d, 1), 8.07 (t, 1), 7.97 (d, 1), 7.93 (m, 2), 7.85 (d, 1), 7.80 (d, 1), 7.75 (t, 1), 7.69 (m, 2), 7.54 (t, 1), 7.49 (d, 1), 7.41 (t, 1), 7.37 (m, 2), 7.31 (m, 2), 7.24 (m, 4), 7.18 (d, 2) 7.13 (d, 2), 7.06 (t, 2), 7.00 (d, 1), 6.45 (s, 1). ^{13}C NMR (125.63 MHz, $(CD_3)_2SO$: 39.52 ppm), δ: 193.91 (s), 166.58 (s), 157.28 (s), 156.22 (s), 156.10 (s), 154.58 (s), 153.34 (br), 149.81 (s), 149.57 (s), 148.79 (s), 148.57 (br), 145.74 (s), 142.48 (s), 138.80 (s), 138.62 (s), 138.36 (s), 136.53 (br), 135.84 (br), 135.61 (s), 135.55 (s), 135.20 (br), 133.87 (br), 128.66 (s), 128.43 (s), 128.30 (s), 128.13 (s), 127.42 (s), 126.43 (s), 124.17 (br), 123.84 (br), 123.52 (br), 123.16 (br), 123.07 (s), 122.86 (s), 104.53 (s). ^{19}F NMR (469.99 MHz $CDCl_3$, $BF_3 \cdot Et_2O$: -153.00 ppm), δ: -70.16 ppm (d, $J_{P,F}$ = 710 Hz). Elemental Analysis Calculated for $C_{43}H_{33}N_5F_6PRuSb$: C, 52.30; N, 7.09; H, 3.37. Found: C, 52.55; N, 6.88; H, 3.63.

Synthesis of [52](PF$_6$)$_2$. AgOTf (146 mg, 0.57 mmol) was added to a solution of (bpy)$_2$RuCl$_2$·2H$_2$O (104 mg, 0.20 mmol) in 20 mL degassed acetone. The mixture was refluxed in the dark 2 h, then filtered through Celite under N_2, reduced, and redissolved in 5 mL degassed EtOH. The solution was transferred into a solution of **50** (159 mg, 0.24 mmol) in 5 mL EtOH under N_2. The mixture was refluxed at 100° C for 18 h, then cooled to room temperature. The mixture was treated with NH_4PF_6 (~250 mg), then the solvent was evaporated and the residue extracted with CH_2Cl_2 and filtered through Celite. The filtrate was reduced and purified by flash chromatography on silica gel, eluting with 10% MeCN in CH_2Cl_2. The second major fraction was evaporated and reprecipitated with Et_2O to yield a dark red-purple solid. Yield: 42 mg (17%). ^{1}H NMR (499.58 MHz, $(CD_3)_2SO$: 2.50 ppm): δ 8.79 (d, 1), 8.73 (d, 1), 8.61 (d, 1), 8.47 (d, 1), 8.32 (d, 1), 8.17 (d, 1), 8.12 (t, 1), 7.95 (m, 3), 7.84 (m, 2), 7.75 (t, 1), 7.71 (d, 1), 7.68 (m, 3), 7.60 (m, 8), 7.46 (m, 7), 7.42 (m, 2), 7.32 (d, 1), 7.18 (t, 1), 7.13 (t, 1), 6.50 (s, 1). ^{13}C NMR (125.61 MHz, $(CD_3)_2SO$: 39.52 ppm), δ: 196.95 (s), 165.32 (s), 157.25 (s), 156.19 (s), 156.15 (s), 154.52 (s), 153.24 (s), 150.28 (s), 149.91 (s), 149.58 (s), 149.27 (s), 148.80 (s), 139.90 (s), 136.94 (s), 136.28 (s), 135.70 (s), 134.97 (s), 134.58 (s), 134.52 (s), 132.27 (s), 130.26 (s), 129.93 (s), 128.83 (s), 128.02 (s), 127.52 (s), 126.77 (s), 126.70 (s), 125.59 (s), 125.44 (s), 124.15 (s), 124.05 (s), 123.67 (s), 123.35 (s), 123.19 (s), 120.26 (s). ^{19}F NMR (469.99 MHz $CDCl_3$, BF_3·Et_2O: -153.00 ppm), δ: -70.16 ppm (d, $J_{P,F}$ = 710 Hz). Elemental Analysis Calculated for $C_{49}H_{38}N_5F_{12}P_2RuSb$: C, 48.65; N, 5.79; H, 3.17. Found: C, 48.44; N, 5.59; H, 3.33.

NMR Spectroscopy. Two-dimensional ^{1}H, ^{1}H COSY NMR was taken on complex [**51**]PF_6 in $(CD_3)_2SO$ using a Varian Unity Inova 500 FT NMR (499.58 MHz for ^{1}H). The resulting contour plot is shown below in Figure 99. For complexes [**51**]PF_6 and [**52**]$(PF_6)_2$, cation:anion ratios were established based on the ^{1}H and ^{19}F NMR spectra shown in Figures 100-103, using 2', 3', 4', 5', 6'-pentafluoroacetophenone as an internal standard.

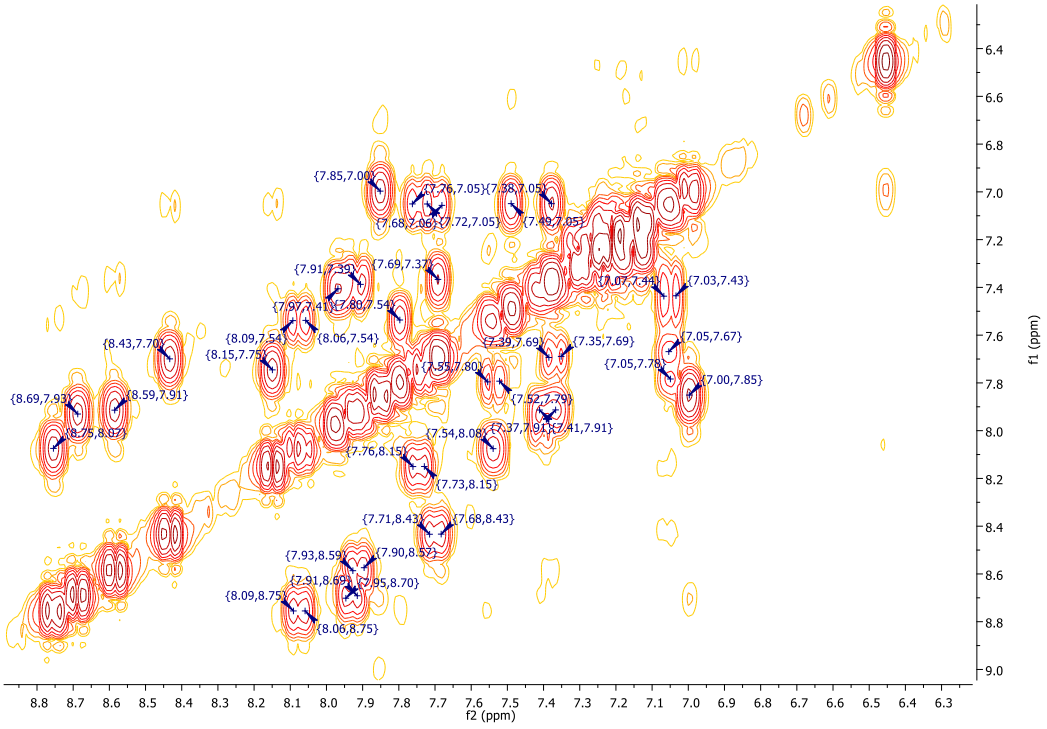

Figure 99. Contour plot of the 2D COSY NMR spectrum of [**51**]PF_6.

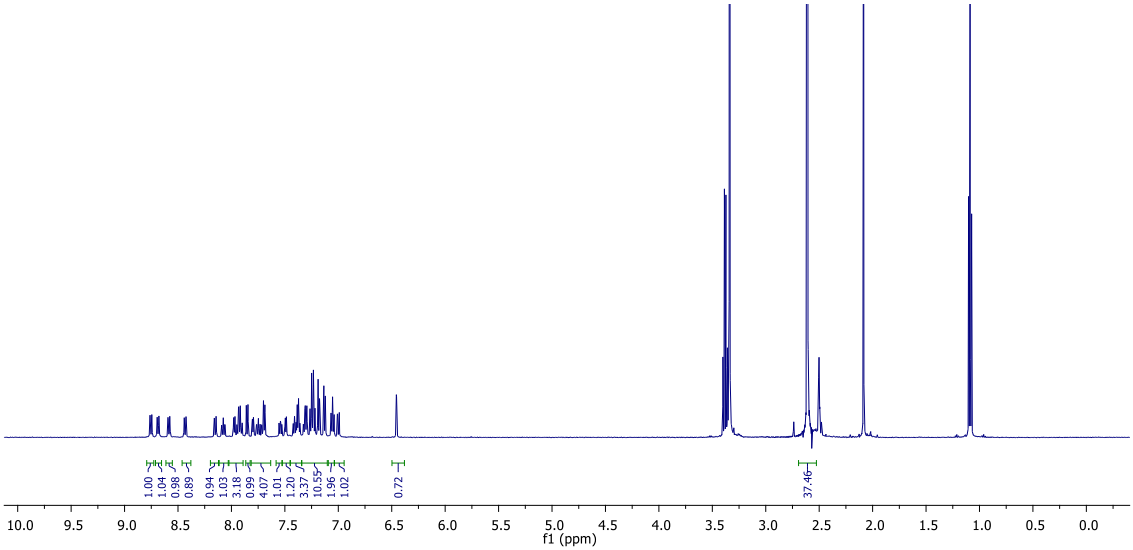

Figure 100. ^{1}H NMR spectrum of [**51**]PF_6 in $(CD_3)_2SO$ with 2', 3', 4', 5', 6'-pentafluoroacetophenone as an internal standard.

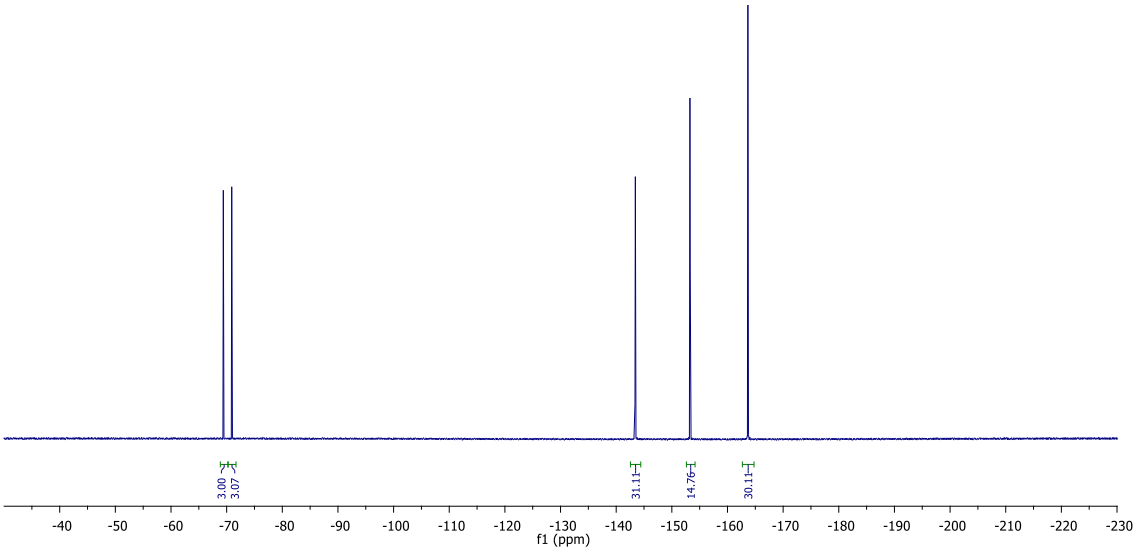

Figure 101. ^{19}F NMR spectrum of [**51**]PF_6 in $(CD_3)_2SO$ with 2', 3', 4', 5', 6'-pentafluoroacetophenone as an internal standard.

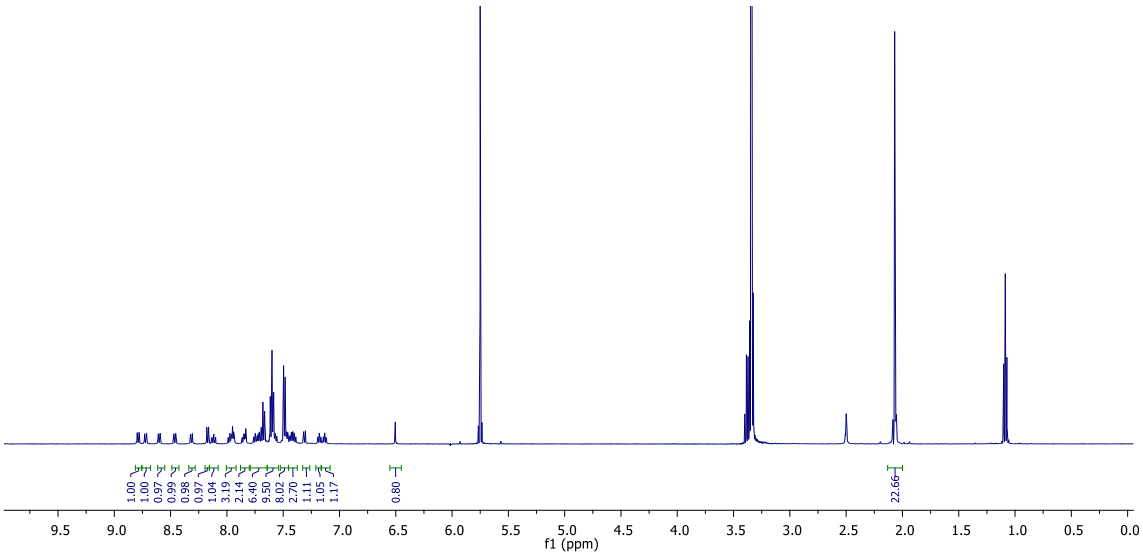

Figure 102. ^{1}H NMR spectrum of [**52**]$(PF_6)_2$ in $(CD_3)_2SO$ with 2', 3', 4', 5', 6'-pentafluoroacetophenone as an internal standard.

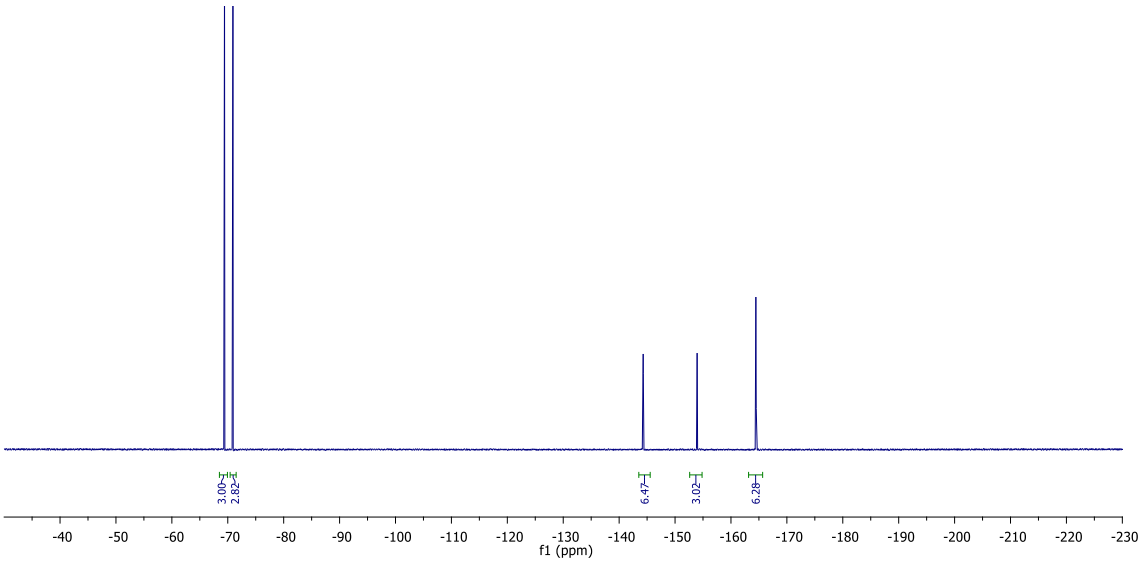

Figure 103. ^{19}F NMR spectrum of [**52**]$(PF_6)_2$ in $(CD_3)_2SO$ with 2', 3', 4', 5', 6'-pentafluoroacetophenone as an internal standard.

Absorption Spectroscopy. Absorption spectra of [**51**]PF_6 and [**52**]$(PF_6)_2$ were determined in acetonitrile against a solvent reference. The molar absorption coefficients at λ_{max} were determined according to Beer-Lambert calibration curves, shown below in Figures 104-105.

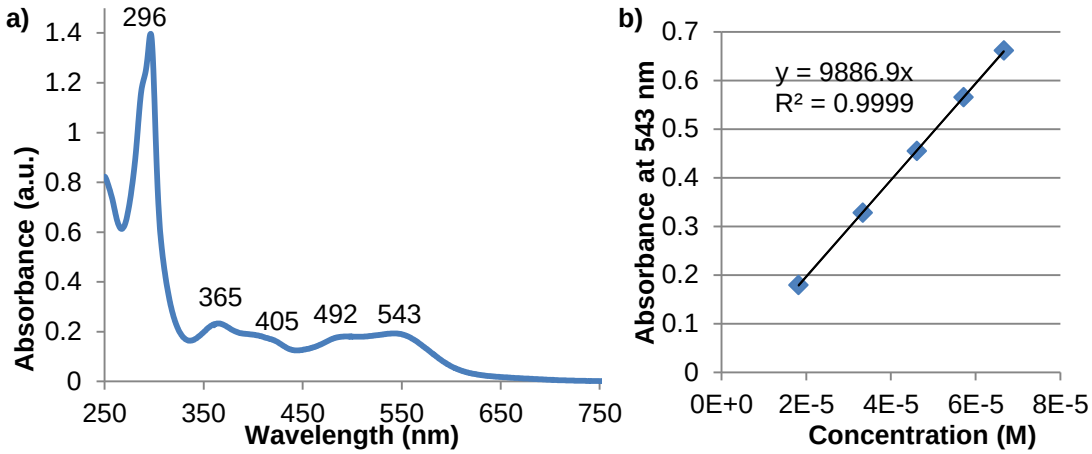

Figure 104. a) Absorption spectrum of [**51**]PF_6 (2.0×10^{-5} M) in MeCN. b) Beer-Lambert calibration plot.

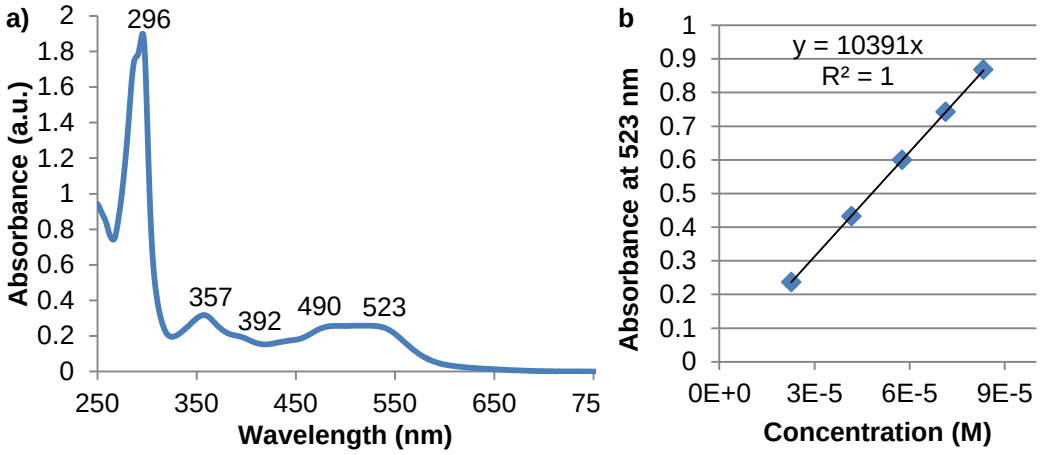

Figure 105. a) Absorption spectrum of [**52**]$(PF_6)_2$ (2.5×10^{-5} M) in MeCN. b) Beer-Lambert calibration plot.

6. ANTIMONY(III) AND ANTIMONY(V) INCORPORATION INTO HETEROCYCLIC FRAMEWORKS FOR DIRECT CONTROL OF COLOR AND LUMINESCENCE

6.1 Introduction

Thus far, we have discussed the properties of antimony- and phosphorus-based sensors with the general structure of a main group element moiety tethered to a pendant fluorophore or chromophore. For these molecules to behave as sensors, the photophysical properties of the pendant reporter group must be modulated by the analyte recognition event at the main group element via a remote effect. We have investigated a number of possible mechanisms for such an effect, as detailed above, including changes in excited state conformations (section 2), spirocyclization with the fluorescent framework (section 3), PeT effects (section 4), and electronic influence on transition metal centers (section 5). In most of these mechanisms, the influence of the main group element on the photophysical properties of the compound is indirect, and the main group moiety is essentially extrinsic to the part of the molecule that imparts the color or fluorescence. As an alternative to these pendant-chromophore designs, we questioned whether the main group element could instead be incorporated into the very framework of an organic dye structure in order to achieve a direct influence over the photophysical properties. We reasoned that this strategy could allow for the rational design of chemical sensors in which the analyte recognition at the main group center directly affects the structure and thus photophysical properties of the chromophore or fluorophore.

In organic dye molecules, the absorption and emission properties are determined primarily by the extent and structure of π-conjugation in the molecule. The transition between the π HOMO and π* LUMO is responsible for the lowest-energy absorption as well as emission bands. As discussed in the Introduction, the anion-binding abilities of antimony(V) Lewis acids derive from low-energy σ* orbitals that accept an electron pair from the anion to form an adduct. For incorporation of an antimony(V) center into a conjugated framework to create a viable sensor for anions, therefore, the antimony-based σ* orbital(s) must interact directly with the π* LUMO of the heterocycle (Figure 106). If this is the case, then anion binding at the antimony center, by engaging the σ* orbital, will alter the extent of π conjugation in the LUMO and induce a change in absorption and/or emission wavelengths.

Numerous examples of π-conjugated molecules and materials incorporating phospholes[5, 220-221, 285-286] and phosphole oxides[287-291] have been reported recently that support the feasibility of this approach with antimony. In one relevant example, Baumgartner and coworkers reported the incorporation of phosphorus into a series of dibenzothienophospholes **53-[56]**$^+$ (Figure 107).[286] The absorption and emission

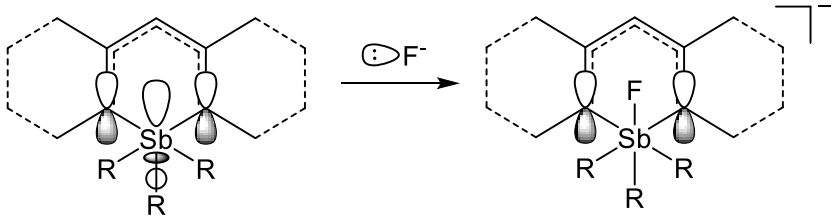

Figure 106. Potential interaction of Sb(V)-based σ* orbital with π conjugation of a heterocyclic system, with the change induced upon anion binding at Sb.

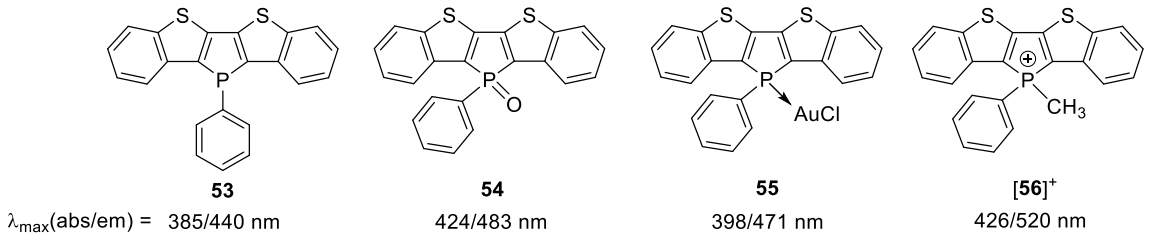

Figure 107. A series of dibenzothienophospholes with changes in absorption and emission colors with chemical modifications at phosphorus.[286]

bands of these derivatives were substantially redshifted from those of the corresponding polythiophene materials lacking the phosphorus group. This effect is attributed not only to the increased rigidification of the bridged dithiophene structure, but also to extension of the π-conjugation over the phosphole moiety through low-lying phosphorus-based σ* orbitals. Importantly, simple modifications such as oxidation or metal coordination at the phosphorus center have significant effects on the photophysical and electronic properties of these polythiophene materials.

Similar incorporation of heavier main group elements into π-conjugated materials, however, has been limited. To our knowledge, only one example of the analogous stibole class of compounds has been reported, by Ohshita and coworkers in 2012 (Compounds **57**-**59**, Figure 108).[292] They also observed significantly redshifted absorption bands compared to the carbon-bridged analogs, with absorbance maxima between 337 and 374 nm and fluorescence bands between 420 and 443 nm. To explain these photophysical effects, they again invoke lowered LUMOs due to the interaction of

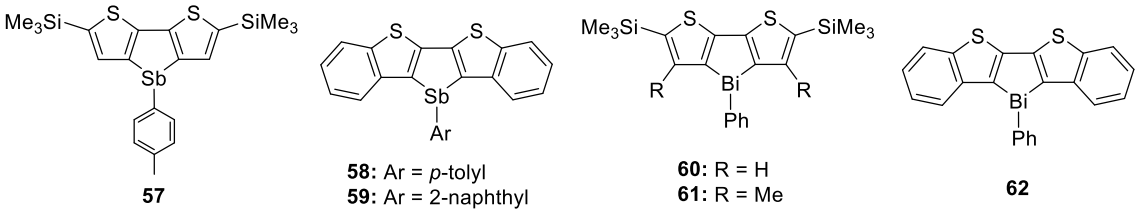

Figure 108. Dithienostiboles and -bismoles reported by Ohshita and coworkers.[292-293]

low-lying σ* orbitals with the π* orbitals of the dithiophene framework, which they support computationally. In this case, the fluorescence quantum yields observed in these materials were very low, presumably due to the heavy atom effect of antimony. No structural characterization of the dithienostibole compounds was obtained, and oxidation of the antimony center to antimony(V) does not appear to have been attempted. The same research group also reported a similar series of dithienobismoles (Compounds **60-62,** Figure 108), which were structurally characterized.[293] These compounds show similarly redshifted absorption and emission bands, but also display intriguing phosphorescence at >600 nm, which can even be observed in the solid state at room temperature in air. Other than these isolated reports, however, incorporation of antimony or bismuth into π-conjugated materials has not been well explored.

Recent research, however, has expanded the synthetic chemistry of heavy main group element incorporation into heterocycles, especially with tellurium.[7, 294-297] Rivard and coworkers recently reported syntheses for a series of substituted tellurophenes and benzotellurophenes, some of which show interesting luminescence phenomena (Figure 109).[298-300] The bis-Bpin-substituted tellurophene **63** (Bpin = pinacolatoboryl) was first

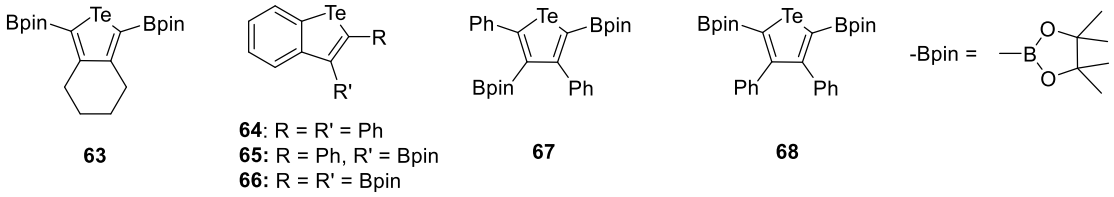

Figure 109. Luminescent tellurophenes reported by Rivard and coworkers.[298-300]

reported to display green aggregation-induced emission and solid-state phosphorescence.[298] Later, benzotellurophenes **64-66** and other Bpin-substituted tellurophenes **67** and **68** were reported to exhibit similar phosphorescence behavior, with colors that were tunable based on the number and position of Bpin groups.[300] Computational studies revealed the presence of the bulky Bpin groups to be essential to the solid-state luminescence properties, while spin-orbit coupling from the heavy tellurium atom was invoked to explain the phosphorescent quality of the emission.[301] These studies showed that a heavy main group element can be an integral part of a luminescent heterocyclic system and also demonstrated a viable synthetic pathway for the creation of such heterocycles.

In this section, we describe the synthesis of a series of substituted benzostiboles and dithienostiboles incorporating antimony centers in both the +III and +V oxidation states. The results provide a proof of concept for our hypothesis that antimony incorporation into π conjugated structures can provide direct control over the photophysical properties of the molecule, which can be harnessed for the design of anion sensors as well as color-tunable materials.

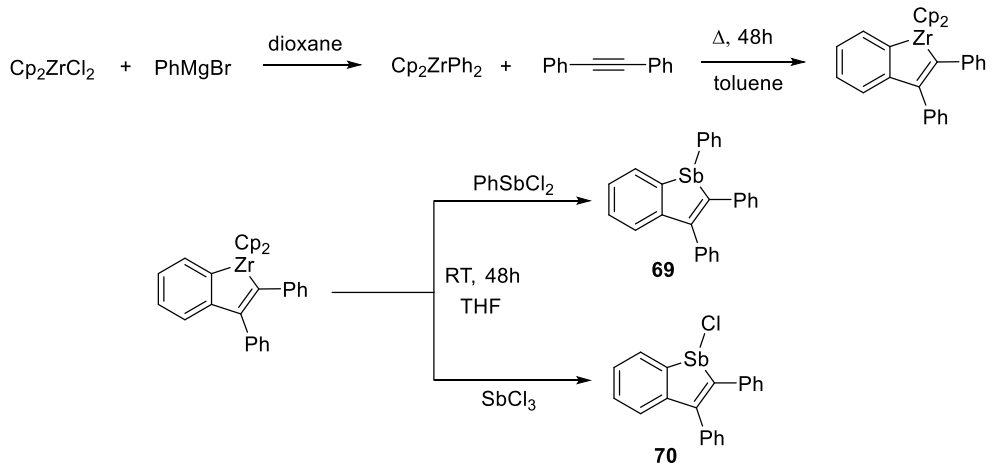

Figure 110. Synthesis of substituted benzostiboles by a Zr-transfer method.

6.2 Synthesis and characterization of benzostiboles with tunable color based on Sb(III) substitution

Inspired by the work of Rivard and coworkers on benzotellurophenes,[300] we first targeted the synthesis of the substituted benzostiboles **69** and **70** (Figure 110). Because of the third substituent at the Sb(III) moiety of a stibole compared to a Te(II) tellurophene, the antimony-containing heterocycles offer an additional handle for tuning the photophysical properties of these molecules, which we sought to exploit. The synthesis of benzostiboles **69** and **70** was straightforward utilizing the Fagan-Nugent zirconium metallacycle-transfer method as reported by Rivard.[296, 300, 302-303] The desired heterocyclic framework is built around a zirconocene fragment from the Cp_2ZrPh_2 reagent and a substituted alkyne, in this case diphenylacetylene, then transferred directly onto the main group metal via halide exchange with $PhSbCl_2$ or $SbCl_3$. Both benzostibole products were bench stable and could be purified by silica gel

chromatography, even in the case of **70** where the remaining Sb-Cl bond might be expected to be sensitive to hydrolysis.

The structures of benzostiboles **69** and **70** in the solid state were confirmed by single-crystal X-ray diffraction analysis (Figure 111). In each case, the Sb atom sits directly in the plane of the benzostibole unit, and the C-Sb-C angle formed by the stibole ring is quite acute at 81-82°, as expected for Sb in a five-membered ring.[26, 49] Each Sb center is highly pyramidalized, placing the third substituent (Ph or Cl) at almost 90° from the plane of the heterocycle. Consequently, in the crystal structures of **69** and **70**, two enantiomers of each compound were observed in a racemic mixture, with chirality depending upon the direction in which the third substituent at Sb extends from the benzostibole plane (Figure 112). The structural parameters of **69** and **70** are very similar

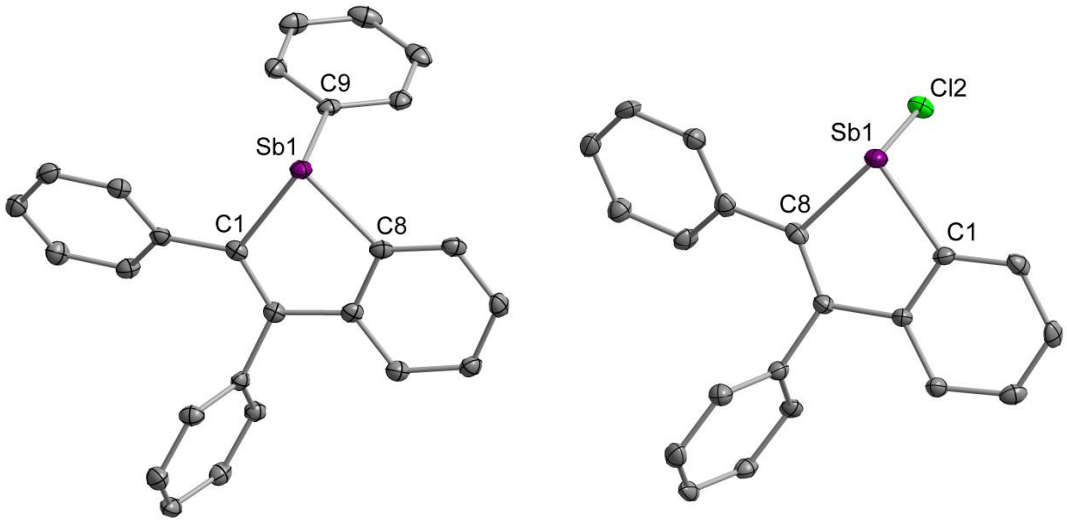

Figure 111. Solid-state structures of **69** and **70.** Hydrogen atoms omitted for clarity. Selected bond angles (°) for **69**: ∠C1-Sb1-C8 81.18(9), ∠C1-Sb1-C9 98.19(9), ∠C8-Sb1-C9 96.47(9). Selected bond angles (°) for **70**: ∠C1-Sb1-C8 81.67(20), ∠C1-Sb1-Cl2 95.78(15), ∠C8-Sb1-Cl2 95.86(15).

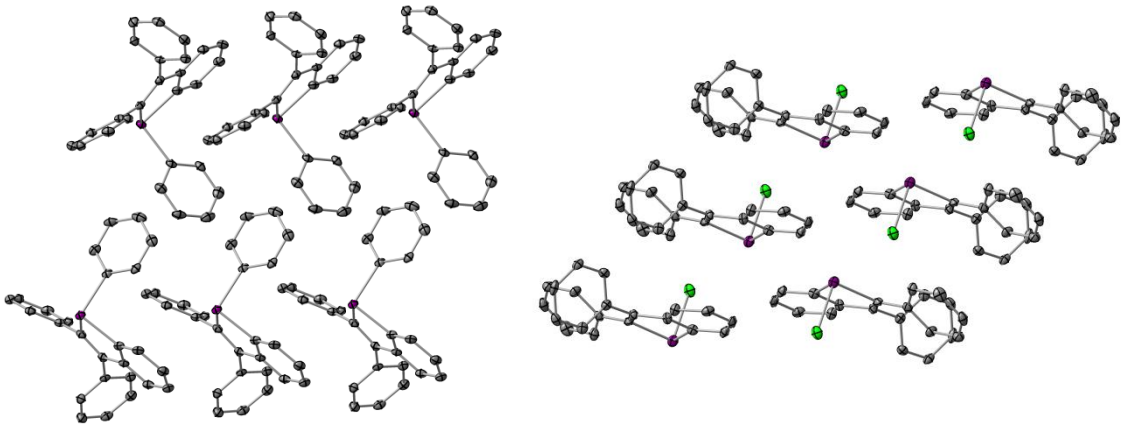

Figure 112. Extended solid-state structures of **69** and **70** showing packing effects and enantiomers. Hydrogen atoms omitted for clarity.

to each other, although the pyramidalization at Sb is slightly more pronounced in **70**, probably for steric reasons due to the smaller size of the chloride group. The molecules of **70** also appear to have closer π stacking interactions in the crystal than those of **69**, also probably for steric reasons. Thus, we can directly compare the properties of **69** and **70** in terms of the electronic effects of Ph vs. Cl as a substituent at Sb.

Because of the orthogonality of the third substituent relative to the benzostibole plane in **69** and **70**, we expect the σ* orbital of the Sb-Ph or Sb-Cl bond to extend directly into the π system of that heterocycle and potentially mix with the π* LUMO. If so, then increasing the electron-withdrawing nature of that substituent should lower the energy of the σ* orbital and increase its contribution to the π conjugation of the LUMO. Indeed, while crystals of **69** appear pale to colorless, those of the chloride-substituted **70** appear a bright yellow. The UV-vis absorption spectra of the two compounds in $CHCl_3$

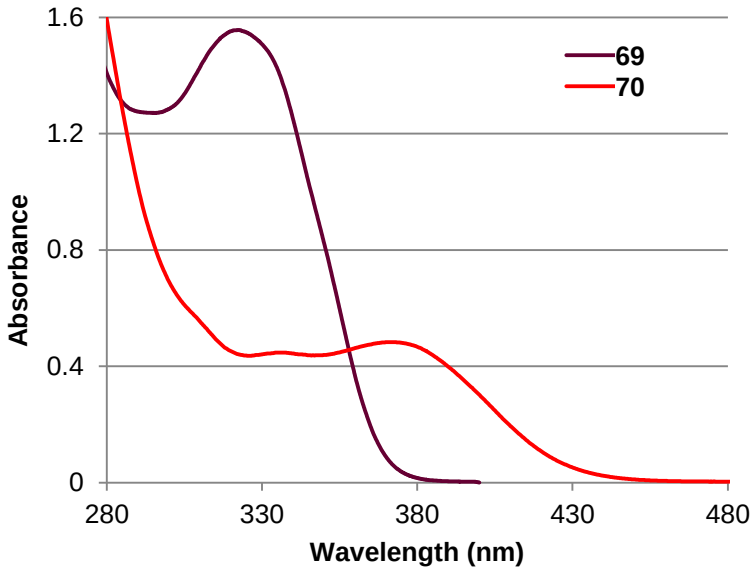

Figure 113. UV-vis absorption spectra of 1.4×10^{-4} M solutions of **69** and **70** in $CHCl_3$.

solution are compared in Figure 113. Although compound **70** has less intense absorption bands than **69** in the near UV, the lowest-energy absorption band is shifted from λ_{max} = 322 nm for **69** to λ_{max} = 372 nm for **70**, with a broad tail into the blue region of the visible spectrum. Clearly, the substitution of the antimony center incorporated into this heterocycle has a marked influence on the photophysical properties.

In order to confirm our hypothesis regarding the role of the Sb-based σ* orbital in the π conjugated benzostibole heterocycles, DFT-optimized structures of **69** and **70** were computed and TD-DFT calculations were performed to analyze the nature of the electronic transitions occurring in these molecules. The calculated ground-state HOMO and LUMO for **69** and **70** are shown in Figure 114. In both cases, the HOMO of the molecule corresponds to the conjugated π system spread across the benzostibole,

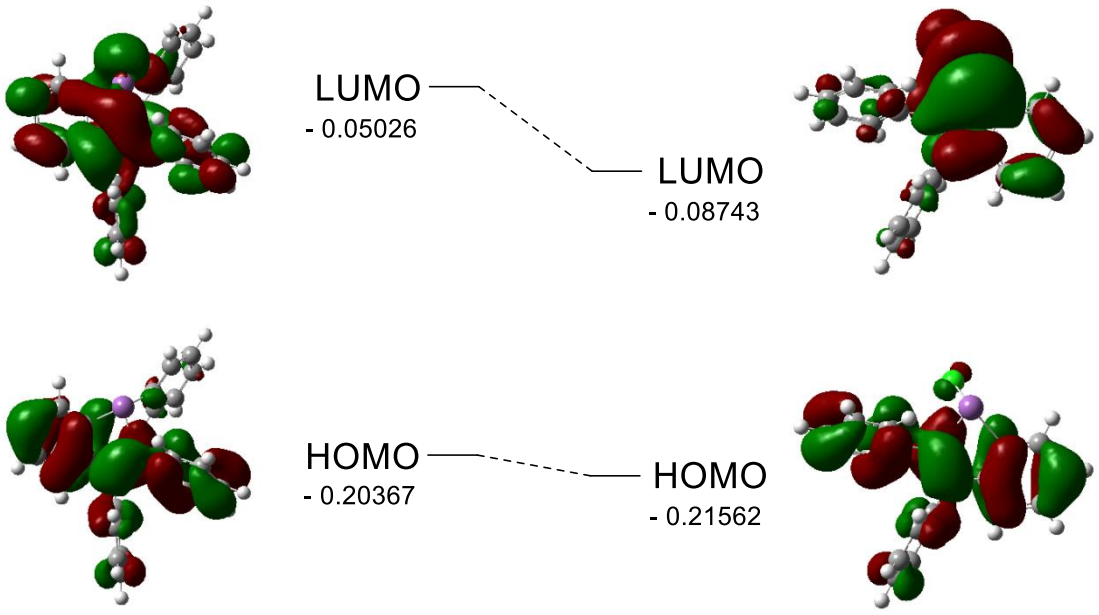

Figure 114. Energies and contour plots of computed frontier molecular orbitals of **69** (left) and **70** (right). Computations carried out using the B3LYP functional with the mixed basis set: Sb, aug-cc-pVTZ-PP; Cl, ECP10MWB; C/H, 6-31g(d). Energies are in units of hartrees.

without, however, any contribution from Sb-based orbitals. The LUMO corresponds to the benzostibole π* system, but in this orbital, a clear contribution from the Sb-R σ* orbital can be seen. This contribution is much more pronounced in the LUMO of **70**, as expected due to the higher electronegativity of Cl. The energies calculated for the frontier molecular orbitals of **69** and **70** also show that the LUMO in **70** is significantly stabilized by this change, thus decreasing the HOMO-LUMO gap in this molecule and accounting for the red-shifted absorbance band observed in the UV-vis spectrum of **70**. TD-DFT calculations of the electronic transitions available to these molecules correspond relatively well to the observed absorption spectra and corroborate the 50-nm shift in the maximum absorption band of **70** compared to **69** (Table 9). The excited state

calculations also confirm that the lowest-energy transition in both molecules derives primarily from the HOMO-LUMO transition, albeit with a lower oscillator strength in the case of **70**, which is consistent with the lower molar absorptivity observed in this compound.

The dramatic change in the absorption properties of **70** compared to **69** shows that substitutions at the antimony center can provide a handle for tuning the photophysical properties of Sb-incorporating conjugated systems. The computational results support our hypothesis that the interaction of Sb-based σ* orbitals with the π system is responsible for the influence of the incorporated antimony atom on the photophysical properties in these heterocycles.

Table 9. Results of TD-DFT calculations of the first three singlet excited states of **69** and **70.** Computations carried out at the ground-state optimized geometries using the MPW1PW91 functional with the mixed basis set: Sb, aug-cc-pVTZ-PP; Cl, ECP10MWB; C/H, 6-31g(d).

Compound	State	Energy	Transition wavelength	Oscillator strength *f*	Orbital character
69	S_1	3.75 eV	331 nm	0.2089	HOMO – LUMO
	S_2	4.17 eV	297 nm	0.0478	HOMO-1 – LUMO HOMO – LUMO+1
	S_3	4.25 eV	292 nm	0.0595	HOMO-1 – LUMO HOMO – LUMO+1
70	S_1	2.97 eV	418 nm	0.0585	HOMO – LUMO
	S_2	3.63 eV	341 nm	0.0277	HOMO-1 – LUMO
	S_3	3.97 eV	313 nm	0.0102	HOMO-2 – LUMO

6.3 Lewis acidic Sb(V) benzostiboles with a “turn-off” colorimetric response to fluoride

We next explored the oxidation of the benzostiboles to obtain Lewis acidic Sb(V) derivatives that could be used as anion sensors. The phenyl-substituted benzostibole **69** could be oxidized cleanly with *ortho*-benzoquinone reagents to yield the Sb(V) catecholates **71** and **72**, shown in Figure 115, which were fully characterized. These compounds are air- and water- stable and soluble in most organic solvents. Despite attempts with a number of different oxidants, however, we were unable to isolate oxidized products of the chloride-substituted benzostibole **70**, obtaining instead decomposition products with apparent cleavage of the stibole ring.

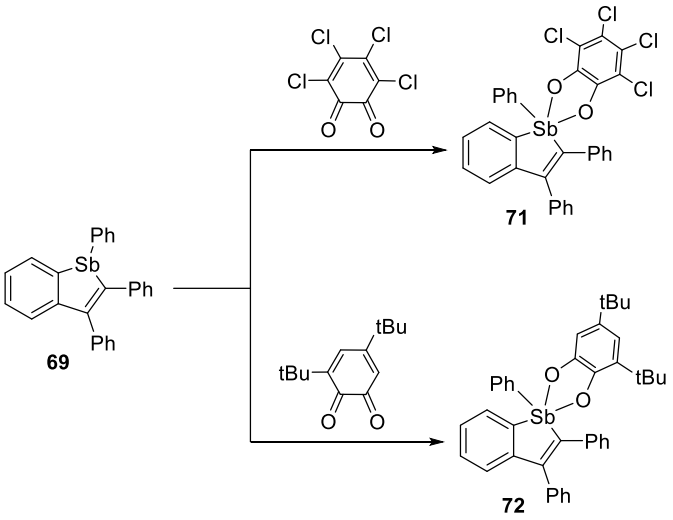

Figure 115. Synthesis of Sb(V) benzostibole catecholates.

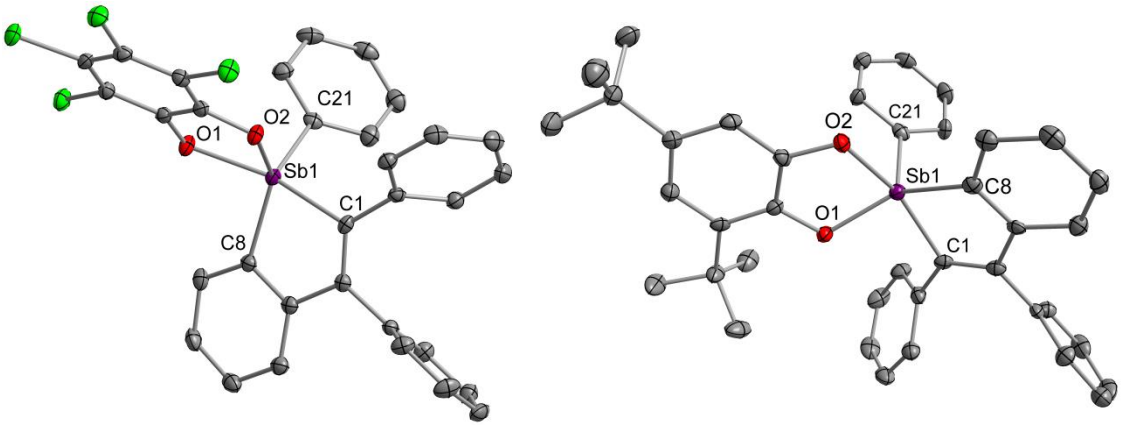

Figure 116. Solid-state structures of one enantiomer of **71** and **72**. Solvate molecules and hydrogen atoms omitted for clarity. Selected bond angles (°) for **71**: ∠C1-Sb1-C8 83.63(8), ∠O1-Sb1-O2 79.31(7), ∠C1-Sb1-O1 160.32(8), ∠C8-Sb1-O2 130.68(8). Selected bond angles (°) for **72**: ∠C1-Sb1-C8 82.87(17), ∠O1-Sb1-O2 81.07(12), ∠C1-Sb1-O2 158.25(16), ∠C8-Sb1-O1 141.97(15).

The solid-state structures of **71** and **72** were investigated by single-crystal X-ray diffraction analysis (Figure 116). Again, two enantiomers of each compound could be seen in the crystals, depending on the orientation of the phenyl and catecholate groups on either side of the benzostibole plane. The geometry at Sb in each compound is highly distorted away from the expected trigonal bipyramidal toward a more square pyramidal structure, as illustrated by the calculated τ values of 0.49 for **71** and 0.27 for **72** based on the bond angles around Sb.[140] This distorted geometry gives rise to a prominent steric opening at each of these Sb(V) centers, which could serve as an open site for the binding of a Lewis base.

Treating **69** with a larger excess of *ortho*-chloranil, crystals of an unexpected product **73** were obtained, the structure of which is shown in Figure 117. In this compound, after oxidization of the Sb center with one equivalent of chloranil, a second

equivalent oxidizes the stibole moiety, cleaving the Sb-C1 bond and inserting the catecholate moiety into the ring, forming a curious 9-membered ring structure. The isolation of this compound shows that the Sb-C bonds of the benzostibole moiety may be vulnerable to decomposition with excess oxidant.

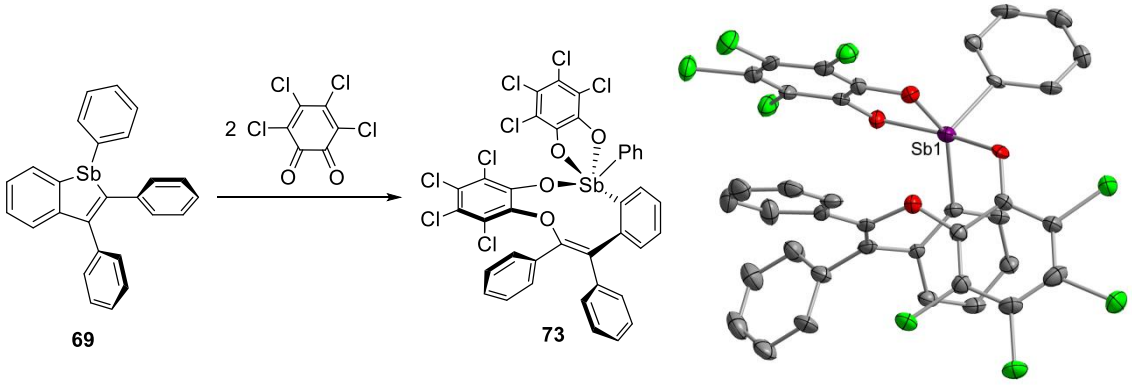

Figure 117. Synthesis and solid-state structure of doubly-oxidized product **73**. Hydrogen atoms in the crystal structure omitted for clarity.

Finally, benzostibole **69** could also be oxidized with one equivalent of methyl triflate to produce the cationic stibole triflate [**74**]OTf (Figure 118). Although we expected [**74**]OTf to behave as a stronger Lewis acid than **71** and **72** due to the positive charge at the Sb center, this compound is still bench stable. The solid-state structure of [**74**]OTf shows that the four carbon substituents surround Sb in a roughly tetrahedral geometry; however, the five-membered stibole ring constrains one angle to less than 85°, leaving one side of the Sb atom relatively exposed. At this open site, the triflate counteranion is seen to coordinate with an Sb-O contact distance of 2.67Å. It is unclear

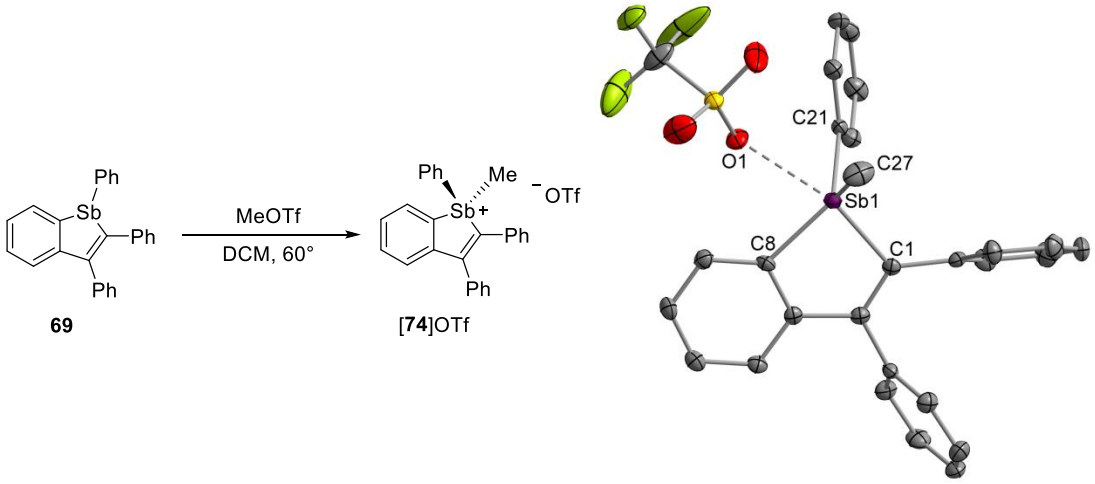

Figure 118. Synthesis and solid-state structure of [**74**]OTf. Hydrogen atoms in the crystal structure omitted for clarity. Selected bond lengths (Å) and angles (°):Sb1-O1 2.67, ∠C1-Sb1-C8 84.31(13), ∠C1-Sb1-C27 110.59(16), ∠C8-Sb1-C21 116.59(15), ∠C21-Sb1-C27 109.20(19).

whether this triflate coordination is operative in solution as well; however, the presence of this relatively short Sb-O interaction hints at the strong Lewis acidity of the Sb(V) center of [**74**]OTf.

The UV-vis absorption spectra of the oxidized benzostiboles **71**, **72**, and [**74**]OTf in $CHCl_3$ are shown in Figure 119. The catecholate derivatives **71** and **72** both appear bright yellow in both the solid and solution state, with broad absorbance bands at 347 nm and 340 nm, respectively. We initially expected to see a significant difference in color between **71** and **72** because of the difference in the electron-withdrawing nature of the tetrachlorocatecholate ligand versus the 3,5-di-*tert*-butylcatecholate; instead, the absorption profiles of the two are almost identical. From this observation, it appears that the substitution of the catecholate ligands has little effect on the π conjugation of the stibole system. However, the fact that these derivatives display absorbance bands

significantly redshifted from those of the parent Sb(III) compound **69** shows that the oxidation of the Sb center still does affect the photophysical properties of the system. Surprisingly, the stibole triflate [**74**]OTf is colorless. The UV-vis spectrum of [**74**]OTf shows a similar absorption pattern to **69**, although the low-energy absorbance band is redshifted slightly, to λ_{max} = 327 nm. It is possible that the distorted tetrahedral arrangement of substituents around Sb in [**74**]OTf precludes a strong involvement of the σ* orbital in the π system, or that ion-pairing with the triflate counteranion in solution suppresses the σ* orbital and shifts the absorption band to higher energy.

In order to understand the origin of the observed absorbance, DFT calculations were performed on **71**, **72**, and [**74**]OTf. The results are summarized in Table 10 below, and representations of the frontier molecular orbitals of **71** and **72** are shown in Figure 120. In the stibole catecholate derivatives **71** and **72**, the π* LUMO does indeed show a significant contribution from the Sb-based σ* orbitals; however, the HOMO does not

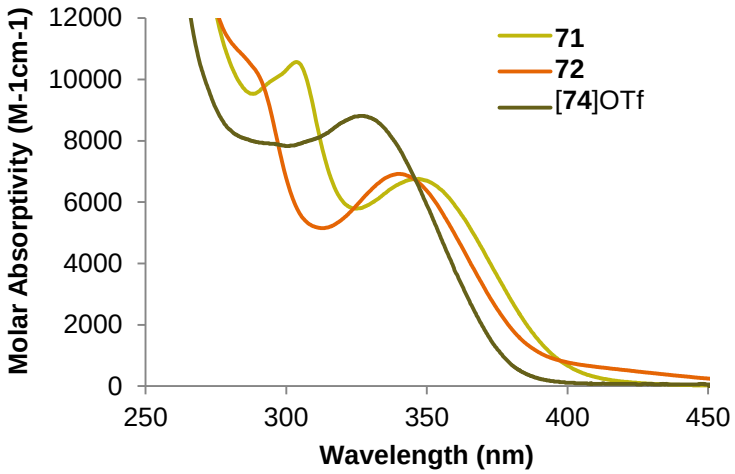

Figure 119. UV-vis absorption spectra of **71**, **72**, and [**74**]OTf in $CHCl_3$.

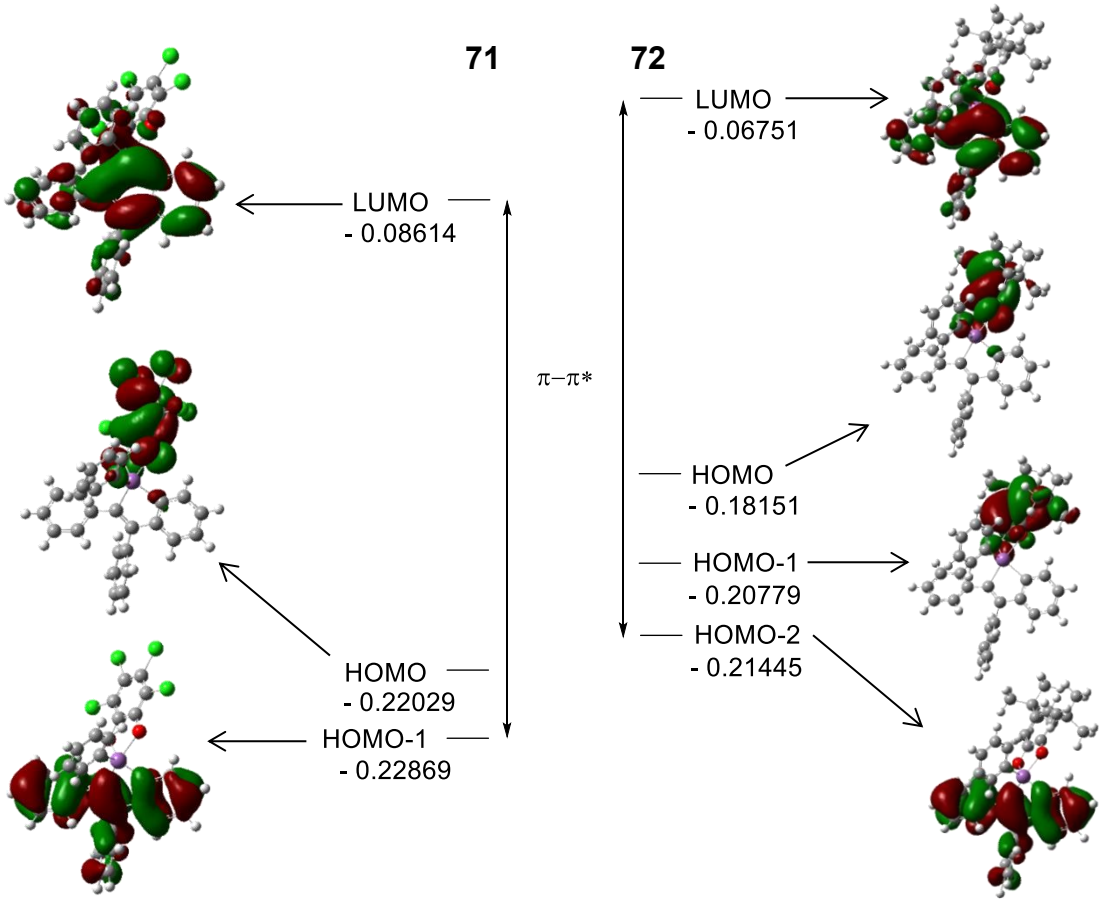

Figure 120. Energy diagram and contour plots of the computed frontier molecular orbitals of **71** and **72**. Computations carried out using the B3LYP functional with the mixed basis set: Sb, aug-cc-pVTZ-PP; Cl, ECP10MWB; C/H/O, 6-31g(d). Energies are reported in units of hartrees.

consist of the corresponding π orbital of the benzostibole, but rather is based on the catecholate moiety itself. The benzostibole π orbital is instead found in the HOMO-1 for **71** and the HOMO-2 for **72**. This being the case, the HOMO-LUMO energy gap in **72** is much smaller than that in **72** due to the electron-donating character of the *tert*-butyl groups on the catecholate ligand. However, TD-DFT calculations confirm that the HOMO-LUMO transition is not responsible for the major absorbance bands observed,

but rather the π-π* transition, which is the lowest-energy transition predicted to have significant oscillator strength. The difference in energy between the π-π* transitions of **71** and **72**, accordingly, is only 0.13 eV, consistent with the small difference in the major absorption wavelengths observed between **71** and **72**. Surprisingly, the TD-DFT calculations indicate that the π-π* transition of compound [**74**]OTf, which in this case is also the HOMO-LUMO transition, ought to occur at a lower energy than those of **71** and **72**. However, this is not observed in the UV-vis spectrum of [**74**]OTf, which instead shows a blueshifted absorbance band. It is likely that close coordination of the triflate counteranion in solution perturbs the photophysical properties of [**74**]OTf, moving the HOMO-LUMO transition to higher energy.

Table 10. Results of TD-DFT calculations of the first three singlet excited states of **71**, **72**, and [**74**]OTf. Computations carried out at the ground-state optimized geometries using the MPW1PW91 functional with the mixed basis set: Sb, aug-cc-pVTZ-PP; Cl, ECP10MWB; C/H/O, 6-31g(d).

Compound	State	Energy	Transition wavelength	Oscillator strength *f*	Orbital character
71	S_1	3.13 eV	396 nm	0.0039	HOMO – LUMO
	S_2	3.41 eV	363 nm	0.1297	HOMO-1 – LUMO
	S_3	3.73 eV	332 nm	0.0013	HOMO – LUMO+1
72	S_1	2.64 eV	469 nm	0.0068	HOMO – LUMO
	S_2	3.48 eV	357 nm	0.0016	HOMO-1 – LUMO
	S_3	3.54 eV	350 nm	0.1535	HOMO-2 – LUMO
[**74**]OTf	S_1	3.31 eV	375 nm	0.1654	HOMO – LUMO
	S_2	3.83 eV	323 nm	0.0342	HOMO-1 – LUMO
	S_3	3.88 eV	320 nm	0.0457	HOMO-2 – LUMO

With this data in hand, we next investigated the responses of Lewis acidic benzostiboles **71**, **72**, and [**74**]OTf to fluoride. Addition of TBAF to solutions of **71** or **72** in $CDCl_3$ results in an immediate color change from yellow to colorless. In the ^{19}F NMR spectrum of each compound, two new singlet peaks of approximately equal integration appear, at -96.39 and -100.62 ppm for **71** and at -90.60 and -97.74 ppm for **72**. ESI mass spectrometry of the final product of **71** with fluoride confirms the presence of the expected fluoride adduct [**71**-F]$^-$, with a molecular ion mass of 716.88 *m/z* in the negative scan. We interpret the two peaks observed in the ^{19}F NMR spectrum as two possible isomers of the fluoride adduct, with fluoride coordinated *trans* to either the phenyl group or the catecholate group (Figure 121). With addition of fluoride to [**74**]OTf, formation of the adduct is also evident by ^{19}F NMR, in which a new peak at -98.54 ppm appears with an integration of 1 compared to the 3 fluorides present in the triflate counteranion. However, [**74**]OTf already being colorless, no visible color change can be observed, although a small absorption response is observable by UV spectroscopy (See Experimental details).

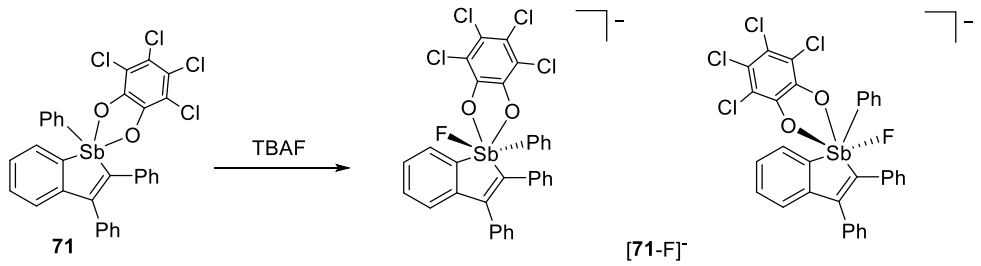

Figure 121. Reaction of **71** with fluoride showing two possible isomers of the fluoride adduct [**71**-F]$^-$.

The "turn-off" responses of **71** and **72** to fluoride are easily monitored by UV-vis spectroscopy. Titrations of **71** and **72** with TBAF in $CHCl_3$ show clean conversion to a new absorbance spectrum as fluoride is added, in which the low-energy absorbance band that tails into the visible range disappears and is replaced with a more intense band at shorter wavelengths (Figure 122). Fluoride binding constants were determined by

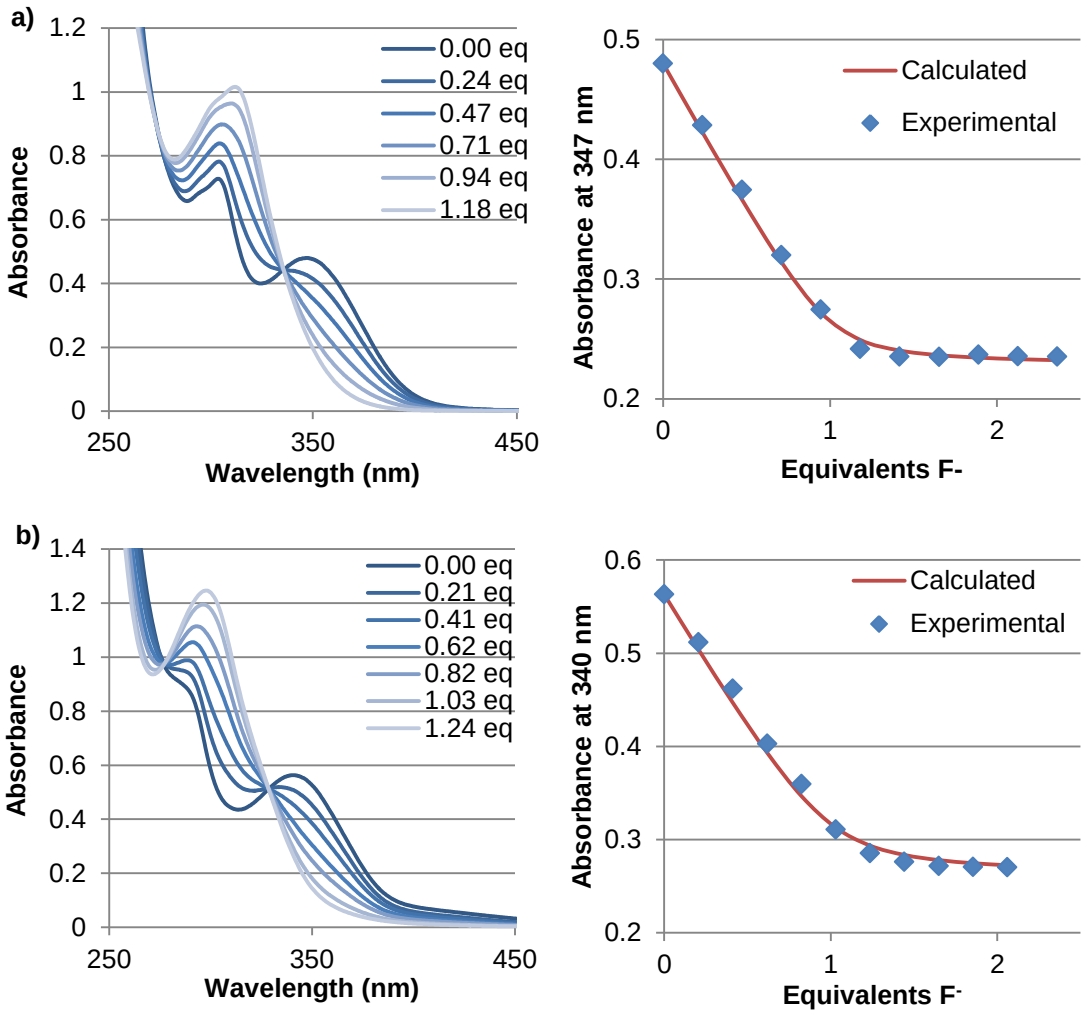

Figure 122. Changes in UV-vis absorption spectra and 1:1 binding isotherms of a) **71** (7.10×10^{-5} M) and b) **72** (8.14×10^{-5} M) upon titration with TBAF in $CHCl_3$.

fitting a 1:1 isotherm to this data, giving a $K(F^-) = 6.2\times10^5(\pm7\times10^4)$ M^{-1} for **71** and $K(F^-) = 3.3\times10^5(\pm4\times10^4)$ M^{-1} for **72** in $CHCl_3$. Thus, the fluoride binding constant for **71** is approximately twice as high as that of **72**, reflecting the stronger electron-withdrawing effect of the tetrachlorocatecholate ligand.

Given the dramatic change in the UV-vis spectra of **71** and **72** in chloroform, we investigated whether these neutral Lewis acids would be able to bind fluoride out of aqueous media. In a 7:3 mixture of THF:H_2O, addition of fluoride as TBAF to **71** still resulted in a colorimetric response, although the magnitude of the change was less than in organic solvent alone (See Experimental details). The initial spectrum of **71** in 7:3 THF:H_2O suggests that water or hydroxide may be binding to the Sb(V) center and dampening the response to fluoride, as has been observed in other neutral Sb(V) systems.[26] Addition of fluoride to **72** under the same conditions produced no response whatsoever, indicating that **72** is not a strong enough anion binder to capture fluoride from an aqueous mixture.

We therefore pursued a study of the aqueous fluoride sensing ability of **71** under biphasic conditions, as reported for our previous neutral Sb(V)-based sensor.[26] 1-mL portions of a 5.9×10^{-4} M solution of **71** in CH_2Cl_2 were layered with 5 mL of an aqueous solution of citrate buffer (10 mM, pH 4.2) containing tetrapropylammonium bromide (TPABr, 20 mM) and 0.0, 1.0, 2.0, or 4.0 ppm of fluoride as KF. TPABr acts as a phase transfer agent to allow **71** to capture fluoride from the aqueous phase; buffering the sample at acidic pH is necessary to prevent hydroxide binding at the Sb(V) center, which would produce a false positive response. After 1 minute of vigorous shaking, the layers

were allowed to partition and 300-uL aliquots from the organic layer were diluted into 3.00 mL of CH_2Cl_2 for absorbance measurements. The resulting absorption spectra and calibration curve obtained are shown in Figure 123. Although the overall absorbance change upon addition of fluoride is less dramatic than in pure organic solvent, a good linear relationship between the absorbance of **71** and the concentration of fluoride to which it is exposed is established. Treatment of **71** with other anions, including Cl^-, Br^-, I^-, CH_3COO^-, and NO_3^- by the same method produced no response (See Experimental details). This sensing system is therefore competent for the selective determination of fluoride concentrations in water at or below the EPA-mandated maximum contaminant

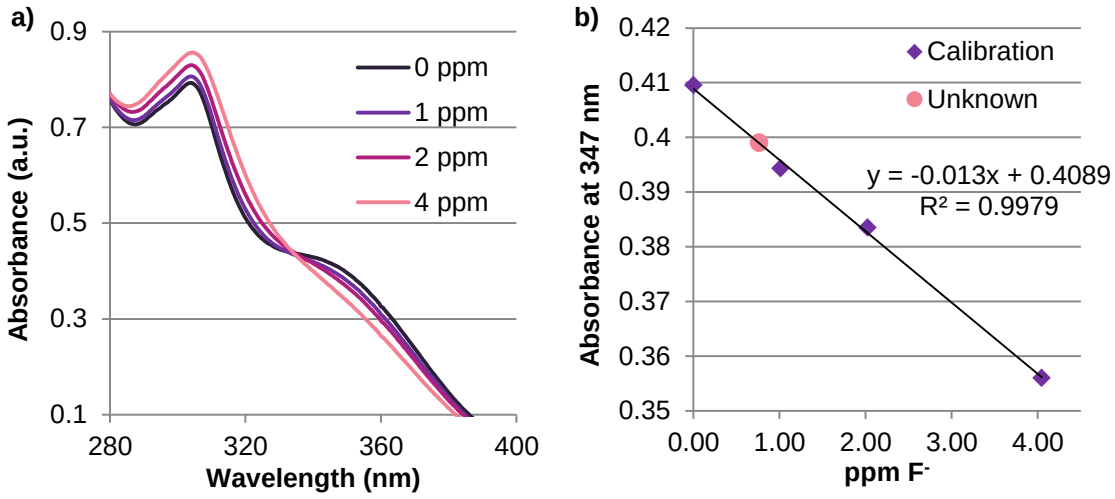

Figure 123. a) Absorption spectra of 5.9×10^{-5} M samples of **71** in CH_2Cl_2 prepared by tenfold dilution of samples treated biphasically with aqueous citrate buffer (10 mM, pH 4.2) with 20 mM TPABr and varying concentrations of fluoride. b) Calibration curve for the colorimetric "turn-off" response of **71** to fluoride, measured at 347 nm. The absorbance of an unknown sample of H-E-B® Baby Purified Water under the same conditions is plotted on the calibration line, giving a measure of its fluoride concentration. Each data point is taken as the average of two determinations under the same conditions.

level for fluoride (4 ppm).[79] We tested the sensing ability of **71** for practical application by analyzing a sample of commercial nursery water (H-E-B® Baby Purified Water with fluoride added), which was advertised to contain up to 1 mg/L of fluoride. The sample of nursery water was buffered with 10 mM citrate/citric acid at pH 4.2 and 20 mM TPABr was added, then a 5-mL portion was used to treat a solution of **71** under the same conditions described above. The resulting absorbance observed at 347 nm was compared to the established calibration curve, giving an experimental fluoride concentration of 0.8 (±0.4) ppm for this sample (Figure 123b). This value is in good accord with that advertised for this commercial sample, albeit with a large margin of error. Additionally, we measured the fluoride content of this sample by ion chromatography and determined the concentration to be 0.6 ppm, again in reasonably good agreement with that measured by the Sb(V)-based sensor **71**.

DFT calculations were again carried out to reveal how fluoride causes the "turn-off" colorimetric response observed in [**71**-F]$^-$. It is evident from the contour plot of the π* LUMO of [**71**-F]$^-$ compared to **71** that coordination of fluoride results in the disappearance of the Sb-based σ* contribution to this orbital (Figure 124). This loss of contribution destabilizes the π* LUMO, and accordingly, the energy of the π-π* transition is increased from 3.41 eV (363 nm) in **71** to 3.93 eV (316 nm) in [**71**-F]$^-$, in agreement with the observed shift in absorbance in the experimental titration data. This confirms our prediction that fluoride binding at Sb, by engaging the σ* orbital, directly influences the extent of π conjugation in the LUMO and thereby the wavelengths of

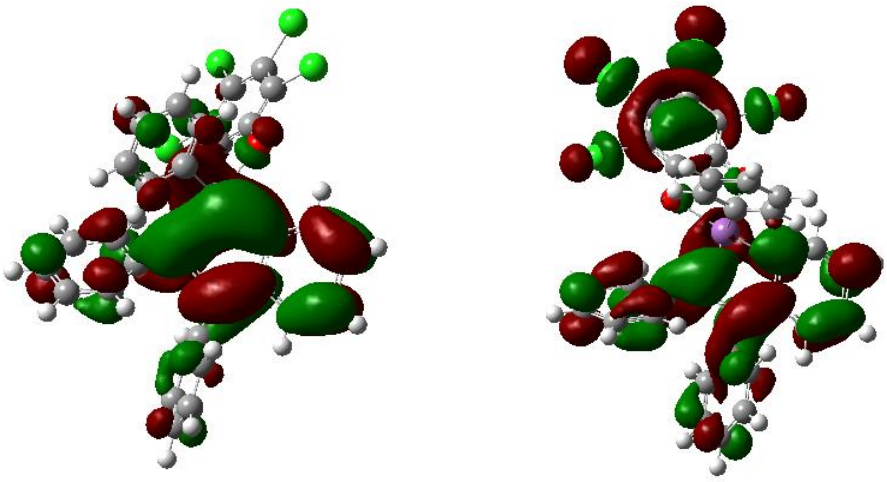

Figure 124. Contour plots of the π* LUMO of **71** and [**71**-F]⁻. Computations carried out using the B3LYP functional with the mixed basis set: Sb, aug-cc-pVTZ-PP; Cl, ECP10MWB; C/H/O, 6-31g(d).

absorption in these molecules. Although the colorimetric sensing response from yellow to colorless in **71** and **72** is less practically advantageous than that of other anion sensors we have explored, the mechanism of its response should apply generally to other heterocycles incorporating antimony in the same manner. More extended conjugated systems containing antimony would offer the possibility of brighter colors and/or luminescence by shifting the π-π* absorption bands into the visible range, and anion binding would be observable as a "turn-off" or ratiometric response. Cationic stibole compounds such as **74** can also be explored for this purpose, since these do display strong Lewis acidity; however, non-coordinating anions will need to be used to prevent suppression of the photophysical response by counteranion binding.

6.4 Pinacolborane-substituted benzostiboles as luminescent materials

In the substituted tellurophenes reported by Rivard, solid-state and aggregation-induced luminescence was observed for derivatives bearing pinacolborane groups.[298-301] We reasoned that the incorporation of antimony in place of tellurium would offer increased color tunability in these materials via substitution and/or oxidation of the antimony centers, potentially leading to a new class of emissive materials. Therefore, we have made initial investigations of benzostibole derivatives substituted with pinacolborane (Bpin) groups.

The synthesis of Bpin-substituted benzostiboles **75** and **76** was accomplished by the same procedure as for **69** above, using a Bpin-substituted alkyne in the cyclization reaction with diphenylzirconocene (Figure 125). Compound **75** was isolated in low yield

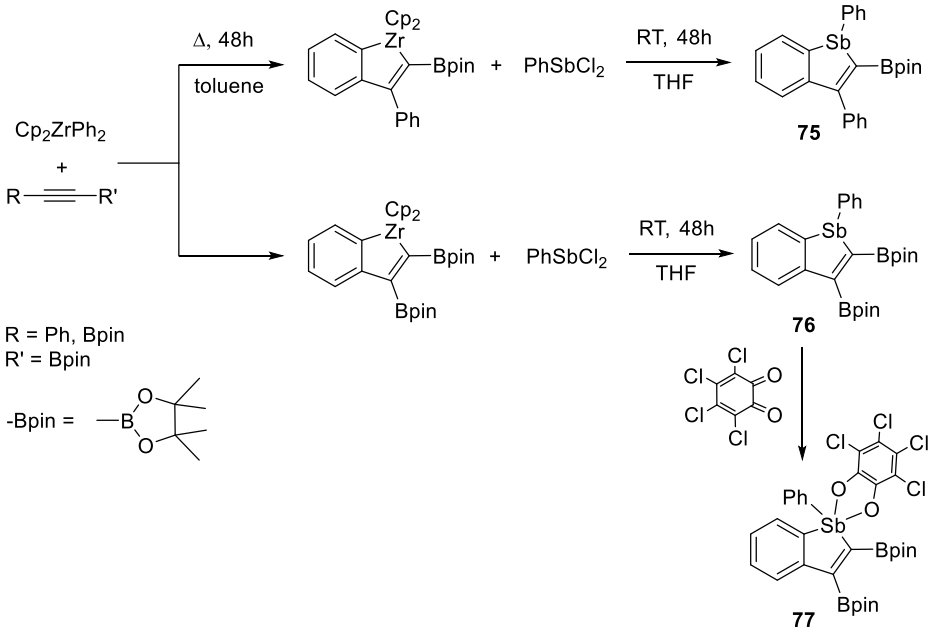

Figure 125. Synthesis of Bpin-substituted benzostiboles.

as a pale-colored solid; however, compound **76** was isolated as an intractable viscous oil. Nevertheless, **76** could be obtained in sufficient purity for reaction with *ortho*-chloranil, which yielded the oxidized product **77** as a pale yellow crystalline solid. All benzostibole products were bench stable.

Solid-state structures of **75** and **77** were obtained by single-crystal X-ray diffraction analysis, confirming the successful synthesis of these compounds. The crystal structure of **75** confirms the formation of a single regioisomer of **75** with the Bpin group adjacent to the Sb moiety, as had also been the case for the analogous benzotellurophene reported by Rivard (Figure 126). Again, the Sb-Ph group is oriented orthogonally to the plane of the benzostibole, and two enantiomers are seen in the crystal. The Bpin substituent at C1 is oriented with the trigonal planar boron center almost in plane with the rest of the heterocycle. This orientation should allow the boron-based empty p orbital to interact with the π system of the benzostibole unit, extending the conjugation. The

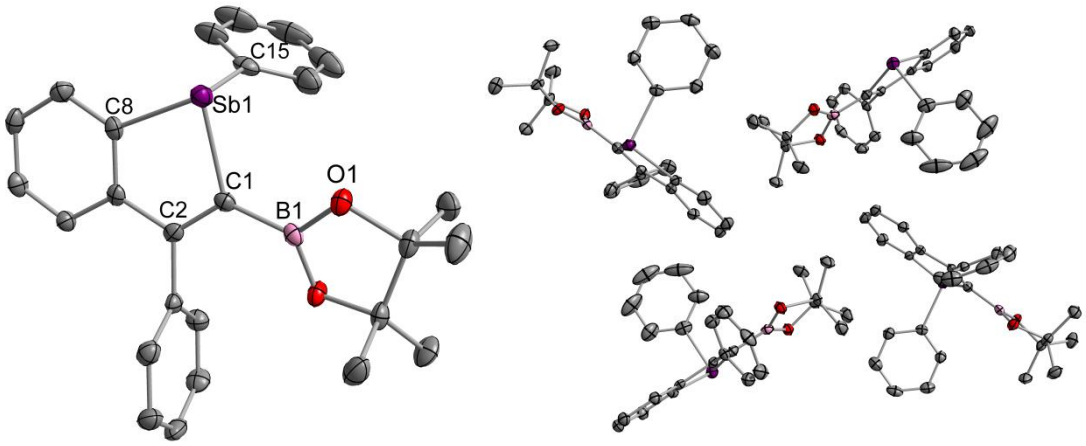

Figure 126. Solid-state structure of **75** with crystal packing. Hydrogen atoms omitted for clarity. Selected bond and torsion angles (°):∠C1-Sb1-C8 81.07(13), ∠C1-Sb1-C15 97.30(15), ∠C8-Sb1-C15 94.90(14), ∠Sb1-C1-B1-O1 13.3(5).

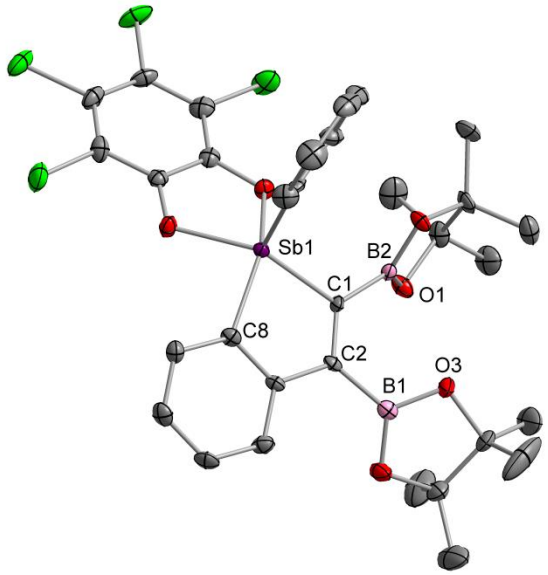

Figure 127. Solid-state structure of **77**. Hydrogen atoms omitted for clarity. Hexane solvate molecules omitted. Selected torsion angles (°):∠Sb1-C1-B2-O1 118.9(5), ∠ C1-C2-B1-O3 27.8(8).

extended crystal structure also reveals a lack of significant intermolecular π-stacking effects—rather, adjacent molecules are kept at a distance from each other in large part because of the bulky Bpin groups. This fact is important to imparting solid-state luminescence properties to this type of material, since π-stacking effects may contribute to nonradiative decay pathways that cause luminescence quenching in condensed phases.[301] The crystal structure of **77** confirms the installation of two Bpin substituents on the benzostibole core and oxidation of Sb by *ortho*-chloranil (Figure 127). In this case, the Bpin group at C1 is not oriented in the plane of the heterocycle, while the Bpin group at C2 is closer, with a torsion angle of less than 30° with the stibole plane. This difference likely reflects the increased steric congestion around the stibole ring both from the oxidized Sb center and the two Bpin groups.

The Bpin-substituted benzostibole **75** showed extremely weak blue emission in $CHCl_3$, but gratifyingly, faint green luminescence could be observed in the solid powder or crystals of **75** (Figure 128). The solution emission spectrum exhibits a small Stokes shift characteristic of fluorescence emission, but the solid-state emission spectrum reveals a broader emission band with a larger Stokes shift, suggesting that this emission may arise from phosphorescence, as reported for the related tellurophenes.[300-301] Importantly, this green emission is visible under air at room temperature, although it becomes brighter at 77 K. This initial finding demonstrates that Bpin-substituted stiboles

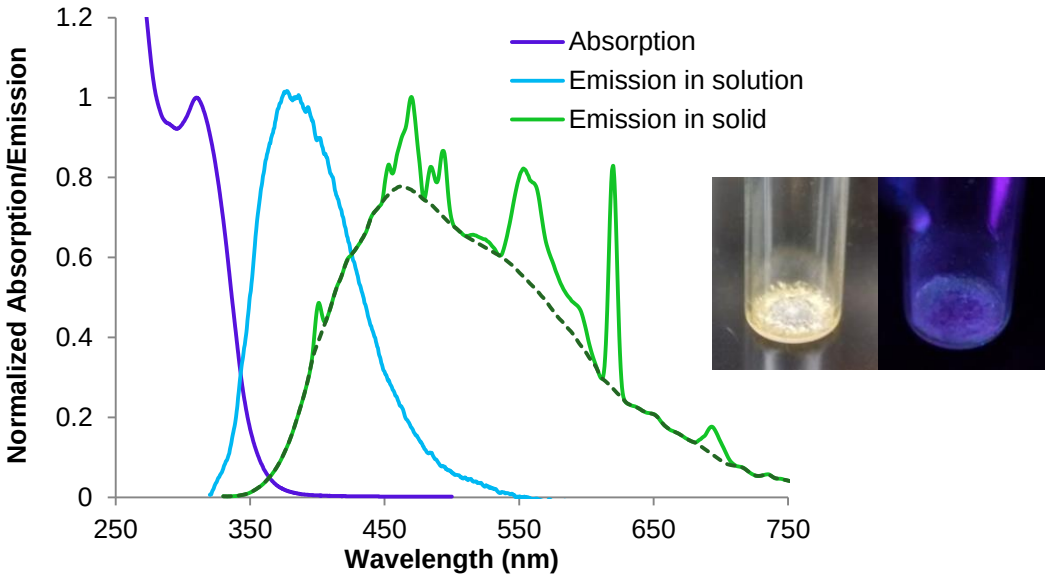

Figure 128. Normalized absorption and emission spectra of **75** in $CHCl_3$ solution and the solid state under air. No change in absorption or emission profiles was observed in a solution of **75** under N_2. Emission spectra taken with λ_{exc} = 310 nm. In the solid-state emission spectrum, the sharp emission features are method artifacts resulting from second-order effects and scattering from the solid sample insert, and can be seen in the absence of sample. A proposed "true" spectrum removing these effects is superimposed in dashed lines. Inset: Photos of crystalline **75** under normal light and under a handheld UV lamp (365 nm), showing the faint green emission of the solid.

may hold promise as air-stable phosphorescent materials similar to the reported tellurophenes.

The absorption spectrum of **77** in $CHCl_3$ shows an intense absorption centered at 306 nm with a shoulder around 330-340 nm (Figure 129). This redshifted shoulder appears to correspond to the π-π* transition as in the case of the redshifted absorption peaks observed in the spectra of **71** and **72**, but is less distinct. This may reflect the lack of planarity of the C1 Bpin group with the rest of the heterocycle (*vide supra*), which curtails the π conjugation across the molecule. To compare it to **71** and **72**, fluoride binding of **77** was tested by titration with TBAF (Figure 129). The results are more complex than in the cases of **71** and **72** due to the presence of Bpin groups, which may also be able to bind fluoride at the boron center. The shoulder at 330-340 nm disappears

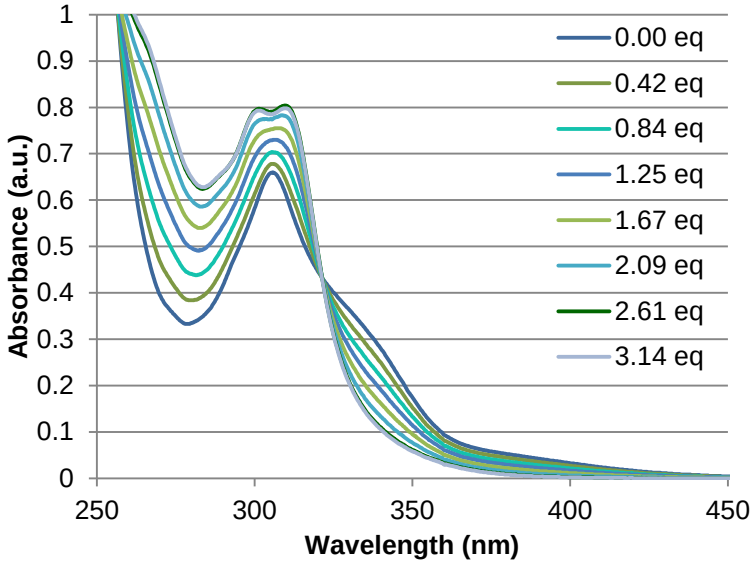

Figure 129. Changes in UV-vis absorption spectrum of **77** upon titration with TBAF in $CHCl_3$.

upon addition of TBAF, as expected if it corresponds to the orbital with contributions from the Sb-based σ*; however, it does not fully disappear until after the addition of >2.5 equivalents of fluoride, indicating that fluoride binding to **77** is not 1:1. At the same time, the sharp absorption at 306 nm broadens and eventually splits into two peaks at 301 and 310 nm after the addition of >2.5 equivalents of fluoride. These absorbance bands likely involve contributions from the boron-based p orbitals, and the observed splitting may indicate fluoride binding at one or the other of the Bpin groups, causing a larger differentiation between them.

No solution or solid-state emission was observed for the oxidized benzostibole **77**. This is likely due to interference of catecholate-based orbitals in the excited state that enable nonradiative decay. Other methods of oxidation at Sb such as methylation could be explored in the future to obtain Sb(V) derivatives of luminescent stiboles. Such materials would offer a wider range of options than the corresponding tellurophenes for tuning solid-state emission colors via substitution and oxidation at the Sb center.

6.5 Sb(III)- and Sb(V)-dibenzothienostiboles as luminescent extended heterocycles

Extension of the π-conjugated framework of chromophores generally results in a narrowing of the HOMO-LUMO gap and thus redshifted absorption and emission wavelengths in these materials. As another iteration of our strategy of incorporating Lewis acidic antimony groups into π-conjugated heterocycles, we chose to pursue the synthesis of Sb(III)- and Sb(V)-containing dibenzothienostiboles, which feature a π-

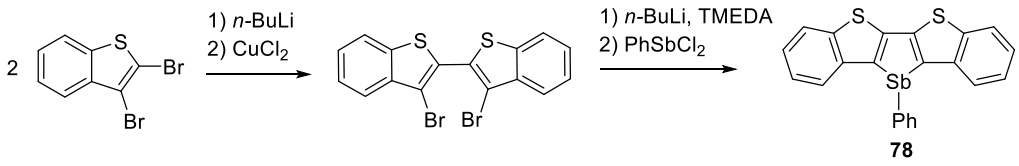

Figure 130. Synthesis of phenyl dibenzothienostibole **78**.

conjugated heteropentacycle structure. Examples of dibenzothienophospholes have been shown to display tunable absorption and emission colors (*vide supra*),[286] and one report of dibenzothienostiboles by Ohshita and coworkers showed similar luminescence properties, although with low quantum yields of fluorescence.[292] However, no Sb(V) derivatives were described in that report, nor was full structural characterization given. We have now synthesized both Sb(III) and Sb(V) derivatives of dibenzothienostiboles and show that fluoride binding to Sb(V) may result in a colorimetric and fluorimetric response.

The synthesis of phenyl dibenzothienostibole **78** is shown in Figure 130. Following the general synthetic route as for previously reported dibenzo-thienophospholes and stiboles,[286, 292] **78** was synthesized by cyclization of a dilithiated dibenzo[*b*]thiophene ligand precursor with $PhSbCl_2$. The yellow solid was obtained in 67% yield and fully characterized by NMR spectroscopy, elemental analysis, and X-ray crystallography.

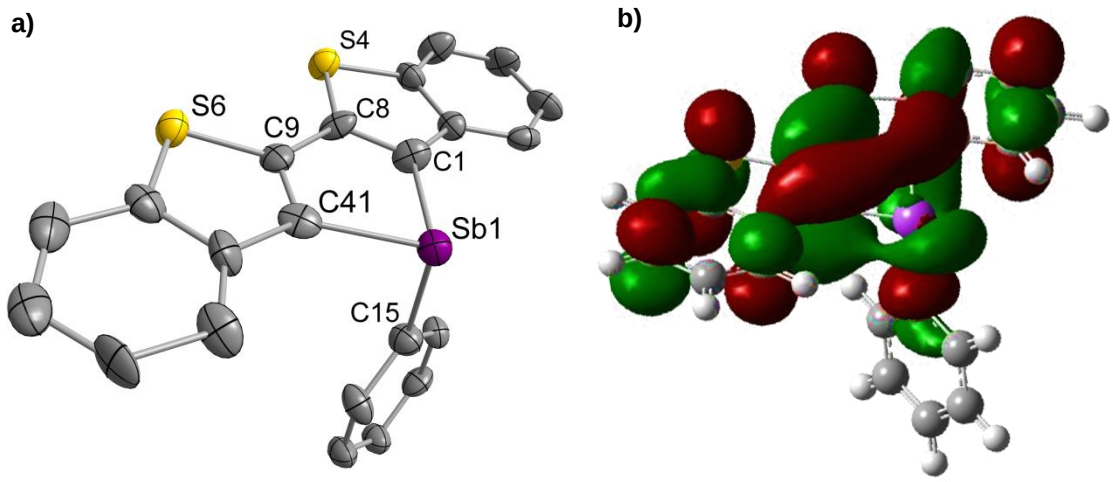

Figure 131. a) Solid-state structure of **78**. Hydrogen atoms omitted for clarity. Selected bond and torsion angles (°):∠C1-Sb1-C41 80.3(5), ∠C1-Sb1-C15 93.9(5), ∠C15-Sb1-C41 93.9(5), ∠Sb1-C1-C8-S4 179.9(7), ∠C1-C8-C9-C41 2.2(2). b) Contour plot of the LUMO of **78** determined by DFT calculations using the B3LYP functional and the mixed basis set: Sb, aug-cc-pVTZ-PP; S, ECP10MWB; C/H/O, 6-31g(d).

The solid-state structure of **78** confirms that the Sb(III) atom is incorporated into the planar heteropentacene backbone and sits in the plane of the chromophore (Figure 131a). As for the benzostiboles discussed above, the Sb center forms an acute bond angle within the five-membered stibole ring and is highly pyramidalized, such that the third phenyl substituent at Sb is oriented almost 90 degrees from the plane of the π structure. This geometry should allow Sb-based σ* orbitals to interact directly with the conjugated π system. Indeed, DFT optimization of **78** reveals significant contribution from the Sb-Ph σ* orbital to the LUMO of the molecule (Figure 131b). This interaction stabilizes the LUMO and gives the Sb atom a direct influence on the π-conjugated system.

Solutions of **78** in CH_2Cl_2 were found to exhibit a broad emission band centered at 442 nm (λ_{exc} = 373 nm), which is visible to the naked eye under a handheld UV lamp as a faint blue luminescence (Figure 132). This emission spectrum is consistent with those reported for dibenzothienostiboles **58** (λ_{max} = 437 nm) and **59** (λ_{max} = 443 nm),[292] and the intensity of the emission is similarly low, with a quantum yield of only 1.6%. This is most likely due to a heavy-atom effect by Sb, which would be expected to decrease the fluorescence quantum yield through intersystem crossing.[304] Some emission due to contamination by 2,2'-dibenzo[*b*]thiophene could also be observed if **78** was exposed to air, indicating that the dibenzothienostibole may be susceptible to oxidative or hydrolytic decomposition. Over time, ^{1}H NMR spectra of **78** in $CDCl_3$ also show peaks corresponding to 2,2'-dibenzo[*b*]thiophene, confirming this decomposition

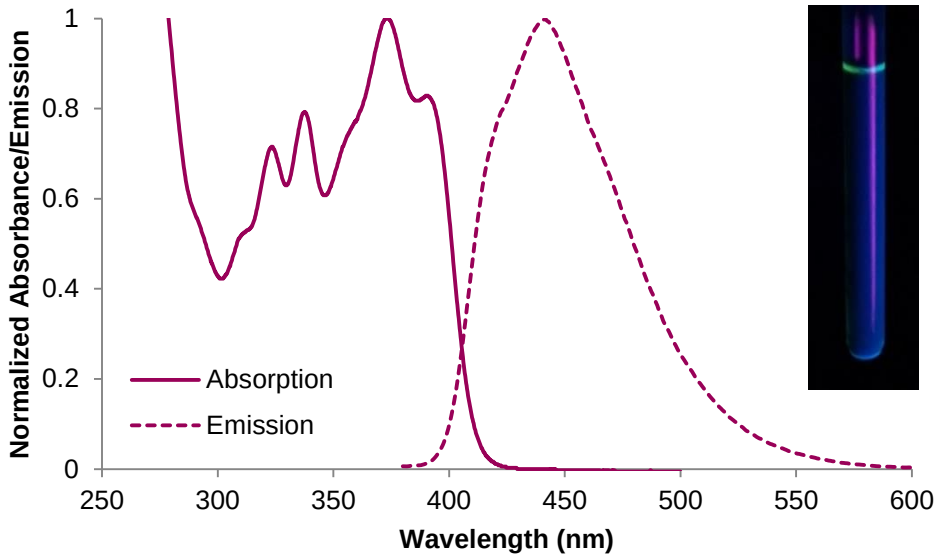

Figure 132. Normalized absorption and emission spectra of **78** in CH_2Cl_2 under N_2. Emission spectrum taken with λ_{exc} = 373 nm. Inset: Photo of the visible emission of **78** under a handheld UV lamp (365 nm).

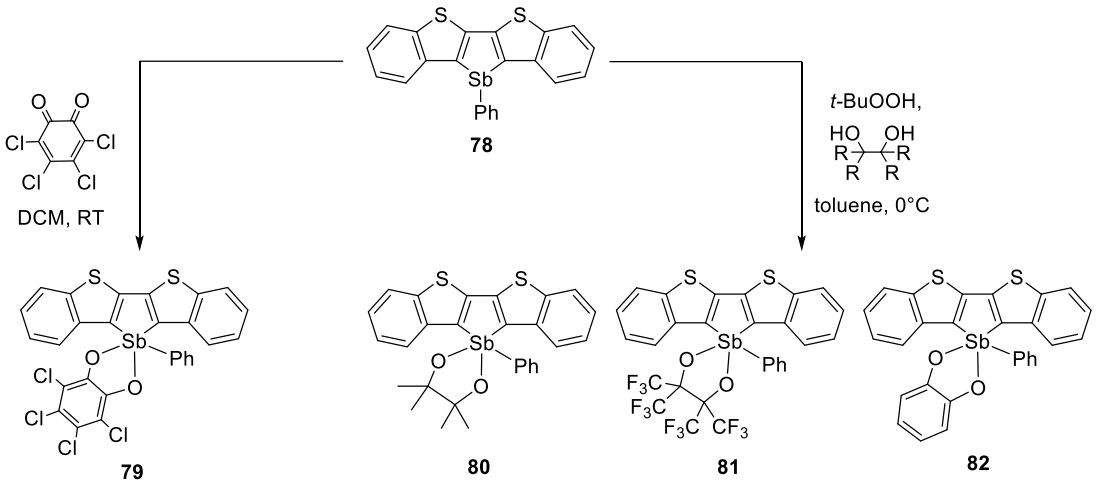

Figure 133. Oxidations of **78** to form Sb(V) spirocyclic dibenzothienostiboles **79-82**.

product. Ohshita and coworkers also mention this issue in their report of dibenzothienostiboles, characterizing the reaction as a photodecomposition. However, we saw that this decomposition could occur even in solid samples stored in the dark, but that solid samples stored under nitrogen remained stable indefinitely.

Oxidation of the Sb(III) dibenzothienostibole **78** was accomplished by several routes to afford Lewis acidic Sb(V) centers incorporated into the dithiophene framework (Figure 133). First, **78** was treated with *ortho*-chloranil to afford the chelated Sb(V) compound **79**, which was characterized by NMR spectroscopy and X-ray crystallography. Oxidations were also carried out using *tert*-butylhydroperoxide and quenching with diols to afford dibenzothienostibole pinacolate **80**, perfluoropinacolate **81**, and catecholate **82** in moderate yields.[189-192] NMR characterization of all of these compounds indicated oxidation of the Sb center by downfield shifts in the aromatic ^{1}H

signals corresponding to the Sb-Ph group. A solid-state structure of perfluoropinacolate compound **81** was also obtained by single-crystal X-ray diffraction.

The solid-state structures of **79** and **81** are compared in Figure 134 below. Both structures confirm the retention of the planar heteropentacene structure of the dibenzothiophene framework about the Sb(V) center with chelation of the catecholate or pinacolate ligand to form an Sb-centered spirocycle . In the structure of **79**, one molecule of THF solvent is also seen to be coordinated to the Sb center, indicating the latent Lewis acidity of the Sb(V) center, which readily accommodates a sixth ligand. In compound **81**, although it would otherwise be expected to exhibit Lewis acidity, a significant amount of steric crowding around the Sb center due to the perfluoropinacolate ligand is evident. The color of each of these derivatives is bright

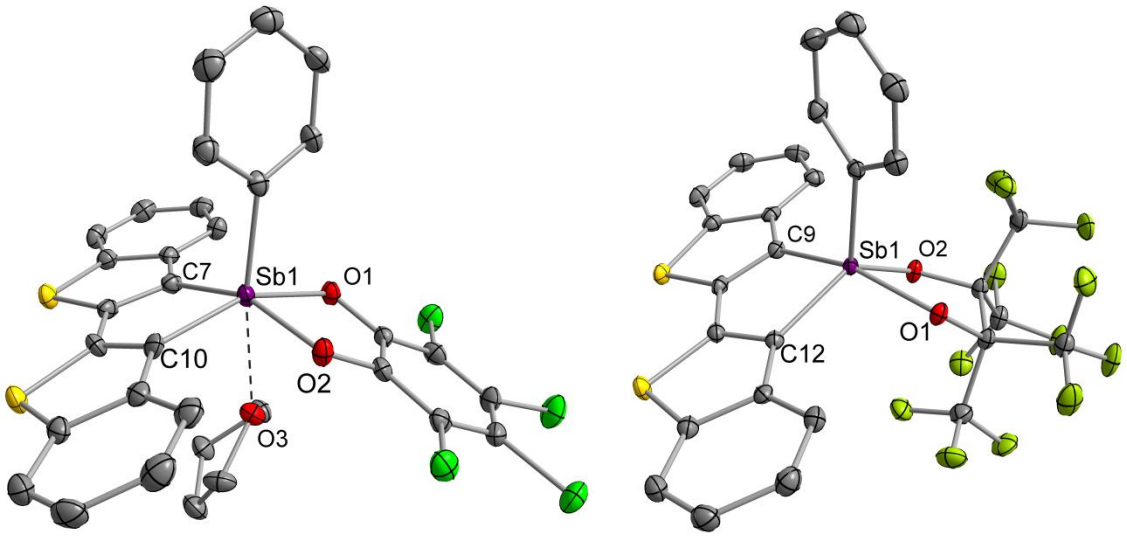

Figure 134. Solid-state structures of **79** and **81**. Hydrogen atoms omitted for clarity. Selected bond lengths (Å) and angles (°) for **79**: Sb1-O3 2.517(3), ∠C7-Sb1-C10 83.78(19), ∠O1-Sb1-O2 80.62(13). Selected bond angles (°) for **81**: ∠C9-Sb1-C12 83.65(7), ∠O1-Sb1-O2 78.59(5).

yellow, and the absorption spectrum of **79** features a broad long-wavelength absorption band centered at λ_{max} = 402 nm, significantly redshifted from those of the unoxidized compound **78** (Figure 135 below). No visible luminescence could be seen in the oxidized dibenzothienostiboles **79-82**, although a very faint emission band with λ_{max} = 444 nm (λ_{exc} = 402 nm) could be observed in the emission spectrum of **79** (Figure 135 below). The oxidized compounds appeared to be more resilient to the decomposition process observed for **78** in air; however, over time, cleavage of the dibenzothiophene backbone yielding 2,2'-dibenzo[*b*]thiophene could still be seen with these compounds.

Addition of TBAF to a $CDCl_3$ solution of **79** appears to result in fluoride binding, producing an immediate color change from yellow to colorless. A peak appears in the ^{19}F NMR spectrum at -85.5 ppm, within the expected range for Sb(V)-F bonds.[25-26] The ^{1}H NMR signals shift and those associated with the dibenzothiophene backbone split, indicating a loss of symmetry, as would be expected on forming an Sb-F bond *trans* from either the dibenzothiophene or tetrachlorocatecholate ligand. Finally, ESI mass spectrometry of the product solution reveals a monoanionic molecular ion peak at the expected mass for the fluoride adduct of 724.80 *m/z*. The colorimetric change induced upon titration of **79** with fluoride was monitored by UV-vis spectroscopy in CH_2Cl_2 (Figure 135). A 1:1 binding isotherm constructed from this data shows a very linear colorimetric response of **79** to the addition of fluoride, with a sharp saturation point indicating a high anion binding constant ($>1\times10^7$ M^{-1}). Interestingly, addition of fluoride to **79** also resulted in the appearance of a faint emission band with λ_{max} = 431 nm (λ_{exc} =

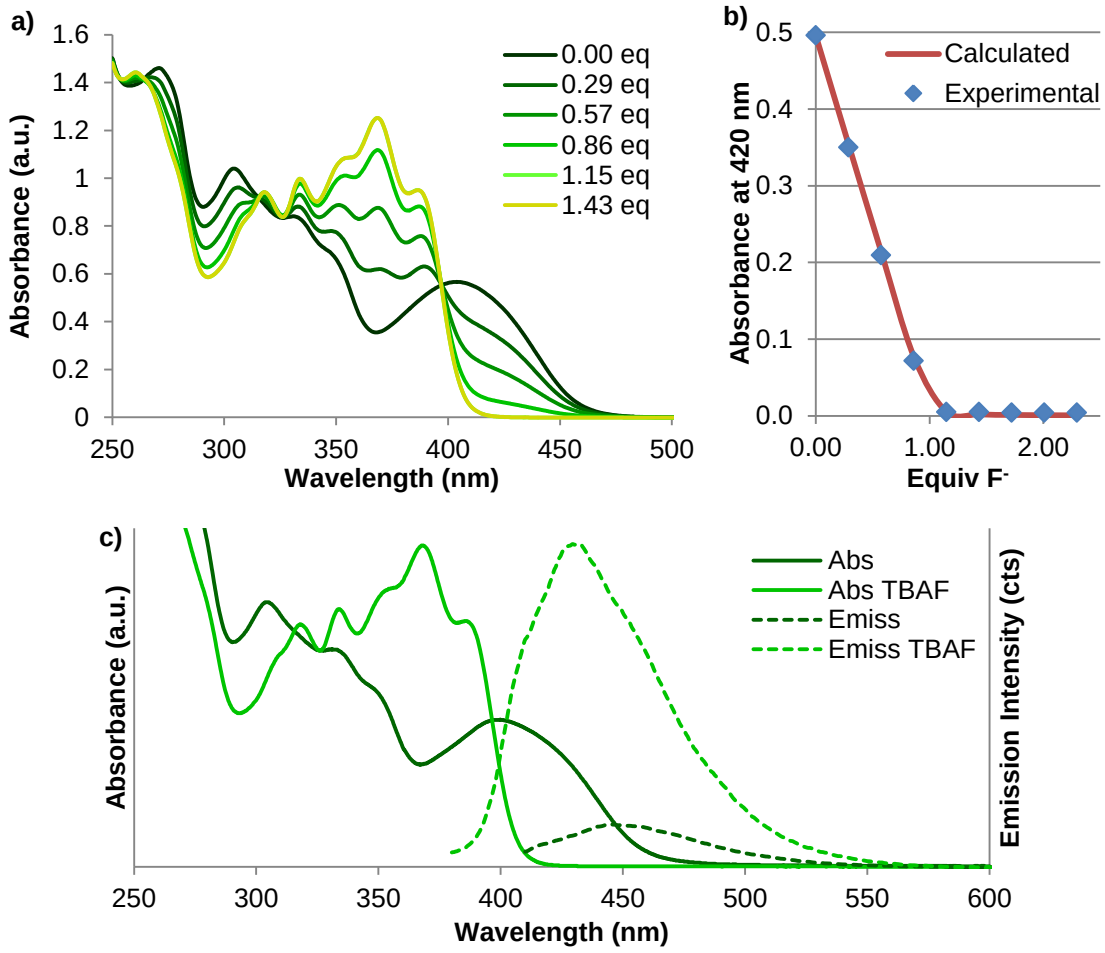

Figure 135. a) UV-vis spectra obtained by titration of **79** with TBAF in CH_2Cl_2. b) Binding isotherm constructed from the absorption data at 420 nm for the titration of **79** with fluoride. The calculated binding curve is shown on the basis of a binding constant of $K(F^-) = 1\times10^7\ M^{-1}$, but the true binding constant was too large to be determined accurately. 1:1 binding is assumed. c) Overall change in absorbance and emission before and after saturation of **79** with TBAF. Emission spectra were collected with λ_{exc} = 402 nm for the initial spectrum and λ_{exc} = 368 nm for the final spectrum.

368 nm) (Figure 135c). The fluorescence "turn-on" response is small in this case, since the final quantum yield of emission is still less than 2%. However, this result is encouraging in that both color and luminescence properties of **79** are modulated by the anion binding at Sb(V). Addition of fluoride to the other Sb(V) dibenzothienostiboles

80-**82** did not produce clean anion binding at Sb. With the pinacolate compounds **80** and **81**, addition of fluoride resulted in cleavage of the pinacolate ligands, as indicated by NMR, and over time, decomposition of the dibenzothienostibole structure was again evident.

DFT calculations performed on **79** and [**79**-F]$^-$ revealed again that the Sb-based σ* orbital is prominent in the LUMO of **79** and is also the source of the Lewis acidity of this compound (Figure 136 below). Coordination of fluoride to Sb(V) engages this σ* orbital, leaving the LUMO with only π* contributions from the dithiophene framework. The coordination also apparently switches the character of the HOMO from the π orbitals of the dithiophene framework to those of the chloranil ligand, which are close in energy in both the free and fluoride-bound forms of **79**. The π-π* transition energy was computed based on TD-DFT calculations as 2.93 eV (423 nm) for **79** and 3.42 eV (362 nm) for **79**-F, respectively. This is in good agreement with the experimental spectra, accounting for the dramatic blueshift of absorption in **79**-F. The increase in emission we observed upon fluoride binding to **79** is more surprising in light of the computational results, which suggest that the tetrachlorocatecholate ligand orbital should interfere with the π-π* transition in **79**-F. However, it is possible that the extremely low emission in **79** is a result of the strong contribution of Sb-based orbitals to the LUMO, which may serve to intensify heavy atom quenching effects from Sb. In that case, the removal of the Sb-based σ* orbital from the LUMO of **79**-F might be expected to ameliorate the quenching effects of the heavy atom and allow a stronger emission from the π-π* system.

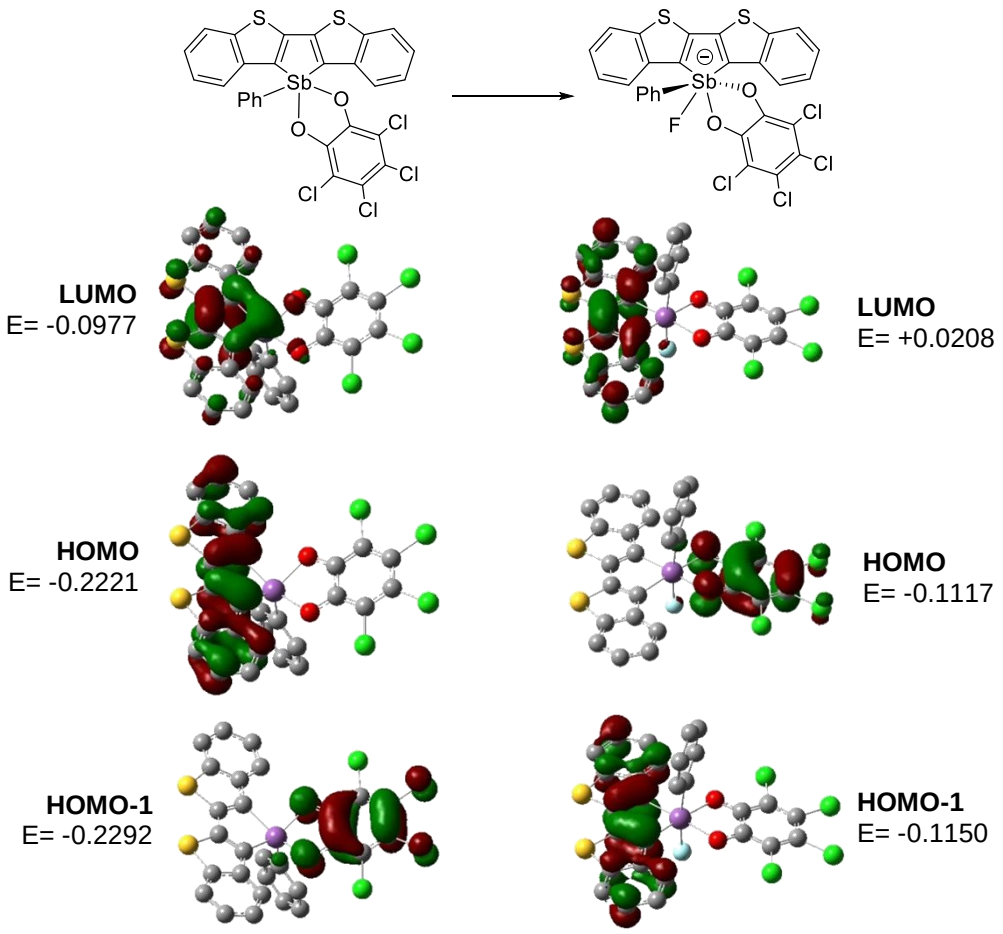

Figure 136. Contour plots of the DFT-calculated frontier MOs of **79** before and after fluoride coordination. Calculations were performed using the B3LYP functional with the mixed basis set: Sb, aug-cc-pVTZ-PP; S, Cl, ECP10MWB; F, 6-31g(d'); C/H/O, 6-31g(d). Energies are reported in units of hartrees.

The dibenzothienostiboles reported here show that we can access structures of Sb(III) and Sb(V) incorporated within the scaffold of an extended, emissive framework. Lewis acidic behavior at Sb(V) was obtained in compound **79**, and anion binding at the Sb center results in both a colorimetric and fluorimetric response. Unfortunately, the usefulness of **79** as a practical sensor is limited by the low quantum yield of emission

obtained and the slow decomposition of the dibenzothiophene backbone in the presence of air and moisture. Thus, this sensor is incompatible with aqueous media. However, these results provide further confirmation that anion binding engaging the Sb-based σ* orbital directly influences the extent of π conjugation and therefore photophysical properties of a surrounding chromophore.

6.6 Conclusions

In these studies, we set out to develop heterocycles incorporating antimony within the conjugated system with direct interaction of the antimony-based σ* orbitals with the π* LUMO of the chromophore. With this approach, chemistry occurring at the antimony center, including substitutions, oxidation to Sb(V), and anion binding, has a dramatic and predictable influence on the photophysical properties via modulation of that σ* orbital interaction.

In the case of benzostiboles **69**-**77**, installation of electron-withdrawing substituents such as chloride and oxidations of the antimony center were both observed to impart visible-range absorption to these heterocycles by stabilizing the antimony-based σ* orbital. Anion binding, on the other hand, removes the σ* orbital from interaction with the heterocycle π* LUMO, thus reducing the extent of π conjugation and inducing a "turn-off" of the long-wavelength absorption. This sensing response is sensitive enough in the case of **71** to be used in a biphasic system for the determination of ppm levels of fluoride in aqueous solution, including drinking water. Although the "turn-off" colorimetric response in this system is less useful for practical sensing than a

"turn-on" or fluorescent response would be, further explorations of similar antimony-containing heterocycles could lead to compounds with longer-wavelength absorptions that would instead function as ratiometric color-change sensors.

The characteristics of dibenzothienostiboles **78-82** support this idea and also show the effects of the incorporated antimony group on luminescence. Antimony incorporation into the pentacyclic framework results in redshifts in absorption and emission wavelengths relative to the unbridged dibenzothiophene, and DFT calculations show the influence of the antimony-based σ* orbital in the π* LUMO of these molecules, especially in the case of the antimony(V) derivative **79**. Luminescence in these compounds was low, possibly due to the influence of the heavy antimony atom and/or interference by catecholate ligand orbitals in **79**. However, **79** displays both a colorimetric "turn-off" and small fluorescent "turn-on" response to fluoride binding in organic solvent. Both the colorimetric and fluorescent changes observed upon fluoride binding are a result of the removal of the antimony-based σ* orbital from the conjugation of the LUMO, which results in a blueshift of absorbance and a small increase in emission, possibly due to the alleviation of heavy atom quenching by antimony when it is no longer directly involved in the fluorescent π system. The practical potential for these dithienostibole molecules as sensors was limited by their low emission and susceptibility toward decomposition. However, their characteristics support the general design principle of incorporating antimony(V) into extended heterocycles to obtain direct influence over the photophysical properties. This design could be further explored in future work to obtain more stable frameworks with longer-

wavelength absorption and higher emission. Antimony-incorporating π-conjugated compounds could also be explored in the context of color-tunable materials and even solid-state luminescent materials, as our preliminary investigations of pinacolborane-substituted benzostiboles **75** and **76** show. These compounds could provide a complementary class of materials to tellurium-containing π-conjugated materials currently under investigation, but with further opportunities for tuning the optoelectronic properties based on the chemistry of antimony.

6.7 Experimental details

General Methods. All preparations were carried out under an N_2 atmosphere using standard Schlenk techniques unless otherwise stated. Solvents were dried by refluxing under N_2 over Na/K (Et_2O, THF) or Na (toluene); all other solvents were ACS reagent grade and used as received. Cp_2ZrPh_2,[305] $PhSbCl_2$,[143] 1-pinacolatoboryl-2-phenylacetylene,[306-307] bis(pinacolatoboryl)acetylene,[308] and 2,3-dibromobenzo-[*b*]thiophene[309-310] were synthesized according to literature procedures. Other starting materials and reagents were purchased and used as received. NMR spectra were recorded using a Varian Unity Inova 500 FT NMR (499.58 MHz for ^1H, 125.63 MHz for ^{13}C, 469.86 MHz for ^{19}F) spectrometer. Chemical shifts (δ) are given in ppm and are referenced against residual solvent signals (^1H, ^{13}C) or external $BF_3 \cdot Et_2O$ (-153.00 ppm) for ^{19}F. Mass spectrometry was carried out by the Texas A&M Chemistry Mass Spectrometry Facility. Elemental analyses were performed at Atlantic Microlab (Norcross, GA). Absorbance measurements were taken on a Shimadzu UV-2502PC UV-

Vis spectrophotometer against a solvent reference. Fluorescence measurements were taken on samples in capped quartz cuvettes under air on a PTI QuantaMaster spectrofluorometer with entrance and exit slit widths of 2 nm. Quantum yield measurements were referenced against a value of 0.93 for POPOP (1,4-bis(5-phenyloxazol-2-yl) benzene) in cyclohexane.[311-312] Ion chromatography measurements were taken on a Thermo Scientific Dionex ICS-900 instrument using 9 mM Na_2CO_3 as the eluent and 0.075 N H_2SO_4 as the regenerant.

Synthesis of 2,3-diphenylbenzozirconocene.[300] Diphenylzirconocene (1.01 g) and diphenylacetylene (466 mg) were combined in 15 mL dry distilled toluene and refluxed at 100 °C under partial vacuum for 48 h. The solution color changed from yellow to deep red. After 48 h, the solvent was evaporated and the brown residue extracted into THF and filtered through Celite under nitrogen. The dark orange filtrate was evaporated to yield a moisture-sensitive orange solid, which was used without further purification. Yield: 1.02 g (69%). ^{1}H NMR (299.91 MHz, $CDCl_3$: 7.26 ppm): δ 7.15-6.60 (m, 14), 6.38 (s, 10). Spectral data are as previously reported.[300]

Synthesis of 69.[300] 2,3-diphenylbenzozirconocene (800 mg) and $PhSbCl_2$ (464 mg) were combined in 20 mL distilled THF and stirred at room temperature for 48 h. The resulting orange solution was reduced and purified by flash chromatography on silica gel, eluting as the second major fraction with 0-10% ethyl acetate in hexanes. The product was dried and recrystallized from a minimal amount of CH_2Cl_2 in hexanes to yield a white solid. Colorless needle-like crystals suitable for X-ray diffraction were obtained by slow evaporation of a CH_2Cl_2:hexane solution. Yield: 273 mg (36%).^{1}H

NMR (499.54 MHz, $CDCl_3$: 7.26 ppm): δ 7.69 (d, 1), 7.52 (dd, 2), 7.34-7.20 (m, 10), 7.09 (d, 1), 7.02 (m, 3), 6.95 (dd, 2). ^{13}C NMR (125.61 MHz, $CDCl_3$: 77.16 ppm): δ 155.03 (s), 153.92 (s), 151.92 (s), 146.24 (s), 141.17 (s), 139.38 (s), 137.40 (s), 135.65 (s), 134.47 (s), 130.45 (br), 130.06 (br), 129.36 (s), 129.08 (s), 128.88 (s), 128.51 (s), 127.98 (s), 127.88 (s), 127.24 (s), 127.06 (s), 126.13 (s). Elemental Analysis Calculated for $C_{26}H_{19}Sb$: C, 68.91; H, 4.23. Found: C, 68.98; H, 4.47.

Synthesis of 70. 2,3-diphenylbenzozirconocene (1.30 g) and $SbCl_3$ (620 mg) were combined in 15 mL distilled THF and stirred at room temperature for 48 h. The resulting yellow solution was reduced and purified by flash chromatography on silica gel, eluting as the second major fraction with 0-100% CH_2Cl_2 in hexanes. The product was evaporated and washed with pentane, then dried under vacuum to yield a bright yellow powder. Yellow-orange needle-like crystals suitable for X-ray diffraction were obtained by slow evaporation of a concentrated CH_2Cl_2 solution. Yield: 809 mg (72%).^1H NMR (499.54 MHz, $CDCl_3$: 7.26 ppm): δ 7.81 (dd, 1), 7.39-7.30 (m, 5), 7.20 (m, 2), 7.14 (m, 5), 6.99 (dd, 1). ^{13}C NMR (125.61 MHz, $CDCl_3$: 77.16 ppm): δ 156.85 (s), 155.25 (s), 153.74 (s), 148.21 (s), 139.48 (s), 137.85 (s), 134.32 (s), 130.72 (s), 129.78 (br), 129.13 (s), 128.80 (s), 128.73 (br), 128.31 (s), 128.16 (s), 127.82 (s), 126.97 (s). Elemental Analysis Calculated for $C_{20}H_{14}ClSb$: C, 58.37; H, 3.43. Found: C, 58.53; H, 3.59.

Synthesis of 71. A solution of **69** (88 mg) in 5 mL CH_2Cl_2 was treated with *ortho*-chloranil (54 mg) in an open vial. The orange solution was stirred 15 minutes, then evaporated and the residue washed with pentane to yield a yellow powder. The product

could be recrystallized from CH_2Cl_2 and washed with hexane to yield bright yellow crystals of the 1:1 CH_2Cl_2 solvate. Yield (crystals): 123 mg (77%). ^{1}H NMR (499.54 MHz, $CDCl_3$: 7.26 ppm): δ 8.16 (d,1), 7.65 (d, 2), 7.56 (t, 1), 7.51 (t, 1), 7.49-7.42 (m, 4), 7.39 (d, 2), 7.35-7.29 (m, 3), 7.20 (m, 4), 7.15 (d, 1), 7.10 (br, 1). ^{13}C NMR (125.61 MHz, $CDCl_3$: 77.16 ppm): δ 150.70 (s), 144.68 (s), 142.85 (s), 137.76 (s), 137.48 (s), 136.21 (s), 134.94 (s), 134.39 (s), 133.20 (s), 133.09 (s), 132.41 (s), 131.30 (s), 130.50 (s), 130.25 (s), 130.16 (s), 129.73 (s), 129.15 (s), 128.75 (s), 128.21 (s), 127.59 (s), 127.30 (s), 121.24 (s), 117.19 (s). Elemental Analysis Calculated for $C_{32}H_{19}Cl_4O_2Sb$: C, 54.98; H, 2.74. Found: C, 55.06; H, 2.90.

Synthesis of 72. A solution of **69** (70 mg) in 5 mL CH_2Cl_2 was treated with 3,5-di-*tert*-butyl-orthobenzoquinone (35 mg) in an open vial. The orange solution was stirred 30 minutes, then evaporated to yield a bright yellow powder. The product could be recrystallized from a $CHCl_3$/hexane solution to yield yellow-orange crystals. Yield (crystals): 69 mg (66%). ^{1}H NMR (499.54 MHz, $CDCl_3$: 7.26 ppm): δ 8.09 (d,1), 7.72 (d, 2), 7.51 (m, 2), 7.43 (m, 3), 7.36 (br, 1), 7.30 (br, 2), 7.25 (br, 1), 7.17-7.08 (m, 7), 6.94 (d, 1), 6.70 (d, 1), 1.29 (s, 18). ^{13}C NMR (125.61 MHz, $CDCl_3$: 77.16 ppm): δ 149.60 (s), 146.72 (s), 143.26 (s), 142.54 (s), 140.19 (s), 139.47 (s), 138.46 (s), 136.96 (s), 134.37 (s), 134.02 (s), 133.97 (s), 132.23 (s), 132.14 (s), 130.85 (s), 130.22 (br), 129.96 (s), 129.87 (s), 128.56 (s), 127.92 (s), 127.79 (s), 127.10 (s), 126.58 (s), 112.97 (s), 108.34 (s), 34.71 (s), 34.63 (s), 31.93 (s), 29.63 (s). Elemental Analysis Calculated for $C_{40}H_{39}O_2Sb$: C, 71.33; H, 5.84. Found: C, 71.46; H, 5.80.

Synthesis of 74. A solution of **69** (80 mg) in 10 mL CH_2Cl_2 under N_2 was treated with excess methyl triflate (144 mg) and refluxed at 60 °C overnight. The solution was evaporated and the residue washed with hexane and Et_2O to yield a white powder. The product was recrystallized from a CH_2Cl_2/hexane solution to yield colorless block crystals. ^{1}H NMR (499.54 MHz, $CDCl_3$: 7.26 ppm): δ 8.50 (d,1), 7.78 (d, 2), 7.60-7.54 (m, 5), 7.46 (br, 1), 7.39 (t, 1), 7.32 (br, 2), 7.25 (d, 1), 7.13-7.07 (m, 4), 6.76 (d, 2), 2.37 (s, 3). ^{13}C NMR (125.62 MHz, $CDCl_3$: 77.16 ppm): δ 154.17 (s), 148.02 (s), 137.08 (s), 136.45 (s), 135.92 (s), 134.86 (s), 134.23 (s), 133.48 (s), 132.86 (s), 130.95 (s), 130.55 (s), 129.78 (br), 129.67 (br), 129.22 (br), 128.95 (s), 128.91 (s), 128.80 (s), 128.70 (s), 127.92 (s), 127.50 (s), 124.73 (s), 121.54 (s), 119.00 (s), 6.42 (s). Elemental Analysis Calculated for $C_{28}H_{22}SF_3O_3Sb$: C, 54.48; H, 3.59. Found: C, 54.74; H, 3.78.

Synthesis of 2-pinacolatoboryl-3-phenylbenzozirconocene.[300] Diphenyl-zirconocene (380 g) and 1-pinacolatoboryl-2-phenylacetylene (231 mg) were combined in 15 mL dry distilled toluene and refluxed at 100 °C under partial vacuum for 48 h. The solution color changed from yellow to deep orange. After 48 h, the solvent was evaporated and the orange residue extracted into THF and filtered through Celite under nitrogen. The orange filtrate was evaporated to yield a moisture-sensitive orange solid, which was used without further purification. Yield: 300 mg (56%). Spectral data are as previously reported.[300]

Synthesis of 75.[300] 2-pinacolatoboryl-3-phenylbenzozirconocene (300 mg) and $PhSbCl_2$ (495 mg) were combined in 20 mL distilled THF and stirred at room temperature for 48 h. The resulting yellow solution was reduced and purified by flash

chromatography on silica gel, eluting as the first major fraction with 0-10% ethyl acetate in hexanes. The product was evaporated to an off-white solid. Pale yellow block crystals suitable for X-ray diffraction were obtained by slow evaporation of a CH_2Cl_2:hexane solution. ^{1}H NMR (499.54 MHz, $CDCl_3$: 7.26 ppm): δ 7.75 (m, 1), 7.51 (m, 2), 7.41-7.35 (m, 5), 7.29 (m, 2), 7.24 (m, 3), 7.19 (m, 1), 1.08 (s, 6), 1.04 (s, 6). ^{13}C NMR (125.61 MHz, $CDCl_3$: 77.16 ppm): δ 168.14 (s), 153.91 (s), 147.75 (s), 141.74 (s), 137.91 (s), 135.56 (s), 134.64 (s), 129.15 (s), 128.86 (s), 128.44 (s), 128.04 (s), 127.91 (s), 127.59 (s), 127.39 (s), 83.42 (s), 24.83 (s), 24.34 (s). ^{11}B NMR (128.17 MHz $CDCl_3$, $BF_3 \cdot Et_2O$: 0.00 ppm), δ: 31.9 ppm. Elemental Analysis Calculated for $C_{26}H_{26}BO_2Sb$: C, 62.08; H, 5.21. Found: C, 62.29; H, 5.22.

Synthesis of 2,3-bis(pinacolatoboryl)benzozirconocene.[300] Diphenyl-zirconocene (680 mg) and bis(pinacolatoboryl)acetylene (496 mg) were combined in 15 mL dry distilled toluene and refluxed at 100 °C under partial vacuum for 48 h. The solution color changed from yellow to dark red-brown. After 48 h, the solvent was evaporated and the residue extracted into THF and filtered through Celite under nitrogen. The red-brown filtrate was evaporated to yield a moisture-sensitive dark orange solid, which was used without further purification. Yield: 1.01 g (98%). ^{1}H NMR (299.91 MHz, $CDCl_3$: 7.26 ppm): δ 7.48 (d, 1), 6.95 (t, 1), 6.76 (t, 1), 6.52 (d, 1), 6.36 (s, 10), 1.30 (s, 12), 1.28 (s, 12). Spectral data are as previously reported.[300]

Synthesis of 76.[300] 2,3-bis(pinacolatoboryl)benzozirconocene (1.00 g) and $PhSbCl_2$ (494 mg) were combined in 20 mL distilled THF and stirred at room temperature for 48 h. The resulting yellow solution was reduced and purified by flash

chromatography on silica gel, eluting as the second major fraction with 0-10% ethyl acetate in hexanes. The product was evaporated to a sticky yellow oil. Yield: 480 mg (50%).[1]H NMR (499.54 MHz, $CDCl_3$: 7.26 ppm): δ 7.84 (d, 1), 7.70 (d, 1), 7.41 (m, 2), 7.37 (t, 1), 7.22 (t, 1), 7.17 (m, 3), 1.42 (d, 12), 1.25 (d, 12).

Synthesis of 77. 76 was treated with 1 equivalent of *ortho*-chloranil in CH_2Cl_2 and stirred for 30 minutes. The product was evaporated, washed with pentane, and recrystallized from a CH_2Cl_2:hexane solution. Colorless plates of the 2:1 hexane solvate were analyzed by X-ray crystallography. [1]H NMR (499.53 MHz, $CDCl_3$: 7.26 ppm): δ 8.08 (dd, 1), 8.04 (dd, 1), 7.83 (d, 2), 7.56 (m, 2), 7.50 (m, 1), 7.44 (m, 1), 1.45 (d, 12), 1.41 (d, 12). [13]C NMR (125.62 MHz, $CDCl_3$: 77.16 ppm): δ 144.92 (s), 140.93 (s), 134.44 (s), 134.41 (s), 133.09 (s), 132.75 (s), 132.59 (s), 131.15 (s), 129.89 (s), 129.36 (s), 127.70 (s), 120.86 (s), 117.03 (s), 85.08 (s), 84.87 (s), 25.29 (s), 25.21 (s), 24.89 (s), 24.71 (s). Elemental Analysis Calculated for $C_{32}H_{33}B_2O_6Cl_4Sb \cdot 0.5(C_6H_{14})$: C, 49.93; H, 4.79. Found: C, 49.94; H, 4.77.

Synthesis of 2,2'-di(3-bromobenzo[*b*]thiophene).[286] 2,3-dibromobenzo-[*b*]thiophene (4.0 g, 13.7 mmol) was dissolved in 100 mL diethyl ether, and *n*-butyllithium (2.3 M in hexanes, 6.25 mL, 14.4 mmol) was added dropwise at -78 °C. The yellow suspension was stirred for 20 minutes at that temperature, then for 1 hour at -20 °C. In another flask, 2.26 g anhydrous $CuCl_2$ (2.30 g, 17.1 mmol) were suspended in 20 mL diethyl ether and chilled to -78 °C. The lithiation mixture was again chilled to -78 °C and cannulated into this flask. The brown mixture was left to stir and warm to room temperature overnight. The flask was then opened to air and the brown precipitate

filtered off. The red-brown solution was washed with 50 mL 5 M HCl, and the green aqueous layer was extracted with chloroform and diethyl ether. The organic fractions were pooled, washed with 5 M HCl and H_2O, dried over $MgSO_4$, and evaporated to a brown residue. The product was washed with acetone and hexanes to yield a tan powder. Yield: 829 mg (29%). ^{1}H NMR (499.42 MHz, $CDCl_3$: 7.26 ppm): δ 7.92 (d, 2H), 7.85 (d, 2H), 7.50 (m, 4H). Spectral data are in accord with those previously reported.[286]

Synthesis of 78.[286, 292] 2,2'-di(3-bromobenzo[*b*]thiophene) (360 mg, 0.85 mmol) was dissolved in 20 mL diethyl ether, and 0.5 mL TMEDA added at -78°C. After 10 minutes of stirring, *n*-butyllithium (2.5 M, 0.75 mL, 1.87 mmol) was added dropwise, and the suspension was again stirred for 10 minutes at -78°C. $PhSbCl_2$ (343 mg, 1.27 mmol) was dissolved in 10 mL diethyl ether and transferred dropwise into the reaction flask. The yellow suspension was left to stir and warm to room temperature overnight. The solvent was evaporated and the yellow residue resuspended in methanol to precipitate the product as a light yellow powder with methanol washings. Product was purified further by silica gel chromatography, eluting with 40:1 hexanes:CH_2Cl_2. Yield: 263 mg (67%). Yellow, needle-like crystals suitable for X-ray diffraction were obtained by slow diffusion of pentane into a THF solution. ^{1}H NMR (499.42 MHz, $CDCl_3$: 7.26 ppm): δ 7.90 (d, 2H), 7.77 (d, 2H), 7.46 (d, 2H), 7.38-7.30 (m, 4H), 7.20 (m, 3H). ^{13}C NMR (125.59 MHz, $CDCl_3$: 77.0 ppm): δ 147.81, 142.67, 142.19, 141.45, 136.84, 135.42, 129.19, 129.02, 125.23, 124.40, 123.80, 123.16. Elemental Analysis Calculated for $C_{22}H_{13}S_2Sb$: C, 57.04; H, 2.83. Found: C, 57.00; H, 2.72. Product was slightly air-sensitive, and the color was observed to change to pink upon standing in air or in

solution, with partial decomposition to 2,2'-dibenzothiophene observed in the NMR: δ 7.81 (d, 2H), 7.77 (d, 2H), 7.52 (s, 2H), 7.35 (m, 4H).

Synthesis of 79. A solution of **78** (60 mg) in 5 mL CH_2Cl_2 was treated with *ortho*-chloranil (50 mg) in an open vial and stirred for 15 minutes. The solvent was evaporated and the residue washed with methanol and pentane to yield a yellow powder. Product could be further purified by silica gel chromatography, using a gradient of 0-100% ethyl acetate in hexanes as eluent. Yield: 76 mg (68%). Yellow crystals suitable for X-ray diffraction were obtained by slow diffusion of pentane into a THF solution. ^{1}H NMR (499.42 MHz, $CDCl_3$: 7.24 ppm): δ 8.42 (d, 2H), 7.90 (d, 2H), 7.73 (d, 2H), 7.55 (t, 3H), 7.44 (m, 4H). ^{13}C NMR (125.62 MHz, $CDCl_3$: 77.16 ppm): δ 147.30 (s), 144.43 (s), 143.22 (s), 139.71 (s), 133.90 (s), 133.59 (s), 130.69 (s), 130.62 (s), 129.79 (s), 126.81 (s), 125.79 (s), 125.34 (s), 123.31 (s), 121.84 (s), 117.44 (s).

General Procedure for Peroxide Oxidation with Vicinal Diols. [189-192] **78** and an equimolar amount of diol were dissolved in 10 mL toluene under an N_2 flow. A slight excess of *t*-butylhydroperoxide (70% aqueous solution) dissolved in 1 mL toluene and added dropwise at 0 °C. The mixture was stirred 15 minutes, then the solvent was evaporated and the residue washed with methanol to precipitate the solid product.

Synthesis of 80. 78 (150 mg, 0.324 mmol) and pinacol (48.2 mg, 0.408 mmol) were reacted with *t*-butylhydroperoxide solution (76.7 mg, 0.596 mmol) according to the general procedure to yield a dark yellow powder. Yield: 120 mg (64%). ^{1}H NMR (499.42 MHz, $CDCl_3$: 7.24 ppm): δ 8.28 (d, 2H), 7.86 (m, 4H), 7.42 (m, 3H), 7.33 (m,

4H), 1.26 (s, 12H). ^{13}C NMR (125.59 MHz, $CDCl_3$: 77.0 ppm): δ 145.91, 143.08, 141.21, 134.75, 134.70, 131.81, 129.40, 125.69, 125.55, 124.62, 122.81, 75.66.

Synthesis of 81. 78 (150 mg, 0.324 mmol) and perfluoropinacol (139 mg, 0.416 mmol) were reacted with *t*-butylperoxide solution (59.1 mg, 0.459 mmol) according to the general procedure to yield a yellow powder. Yield: 93.5 mg (36%). Yellow crystals suitable for X-ray diffraction were obtained by slow diffusion of pentane into a THF solution. ^{1}H NMR (499.42 MHz, $CDCl_3$: 7.24 ppm): δ 8.15 (d, 2H), 7.89 (d, 2H), 7.78 (d, 2H), 7.51 (m, 3H), 7.42 (m, 4H). ^{19}F NMR (469.86 MHz, $CDCl_3$, $BF_3{\cdot}Et_2O$: -153.00 ppm): δ – 69.41 (s, 12F). ^{13}C NMR (125.59 MHz, $CDCl_3$: 77.0 ppm): δ 146.65, 142.91, 139.46, 134.14, 133.26, 130.54, 130.12, 129.21, 126.51, 125.59, 124.78, 123.11.

Synthesis of 82. 78 (150 mg, 0.324 mmol) and catechol (34.7 mg, 0.354 mmol) were reacted with *t*-butylperoxide solution (73.3 mg, 0.569 mmol) according to the general procedure to yield a yellow-green powder. Yield: 105.7 mg (58%). ^{1}H NMR (499.42 MHz, $CDCl_3$: 7.24 ppm): δ 8.38 (d, 2H), 7.88 (d, 2H), 7.75 (d, 2H), 7.50 (m, 4H), 7.39 (m, 5H), 7.02 (m, 2H), 6.71 (m, 2H).

Crystallography. Crystal data, details of data collection, and structure refinement parameters for compounds **69-81** are compiled in Tables 11-14. The crystallographic measurements were performed at 110(2) K using a Bruker APEX-II CCD area detector diffractometer, with a graphite-monochromated Mo-Kα radiation (λ = 0.71069 Å). In each case, a specimen of suitable size and quality was selected and mounted onto a nylon loop. The semi-empirical method SADABS[146] was applied for absorption correction. The structure was solved by direct methods and refined by the

full-matrix least-square technique against F2 with the anisotropic temperature parameters for all non-hydrogen atoms. All H atoms were geometrically placed and refined in riding model approximation. Data reduction and further calculations were performed using the Bruker SHELXTL[147] and ShelXle[148] program packages.

Table 11. Crystallographic details for **69, 70**, and **73.**

	69	**70**	**73**
Chemical formula	$C_{26}H_{19}Sb$	$C_{20}H_{14}ClSb$	$C_{38}H_{19}Cl_8O_4Sb$
M_r	453.16	411.51	944.88
Crystal system, space group	Monoclinic, $P2_1/c$	Triclinic, P	Triclinic, P
a, b, c (Å)	12.0289 (19), 5.8422 (9), 26.884 (4)	5.755 (3), 11.040 (5), 12.579 (6)	12.433 (6), 12.676 (6), 13.188 (6)
α, β, γ (°)	90, 91.784 (2), 90	77.67 (2), 86.12 (2), 81.86 (2)	67.517 (4), 69.665 (4), 87.813 (5)
V (Å^3)	1888.4 (5)	772.4 (7)	1790.0 (15)
Z	4	2	2
μ (mm^{-1})	1.47	1.95	1.41
Crystal size (mm)	0.61 × 0.08 × 0.04	0.59 × 0.13 × 0.11	0.33 × 0.24 × 0.11
No. of measured, independent and observed [$I > 2\sigma(I)$] reflections	42573, 4678, 3929	10281, 3895, 3158	47813, 7734, 4785
R_{int}	0.069	0.074	0.140
$R[F^2 > 2\sigma(F^2)]$, $wR(F^2)$, S	0.029, 0.060, 1.03	0.050, 0.148, 1.05	0.063, 0.200, 1.11
No. of reflections	4678	3895	7734
No. of parameters	244	199	460
$\Delta\rho_{max}$, $\Delta\rho_{min}$ (e Å^{-3})	0.61, −0.49	0.89, −1.39	2.13, −1.38

Table 12. Crystallographic details for **71, 72,** and [**74**]OTf.

	71	**72**	[**74**]OTf
Chemical formula	$C_{32}H_{19}Cl_4O_2Sb$ $\cdot(CH_2Cl_2)$	$C_{40}H_{39}O_2Sb$	$C_{27}H_{22}Sb$ $\cdot(CF_3O_3S)$
M_r	783.95	673.46	617.26
Crystal system, space group	Triclinic, *P*	Triclinic, *P*	Orthorhombic, $P2_12_12_1$
a, *b*, *c* (Å)	9.7449 (5), 12.4161 (7), 14.4854 (7)	10.135 (4), 12.117 (5), 14.440 (5)	9.2260 (5), 15.2540 (9), 18.1770 (11)
α, β, γ (°)	69.312 (2), 86.843 (3), 68.304 (2)	96.089 (4), 105.299 (4), 107.602 (4)	90, 90, 90
V (Å^3)	1517.71 (14)	1596.7 (11)	2558.1 (3)
Z	2	2	4
μ (mm^{-1})	1.47	0.90	1.21
Crystal size (mm)	0.51 × 0.20 × 0.11	0.28 × 0.19 × 0.05	0.47 × 0.23 × 0.20
No. of measured, independent and observed [$I > 2\sigma(I)$] reflections	50620, 7783, 6734	42447, 6723, 5337	49747, 6515, 6105
R_{int}	0.050	0.113	0.052
$R[F^2 > 2\sigma(F^2)]$, $wR(F^2)$, *S*	0.028, 0.058, 1.05	0.047, 0.119, 1.08	0.026, 0.069, 1.12
No. of reflections	7783	6723	6515
No. of parameters	379	394	326
$\Delta\rho_{max}$, $\Delta\rho_{min}$ (e Å^{-3})	0.48, −0.57	0.78, −1.19	0.49, −0.65

Table 13. Crystallographic details for **75** and **77.**

	75	**77**
Chemical formula	$C_{26}H_{26}BO_2Sb$	$C_{32}H_{33}B_2Cl_4O_6Sb{\cdot}0.5(C_6H_{14})$
M_r	503.03	841.84
Crystal system, space group	Triclinic, *P*	Monoclinic, $P2_1/c$
a, *b*, *c* (Å)	10.7761 (7), 13.4313 (8), 15.9334 (9)	9.4383 (7), 13.7154 (10), 29.753 (2)
α, β, γ (°)	84.250 (3), 82.358 (3), 81.583 (3)	90, 99.055 (3), 90
V (Å^3)	2253.4 (2)	3803.5 (5)
Z	4	4
μ (mm^{-1})	1.24	1.05
Crystal size (mm)	0.64 × 0.28 × 0.22	0.44 × 0.38 × 0.05
No. of measured, independent and observed [$I > 2\sigma(I)$] reflections	73944, 11420, 8251	48938, 8277, 5854
R_{int}	0.086	0.113
$R[F^2 > 2\sigma(F^2)]$, $wR(F^2)$, *S*	0.040, 0.088, 1.01	0.062, 0.176, 1.07
No. of reflections	11420	8277
No. of parameters	549	442
$\Delta\rho_{max}$, $\Delta\rho_{min}$ (e Å^{-3})	0.78, −0.82	1.07, −1.01

Table 14. Crystallographic details for **78, 79**, and **81.**

	78	**79**	**81**
Chemical formula	$C_{22}H_{13}S_2Sb$	$C_{32}H_{21}Cl_4O_3S_2Sb$	$C_{28}H_{13}F_{12}O_2S_2Sb$
M_r	463.19	781.16	795.25
Crystal system, space group	Triclinic, *P -1*	Triclinic, *P -1*	Monoclinic, $P2_1/c$
a, *b*, *c* (Å)	5.609 (3), 18.295 (11), 19.204 (11)	16.5596 (16), 18.3745 (18), 20.765 (2)	9.243 (3), 19.701 (6), 15.069 (5)
α, β, γ (°)	89.946 (9), 89.967 (9), 82.100 (9)	95.181 (1), 102.240 (1), 98.176 (1)	90, 91.477 (4), 90
V (Å^3)	1952 (2)	6064.3 (10)	2743.0 (15)
Z	4	8	4
μ (mm^{-1})	1.63	1.44	1.27
Crystal size (mm)			0.45 × 0.28 × 0.24
No. of measured, independent and observed [$I > 2\sigma(I)$] reflections	20854, 7891, 3890	71025, 28445, 20435	32021, 6644, 6147
R_{int}	0.126	0.038	0.035
$R[F^2 > 2\sigma(F^2)]$, $wR(F^2)$, *S*	0.079, 0.268, 1.04	0.050, 0.145, 1.02	0.022, 0.052, 1.04
No. of reflections	7891	28445	6644
No. of parameters	451	1496	406
$\Delta\rho_{max}$, $\Delta\rho_{min}$ (e Å^{-3})	2.11, −1.78	8.51, −1.09	0.44, −0.36

Absorption and Emission Spectroscopy. The molar absorption coefficients of **69-72** and [**74**]OTf at λ_{max} were determined according to Beer-Lambert calibration curves (shown below in Figures 137-141). The fluorescence quantum yield of **78** was calculated based on gradients of integrated emission (IE) versus absorbance at λ_{exc} (Abs) for a series of measurements on the sample and fluorescence standard (POPOP in cyclohexane)[311-312] according to the following equation:[149]

$$\Phi_{sample} = \Phi_{std} \times \frac{IE_{sample}}{IE_{std}} \times \frac{Abs_{std}}{Abs_{sample}} \times \left(\frac{\eta_{sample}}{\eta_{std}}\right)^2$$

$$= \Phi_{std} \times \frac{Grad_{sample}}{Grad_{std}} \times \left(\frac{\eta_{sample}}{\eta_{std}}\right)^2$$

where η was taken as 1.4262 for cyclohexane and as 1.4241 for CH_2Cl_2. The resulting gradient plot obtained is shown below in Figure 142.

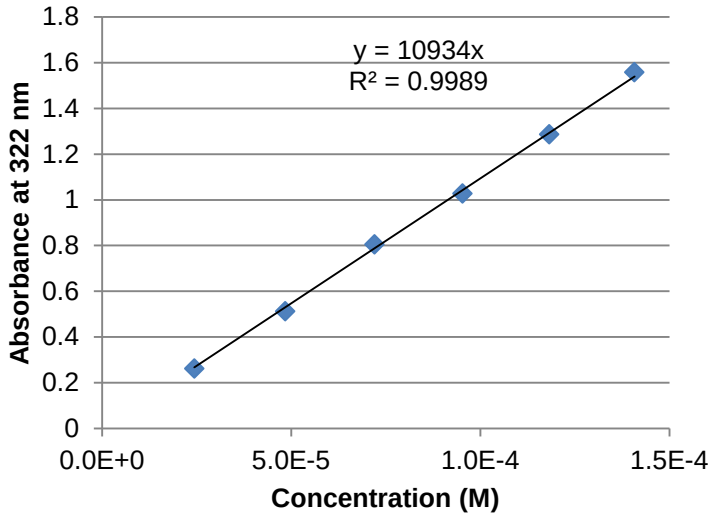

Figure 137. Beer-Lambert absorbance plot for **69**.

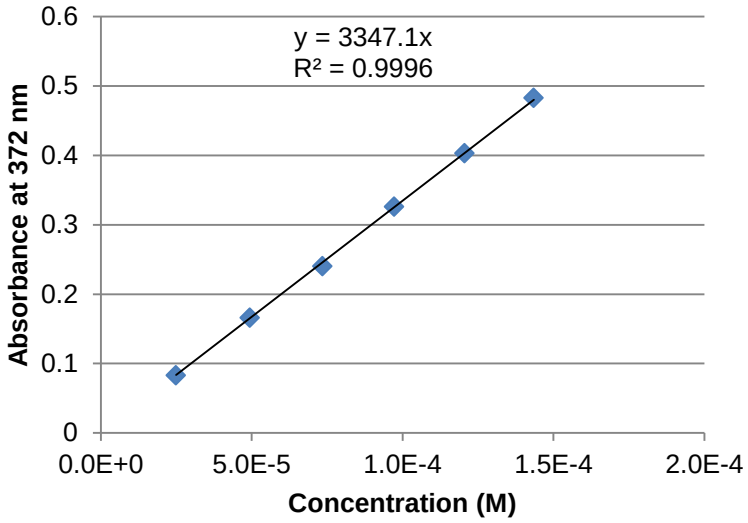

Figure 138. Beer-Lambert absorbance plot for **70**.

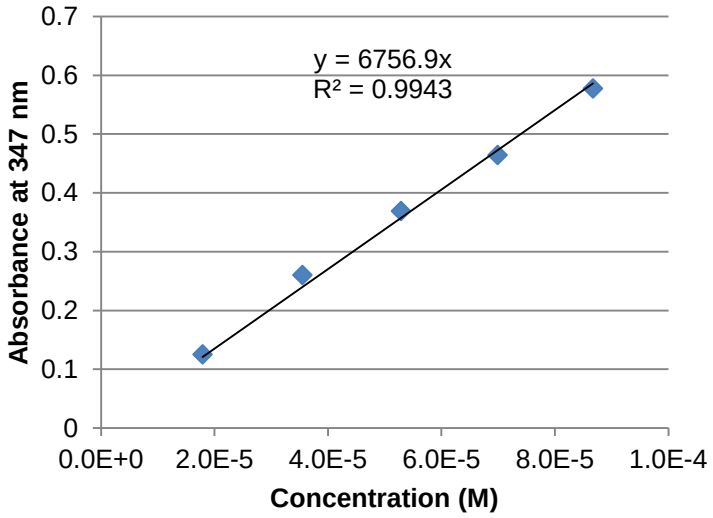

Figure 139. Beer-Lambert absorbance plot for **71**.

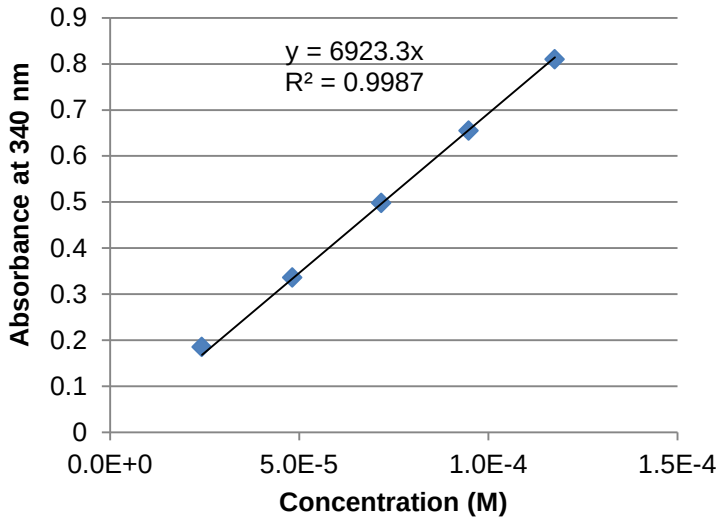

Figure 140. Beer-Lambert absorbance plot for **72**.

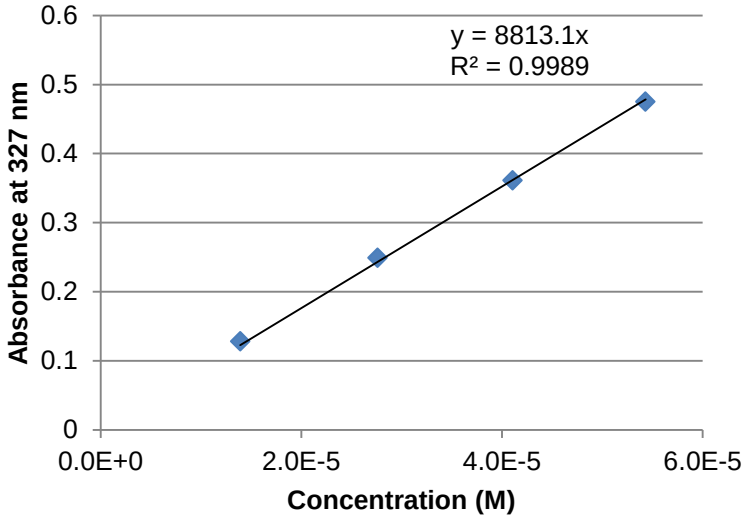

Figure 141. Beer-Lambert absorbance plot for [**74**]OTf.

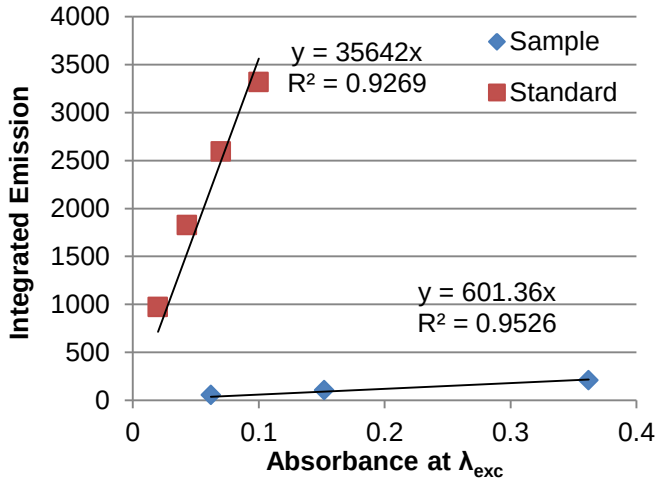

Figure 142. Quantum yield gradient plot for **78**.

Fluoride Binding of [74]OTf. A 1.05×10^{-4} M solution of [**74**]OTf in $CHCl_3$ was treated with incremental aliquots of TBAF and the UV absorption spectrum obtained after 1 minute of mixing at each point. The resulting changes in the spectra are shown below in Figure 143.

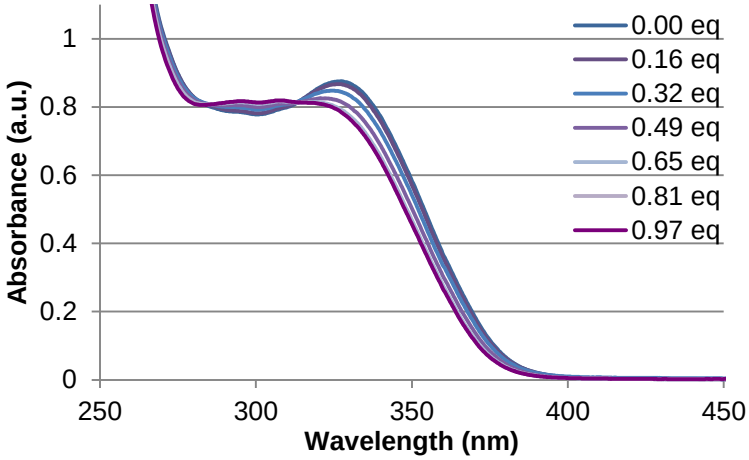

Figure 143. Changes in UV absorption spectrum of [**74**]OTf upon incremental addition of TBAF in $CHCl_3$.

Fluoride Addition to 71 and 72 in Aqueous Mixtures. Solutions of **71** and **72** were prepared in a 7:3 THF:H_2O mixture and treated with an excess of aqueous TBAF. The UV-vis absorption spectra obtained are shown below in Figure 144.

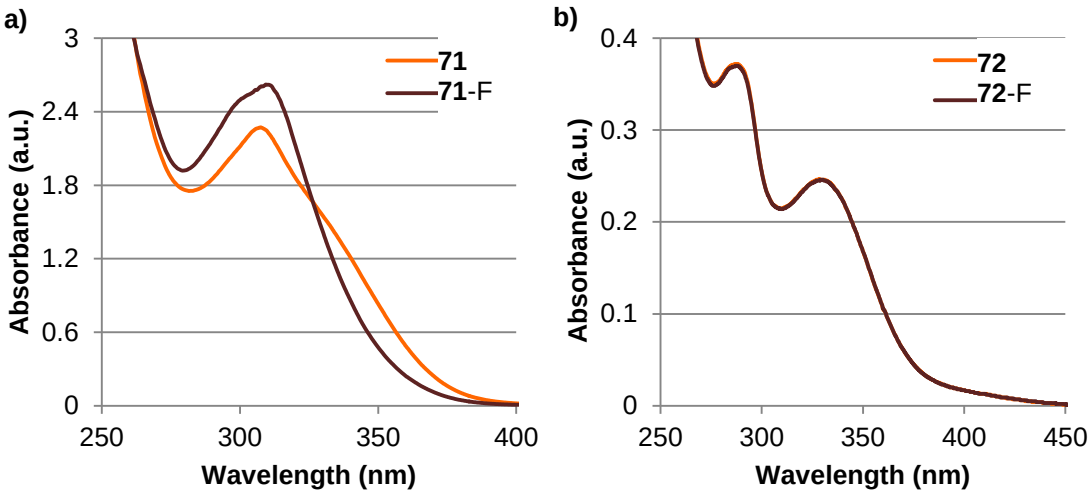

Figure 144. UV-vis absorption spectra for a) **71** and b) **72** before and after the addition of excess TBAF in 7:3 THF:H_2O.

General Procedure for Biphasic Fluoride Sensing with 71. 1-mL samples of 5.9×10^{-4} M **71** in CH_2Cl_2 were layered with 5-mL samples of water containing 10 mM citrate buffer (pH 4.2) and 20 mM TPABr. The biphasic mixture was shaken vigorously for 1 minute, and the layers were allowed to partition. 300 μL aliquots were then taken from the organic layer and diluted tenfold in CH_2Cl_2 in order to obtain UV-vis absorption spectra.

Biphasic Anion Selectivity of 71. 1-mL samples of 5.9×10^{-4} M **71** in CH_2Cl_2 were treated biphasically according to the general procedure with 5-mL aliquots of water containing 5 equivalents of various anions (F^-, Cl^-, Br^-, I^-, CH_3COO^-, NO_3^-) as sodium or potassium salts. 300 μL from the organic layer were diluted tenfold in CH_2Cl_2 and the resulting absorption spectra measured (Figure 145).

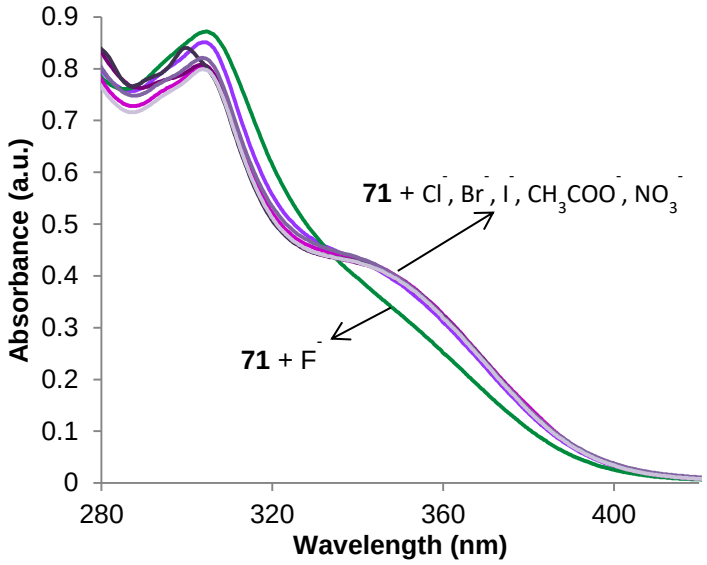

Figure 145. UV-vis absorption spectra for biphasic addition of anions to **71** (5.9×10^{-4} M).

7. CONCLUSIONS

7.1 Summary

The research described herein has focused on developing the chemistry of heavy Group 15-incorporating compounds with improved photophysical properties for applications in chemical sensing. To this end, we have synthesized and studied the properties of antimony(V)-based fluorescent and colorimetric sensors for fluoride and cyanide anions, an antimony-based fluorescent sensor for peroxide, a phosphorus-based fluorescent sensor for gold(III) ions in aqueous solution, and antimony(III)- and antimony(V)-incorporating heterocycles featuring direct interaction of the heavy main group element with the organic π system. In each of these studies, we have focused on the fundamental scientific question: how does chemistry at the main group element modulate the color and/or luminescence properties of the compound? Through thorough structural and spectroscopic characterization supported by DFT computational methods, we have sought to uncover the mechanisms of the sensing response observed in each of these compounds. Thus, we have not only developed new examples of phosphorus- and antimony-based chemical sensors, but also established an understanding of principles governing their function that will benefit the design of main group element-based sensors in the future.

We have previously shown that Lewis acidic organoantimony(V) compounds can act as fluorescent and/or colorimetric sensors for fluoride anions, even in aqueous media.[22, 24-26] However, our initially-reported sensors suffered from low fluorescent

quantum yields and/or absorption in the UV range. We therefore explored the substitution of antimony(V) Lewis acids with more intensely fluorescent and colored groups. In one case, we synthesized and structurally characterized a highly fluorescent BODIPY dye substituted by a Lewis acidic methylstibonium group.[313] Compound [**30**]$^+$ shows evidence for selective binding of fluoride and cyanide in acetonitrile, which is accompanied by an approximate doubling of the fluorescence intensity, allowing this compound to be used as a dual sensor for these two anions. Computational studies indicate that this "turn-on" response originates from the interference of antimony-based σ* orbitals with the BODIPY emission in stibonium [**30**]$^+$ via an excited-state mechanism; anion binding at the Sb(V) center neutralizes this effect and restores strong fluorescence. We propose this excited-state mechanism to be a general phenomenon for "turn-on" anion sensors based on stibonium-decorated fluorophores, based on this and prior work.[100] This sensor is the first we have reported showing a "turn-on" response to cyanide anions in addition to fluoride, hinting at the possibility of expanding the scope of Lewis acidic antimony(V)-based sensors.

In another case, we explored a luminescent antimony(III)-substituted derivative of fluorescein as a sensor for peroxide. In contrast to the analogous phosphine-decorated fluorescein, which increases its fluorescence with oxidation at phosphorus, compound **34** displayed a complete "turn-off" of both color and fluorescence upon reaction with peroxide. This response was found to be the result of stibine oxide spirocyclization with the fluorescein structure, which results in a loss of π conjugation across the fluorophore.

The divergent reactivity between the antimony and phosphorus derivatives stems from the difference in the ability of antimony to support discrete double bonds with oxygen.

The phosphine-decorated fluorescein derivative **39** was further investigated as a reaction- and coordination-based sensor for late transition metals.[178] Although a number of fluorescent phosphines have been reported as sensors for peroxide based on oxidation of the phosphorus atom, the effect of metal coordination on the photophysical properties of a phosphine-bound fluorescent group had not been well studied. Two gold(I) complexes of compound **39** were structurally and spectroscopically characterized and showed that the phosphine-gold complexes display greatly increased fluorescence compared to the free ligand, in which photoinduced electron transfer effects from the lone-pair-bearing phosphine cause low emission. We then tested **39** in a simple sensing system for metal ions in aqueous solution; the fluorophore shows a "turn-on" response to gold, silver, and mercury, with an especially dramatic response to gold(III) species that is detectable even at gold(III) concentrations into the nanomolar range. The selectivity and sensitivity for gold(III) was determined to be the result of a unique "double turn-on" response in which one equivalent of phosphine is oxidized by gold(III) while another equivalent coordinates to the gold(I) species thus formed, both of which processes result in products with greatly increased fluorescence. This study showed the potential for phosphine donor groups to be used in sensitive and selective PeT-based sensors for late transition metals.

We explored another class of strong chromophore by synthesizing a cyclometalated ruthenium polypyridyl complex substituted with a Lewis acidic

stibonium group. The strong electron-withdrawing effect of the antimony(V) group results in a pronounced blueshift in the MLCT absorption bands of the metal complex as well as a shift in the ruthenium(II/III) redox couple to higher potential. Fluoride or cyanide binding at the antimony(V) center of **52** modulates this electron-withdrawing effect and thus induces a colorimetric and electrochemical change in the complex. The behavior of **52** parallels the behavior of a previously-reported borane-substituted ruthenium polypyridyl complex, although the binding of cyanide is weaker in the case of the antimony-based sensor. Complex **52** nevertheless represents a rationally designed colorimetric anion sensor based on antimony.

Finally, as an alternative to Sb-based sensors bearing the chromophore or fluorophore as a pendant side group, we have begun to explore the incorporation of antimony(III) and antimony(V) centers within the framework of π-conjugated dye structures. We hypothesized that this strategy could allow for the rational design of chemical sensors in which the analyte recognition at the main group center directly affects the structure and thus photophysical properties of the chromophore or fluorophore. We have therefore investigated the synthesis of antimony-containing heterocycles including substituted benzostiboles and dibenzothienostiboles. In both cases, computational studies confirm that the antimony atom participates in the π conjugation of the heterocycle via low-lying σ* orbitals. In the simple case of benzostiboles, substitution of a phenyl ligand with an electron-withdrawing chloride ligand at antimony(III) dramatically stabilizes the antimony-based σ* orbital and thereby the π* LUMO, inducing a 50-nm redshift in the lowest-energy absorption band of the

molecule. Oxidation of antimony(III) to antimony(V) to obtain spirocyclic benzostibole catecholates similarly stabilizes the σ* orbital and imparts color to these compounds by narrowing the π-π* energy gap. Fluoride binding to these neutral Lewis acids engages the σ* orbital in forming the Lewis adduct, removing its contribution to the π conjugation and causing a colorimetric "turn-off" response. In the case of **71**, this fluoride binding effect can be observed even upon exposure of **71** to aqueous samples of fluoride under biphasic conditions, in a sensing system competent in the analysis of drinking water samples containing ppm levels of fluoride. Similarly, antimony(III) and antimony(V) dibenzothienostiboles showed evidence for involvement of the antimony-based σ* orbital in the π conjugation of a more extended, luminescent heterocycle. Though practically limited due to decomposition of the dibenzothiophene backbone, **79** also displays a strong colorimetric "turn-off" response to fluoride along with a small fluorescent "turn-on" response. Our initial results with these compounds provide a proof of concept for our hypothesis that antimony incorporation into π-conjugated structures can provide direct control over the photophysical properties of the molecule.

7.2 Future directions

The work we have described points the way toward new possible avenues for application of Group 15 compounds as chemical sensors and in color-tunable materials. In our studies of antimony-substituted fluorophores and chromophores, we have obtained initial evidence that antimony(V) Lewis acids may show selective binding of anions other than fluoride, including cyanide and potentially azide. Further studies could

be carried out to design antimony-based sensors that are selective for cyanide, azide, or other anions. Solvent conditions are an important consideration in achieving selectivity in anion binding, since the solvent will affect the relative basicity and binding strength of different anions. For practical application, however, these sensors would need to be designed to function in water or biphasic mixtures. The incorporation of water-solubilizing groups such as alcohols or sulfonates on the sensor compound may be necessary to achieve full aqueous compatibility, in such a way as not to impede the function of the Lewis acidic moiety.

In addition to anions, antimony-based sensors may be designed for neutral species of interest, as we have shown for peroxide in the case of compound **35**. In that case, the sensing response is a result of oxidation of antimony(III) by the peroxide species and subsequent cyclization of the stibine oxide group with the dye structure. Similar sensors for peroxide could be designed based on this strategy, with modifications of the dye structure to achieve stronger color and/or fluorescence and aqueous solubility. Such developments would also provide an application for antimony(III) compounds in chemical sensing, as complements to the antimony(V) compounds we have previously studied.

Our study of phosphinofluorescein **39** as a "turn-on" sensor for gold(III) ions in water shows that phosphine donor groups can be used within PeT-based sensors not only for peroxide or ROS detection, but also for heavy late metal detection. As larger, softer donor groups than N- or O-donors, phosphines can confer selectivity for heavier, softer metals such as gold, silver, and mercury, for which relatively few molecular sensors

have been developed to date. While substantial selectivity for gold(III) was achieved in our system using a single phosphine donor group, the combination of phosphines with other donor groups within PeT sensors could be explored to obtain selectivity for other metal species. This strategy may find utility in environmental analysis and potentially biological monitoring of heavy late metal species, which will be beneficial as the use of these metals in industrial catalysis, pharmaceutical synthesis, and therapeutics continues to grow.

Finally, the incorporation of antimony(III) and antimony(V) groups within π-conjugated frameworks could enable the development of designed sensors and materials with controllable color. In the case of benzostiboles **69**-**77**, differential substitution, oxidation, and/or anion binding at the antimony centers directly influenced the absorption properties of the molecule based on the extent of interaction of antimony-based σ* orbitals with the π* orbital of the conjugated system. In the compounds we have studied, the absorption bands remained in the near UV and the colorimetric response of **71** and **72** to anion binding registered as a "turn-off" of the yellow color. However, the results also point the way toward a design strategy for more efficient sensors with longer-wavelength absorptions. First, the installation of more electron-withdrawing substituents at antimony should increase the σ* contribution to the LUMO and redshift absorption. Although the chloride ligand we explored in compound **70** did not appear stable toward antimony oxidation, other electron-withdrawing ligands such as C_6F_5 could be explored in future work. These ligands would also be expected to further increase the Lewis acidity of Sb(V) derivatives.[36, 102] Second, further extension of the π-

conjugated heterocyclic framework about antimony would also be expected to shift absorption further into the visible range. With a sufficiently redshifted absorbance band in such a heterocycle, the "turn-off" response observed in **71** and **72** would instead be observed as a color change from longer- to shorter-wavelength visible absorption (Figure 146). This type of response would offer the possibility of ratiometric sensing with these antimony-based chromophores, a strategy that increases sensor sensitivity by providing a built-in correction for environmental and instrumental interferences.[105, 131, 234, 244, 314]

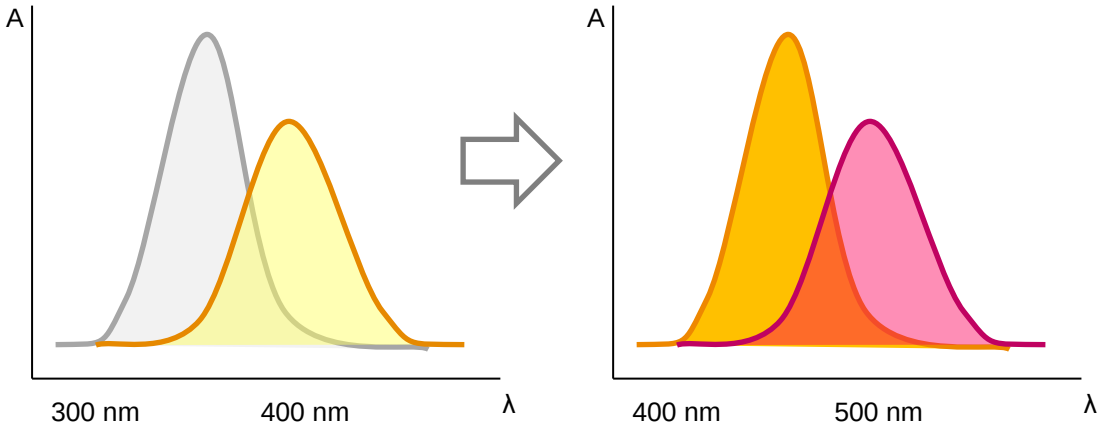

Figure 146. Conceptual scheme for the conversion of "turn-off" colorimetric sensors to dual-color ratiometric sensors by extending absorption farther into the visible range.

Our synthesis of dibenzothienostiboles **78**-**82** represent an initial step in this direction and also shows the effect of an antimony group on a luminescent framework. Again, we saw relatively high-energy absorption bands and excitation in the UV range was required to observe emission; however, the absorption and emission were much further redshifted than in the case of the benzostiboles. In fact, the colorimetric "turn-

off" response observed for fluoride addition to **79** could potentially be monitored ratiometrically, although the absorption band that increases is in the near UV rather than the visible range. Thus, similar antimony-incorporating extended π frameworks could be explored in the future to obtain visible-wavelength ratiometric sensors by the same strategy. Many variations in the conjugated structure could be envisioned for these compounds, potentially allowing for the development of a whole new class of π-conjugated organoantimony materials.

Finally, these studies suggest the intriguing possibility of using antimony within organic/inorganic hybrid materials in order to control the optoelectronic properties of those materials. Our preliminary syntheses of pinacolborane-substituted benzostiboles **75** and **76** show that antimony-containing heterocycles can display similar solid-state luminescence properties to the previously-reported tellurium-containing systems. The interaction of the σ* orbital at antimony with the π* LUMO appears to have similar effects on the optoelectronic properties of the materials as have been reported for other heavy main group elements.[7, 294-295, 315-316] However, the diverse possibilities for substitution, oxidation, and/or Lewis adduct formation at antimony centers offer superior opportunities for tuning of those properties compared to Group 14 or Group 16 elements. Thus, the incorporation of antimony centers into π-conjugated molecules and materials may find further applications outside of the realm of chemical sensing.

REFERENCES

1. Power, P. P.; Gabbaï, F. P. *Inorg. Chem.* **2011,** *50*, 12221-12222.

2. Fischer, R. C.; Power, P. P. *Chem. Rev.* **2010,** *110*, 3877-3923.

3. Power, P. P. *Chem. Rev.* **1999,** *99*, 3463-3504.

4. Shigehiro, Y.; Kohei, T. *Chem. Lett.* **2005,** *34*, 2-7.

5. Baumgartner, T.; Réau, R. *Chem. Rev.* **2006,** *106*, 4681-4727.

6. Priegert, A. M.; Rawe, B. W.; Serin, S. C.; Gates, D. P. *Chem. Soc. Rev.* **2016,** *45*, 922-953.

7. Parke, S. M.; Boone, M. P.; Rivard, E. *Chem. Commun.* **2016,** *52*, 9485-505.

8. Power, P. P. *Nature* **2010,** *463*, 171-177.

9. Housecroft, C. E.; Sharpe, A. G. *Inorganic Chemistry*. 4th ed.; Pearson: Harlow, England, 2012.

10. Burt, J.; Levason, W.; Reid, G. *Coord. Chem. Rev.* **2014,** *260*, 65-115.

11. J. Holmes, N.; Levason, W.; Webster, M. *J. Chem. Soc., Dalton Trans.* **1997**, 4223-4230.

12. Benjamin, S. L.; Reid, G. *Coord. Chem. Rev.* **2015,** *297–298*, 168-180.

13. Gutmann, V.; Hubacek, H.; Steininger, A. *Monatsh. Chem.* **1964,** *95*, 678-686.

14. Olah, G. A.; Schlosberg, R. H. *J. Am. Chem. Soc.* **1968,** *90*, 2726-2727.

15. Olah, G. A. *J. Org. Chem.* **2005,** *70*, 2413-2429.

16. Krossing, I.; Raabe, I. *Chem. Eur. J.* **2004,** *10*, 5017-5030.

17. Gray, P. A.; Burford, N. *Coord. Chem. Rev.* **2016,** *324*, 1-16.

18. Chitnis, S. S.; Robertson, A. P. M.; Burford, N.; Patrick, B. O.; McDonald, R.; Ferguson, M. J. *Chem. Sci.* **2015,** *6*, 6545-6555.

19. Robertson, A. P. M.; Chitnis, S. S.; Jenkins, H. A.; McDonald, R.; Ferguson, M. J.; Burford, N. *Chem. Eur. J.* **2015,** *21*, 7902-7913.

20. Raţ, C. I.; Silvestru, C.; Breunig, H. J. *Coord. Chem. Rev.* **2013,** *257*, 818-879.

21. Wade, C. R.; Broomsgrove, A. E. J.; Aldridge, S.; Gabbaï, F. P. *Chem. Rev.* **2010,** *110*, 3958-3984.

22. Hirai, M.; Myahkostupov, M.; Castellano, F. N.; Gabbaï, F. P. *Organometallics* **2016,** *35*, 1854-1860.

23. Zhao, H.; Leamer, L. A.; Gabbai, F. P. *Dalton Trans.* **2013,** *42*, 8164-8178.

24. Wade, C. R.; Ke, I.-S.; Gabbaï, F. P. *Angew. Chem. Int. Ed.* **2012,** *51*, 478-481.

25. Ke, I.-S.; Myahkostupov, M.; Castellano, F. N.; Gabbaï, F. P. *J. Am. Chem. Soc.* **2012,** *134*, 15309-15311.

26. Hirai, M.; Gabbai, F. P. *Chem. Sci.* **2014,** *5*, 1886-1893.

27. Hansmann, M. M.; López-Andarias, A.; Rettenmeier, E.; Egler-Lucas, C.; Rominger, F.; Hashmi, A. S. K.; Romero-Nieto, C. *Angew. Chem. Int. Ed.* **2015**, n/a-n/a.

28. Yamaguchi, S.; Akiyama, S.; Tamao, K. *J. Am. Chem. Soc.* **2001,** *123*, 11372-11375.

29. Stephan, D. W.; Erker, G. *Angew. Chem. Int. Ed.* **2010,** *49*, 46-76.

30. Stephan, D. W. *J. Am. Chem. Soc.* **2015,** *137*, 10018-10032.

31. Abakumov, G. A.; Poddel'sky, A. I.; Grunova, E. V.; Cherkasov, V. K.; Fukin, G. K.; Kurskii, Y. A.; Abakumova, L. G. *Angew. Chem. Int. Ed.* **2005,** *44*, 2767-2771.

32. Poddel'sky, A. I.; Kurskii, Y. A.; Piskunov, A. V.; Somov, N. V.; Cherkasov, V. K.; Abakumov, G. A. *Appl. Organomet. Chem.* **2011,** *25*, 180-189.

33. Smolyaninov, I. V.; Antonova, N. A.; Poddel'sky, A. I.; Smolyaninova, S. A.; Osipova, V. P.; Luzhnova, S. A.; Berberova, N. T.; Pimenov, Y. T. *Appl. Organomet. Chem.* **2014,** *28*, 274-279.

34. Cherkasov, V. K.; Abakumov, G. A.; Grunova, E. V.; Poddel'sky, A. I.; Fukin, G. K.; Baranov, E. V.; Kurskii, Y. V.; Abakumova, L. G. *Chem. Eur. J.* **2006,** *12*, 3916-3927.

35. Stephan, D. W. *Acc. Chem. Res.* **2015,** *48*, 306-316.

36. Pan, B.; Gabbai, F. P. *J. Am. Chem. Soc.* **2014,** *136*, 9564-7.

37. Hirai, M.; Cho, J.; Gabbaï, F. P. *Chem. Eur. J.* **2016,** *22*, 6537-6541.

38. Morgan, M. M.; Marwitz, A. J. V.; Piers, W. E.; Parvez, M. *Organometallics* **2013,** *32*, 317-322.

39. Parks, D. J.; Piers, W. E.; Yap, G. P. A. *Organometallics* **1998,** *17*, 5492-5503.

40. Qiu, R.; Chen, Y.; Yin, S.-F.; Xu, X.; Au, C.-T. *RSC Adv.* **2012,** *2*, 10774-10793.

41. Lim, C.-H.; Holder, A. M.; Hynes, J. T.; Musgrave, C. B. *Inorg. Chem.* **2013**.

42. Massey, A. G.; Park, A. J. *J. Organomet. Chem.* **1964,** *2*, 245-250.

43. Massey, A. G.; Park, A. J. *J. Organomet. Chem.* **1966,** *5*, 218-225.

44. Moffett, K. D.; Simmler, J. R.; Potratz, H. A. *Anal. Chem.* **1956,** *28*, 1356-1356.

45. Bowen, L. H.; Rood, R. T. *J. Inorg. Nucl. Chem.* **1966,** *28*, 1985-1990.

46. Jean, M. *Anal. Chim. Acta* **1971,** *57*, 438-439.

47. Wade, C. R.; Gabbaï, F. P. *Organometallics* **2011,** *30*, 4479-4481.

48. Hirai, M.; Gabbaï, F. P. *Angew. Chem. Int. Ed.* **2015,** *54*, 1205-1209.

49. Holmes, R. R.; Day, R. O.; Chandrasekhar, V.; Holmes, J. M. *Inorg. Chem.* **1987,** *26*, 157-163.

50. Bissell, R. A.; de Silva, A. P.; Gunaratne, H. Q. N.; Lynch, P. L. M.; Maguire, G. E. M.; Sandanayake, K. R. A. S. *Chem. Soc. Rev.* **1992,** *21*, 187-195.

51. de Silva, A. P.; Fox, D. B.; Huxley, A. J. M.; Moody, T. S. *Coord. Chem. Rev.* **2000,** *205*, 41-57.

52. de Silva, A. P.; Gunaratne, H. Q. N.; Gunnlaugsson, T.; Huxley, A. J. M.; McCoy, C. P.; Rademacher, J. T.; Rice, T. E. *Chem. Rev.* **1997,** *97*, 1515-1566.

53. Chan, J.; Dodani, S. C.; Chang, C. J. *Nat Chem* **2012,** *4*, 973-984.

54. Ueno, T.; Nagano, T. *Nat. Meth.* **2011,** *8*, 642-645.

55. Chen, X.; Zhou, Y.; Peng, X.; Yoon, J. *Chem. Soc. Rev.* **2010,** *39*, 2120-2135.

56. Lin, V. S.; Dickinson, B. C.; Chang, C. J. In *Methods in Enzymology*, Enrique, C.; Lester, P., Eds. Academic Press: 2013; Vol. Volume 526, pp 19-43.

57. Dickinson, B. C.; Huynh, C.; Chang, C. J. *J. Am. Chem. Soc.* **2010,** *132*, 5906-5915.

58. Setsukinai, K.-i.; Urano, Y.; Kakinuma, K.; Majima, H. J.; Nagano, T. *J. Biol. Chem.* **2003,** *278*, 3170-3175.

59. Tanaka, K.; Miura, T.; Umezawa, N.; Urano, Y.; Kikuchi, K.; Higuchi, T.; Nagano, T. *J. Am. Chem. Soc.* **2001,** *123*, 2530-2536.

60. Hirano, T.; Kikuchi, K.; Urano, Y.; Nagano, T. *J. Am. Chem. Soc.* **2002,** *124*, 6555-6562.

61. Cotruvo, J. J. A.; Aron, A. T.; Ramos-Torres, K. M.; Chang, C. J. *Chem. Soc. Rev.* **2015**.

62. Carter, K. P.; Young, A. M.; Palmer, A. E. *Chem. Rev.* **2014,** *114*, 4564-4601.

63. Busschaert, N.; Caltagirone, C.; Van Rossom, W.; Gale, P. A. *Chem. Rev.* **2015,** *115*, 8038-8155.

64. Cametti, M.; Rissanen, K. *Chem. Commun.* **2009**, 2809-2829.

65. Zhou, Y.; Zhang, J. F.; Yoon, J. *Chem. Rev.* **2014,** *114*, 5511-5571.

66. Aaseth, J.; Shimshi, M.; Gabrilove, J. L.; Birketvedt, G. S. *J. Trace Elem. Exp. Med.* **2004,** *17*, 83-92.

67. Briancon, D. *Rev Rhum Engl Ed* **1997,** *64*, 78-81.

68. Zimmer, S. *Caries Research* **2001,** *35(suppl 1)*, 18-21.

69. Jagtap, S.; Yenkie, M. K.; Labhsetwar, N.; Rayalu, S. *Chem. Rev.* **2012,** *112*, 2454-2466.

70. Vallejos-Sanchez, A. A.; Medina-Solis, C. E.; Casanova-Rosado, J. F.; Maupome, G.; Minaya-Sanchez, M.; Perez-Olivares, S. *Acta Odontol. Scand.* **2006** *64*, 209-213.

71. Kalia, L. V.; Lee, L.; Kalia, S. K.; Pirouzmand, F.; Rapoport, M. J.; Aviv, R. I.; Mozeg, D.; Symons, S. P. *Can. J. Neurol. Sci.* **2010,** *37*, 276-278.

72. Kakumanu, N.; Rao, S. D. *New England J. Med.* **2013,** *368*, 1140-1140.

73. Matsuo, S.; Kiyomiya, K.-i.; Kurebe, M. *Arch. Toxicol.* **1998,** *72*, 798-806.

74. Ayoob, S.; Gupta, A. K. *Crit. Rev. Env. Sci. Technol.* **2006,** *36*, 433-487.

75. Singh, B.; Gaur, S.; Garg, V. K. *J. Hazard. Mater.* **2007,** *144*, 147-151.

76. Bo, Z.; Mei, H.; Yongsheng, Z.; Xueyu, L.; Xuelin, Z.; Jun, D. *Environ. Geochem. Health* **2003,** *25*, 421-431.

77. Murray, J. J., Appropriate use of fluorides for human health. World Health Organization: Geneva, 1986. http://apps.who.int/iris/handle/10665/39103?mode=simple (accessed January 9, 2016).

78. Fawell, J. K., Fluoride in Drinking-water: Background document for development of WHO Guidelines for Drinking-water Quality. World Health Organization: Geneva, 2004. http://www.who.int/water_sanitation_health/dwq/chemicals/fluoride.pdf (accessed January 9, 2017).

79. *Fluoride in Drinking Water: A Scientific Review of EPA's Standards*; 978-0-309-10128-8; National Research Council Washington, DC, 2006.

80. Sebelius, K. *Federal Register* **2011,** *76*, 2383-2388.

81. Backgrounder on Uranium Enrichment. U. S. Nuclear Regulatory Commission: 2016. https://www.nrc.gov/reading-rm/doc-collections/fact-sheets/enrichment.html (accessed.

82. Deconversion of Depleted Uranium. U. S. Nuclear Regulatory Commission: 2017. https://www.nrc.gov/materials/fuel-cycle-fac/ur-deconversion.html (accessed.

83. Fischer, E.; Blum, M.-M.; Alwan, W. S.; Forman, J. E. *Pure Appl. Chem.* **2016**.

84. Light, T. S.; Cappuccino, C. C. *J. Chem. Ed.* **1975,** *52*, 247.

85. Itai, K.; Tsunoda, H. *Clin. Chim. Acta* **2001,** *308*, 163-171.

86. Marcus, Y. *J. Chem. Soc., Faraday Trans. 1* **1987,** *83*, 339-349.

87. Schmidtchen, F. P.; Berger, M. *Chem. Rev.* **1997,** *97*, 1609-1646.

88. Hudnall, T. W.; Chiu, C.-W.; Gabbaï, F. P. *Acc. Chem. Res.* **2009,** *42*, 388-397.

89. Lin, T.-P.; Nelson, R. C.; Wu, T.; Miller, J. T.; Gabbai, F. P. *Chem. Sci.* **2012,** *3*, 1128-1136.

90. Wade, C. R.; Lin, T.-P.; Nelson, R. C.; Mader, E. A.; Miller, J. T.; Gabbaï, F. P. *J. Am. Chem. Soc.* **2011,** *133*, 8948-8955.

91. Ke, I.-S.; Jones, J. S.; Gabbaï, F. P. *Angew. Chem. Int. Ed.* **2014,** *53*, 2633-2637.

92. Guan, W.; Yamabe, S.; Sakaki, S. *Dalton Trans.* **2013,** *42*, 8717-8728.

93. Yamaguchi, S.; Akiyama, S.; Tamao, K. *J. Am. Chem. Soc.* **2000,** *122*, 6335-6336.

94. Yamaguchi, S.; Akiyama, S.; Tamao, K. *J. Am. Chem. Soc.* **2001,** *123*, 11372-11375.

95. Yamaguchi, S.; Akiyama, S.; Tamao, K. *J. Am. Chem. Soc.* **2000,** *122*, 6793-6794.

96. Yamaguchi, S.; Akiyama, S.; Tamao, K. *J. Organomet. Chem.* **2002,** *646*, 277-281.

97. Yamaguchi, S.; Akiyama, S.; Tamao, K. *J. Organomet. Chem.* **2002,** *652*, 3-9.

98. Yamaguchi, S.; Shirasaka, T.; Tamao, K. *Organometallics* **2002,** *21*, 2555-2558.

99. Yamaguchi, S.; Wakamiya, A. *Pure Appl. Chem.* **2006,** *78*, 1413-1424.

100. Usui, K.; Ando, M.; Yokogawa, D.; Irle, S. *J. Phys. Chem. A* **2015,** *119*, 12693-12698.

101. Wade, C. R.; Gabbai, F. P. *Z. Naturforsch.* **2014,** *69*, 1199-1205.

102. Tofan, D.; Gabbai, F. P. *Chem. Sci.* **2016,** *7*, 6768-6778.

103. Yoon, S.; Albers, A. E.; Wong, A. P.; Chang, C. J. *J. Am. Chem. Soc.* **2005,** *127*, 16030-16031.

104. Caballero, A.; Martínez, R.; Lloveras, V.; Ratera, I.; Vidal-Gancedo, J.; Wurst, K.; Tárraga, A.; Molina, P.; Veciana, J. *J. Am. Chem. Soc.* **2005,** *127*, 15666-15667.

105. Dong, M.; Wang, Y.-W.; Peng, Y. *Org. Lett.* **2010,** *12*, 5310-5313.

106. Chen, D.-M.; Wang, S.; Li, H.-X.; Zhu, X.-Z.; Zhao, C.-H. *Inorg. Chem.* **2014**.

107. Zhao, N.; Lam, J. W. Y.; Sung, H. H. Y.; Su, H. M.; Williams, I. D.; Wong, K. S.; Tang, B. Z. *Chem. Eur. J.* **2013**, n/a-n/a.

108. Zhang, J. F.; Zhou, Y.; Yoon, J.; Kim, J. S. *Chem. Soc. Rev.* **2011,** *40*, 3416-3429.

109. Singha, S.; Kim, D.; Seo, H.; Cho, S. W.; Ahn, K. H. *Chem. Soc. Rev.* **2015,** *44*, 4367-99.

110. Wang, B.; Fu, T.; Yang, S.; Li, J.; Chen, Y. *Anal. Meth.* **2013,** *5*, 3639-3641.

111. Seo, H.; Jun, M. E.; Ranganathan, K.; Lee, K.-H.; Kim, K.-T.; Lim, W.; Rhee, Y. M.; Ahn, K. H. *Org. Lett.* **2014,** *16*, 1374-1377.

112. Kambam, S.; Wang, B.; Wang, F.; Wang, Y.; Chen, H.; Yin, J.; Chen, X. *Sens. Actuators, B* **2015,** *209*, 1005-1010.

113. Cai, S.; Lu, Y.; He, S.; Wei, F.; Zhao, L.; Zeng, X. *Chem. Commun.* **2013,** *49*, 822-824.

114. Song, F.; Garner, A. L.; Koide, K. *J. Am. Chem. Soc.* **2007,** *129*, 12354-12355.

115. Nyarko, E.; Hara, T.; Grab, D. J.; Habib, A.; Kim, Y.; Nikolskaia, O.; Fukuma, T.; Tabata, M. *Chem. Biol. Interact.* **2004,** *148*, 19-25.

116. Goodman, C. M.; McCusker, C. D.; Yilmaz, T.; Rotello, V. M. *Bioconjugate Chem.* **2004,** *15*, 897-900.

117. Habib, A.; Tabata, M. *J. Inorg. Biochem.* **2004,** *98*, 1696-1702.

118. Ulrich, G.; Ziessel, R.; Harriman, A. *Angew. Chem. Int. Ed.* **2008,** *47*, 1184-1201.

119. Lavis, L. D.; Raines, R. T. *ACS Chem. Biol.* **2014,** *9*, 855-866.

120. Canturk, C.; Ucuncu, M.; Emrullahoglu, M. *RSC Adv.* **2015,** *5*, 30522-30525.

121. Tasan, S.; Zava, O.; Bertrand, B.; Bernhard, C.; Goze, C.; Picquet, M.; Le Gendre, P.; Harvey, P.; Denat, F.; Casini, A.; Bodio, E. *Dalton Trans.* **2013,** *42*, 6102-6109.

122. Vasiuta, R.; Plenio, H. *Chem. Eur. J.* **2016,** *22*, 6353-6360.

123. Esnal, I.; Valois-Escamilla, I.; Gómez-Durán, C. F. A.; Urías-Benavides, A.; Betancourt-Mendiola, M. L.; López-Arbeloa, I.; Bañuelos, J.; García-Moreno, I.; Costela, A.; Peña-Cabrera, E. *ChemPhysChem* **2013,** *14*, 4134-4142.

124. Loudet, A.; Burgess, K. *Chem. Rev.* **2007,** *107*, 4891-4932.

125. Swamy P, C. A.; Mukherjee, S.; Thilagar, P. *Inorg. Chem.* **2014,** *53*, 4813-4823.

126. Swamy P, C. A.; Priyanka, R. N.; Mukherjee, S.; Thilagar, P. *Eur. J. Inorg. Chem.* **2015,** *2015*, 2338-2344.

127. Swamy P, C. A.; Mukherjee, S.; Thilagar, P. *Chem. Commun.* **2013,** *49*, 993-995.

128. Sarkar, S. K.; Thilagar, P. *Chem. Commun.* **2013,** *49*, 8558-8560.

129. P, C. A. S.; Thilagar, P. *Inorg. Chem.* **2014,** *53*, 2776-2786.

130. Liu, S.-R.; Wu, S.-P. *Org. Lett.* **2013,** *15*, 878-881.

131. Wang, B.; Li, P.; Yu, F.; Chen, J.; Qu, Z.; Han, K. *Chem. Commun.* **2013,** *49*, 5790-5792.

132. Wang, B.; Li, P.; Yu, F.; Song, P.; Sun, X.; Yang, S.; Lou, Z.; Han, K. *Chem. Commun.* **2013,** *49*, 1014-1016.

133. Davies, L. H.; Harrington, R. W.; Clegg, W.; Higham, L. J. *Dalton Trans.* **2014,** *43*, 13485-13499.

134. Davies, L. H.; Stewart, B.; Harrington, R. W.; Clegg, W.; Higham, L. J. *Angew. Chem. Int. Ed.* **2012,** *51*, 4921-4924.

135. More, A. B.; Mula, S.; Thakare, S.; Sekar, N.; Ray, A. K.; Chattopadhyay, S. *J. Org. Chem.* **2014,** *79*, 10981-10987.

136. Christianson, A. M.; Gabbai, F. P. *Chem. Commun.* **2017,** *53*, 2471-2474.

137. Benniston, A. C.; Copley, G.; Elliott, K. J.; Harrington, R. W.; Clegg, W. *Eur. J. Org. Chem.* **2008,** *2008*, 2705-2713.

138. Magde, D.; Wong, R.; Seybold, P. G. *Photochem. Photobiol.* **2002,** *75*, 327-334.

139. Porrès, L.; Holland, A.; Pålsson, L.-O.; Monkman, A.; Kemp, C.; Beeby, A. *J. Fluoresc.* **2006,** *16*, 267-273.

140. Addison, A. W.; Rao, T. N.; Reedijk, J.; van Rijn, J.; Verschoor, G. C. *J. Chem. Soc., Dalton Trans.* **1984**, 1349-1356.

141. Shuai, Z.; Wang, D.; Peng, Q.; Geng, H. *Acc. Chem. Res.* **2014,** *47*, 3301-3309.

142. Casalboni, M.; De Matteis, F.; Prosposito, P.; Quatela, A.; Sarcinelli, F. *Chem. Phys. Lett.* **2003,** *373*, 372-378.

143. Chalmers, B. A.; Bühl, M.; Athukorala Arachchige, K. S.; Slawin, A. M. Z.; Kilian, P. *Chem. Eur. J.* **2015,** *21*, 7520-7531.

144. Jiao, L.; Yu, C.; Li, J.; Wang, Z.; Wu, M.; Hao, E. *J. Org. Chem.* **2009,** *74*, 7525-7528.

145. Frisch, M. J.; Trucks, G. W.; Schlegel, H. B.; Scuseria, G. E.; Robb, M. A.; Cheeseman, J. R.; Scalmani, G.; Barone, V.; Mennucci, B.; Petersson, G. A.; Nakatsuji, H.; Caricato, M.; Li, X.; Hratchian, H. P.; Izmaylov, A. F.; Bloino, J.;

Zheng, G.; Sonnenberg, J. L.; Hada, M.; Ehara, M.; Toyota, K.; Fukuda, R.; Hasegawa, J.; Ishida, M.; Nakajima, T.; Honda, Y.; Kitao, O.; Nakai, H.; Vreven, T.; Montgomery Jr., J. A.; Peralta, J. E.; Ogliaro, F.; Bearpark, M. J.; Heyd, J.; Brothers, E. N.; Kudin, K. N.; Staroverov, V. N.; Kobayashi, R.; Normand, J.; Raghavachari, K.; Rendell, A. P.; Burant, J. C.; Iyengar, S. S.; Tomasi, J.; Cossi, M.; Rega, N.; Millam, N. J.; Klene, M.; Knox, J. E.; Cross, J. B.; Bakken, V.; Adamo, C.; Jaramillo, J.; Gomperts, R.; Stratmann, R. E.; Yazyev, O.; Austin, A. J.; Cammi, R.; Pomelli, C.; Ochterski, J. W.; Martin, R. L.; Morokuma, K.; Zakrzewski, V. G.; Voth, G. A.; Salvador, P.; Dannenberg, J. J.; Dapprich, S.; Daniels, A. D.; Farkas, Ö.; Foresman, J. B.; Ortiz, J. V.; Cioslowski, J.; Fox, D. J. *Gaussian 09*, Gaussian, Inc.: Wallingford, CT, USA, 2009.

146. Sheldrick, G. M. *SADABS*, Version 2007/4; Bruker Analytical X-ray Systems Inc.: Madison, Wisconsin, USA, 2007.

147. Sheldrick, G. M. *SHELXTL*, Version 6.1; Bruker Analytical X-ray Systems Inc.: Madison, Wisconsin, USA, 2000.

148. Hubschle, C. B.; Sheldrick, G. M.; Dittrich, B. *J. Appl. Crystallogr.* **2011,** *44*, 1281-1284.

149. Würth, C.; Grabolle, M.; Pauli, J.; Spieles, M.; Resch-Genger, U. *Nat. Protocols* **2013,** *8*, 1535-1550.

150. Shortreed, M.; Kopelman, R.; Kuhn, M.; Hoyland, B. *Anal. Chem.* **1996,** *68*, 1414-1418.

151. Wang, J.; Lin, W.; Yuan, L.; Song, J.; Gao, W. *Chem. Commun.* **2011,** *47*, 12506-12508.

152. Sjöback, R.; Nygren, J.; Kubista, M. *Spectrochim. Acta, Part A* **1995,** *51*, L7-L21.

153. Zhang, X.-F. *Photochem. Photobiol. Sci.* **2010,** *9*, 1261-1268.

154. Han, J.; Burgess, K. *Chem. Rev.* **2009,** *110*, 2709-2728.

155. Nekongo, E. E.; Bagchi, P.; Fahrni, C. J.; Popik, V. V. *Org. Biomol. Chem.* **2012,** *10*, 9214-9218.

156. Ma, Q.-J.; Li, H.-P.; Yang, F.; Zhang, J.; Wu, X.-F.; Bai, Y.; Li, X.-F. *Sens. Actuators, B* **2012,** *166–167*, 68-74.

157. Best, Q. A.; Liu, C.; van Hoveln, P. D.; McCarroll, M. E.; Scott, C. N. *J. Org. Chem.* **2013,** *78*, 10134-10143.

158. Burdette, S. C.; Walkup, G. K.; Spingler, B.; Tsien, R. Y.; Lippard, S. J. *J. Am. Chem. Soc.* **2001,** *123*, 7831-7841.

159. Domaille, D. W.; Que, E. L.; Chang, C. J. *Nat Chem Biol* **2008,** *4*, 168-175.

160. Adhikari, S.; Mandal, S.; Ghosh, A.; Das, P.; Das, D. *J. Org. Chem.* **2015,** *80*, 8530-8538.

161. Wang, T.; Zhao, Q.-J.; Hu, H.-G.; Yu, S.-C.; Liu, X.; Liu, L.; Wu, Q.-Y. *Chem. Commun.* **2012,** *48*, 8781-8783.

162. Komatsu, K.; Kikuchi, K.; Kojima, H.; Urano, Y.; Nagano, T. *J. Am. Chem. Soc.* **2005,** *127*, 10197-10204.

163. Hirano, T.; Kikuchi, K.; Urano, Y.; Higuchi, T.; Nagano, T. *J. Am. Chem. Soc.* **2000,** *122*, 12399-12400.

164. Best, Q. A.; Sattenapally, N.; Dyer, D. J.; Scott, C. N.; McCarroll, M. E. *J. Am. Chem. Soc.* **2013,** *135*, 13365-13370.

165. Koide, Y.; Kawaguchi, M.; Urano, Y.; Hanaoka, K.; Komatsu, T.; Abo, M.; Terai, T.; Nagano, T. *Chem. Commun.* **2012,** *48*, 3091-3093.

166. Koide, Y.; Urano, Y.; Hanaoka, K.; Terai, T.; Nagano, T. *J. Am. Chem. Soc.* **2011,** *133*, 5680-5682.

167. Kawai, K.; Ieda, N.; Aizawa, K.; Suzuki, T.; Miyata, N.; Nakagawa, H. *J. Am. Chem. Soc.* **2013**.

168. Sasakura, K.; Hanaoka, K.; Shibuya, N.; Mikami, Y.; Kimura, Y.; Komatsu, T.; Ueno, T.; Terai, T.; Kimura, H.; Nagano, T. *J. Am. Chem. Soc.* **2011,** *133*, 18003-18005.

169. Choi, M. G.; Cha, S.; Lee, H.; Jeon, H. L.; Chang, S.-K. *Chem. Commun.* **2009**, 7390-7392.

170. Kojima, H.; Nakatsubo, N.; Kikuchi, K.; Kawahara, S.; Kirino, Y.; Nagoshi, H.; Hirata, Y.; Nagano, T. *Anal. Chem.* **1998,** *70*, 2446-2453.

171. Urano, Y.; Kamiya, M.; Kanda, K.; Ueno, T.; Hirose, K.; Nagano, T. *J. Am. Chem. Soc.* **2005,** *127*, 4888-4894.

172. Terai, T.; Tomiyasu, R.; Ota, T.; Ueno, T.; Komatsu, T.; Hanaoka, K.; Urano, Y.; Nagano, T. *Chem. Commun.* **2013,** *49*, 3101-3103.

173. Xiang, Y.; He, B.; Li, X.; Zhu, Q. *RSC Adv.* **2013,** *3*, 4876-4879.

174. Koide, Y.; Urano, Y.; Hanaoka, K.; Piao, W.; Kusakabe, M.; Saito, N.; Terai, T.; Okabe, T.; Nagano, T. *J. Am. Chem. Soc.* **2012,** *134*, 5029-5031.

175. Koide, Y.; Urano, Y.; Hanaoka, K.; Terai, T.; Nagano, T. *ACS Chem. Biol.* **2011,** *6*, 600-608.

176. Shi, J.; Zhang, X.; Neckers, D. C. *J. Org. Chem.* **1992,** *57*, 4418-4421.

177. Baeyer, A. *Ber. Dtsch. Chem. Ges.* **1871,** *4*, 555-558.

178. Christianson, A. M.; Gabbaï, F. P. *Inorg. Chem.* **2016,** *55*, 5828-35.

179. Nagano, T.; Urano, Y. JP2000321262A, 2000.

180. Akasaka, K.; Suzuki, T.; Ohrui, H.; Meguro, H. *Anal. Lett.* **1987,** *20*, 731-745.

181. Onoda, M.; Uchiyama, S.; Endo, A.; Tokuyama, H.; Santa, T.; Imai, K. *Org. Lett.* **2003,** *5*, 1459-1461.

182. Okimoto, Y.; Watanabe, A.; Niki, E.; Yamashita, T.; Noguchi, N. *FEBS Letters* **2000,** *474*, 137-140.

183. Soh, N.; Sakawaki, O.; Makihara, K.; Odo, Y.; Fukaminato, T.; Kawai, T.; Irie, M.; Imato, T. *Bioorg. Med. Chem.* **2005,** *13*, 1131-1139.

184. Pan, J.; Downing, J. A.; McHale, J. L.; Xian, M. *Mol. Biosyst.* **2009,** *5*, 918-920.

185. Lemieux, G. A.; de Graffenried, C. L.; Bertozzi, C. R. *J. Am. Chem. Soc.* **2003,** *125*, 4708-4709.

186. Inoue, N.; Suzuki, Y.; Yokoyama, K.; Karube, I. *Biosci., Biotechnol., Biochem.* **2009,** *73*, 1215-1217.

187. Batsanov, S. S. *Inorg. Mater.* **2001,** *37*, 871-885.

188. Cordero, B.; Gomez, V.; Platero-Prats, A. E.; Reves, M.; Echeverria, J.; Cremades, E.; Barragan, F.; Alvarez, S. *Dalton Trans.* **2008**, 2832-2838.

189. Razuvaev, G. A.; Brilkina, T. G.; Krasilnikova, E. V.; Zinovjeva, T. I.; Filimonov, A. I. *J. Organomet. Chem.* **1972,** *40*, 159-162.

190. Gushchin, A. V.; Dodonov, V. A.; Usyatinsky, R. I.; Koreshkova, E. R.; Tipanov, B. B. *Russ Chem Bull* **1994,** *43*, 1239-1241.

191. Dodonov, V. A.; Fedorov, A. Y.; Usyatinsky, R. I.; Zaburdyaeva, S. N.; Gushchin, A. V. *Russ Chem Bull* **1995,** *44*, 730-733.

192. Stolyarova, T. E.; Shavyr, A. S.; Finet, J.-P.; Fedorov, A. Y. *Russ Chem Bull* **2003,** *52*, 1736-1739.

193. Beckmann, J.; Finke, P.; Hesse, M.; Wettig, B. *Angew. Chem. Int. Ed.* **2008,** *47*, 9982-9984.

194. Matano, Y.; Nomura, H.; Hisanaga, T.; Nakano, H.; Shiro, M.; Imahori, H. *Organometallics* **2004,** *23*, 5471-5480.

195. Bordner, J.; Doak, G. O.; Everett, T. S. *J. Am. Chem. Soc.* **1986,** *108*, 4206-4213.

196. Ferguson, G.; Glidewell, C.; Kaitner, B.; Lloyd, D.; Metcalfe, S. *Acta Crystallogr., Sect. C* **1987,** *43*, 824-826.

197. Kather, R.; Svoboda, T.; Wehrhahn, M.; Rychagova, E.; Lork, E.; Dostal, L.; Ketkov, S.; Beckmann, J. *Chem. Commun.* **2015,** *51*, 5932-5935.

198. Grover, P. K.; Shah, G. D.; Shah, R. C. *J. Chem. Soc.* **1955**, 3982-3985.

199. Levason, W.; McAuliffe, C. A.; Murray, S. G. *J. Organomet. Chem.* **1975,** *88*, 171-174.

200. Lin, Y.; Yin, J.; Yuan, J.; Hu, M.; Li, Z.; Yu, G.-A.; Liu, S. H. *Organometallics* **2010,** *29*, 2808-2814.

201. Osawa, M.; Hoshino, M.; Akita, M.; Wada, T. *Inorg. Chem.* **2005,** *44*, 1157-1159.

202. Cauteruccio, S.; Loos, A.; Bossi, A.; Blanco Jaimes, M. C.; Dova, D.; Rominger, F.; Prager, S.; Dreuw, A.; Licandro, E.; Hashmi, A. S. K. *Inorg. Chem.* **2013,** *52*, 7995-8004.

203. Lifschitz, A. M.; Shade, C. M.; Spokoyny, A. M.; Mendez-Arroyo, J.; Stern, C. L.; Sarjeant, A. A.; Mirkin, C. A. *Inorg. Chem.* **2013,** *52*, 5484-5492.

204. Lim, S.-G.; Blum, S. A. *Organometallics* **2009,** *28*, 4643-4645.

205. Neumann, T.; Dienes, Y.; Baumgartner, T. *Org. Lett.* **2006,** *8*, 495-497.

206. Dienes, Y.; Eggenstein, M.; Karpati, T.; Sutherland, T. C.; Nyulaszi, L.; Baumgartner, T. *Chem.--Eur. J.* **2008,** *14*, 9878-9889.

207. Stolar, M.; Borau-Garcia, J.; Toonen, M.; Baumgartner, T. *J. Am. Chem. Soc.* **2015,** *137*, 3366-3371.

208. Romero-Nieto, C.; Kamada, K.; Cramb, D. T.; Merino, S.; Rodríguez-López, J.; Baumgartner, T. *Eur. J. Org. Chem.* **2010,** *2010*, 5225-5231.

209. Ren, Y.; Linder, T.; Baumgartner, T. *Can. J. Chem.* **2009,** *87*, 1222-1229.

210. Ren, Y.; Baumgartner, T. *Chem. Asian J.* **2010,** *5*, 1918-1929.

211. He, X.; Lin, J.-B.; Kan, W. H.; Dong, P.; Trudel, S.; Baumgartner, T. *Adv. Funct. Mater.* **2014,** *24*, 897-906.

212. He, X.; Borau-Garcia, J.; Woo, A. Y. Y.; Trudel, S.; Baumgartner, T. *J. Am. Chem. Soc.* **2013**.

213. Hay, C.; Fischmeister, C.; Hissler, M.; Toupet, L.; Réau, R. *Angew. Chem. Int. Ed.* **2000,** *39*, 1812-1815.

214. Fave, C.; Cho, T.-Y.; Hissler, M.; Chen, C.-W.; Luh, T.-Y.; Wu, C.-C.; Réau, R. *J. Am. Chem. Soc.* **2003,** *125*, 9254-9255.

215. Dienes, Y.; Eggenstein, M.; Neumann, T.; Englert, U.; Baumgartner, T. *Dalton Trans.* **2006**, 1424-1433.

216. Dienes, Y.; Durben, S.; Kárpáti, T.; Neumann, T.; Englert, U.; Nyulászi, L.; Baumgartner, T. *Chem. Eur. J.* **2007,** *13*, 7487-7500.

217. Chua, C. J.; Ren, Y.; Stolar, M.; Xing, S.; Linder, T.; Baumgartner, T. *Eur. J. Inorg. Chem.* **2014,** *2014*, 1767-1774.

218. Chua, C. J.; Ren, Y.; Baumgartner, T. *Organometallics* **2012,** *31*, 2425-2436.

219. Baumgartner, T.; Neumann, T.; Wirges, B. *Angew. Chem. Int. Ed.* **2004,** *43*, 6197-6201.

220. Baumgartner, T.; Bergmans, W.; Kárpáti, T.; Neumann, T.; Nieger, M.; Nyulászi, L. *Chem. Eur. J.* **2005,** *11*, 4687-4699.

221. Baumgartner, T. *Acc. Chem. Res.* **2014,** *47*, 1613-1622.

222. Wu, Y.; Lai, R. Y. *Anal. Chem.* **2016,** *88*, 2227-2233.

223. Kumeria, T.; Santos, A.; Losic, D. *ACS Appl. Mater. Interfaces* **2013,** *5*, 11783-11790.

224. Wang, Y.; Liu, M.; Cao, R.; Zhang, W.; Yin, M.; Xiao, X.; Liu, Q.; Huang, N. *J. Med. Chem.* **2013,** *56*, 1455-1466.

225. Sivaram, H.; Tan, J.; Huynh, H. V. *Dalton Trans.* **2013,** *42*, 12421-12428.

226. Nobili, S.; Mini, E.; Landini, I.; Gabbiani, C.; Casini, A.; Messori, L. *Med. Res. Rev.* **2010,** *30*, 550-580.

227. Balasingham, R. G.; Williams, C. F.; Mottram, H. J.; Coogan, M. P.; Pope, S. J. A. *Organometallics* **2012,** *31*, 5835-5843.

228. Rudolph, M.; Hashmi, A. S. K. *Chem. Soc. Rev.* **2012,** *41*, 2448-2462.

229. Hashmi, A. S. K.; Rudolph, M. *Chem. Soc. Rev.* **2008,** *37*, 1766-1775.

230. Marion, N.; Nolan, S. P. *Chem. Soc. Rev.* **2008,** *37*, 1776-1782.

231. Hashmi, A. S. K. *Angew. Chem. Int. Ed.* **2005,** *44*, 6990-6993.

232. Inagaki, F.; Matsumoto, C.; Okada, Y.; Maruyama, N.; Mukai, C. *Angew. Chem. Int. Ed.* **2014**, n/a-n/a.

233. Yuan, L.; Lin, W.; Yang, Y.; Song, J. *Chem. Commun.* **2011,** *47*, 4703-4705.

234. Young Choi, J.; Kim, G.-H.; Guo, Z.; Yeon Lee, H.; Swamy, K. M. K.; Pai, J.; Shin, S.; Shin, I.; Yoon, J. *Biosens. Bioelectron.* **2013,** *49*, 438-441.

235. Egorova, O. A.; Seo, H.; Chatterjee, A.; Ahn, K. H. *Org. Lett.* **2010,** *12*, 401-403.

236. Kim, J.-H.; Jeong, Y.-H.; Yoon, H.-J.; Tran, H.; Campos, L. M.; Jang, W.-D. *Chem. Commun.* **2014,** *50*, 11500-11503.

237. Öztaş, Z.; Pamuk, M.; Algi, F. *Tetrahedron* **2013,** *69*, 2048-2051.

238. Chinapang, P.; Ruangpornvisuti, V.; Sukwattanasinitt, M.; Rashatasakhon, P. *Dyes Pigm.* **2015,** *112*, 236-238.

239. Yang, Y.; Yin, C.; Huo, F.; Chao, J. *RSC Adv.* **2013,** *3*, 9637-9640.

240. Zhang, X.-F.; Zhang, J.; Liu, L. *J. Fluoresc.* **2014,** *24*, 819-826.

241. Royzen, M.; Durandin, A.; Young, V. G.; Geacintov, N. E.; Canary, J. W. *J. Am. Chem. Soc.* **2006,** *128*, 3854-3855.

242. Kumaran, R.; Ramamurthy, P. *J. Phys. Chem. B* **2006,** *110*, 23783-23789.

243. Banthia, S.; Samanta, A. *J. Phys. Chem. B* **2006,** *110*, 6437-6440.

244. Ashokkumar, P.; Ramakrishnan, V. T.; Ramamurthy, P. *J. Phys. Chem. A* **2011,** *115*, 14292-14299.

245. Harriman, A. *J. Chem. Soc., Faraday Trans. 2* **1981,** *77*, 1281-1291.

246. Pearson, R. G. *J. Am. Chem. Soc.* **1963,** *85*, 3533-3539.

247. Socol, S. M.; Verkade, J. G. *Inorg. Chem.* **1984,** *23*, 3487-3493.

248. Burmeister, J. L.; DeStefano, N. J. *Inorg. Chem.* **1971,** *10*, 998-1003.

249. Baenziger, N. C.; Bennett, W. E.; Soborofe, D. M. *Acta Crystallogr., Sect. B* **1976,** *32*, 962-963.

250. Whited, M. T.; Rivard, E.; Peters, J. C. *Chem. Commun.* **2006**, 1613-1615.

251. Patel, D. V.; Mihalcik, D. J.; Kreisel, K. A.; Yap, G. P. A.; Zakharov, L. N.; Kassel, W. S.; Rheingold, A. L.; Rabinovich, D. *Dalton Trans.* **2005**, 2410-2416.

252. Uson, R.; Laguna, A.; Laguna, M.; Briggs, D. A.; Murray, H. H.; Fackler, J. P. In *Inorg. Synth.*, John Wiley & Sons, Inc.: 2007; pp 85-91.

253. Diéguez, L.; Darwish, N.; Mir, M.; Martínez, E.; Moreno, M.; Samitier, J. *Sensor Lett.* **2009,** *7*, 851-855.

254. Meyer, T. J. *Acc. Chem. Res.* **1989,** *22*, 163-170.

255. Blakemore, J. D.; Crabtree, R. H.; Brudvig, G. W. *Chem. Rev.* **2015,** *115*, 12974-13005.

256. Prier, C. K.; Rankic, D. A.; MacMillan, D. W. C. *Chem. Rev.* **2013,** *113*, 5322-5363.

257. Li, X.-H.; Shi, Z.; Wang, L.; Cheng, X.; Li, C.; Zhang, A. *Inorg. Chem. Commun.* **2013,** *29*, 175-178.

258. Clarke, M. J. *Coord. Chem. Rev.* **2003,** *236*, 209-233.

259. Howerton, B. S.; Heidary, D. K.; Glazer, E. C. *J. Am. Chem. Soc.* **2012,** *134*, 8324-8327.

260. O'Neill, L.; Perdisatt, L.; O'Connor, C. *J. Phys. Chem. A* **2012,** *116*, 10728-10735.

261. Huang, H.; Zhang, P.; Yu, B.; Chen, Y.; Wang, J.; Ji, L.; Chao, H. *J. Med. Chem.* **2014,** *57*, 8971-8983.

262. Kalyanasundaram, K.; Grätzel, M. *Coord. Chem. Rev.* **1998,** *177*, 347-414.

263. Polo, A. S.; Itokazu, M. K.; Murakami Iha, N. Y. *Coord. Chem. Rev.* **2004,** *248*, 1343-1361.

264. Labat, F.; Ciofini, I.; Hratchian, H. P.; Frisch, M. J.; Raghavachari, K.; Adamo, C. *J. Phys. Chem. C* **2011,** *115*, 4297-4306.

265. Pashaei, B.; Shahroosvand, H.; Graetzel, M.; Nazeeruddin, M. K. *Chem. Rev.* **2016,** *116*, 9485-9564.

266. Bomben, P. G.; Robson, K. C. D.; Koivisto, B. D.; Berlinguette, C. P. *Coord. Chem. Rev.* **2012,** *256*, 1438-1450.

267. Boston, D. J.; Pachón, Y. M. F.; Lezna, R. O.; de Tacconi, N. R.; MacDonnell, F. M. *Inorg. Chem.* **2014,** *53*, 6544-6553.

268. Albrecht, M. *Chem. Rev.* **2010,** *110*, 576-623.

269. Djukic, J.-P.; Sortais, J.-B.; Barloy, L.; Pfeffer, M. *Eur. J. Inorg. Chem.* **2009,** *2009*, 817-853.

270. Constable, E. C.; Holmes, J. M. *J. Organomet. Chem.* **1986,** *301*, 203-208.

271. Reveco, P.; Schmehl, R. H.; Cherry, W. R.; Fronczek, F. R.; Selbin, J. *Inorg. Chem.* **1985,** *24*, 4078-4082.

272. Reveco, P.; Cherry, W. R.; Medley, J.; Garber, A.; Gale, R. J.; Selbin, J. *Inorg. Chem.* **1986,** *25*, 1842-1845.

273. Constable, E. C.; Housecroft, C. E. *Polyhedron* **1990,** *9*, 1939-1947.

274. Sasaki, I.; Vendier, L.; Sournia-Saquet, A.; Lacroix, P. G. *Eur. J. Inorg. Chem.* **2006,** *2006*, 3294-3302.

275. Wade, C. R.; Gabbaï, F. P. *Inorg. Chem.* **2010,** *49*, 714-720.

276. Christianson, A. M.; Gabbaï, F. P. *J. Organomet. Chem.*

277. Colombo, M. G.; Guedel, H. U. *Inorg. Chem.* **1993,** *32*, 3081-3087.

278. Zhou, G.; Ho, C.-L.; Wong, W.-Y.; Wang, Q.; Ma, D.; Wang, L.; Lin, Z.; Marder, T. B.; Beeby, A. *Adv. Funct. Mater.* **2008,** *18*, 499-511.

279. Reveco, P.; Medley, J. H.; Garber, A. R.; Bhacca, N. S.; Selbin, J. *Inorg. Chem.* **1985,** *24*, 1096-1099.

280. Gillard, R. D.; Williams, P. A. *Transition Met. Chem.* **1977,** *2*, 247-251.

281. Sagues, J. A. A.; Gillard, R. D.; Williams, P. A. *Transition Met. Chem.* **1989,** *14*, 110-114.

282. Wade, C. R.; Gabbai, F. P. *Dalton Trans.* **2009**, 9169-9175.

283. Arias Ugarte, R.; Devarajan, D.; Mushinski, R. M.; Hudnall, T. W. *Dalton Trans.* **2016,** *45*, 11150-11161.

284. Sullivan, B. P.; Salmon, D. J.; Meyer, T. J. *Inorg. Chem.* **1978,** *17*, 3334-3341.

285. Ren, Y.; Baumgartner, T. *Dalton Trans.* **2012,** *41*, 7792-7800.

286. Dienes, Y.; Eggenstein, M.; Kárpáti, T.; Sutherland, T. C.; Nyulászi, L.; Baumgartner, T. *Chem. Eur. J.* **2008,** *14*, 9878-9889.

287. Yamaguchi, E.; Wang, C.; Fukazawa, A.; Taki, M.; Sato, Y.; Sasaki, T.; Ueda, M.; Sasaki, N.; Higashiyama, T.; Yamaguchi, S. *Angew. Chem. Int. Ed.* **2015,** *54*, 4539-43.

288. Wang, C.; Fukazawa, A.; Taki, M.; Sato, Y.; Higashiyama, T.; Yamaguchi, S. *Angew. Chem. Int. Ed.* **2015**, n/a-n/a.

289. Jiang, X.-D.; Zhao, J.; Xi, D.; Yu, H.; Guan, J.; Li, S.; Sun, C.-L.; Xiao, L.-J. *Chem. Eur. J.* **2015,** *21*, 6079-6082.

290. Fukazawa, A.; Suda, S.; Taki, M.; Yamaguchi, E.; Grzybowski, M.; Sato, Y.; Higashiyama, T.; Yamaguchi, S. *Chem. Commun.* **2016,** *52*, 1120-1123.

291. Fukazawa, A.; Ichihashi, Y.; Kosaka, Y.; Yamaguchi, S. *Chem. Asian J.* **2009,** *4*, 1729-1740.

292. Ohshita, J. *Chem. Lett.* **2012,** *41*, 1002.

293. Ohshita, J.; Matsui, S.; Yamamoto, R.; Mizumo, T.; Ooyama, Y.; Harima, Y.; Murafuji, T.; Tao, K.; Kuramochi, Y.; Kaikoh, T.; Higashimura, H. *Organometallics* **2010,** *29*, 3239-3241.

294. Rivard, E. *Chem. Lett.* **2015,** *44*, 730-736.

295. He, G.; Kang, L.; Torres Delgado, W.; Shynkaruk, O.; Ferguson, M. J.; McDonald, R.; Rivard, E. *J. Am. Chem. Soc.* **2013,** *135*, 5360-5363.

296. Yan, X.; Xi, C. *Acc. Chem. Res.* **2015,** *48*, 935-946.

297. Carrera, E. I.; Seferos, D. S. *Macromolecules* **2015,** *48*, 297-308.

298. He, G.; Torres Delgado, W.; Schatz, D. J.; Merten, C.; Mohammadpour, A.; Mayr, L.; Ferguson, M. J.; McDonald, R.; Brown, A.; Shankar, K.; Rivard, E. *Angew. Chem. Int. Ed.* **2014,** *53*, 4587-4591.

299. Torres Delgado, W.; Shahin, F.; Ferguson, M. J.; McDonald, R.; He, G.; Rivard, E. *Organometallics* **2016,** *35*, 2140-2148.

300. He, G.; Wiltshire, B. D.; Choi, P.; Savin, A.; Sun, S.; Mohammadpour, A.; Ferguson, M. J.; McDonald, R.; Farsinezhad, S.; Brown, A.; Shankar, K.; Rivard, E. *Chem. Commun.* **2015,** *51*, 5444-5447.

301. Braun, C. A.; Zomerman, D.; de Aguiar, I.; Qi, Y.; Delgado, W. T.; Ferguson, M. J.; McDonald, R.; de Souza, G. L. C.; He, G.; Brown, A.; Rivard, E. *Faraday Discuss.* **2017**.

302. Fagan, P. J.; Nugent, W. A. *J. Am. Chem. Soc.* **1988,** *110*, 2310-12.

303. Fagan, P. J.; Nugent, W. A.; Calabrese, J. C. *J. Am. Chem. Soc.* **1994,** *116*, 1880-1889.

304. Harriman, A. *J. Chem. Soc., Faraday Trans. 2* **1981,** *77*, 1281-1291.

305. Jantunen, K. C.; Scott, B. L.; Kiplinger, J. L. *J. Alloys Compd.* **2007,** *444–445*, 363-368.

306. Gandon, V.; Leca, D.; Aechtner, T.; Vollhardt, K. P. C.; Malacria, M.; Aubert, C. *Org. Lett.* **2004,** *6*, 3405-3407.

307. Brown, H. C.; Bhat, N. G.; Srebnik, M. *Tetrahedron Lett.* **1988,** *29*, 2631-2634.

308. Kang, Y. K.; Deria, P.; Carroll, P. J.; Therien, M. J. *Org. Lett.* **2008,** *10*, 1341-1344.

309. Heynderickx, A.; Samat, A.; Guglielmetti, R. *Synthesis* **2002,** *2002*, 0213-0216.

310. Miyata, K.; Hasegawa, Y.; Kuramochi, Y.; Nakagawa, T.; Yokoo, T.; Kawai, T. *Eur. J. Inorg. Chem.* **2009,** *2009*, 4777-4785.

311. Berlman, I. B. *Handbook of fluorescence spectra of aromatic molecules*. 2nd ed.; Academic Press: New York, 1971.

312. Pavlopoulos, T. G.; Hammond, P. R. *J. Am. Chem. Soc.* **1974,** *96*, 6568-6579.

313. Christianson, A. M.; Gabbai, F. P. *Chem. Commun.* **2017**.

314. Xu, W.-J.; Liu, S.-J.; Zhao, X.-Y.; Sun, S.; Cheng, S.; Ma, T.-C.; Sun, H.-B.; Zhao, Q.; Huang, W. *Chem. Eur. J.* **2010,** *16*, 7125-7133.

315. Ohshita, J. *Macromol. Chem. Phys.* **2009,** *210*, 1360-1370.

316. Tanaka, D.; Ohshita, J.; Ooyama, Y.; Kobayashi, N.; Higashimura, H.; Nakanishi, T.; Hasegawa, Y. *Organometallics* **2013,** *32*, 4136-4141.

APPENDIX

LIST OF COMPOUNDS

$[1]^+$	(*ortho*-Phenylene) borane-stibonium
$[2]^+$	(*ortho*-Phenylene) borane-phosphonium
3	Biphenyl-Sb tetrachlorocatecholate
4	Bis(stiboranyl)xanthene
$[5]^+$	Tris(phosphino)stibine-palladium complex
6	Bis(phosphino)stibine-platinum dichloride
7	Bis(phosphino)stiboranyl-platinum complex
8	Tri(9-anthryl)borane
9-F	Trianthrylfluorosilane
10	Trianthrylphosphine
11	Trianthrylbismuthine
$[12]^+$	9-Anthrylstibonium
$[13]^+$	1-Pyrenylstibonium
$[14]^+$	3-Perylenylstibonium
15	Alizarin red biphenylstiborane
16	$(C_6F_5)_3Sb$ tetrachlorocatecholate
17	*ortho*-Phosphinophenylene $(C_6F_5)_2Sb$ tetrachlorocatecholate
18	*para*-$BMes_2$-BODIPY
19	$BMes_2$-dithiophene-BODIPY
20	$BMes_2$-NPh_3-BODIPY
21	*meta*-$BMes_2$-BODIPY
22	*ortho*-Se-BODIPY
23	*para*-Se-BODIPY
24	PPh_2-BODIPY-Me_2
25	PCy_2-BODIPY-Me_2
26	PPh_2-BODIPY-Ph_2
27	PCy_2-BODIPY-Ph_2
28	Br-BODIPY precursor
29	Sb(III)-BODIPY
$[30]^+$	Sb(V)-BODIPY
31	TPEN-fluorescein Zn2+ sensor
32	*para*-P-fluorescein
33	*para*-P-dichlorofluorescein
34	Sb-fluoresceinOH
35	Sb-fluoresceinOMe

36 SbBr2-fluoresceinOMe
37 Sbchloranil-fluoresceinOMe
38 Sbperfluoropinacol-fluoresceinOMe
39 P-fluorescein
40 P=O-fluorescein
[41a]$^{+}$ Sb-xanthylium
42 P-pyrene
43 P-benzoxadiazole
44 P-hydroxycoumarin
45 P-BODIPY Ph
46 P-BODIPY Cy
47 P-rhodamine Pd sensor
48 (B-ppy)Ru(bpy)2
49 Sb(III)-ppy
50 Sb(V)-ppy
[51]$^{+}$ (bpy)2Ru(SbIII-ppy)
[52]$^{2+}$ (bpy)2Ru(SbV-ppy)
53 Dibenzothienophosphole
54 Dibenzothienophosphole oxide
55 Dibenzothienophosphole AuCl
[56]$^{+}$ Dibenzothienophosphole methyl cation
57 SiMe3-dithienostibole
58 Tolyl dibenzothienostibole
59 Naphtyl dibenzothienostibole
60 SiMe3-dithienobismole-H
61 SiMe3-dithienobismole-Me
62 Dibenzothienobismole
63 (Bpin)2-cyclohexyltellurophene
64 Ph2-benzotellurophene
65 Ph,Bpin-benzotellurophene
66 (Bpin)2-benzotellurophene
67 (Bpin)2Ph2-tellurophene 1
68 (Bpin)2Ph2-tellurophene 2
69 BenzoPh2SbPh
70 BenzoPh2SbCl
71 BenzoPh2SbPh tetrachlorocatecholate
72 BenzoPh2SbPh 3,5-di-t-butylcatecholate
73 BenzoPh2SbPh bis(tetrachlorocatecholate)
[74]$^{+}$ BenzoPh2SbPh methyl triflate
75 BenzoBpinPhSbPh
76 Benzo(Bpin)2SbPh

77 Benzo(Bpin)2SbPh tetrachlorocatecholate
78 Dibenzothienostibole
79 Dibenzothienostibole tetrachlorocatecholate
80 Dibenzothienostibole pinacolate
81 Dibenzothienostibole perfluoropinacolate
82 Dibenzothienostibole catecholate